Diagrammatic perturbation theory based investigations of the Mott transition physics

A Thesis
Submitted For the Degree of
DOCTOR OF PHILOSOPHY
in the Faculty of Science

by

Himadri Barman

THEORETICAL SCIENCES UNIT
JAWAHARLAL NEHRU CENTRE FOR ADVANCED SCIENTIFIC RESEARCH
Bangalore – 560 064

MARCH 2013

DECLARATION

I hereby declare that the matter embodied in the thesis entitled "**Diagrammatic perturbation theory based investigations of the Mott transition physics**" is the result of investigations carried out by me at the Theoretical Sciences Unit, Jawaharlal Nehru Centre for Advanced Scientific Research, Bangalore, India under the supervision of Dr. N. S. Vidhyadhiraja and that it has not been submitted elsewhere for the award of any degree or diploma.

In keeping with the general practice in reporting scientific observations, due acknowledgement has been made whenever the work described is based on the findings of other investigators.

Himadri Barman

CERTIFICATE

I hereby certify that the matter embodied in this thesis entitled "**Diagrammatic perturbation theory based investigations of the Mott transition physics**" has been carried out by Mr. Himadri Barman at the Theoretical Sciences Unit, Jawaharlal Nehru Centre for Advanced Scientific Research, Bangalore, India under my supervision and that it has not been submitted elsewhere for the award of any degree or diploma.

Dr. N. S. Vidhyadhiraja
(Research Supervisor)

Abstract

The interaction driven metal-to-insulator transition, widely known as *Mott transition*, is still an open problem in electronic correlation physics. In this thesis, we use quantum many-body approaches within the framework of dynamical mean-field theory (DMFT) to understand issues related to the Mott transition. Specifically, diagrammatic perturbation theory based approximations have been made for the self-energy associated with the impurity problem in this context. We apply our approaches to the single band Hubbard model, which is a standard and simplest model to study Mott transition physics.

One of our approximation for the self-energy is the iterated perturbation theory (IPT), where a second order diagram constructed using Hartree propagators is used as an ansatz for the self-energy in the particle-hole symmetric case. Though IPT has been extensively used earlier for the Hubbard model, here we develop an improved implementation that can capture the sharp features of the spectral function near the Mott transition. We use analytical approaches as well to predict the residue of the pole that arises in the self-energy at the chemical potential in the Mott insulating and the coexistence regimes. We make successful comparison with pressure dependent resistivity

experiments on Se-doped NiS_2 and resistivity hysteresis found in V_2O_3 . We discuss the optical conductivity in great detail and point out an anomaly that arises in the specific heat calculation.

The second approach, which underlies a major part of this thesis, is another diagrammatic approximation, known as the local moment approach (LMA) for the impurity solver within DMFT. The LMA considers a spin-symmetry broken mean field as its starting point in contrast to the Hartree limit used in IPT. The self-energy ansatz here incorporates spin-flip dynamics to all orders through random phase approximation (RPA). In order to restore the spin-independent Fermi liquid metallic phase, we impose the condition of adiabatic continuity to the non-interacting limit. With this approach, we study properties for the particle-hole symmetric and asymmetric cases both at zero and finite temperature. In the zero temperature symmetric case, we find Mott transition and coexistence regime, similar to what we have already seen in IPT (though values are different). In the metallic regime, apart from the Fermi liquid at very low frequencies, we find a strong correlation induced universal scaling regime which is very different from the renormalized non-interacting limit and extends all the way to infinity as we approach the Mott insulator. We find similar strong-coupling universality in the asymmetric and the finite temperature cases as well. We report the doping dependence of the spectra and compare that to our IPT results. Very interestingly, we find a large T-linear regime in the temperature dependence of resistivity along with presence of negligibly small T^2-regime, specially in the vicinity of a doped Mott insulator. We show that this happens due to the marginal Fermi liquid nature of the self-energy that emerges from our theory. Thus we infer that, presence of local transverse spin-flip scattering can bring a possible scenario where one can indeed observe linear temperature dependence of resistivity extending over a decade or more (in temperature). This could be relevant for understanding the "normal" state of high temperature cuprate superconductors.

The last chapter in this thesis deviates from the other chapters in terms of the techniques, but does conform to the theme of this thesis namely Mott transition physics. In this, we examine the out-of-equilibrium physics associated with the Mott transition, namely hysteresis and avalanches in the resistivity as observed in experiments on transition metal oxides. Since hysteresis is a non-equilibrium phenomenon involving inhomogeneities, the DMFT becomes inappropriate as it is a single-site equilibrium approach. Motivated by recent resistance experiments on VO_2 thin films by Sharoni *et al* (2008), we formulate an approach that may produce the correct statistical behavior associated with the avalanche sizes in the resistance hysteresis experiments (e.g. device size effect, power law behavior). In our approach we use a mapping from the random-field Ising model to a resistor network model. By this scheme we find reasonable agreement with experiments. We also discuss possibilities to get more quantitative agreement and predict results (e.g. dependence of power law exponent on the contrast ratio) that can be verified in future experiments.

Acknowledgements

First I would like to thank my research advisor, Dr. N. S. Vidhyadhiraja (popularly known as Raja), for introducing the world of strongly correlated electronic systems to me. I did a specialization in quantum field-theory during my Masters and hence was intending to pursue academic career of high-energy physics. It is partly Raja's credit that he showed that many-body physics in condensed matter could be no less interesting than cosmology or particle physics. I have always found him to encourage any sort of idea that came up in my mind. I have also collected many technical tips and tricks, programming and UNIX related, from him.

I must thank my graduate school teachers and faculty members, specially Prof. S. Narasimhan, Prof. U. V. Waghmare, Prof. S. Sastry, and Prof. S. K. Pati, Prof. S. Balasubramanian, Prof. N. Chandrabhas, Prof. M. Alam.

I acknowledge Prof. Rahul Pandit, Prof. H. R. Krishnamurthy, Prof. C. Dasgupta, and specially Prof. V. B. Shenoy for his constant effort to encourage students in the field of science.

I am indebted to E. W. Carlson and J. M. Honig of Purdue University and Prof. K. A. Dahmen of University of Illinois, Urbana-Champaign for useful discussions during the APS March meeting 2011 and visit to the Purdue

university.

Though I have barely interacted in person, I must thank Prof. D. E. Logan of Oxford University, for his useful suggestions to our work and Dr. Michael P. Eastwood for resolving some of my basic doubts through emails.

I must not forget to thank my fellow graduate students and labmates. Specially I owe to Sudeshna Sen and Deb Sankar De, who helped me a lot at the last moment of submitting my thesis.

The two-volume book named *Physics for Entertainment* by Yakov Isidorovich Perelman and my school teacher late Rabindranath Mandal deserve gratitude from me for moving me towards physics. Also I owe to my M. Sc. teachers Dr. P. Durganandini and Prof. A. D. Gangal of Pune University, for enhancing and encouraging my interests in theoretical physics.

I am indebted to Dr. Biswajit Santra, who sent me the most number of journals that were inaccessible from our institution.

I coincidentally found my childhood and college friend, Dr. Amit Lahiri, in IISc, Bangalore, who always remained a local support during my stay in Bangalore.

I thank Prof. C. N. R. Rao for being an inspiration for any Indian scientists.

I acknowledge the Department of Science and Technology (DST), Govt. of India, for providing financial support for my research.

Finally I must thank my family for being a constant non-academic support.

Contents

List of Figures

List of acronyms

- **BL:** Bethe lattice
- **DMFT:** dynamical mean field theory
- **FL:** Fermi liquid
- **FWHM:** full width at half-maximum
- **HCL:** hypercubic lattice
- **HM:** Hubbard model
- **IPT:** iterated perturbation theoery
- **LMA:** local moment approach
- **MFL:** marginal Fermi liquid
- **MIT:** metal-to-insulator transition
- **MLE:** maximum likelihood estimation

- **NFL:** non-Fermi liquid

- **RFIM:** random field Ising model

- **RG:** renormalization group

- **RNIL:** renormalized non-interacting limit

- **RPA:** random phase approximation

- **SIAM:** single impurity Anderson model

Chapter 0

Introduction

0.1 Condensed matter physics: a field with wide applications

Physics is a subject of understanding the laws of nature. However, it does not remain limited by finding or explaining such laws. Rather the triumph of modern physics comes after the application or implementation of such laws. Applications ranging from rocket science to today's internet and mobile technology owe to physics in this sense. Since condensed matter physics offers a materials-based approach and all objects that we deal with in our daily life are made of different materials with different physical and chemical states, it has become one of the essential subjects of research underlying our modern technology. Moreover, experiments and tests of theories in this branch are easily accessible compared to that in other contemporary fields, e.g. high-energy and particle physics, and cosmology. Surprisingly many high-energy physics aspects have been realized or potentially realizable in many low-energy solid state materials, e.g. Anderson-Higgs mechanism in superconductors [1], Dirac electrons in graphene [2], Majorana fermions in topological superconductors or the Moor-Read state in fractional quantum Hall effect [3]. Furthermore, the recent anti-de Sitter/conformal field theory (AdS-CFT) correspondence of the string theory could be a breakthrough approach to understand strongly-correlated condensed matter systems, e.g. superfluid-insulator transition near the quantum criticality [4]. Therefore the field of condensed matter physics promises table-top experimental realizations of phenomena with a wide range of energy, length and time scales.

0.2 Early successes in condensed matter physics: From Drudé model to density functional theory

The Drudé [6, 7] model was one of the initial successes that could describe the behavior of most metals. For instance, the residual resistivity at low temperature, the temperature independence of magnetic susceptibility, and the linear temperature dependence of the specific heat at low temperature in many metals (see Fig. 1) can be described through the non-interacting free electron gas picture. Later nearly free electron (NFE) model or the band theory [8] which incorporated the periodic potential of the lattice could

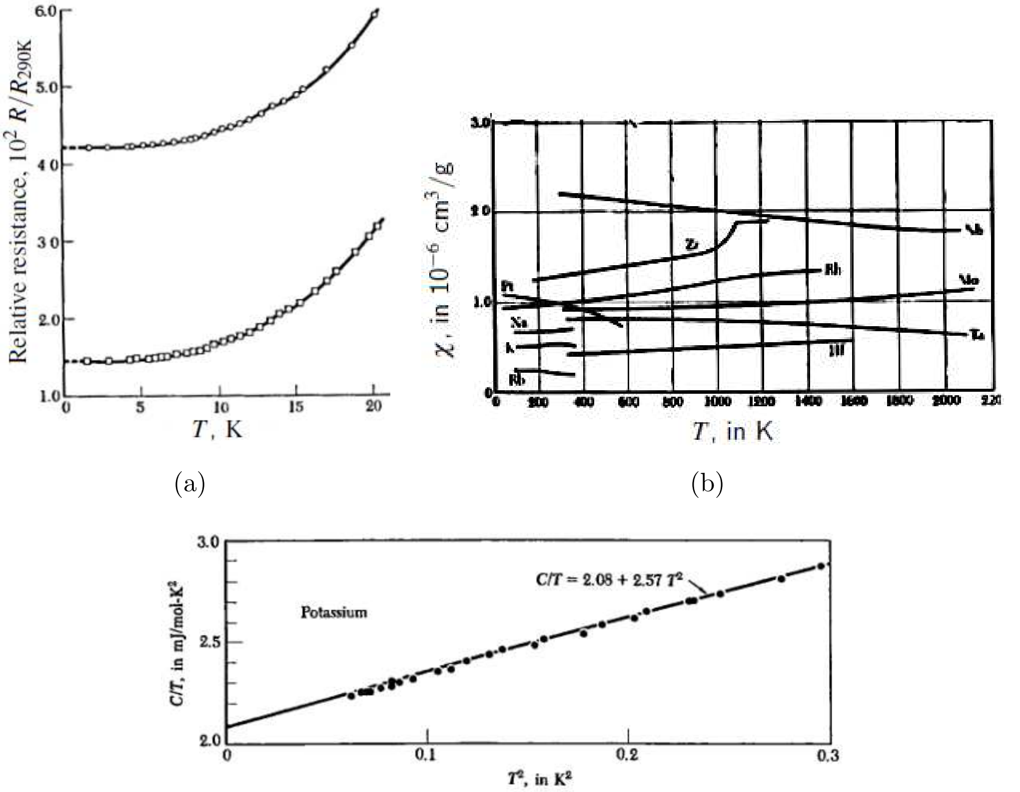

(a)

(b)

(c)

Fig. 1: Behavior of (a) resistivity, (b) susceptibility and (c) specific heat in metals with temperature, follows the Drudé model. However, the T^2 behavior of resistivity (as in (a) for potassium with two different impurity concentrations) has been later explained using the Fermi liquid theory. Reproduced from Kittel's *Introduction to Solid State Physics* [5].

not only describe metals, but turned out to be a powerful approach for describing non-metallic materials, termed as insulators and semiconductors. Band structure calculations have been extended to more realistic situation for many-body electrons by taking the electronic exchange mechanisms and the Coulomb interactions into account in a mean-field way. This is known as the Hartree-Fock theory where the many-body wave functions are written in terms of Slater determinants. However, working with Slater determinants could be extremely expensive for a real material having large number of electrons ($\sim 10^{22}$). An alternative method was developed by W. Kohn and L. J. Sham [9], which enables one to write the many-body ground state energy as a unique functional of the electronic density. This treatment is known as the density functional theory (DFT) and has become successful in predicting ground state for several materials over the last few decades. However, DFT fails to explain wide range of materials that have been described in the next section.

0.3 Strongly correlated electron systems (SCES): an interesting paradigm

Despite huge success of the band theory and the DFT for a range of materials, there remain many classes of solid state materials that are not amenable to these approaches and hence demand new theories. In 1937, de Boer and Verwey [10] reported transparent insulating behavior for transition metal oxides like NiO and CoO even though their incomplete *d*-shells predict them to be metals from the band theory picture. Nevil Mott [11, 12] argued that the Coulombic repulsion between electrons prevents metallicity and hence such materials are coined as *Mott insulators.* Mott insulator can arise from a Fermi liquid metal due to change in the interaction strength and such a metal-to-insulator transition (MIT) is known as the *Mott transition* (see Sec. 0.5 for a detailed discussion). The metals that undergo Mott transitions often show high resistivity and specific heat coefficient (see Fig. 2 for experimental results on V_2O_3 compounds). Thus they are 'bad metals' even though they show good Fermi liquid properties.

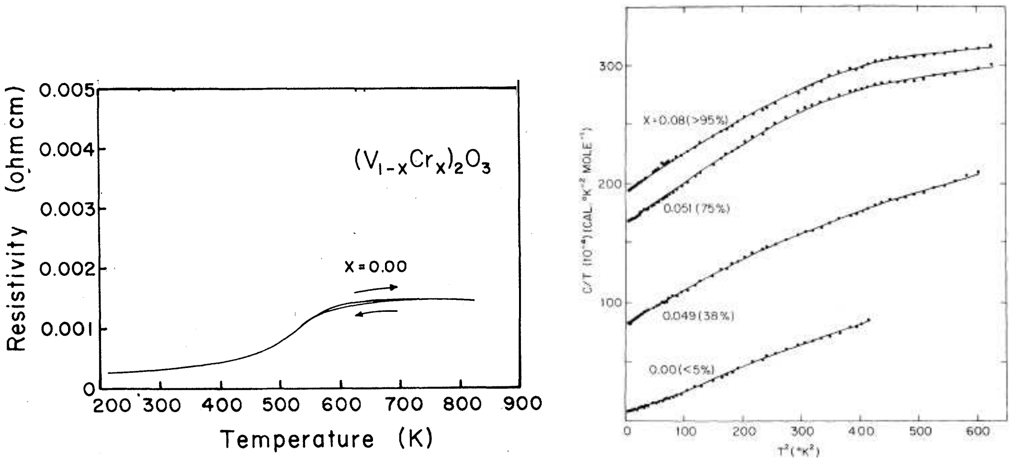

(a) (b)

Fig. 2: (a) High resistivity coefficient in V_2O_3. Reproduced from Ref. 13. (b) High specific heat coefficients ($\gamma = C/T$) for different dopings as functions of squared temperature (from Ref. 14).

Subsequently an interesting feature was found in resistivity experiments on some transition metal compounds containing magnetic impurities. Fig. 3(a) shows that a minimum occurs in the resistivity at a specific temperature in Mo-Nb alloys with dilute impurity of Fe ions. This resistivity minimum remained a paradox until 1964, when Jun Kondo first showed that the minimum arises due to a competition between electron-phonon scattering and spin-spin scattering (that gives rise to a logarithmic dependence of resistivity on temperature [15]). Thereafter this effect was named as the Kondo effect. However, the role of impurity still bears open issues in the context of two classes of materials, namely the Heavy fermions and the Kondo insulators.

A new era of rich physics emerged after the discovery of the high T_c superconductors. For instance, there are metallic regime that shows linear T-dependence of resistivity (Fig. 3(b)). This sort of non-T^2 behavior is believed to arise from an underlying quantum critical point and a non-Fermi liquid (NFL) ground state. Similar NFL behavior has been observed in the resistivity of heavy fermion metals like $\mathrm{CuCe_2Si_2}$ and $\mathrm{YbRh_2Si_2}$ in the vicinity of the quantum critical point (QCP). In those materials, resistivity shows a fractional power law of temperature: $\rho(T) = T^{\epsilon}$,where $1 \leq \epsilon < 2$.

This sort of behavior occurs mainly due to strong electron-electron interaction and all such materials belong to the class called strongly correlated electron systems (SCES) have led to the emergence of a separate paradigm in the field of condensed matter physics. The naming comes from the fact that the electron-electron interaction or correlation becomes comparable or dominant over the electron's kinetic energy in such systems. Apart from the above-mentioned examples, strong correlations have been found to be prevalent in fullerenes [16], graphenes [17] and soft-matter [18] like polymers.

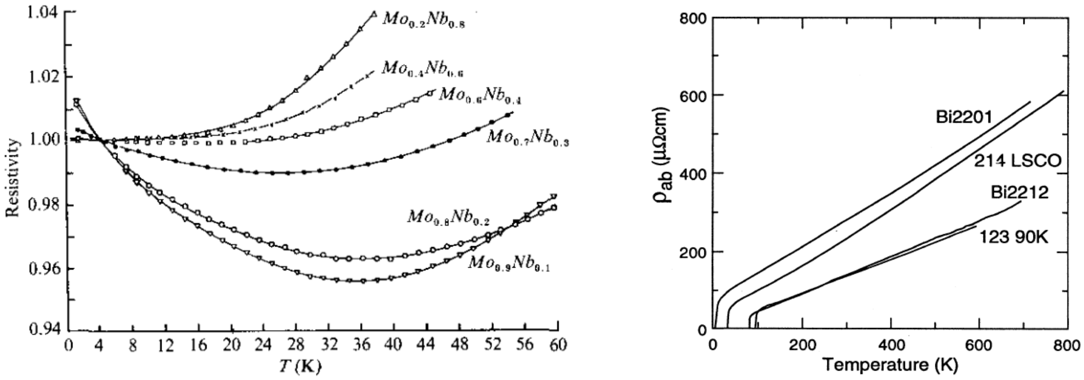

(a) (b)

Fig. 3: (a) Resistivity minima observed in Mo-Nb alloy for different doping with dilute concentration Fe as magnetic impurity, reproduced from the book *The Kondo Problem to Heavy Fermions* by Hewson [19]. (b) Linear behavior of resistivity with temperature in different high-T_c superconductors, reproduced from Ref. [20].

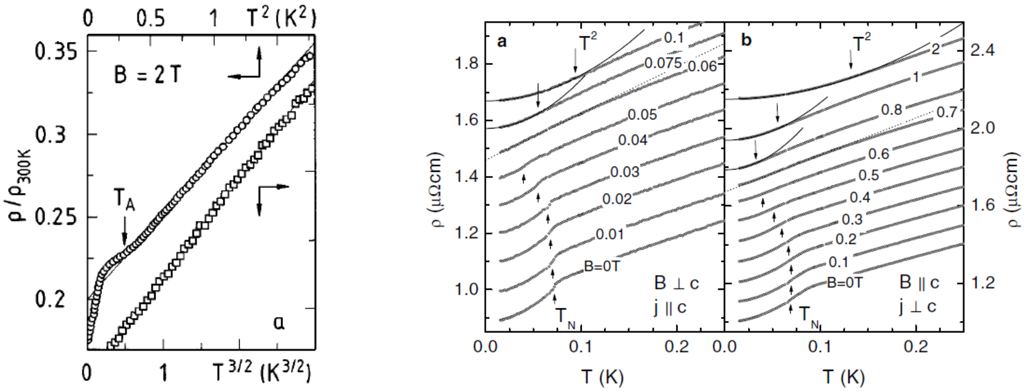

Fig. 4: $\rho(T) = T^{\epsilon}$ behavior with $1 \leq \epsilon < 2$. (a) $CuCe_2Si_2$. (b) $YbRh_2Si_2$. Experiments done by Gegenwart *et al.* [21, 22]

0.4 Microscopic Fermi liquid theory

The low temperature behavior of a large subset of the strongly correlated systems has been observed to be the same as conventional metals or semiconductors, albeit with renormalized parameters, like a large effective mass or a large density of states. Such conventional behavior emerges despite strong electron-electron interactions present in some d or f orbital systems, such as $\mathrm{CeAl_3}$. Lev Landau in 1956 came up with a phenomenological Fermi liquid theory [23, 24] which put the renormalized non-interacting limit on a firm formal footing. The phenomenological idea was that the low energy excitation spectrum due to interactions has a one-to-one correspondence with the non-interacting state and the former state can be achieved by adiabatically[1] switching on the interaction. His empirical arguments were later validated by Abrikosov and Khalatnikov [25] using the formalism of diagrammatic perturbation theory and which has come to be known as microscopic Fermi liquid theory. The non-interacting single particle propagator (Green's function) can be written as

$$\mathcal{G}(\mathbf{k},\omega) = \frac{1}{\omega - \epsilon_{\mathbf{k}} + \mu + i\eta} \tag{1}$$

where $\eta \to 0+$, μ is the chemical potential, and $\epsilon_{\mathbf{k}}$ is the non-interacting dispersion relation ($\epsilon_{\mathbf{k}} = \hbar^2\mathbf{k}^2/(2m)$ for Fermi gases with particle mass m.) Interactions modify the above equation by an extra term $\Sigma(\mathbf{k},\omega)$, known as the self-energy:

$$G(\mathbf{k},\omega) = \frac{1}{\omega - \epsilon_{\mathbf{k}} + \mu - \Sigma(\mathbf{k},\omega) + i\eta} \tag{2}$$

---

[1] In a loose sense, it means *very slowly*

For states close to the Fermi surface, the real and imaginary parts of $\Sigma(\mathbf{k},\omega)$ can be written as Taylor series expansions:

$$\begin{aligned}
\mathrm{Re}\Sigma(\mathbf{k},\omega) &= \mathrm{Re}\Sigma(\mathbf{k}=\mathbf{k}_F,\omega=\mu) - b(\mathbf{k}_F)(\omega-\mu) \\
&\quad - \mathcal{O}((\omega-\mu))^2 + a(\mathbf{k}_F)(k-k_F) + \mathcal{O}((k-k_F)^2) \qquad (3) \\
\mathrm{Im}\Sigma(\mathbf{k},\omega) &= -\Gamma(\omega-\mu))^2 + \mathcal{O}((\omega-\mu))^3 \\
&\quad + \zeta(\mathbf{k}_F)(k-k_F)^2 + \mathcal{O}((k-k_F)^3) \qquad (4)
\end{aligned}$$

This expansion when substituted in the Green's function yields a renormalized Green's function,

$$G^R(\mathbf{k},\omega) \simeq \frac{Z_{\mathbf{k}_F}}{\omega - \epsilon^*(\mathbf{k}-\mathbf{k}_F) + i[Z_{\mathbf{k}_F}\{\Gamma(\omega-\mu)^2 - \zeta(\mathbf{k}_F)(\mathbf{k}-\mathbf{k}_F)^2\}]} \qquad (5)$$

where

$$Z_{\mathbf{k}_F} = \frac{1}{1+b(\mathbf{k}_F)} \qquad (6)$$

and

$$\epsilon^*(\mathbf{k}-\mathbf{k}_F) \simeq Z_{\mathbf{k}_F}[\epsilon_0 + a(\mathbf{k})(\mathbf{k}-\mathbf{k}_F)] \qquad (7)$$

$Z_{\mathbf{k}_F}$ is called the quasiparticle weight or quasiparticle residue. Thus if we ignore the $\mathbf{k}$ dependence (such a situation will be discussed in a forthcoming section), then as $\omega \to \mu$, the imaginary part of the self-energy becomes

$$\mathrm{Im}\Sigma(\omega) \propto -(\omega-\mu)^2 \qquad (8)$$

whereas the real part behaves as

$$\mathrm{Re}\Sigma(\omega) \propto -(\omega - \mu) + \mathrm{const.} \tag{9}$$

and

$$Z = \left[1 - \frac{\partial \mathrm{Re}\Sigma(\omega)}{\partial \omega}\right]^{-1} \quad . \tag{10}$$

0.4.1 Luttinger theorem

In 1960, Luttinger showed that for a Fermi liquid (FL), the volume of the Fermi surface (FS) remains the same though its shape may change due to interaction [26]. This is known as the *Luttinger theorem*, and the later work by Langer and Ambegaokar (1961) [27] and by Langreth (1966) [28] gave a generalized Friedel sum-rule for a FL :

$$\mathrm{Im}\int_{-\infty}^{\mu} d\omega\, G(\omega)\frac{\partial \Sigma(\omega)}{\partial \omega} = 0 \quad . \tag{11}$$

0.5 Mott transition and Hubbard model

The correlation or the interaction driven metal to insulator transition (MIT) is known as the Mott transition. Hence, as mentioned before, the insulator in this context is a Mott insulator. Transition metal oxides, e.g. V_2O_3, VO_2, NiS_2 are believed to be the prototypes of Mott insulators. In real experiments transition occurs by varying physical pressure or by chemical pressure, i.e. doping with other atoms of different radii but the same valency (e.g. Cr in V_2O_3). These systems also show a temperature driven metal-insulator transition (MIT), which is discontinuous below a critical temperature and continuous above that. The transition is inferred in practice by looking at the change of resistivity or the slope in resistivity (positive for metals, negative for insulators) with respect to temperature. However, the metals are often bad metals since they possess very high residual resistivity and T^2 coefficient. Also the specific heat coefficient γ can range from 10 to 500 times the values in conventional alkali metals in the Cr-doped V_2O_3 samples for different doping concentrations.

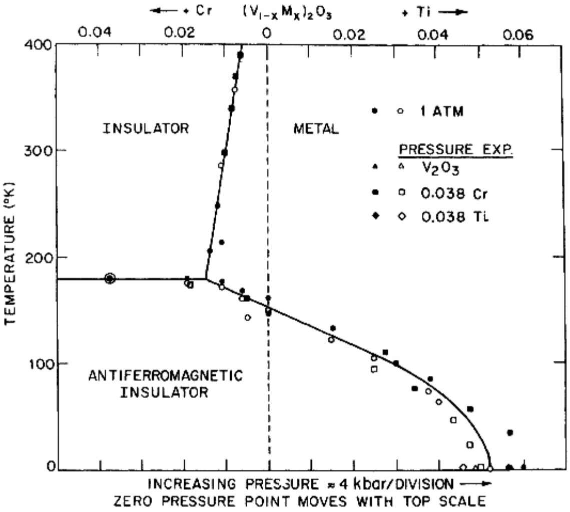

Fig. 5: The phase diagram on pressure-temperature plane in Cr/Ti-doped V_2O_3 showing three distinguishable phases: antiferromagnetic insulator, insulator (paramagnetic) and metal, separated by first order phase boundary lines. Closed and open symbols represent increasing and decreasing pressure or temperature respectively. Reproduced from the work by McWhan *et al* [14, 29].

The simplest model that can capture the underlying physics of Mott transition is the Hubbard model (HM) [30–33]. The single-band HM in standard notation is given by

$$\hat{H} = -\sum_{<ij>,\sigma} t_{ij}(c^{\dagger}_{i\sigma}c_{j\sigma} + \text{h.}c.) + \epsilon_d \sum_{i\sigma} c^{\dagger}_{i\sigma}c_{i\sigma} + U\sum_{i} n_{i\uparrow}n_{i\downarrow} \tag{12}$$

where t_{ij} is the amplitude of hopping of electrons from site-i to site-j , ϵ_d is the electron's orbital energy and U is the on-site Coulomb repulsion. The operator $c_{i\sigma}$ ($c^{\dagger}_{i\sigma}$) annihilates (creates) an electron of spin σ at site i.

Though the finite temperature insulator is found to be paramagnetic, the low temperature insulating phase is often found to be an anti-ferromagnet in many materials that exhibit the Mott transition. It has been argued by Slater [34] that long-range anti-ferromagnetic order can happen for bipartite lattices that show the perfect nesting property within the Hartree-Fock approximation and by Anderson [35] as a consequence of superexchange mechanism due to strong correlation.

0.6 Methods to solve single-band HM

The theoretical techniques that have been employed in an attempt to solve the HM are diverse, e.g. Hartree-Fock approximation [36–38], Hubbard's Green's function approximations [39,40], variational wave function method [33, 41], slave Boson approach [42], etc. However, to date the general HM remains unsolved except for the one-dimensional case [43]. A lot of progress has been made in recent years in this direction through the dynamical mean field theory (DMFT) [44, 45], where the lattice model is mapped onto an effective single impurity model with a self-consistently determined hybridization (will be discussed in detail in forthcoming sections). Within the DMFT context, special interests are being devoted towards the infinite dimensional HM since the mapping becomes exact in the limit and simplifies many major issues of many-body approaches.

0.7 Kondo model or the Anderson model

Kondo used the s-d model [15] to solve the dilute magnetic impurity in a metal problem. Three years before Kondo came up with his model, Anderson proposed a more general model [46], where a single correlated impurity electron is coupled through a hybridization function V_i to a sea or bath of conduction electrons. This model is popularly known as the single impurity Anderson model (SIAM), and the Hamiltonian is written as

$$\begin{aligned}\hat{H}^{\mathrm{SIAM}} = -\sum_{<ij>,\,\sigma}(t_{ij}\, c^{\dagger}_{i\sigma}c_{j\sigma} + \text{h. c.}) + \sum_{i\sigma}\epsilon_d\, c^{\dagger}_{i\sigma}c_{i\sigma} + \sum_{\sigma}\epsilon_f\, a^{\dagger}_{\sigma}a_{\sigma} + Un_{0\uparrow}n_{0\downarrow} \\ + \sum_{i\sigma}(V_i c^{\dagger}_{i\sigma}a_{\sigma} + \text{h. c.})\end{aligned} \tag{13}$$

where $c^{\dagger}_{i\sigma}/c_{i\sigma}$ is creation/annihilation operator for a conduction electron (with orbital energy ϵ_f) at site$i$ and $a^{\dagger}_{\sigma}/a_{\sigma}$ is creation/annihilation operator for an electron (with orbital energy ϵ_f) at single impurity site 0. U is the impurity site Coulomb repulsion and V is the hybridization function that allows impurity electrons to move to the conduction band.

In momentum ($\mathbf{k}$) space we can write the same as

$$\hat{H}^{\text{SIAM}} = \sum_{\mathbf{k}\sigma}(\epsilon_{\mathbf{k}}\, c^{\dagger}_{\mathbf{k}\sigma} c_{\mathbf{k}\sigma} + \text{h. c.}) + \sum_{\mathbf{k}\sigma} \epsilon_d\, c^{\dagger}_{\mathbf{k}\sigma} c_{\mathbf{k}\sigma} + \sum_{\sigma} \epsilon_f\, a^{\dagger}_{\sigma} a_{\sigma} + U n_{0\downarrow} n_{0\uparrow} + \sum_{\mathbf{k}\sigma}(V_{\mathbf{k}\sigma} c^{\dagger}_{\mathbf{k}\sigma} a_{\sigma} + \text{h. c.}) \tag{14}$$

The non-interacting (without Hubbard interaction U) Green's function can be written as

$$\mathcal{G}^{\text{SIAM}}(\omega) = \left[\omega^{+} - \epsilon_f - \frac{1}{\pi}\int_{-\infty}^{\infty} d\omega' \frac{\Delta(\omega')}{\omega - \omega'}\right]^{-1} \tag{15}$$

where

$$\Delta(\omega) = \pi \sum_{\mathbf{k}} |V_{\mathbf{k}}|^2 \delta(\omega - \epsilon_{\mathbf{k}}) \tag{16}$$

In fact, a canonical transformation proposed by Schrieffer and Wolff [47] shows that the two models are equivalent and that the SIAM can be mapped onto an effective *s*-*d* Hamiltonian.

0.8 Dynamical mean field theory (DMFT)

In 1989, Metzner and Vollhardt [44] showed the importance of infinite dimensionality in the HM as it simplifies the lattice problem with proper scaling. In the same year Müller-Hartmann [48] extended the same idea in a more generic sense. The motivation of such an idea arises from the classical spin-systems for which the spatial fluctuations are suppressed in the limit of large dimensions. The most prominent advantage of infinite dimensionality is that the self-energy becomes momentum independent, i.e. purely local. This great benefit leads the lattice model to be mapped on to a single impurity problem since the self-energy is essentially local as the only local interaction (Coulomb repulsion) appears at single impurity site. The mean-field differs radically in spirit from the classical spin mean field since it still contains the dynamic quantum fluctuations. In the infinite-dimensional limit, a quantum lattice is mapped onto an effective self-consistent single-site that hybridizes with an external bath that includes the dynamics of the degrees of freedom of the other sites. For example, the effective action for a lattice model like the HM(Eq. (12)) can be written as

$$S_{\text{eff}} = -\int_0^\beta d\tau \int_0^\beta d\tau' \sum_\sigma c^\dagger_{0\sigma}(\tau)\mathcal{G}_0^{-1}(\tau-\tau')c_{0\sigma}(\tau') + U\int_0^\beta d\tau\, n_{0\uparrow}(\tau)n_{0\downarrow}(\tau) \tag{17}$$

where τ, τ' are imaginary time and $\mathcal{G}_0$ is the effective single-site propagator (often called as the *Weiss Green's function*) at site 0. In contrast to the classical effective field, which is a number, this Weiss mean-field Green's function is imaginary time-dependent and hence capable of capturing the dynamic (temporal) local quantum fluctuations which are crucial to study correlated physics. The local, retarded Green's function in the paramagnetic case is given by

$$G(\omega) = \sum_{\mathbf{k}} \frac{1}{\omega^+ - \epsilon_k - \epsilon_d - \Sigma(\omega)} \tag{18}$$

where $\omega^+ = \omega + i\eta$, $\eta \to 0^+$ and $\Sigma(\omega)$ is the real-frequency self-energy. The $\mathbf{k}$ sum may be transformed to a density of states integral and thus may be written as

$$G(\omega) = \mathcal{H}[\gamma(\omega)] \tag{19}$$

where $\mathcal{H}[z] \equiv \int d\epsilon\, D_0(\epsilon)/(z-\epsilon)$ is the Hilbert transform of the non-interacting lattice density of states (DoS) $D_0(\epsilon)$ over z and $\gamma(\omega) = \omega^+ - \epsilon_d - \Sigma(\omega)$. We specifically choose two kinds of lattice DoS for our calculations, namely the hypercubic lattice (HCL) with

$$D_0(\epsilon) = \frac{1}{\sqrt{\pi}t_*} e^{-(\epsilon/t_*)^2} \tag{20}$$

and the Bethe lattice with

$$D_0(\epsilon) = \frac{2}{\pi t_*}\sqrt{1-(\epsilon/t_*)^2} \tag{21}$$

Since a lattice model can be mapped onto an impurity model within DMFT with the self-consistency condition that the impurity self-energy is the same as the lattice self-energy, one can find the host or medium Green's function $\mathcal{G}(\omega)$ for the impurity through the Dyson equation

$$\mathcal{G}^{-1}(\omega) = G^{-1}(\omega) + \Sigma(\omega) \tag{22}$$

Solution of the impurity model in terms of $\mathcal{G}(\omega)$ would then yield a new $\Sigma(\omega)$ which when put back in equation Eq. (19) gives $G(\omega)$. Thus, given an impurity solver technique, one can self-consistently solve for the Green's functions, and hence the self-energy. This self-consistency loop is shown schematically in Fig. 6. Exact diagonalization (ED) [49], numerical renormalization group

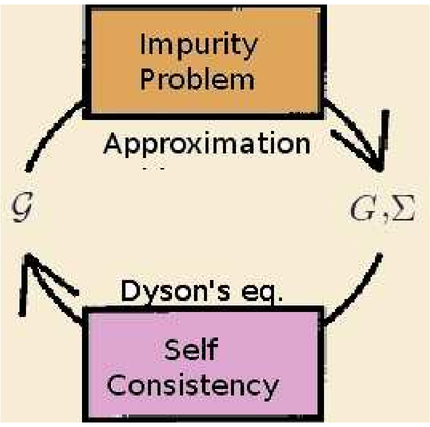

Fig. 6: Schematic representation of DMFT self-consistency loop (see text for discussion).

(NRG) [50], quantum Monte Carlo (QMC) [51, 52], Iterated perturbation theory (IPT) [53, 54] and local moment approach (LMA) [55, 56] have been widely used as such impurity solvers. We use the IPT and LMA and discuss their implementations and outcomes in the forthcoming chapters of the thesis (An overview has been given in Sec. 0.11).

0.9 Non-equilibrium properties across the Mott transition

The resistivity or the conductivity experiments in many Mott transition materials are quite fascinating since the experiments give rise to pressure and temperature-driven hysteresis. Such hystereses certainly indicate non-equilibrium physics to play role and any sort of mean-field may not suffice to capture it. V_2O_3 has remained a long-standing candidate which shows such a hysteresis in resistivity. Fig. 7 shows a conductivity experiment on single crystal V_2O_3 , by M. Föex in 1946, that reveals transition with temperature-driven (thermal) hysteresis. However, during early '70s, McWhan group, who extensively studied the same system [14, 29, 58–60], reported finding of small hysteresis (2-3 Kbar in the pressure direction) [29], as the closed and open symbols (representing increase and decrease in pressure/temperature) do not match all the way in the phase diagram (Fig. 5) [14, 29]. Later Kuwamoto *et al* [13] showed strong evidence of thermal hysteresis and recently Limelette *et al* [61] very carefully studied the pressure-driven hysteresis in Cr-doped V_2O_3. If we notice carefully, the hystereses are often associated with jumps or step like features along the resistivity or conductivity (see Fig. 8). This phenomenon is known as avalanches and it bears close resemblance with the Barkhausen noise associated with magnetic hysteresis (see Fig. 9). Hysteretic behavior in resistivity has been found in other prototypes, e.g. VO_2 . Very recently Sharoni *et al* studied the statistical distribution of the

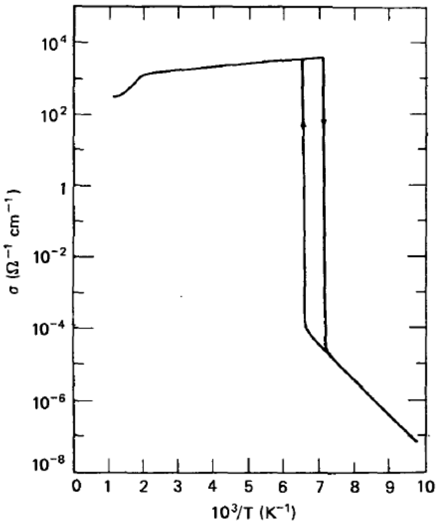

Fig. 7: Conductivity experiment on a single crystal V_2O_3 by M. Föex in 1946. Reproduced from the book *Metal Insulator Transitions* by N. F. Mott. [57]

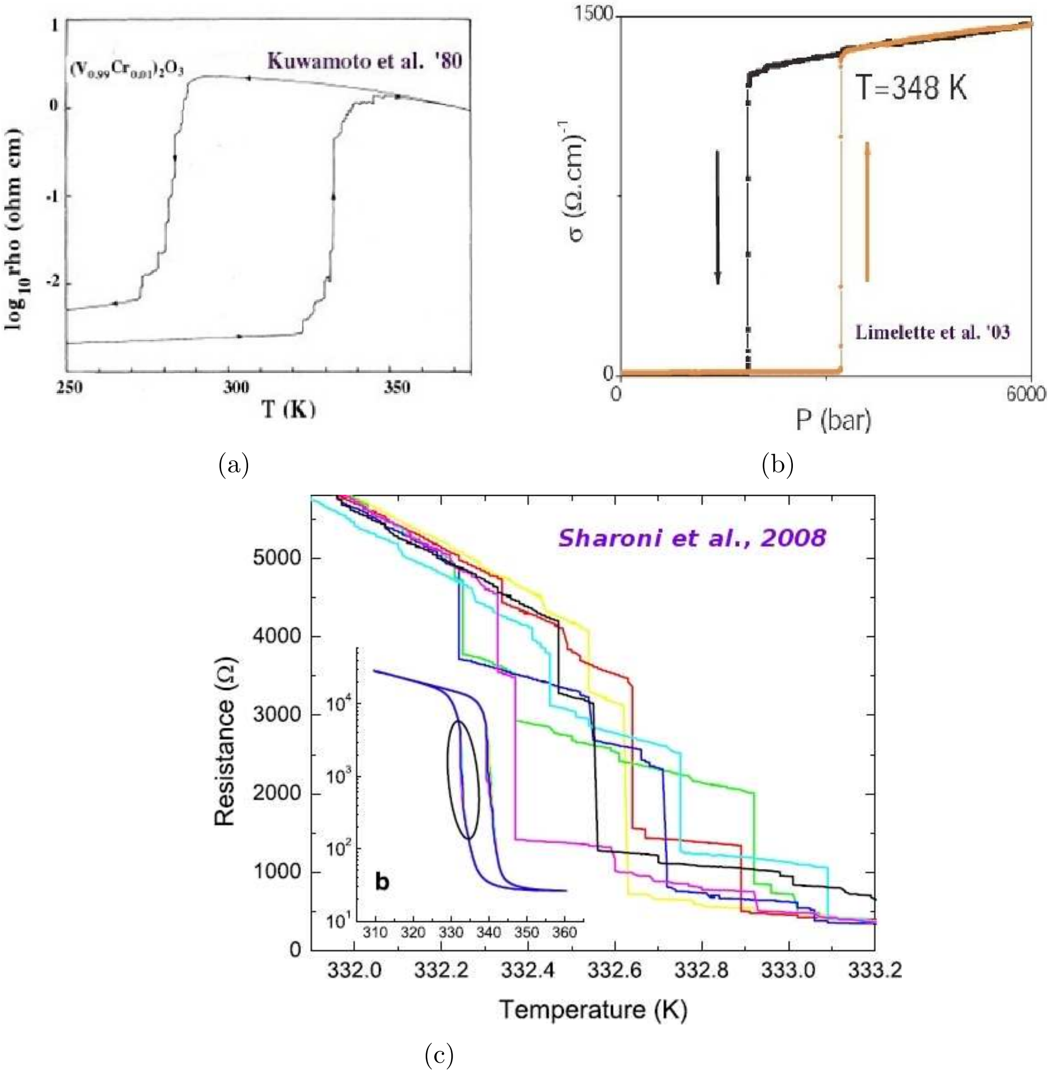

(a)

(b)

(c)

Fig. 8: Hysteresis and avalanches in resistance/conductivity. (a) Temperature driven hysteresis in Cr-doped V_2O_3 (reproduced from Ref. 13). (b) Pressure driven hysteresis on the same material (reproduced from Ref. 61). (c) Temperature driven hysteresis on VO_2 thin films (reproduced from Ref. 62).

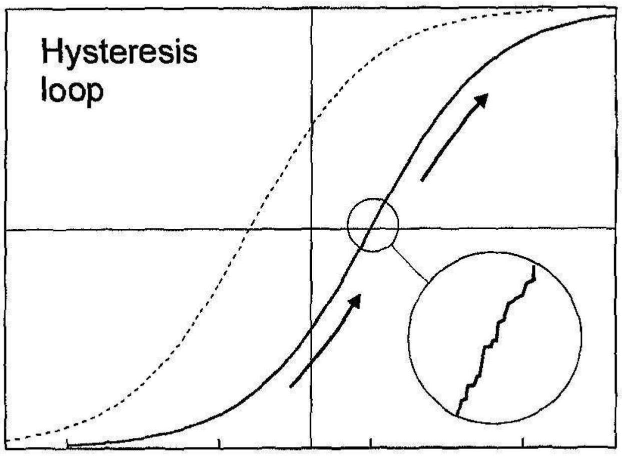

Fig. 9: Barkhausen noise observed in a ferromagnet as a part of the magnetic hysteresis curve is blown up in the inset. From the book *Hysteresis in Magnetism* by Bertotti [63].

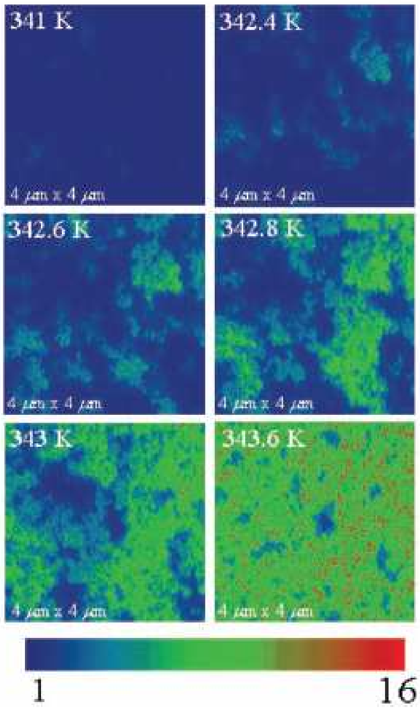

Fig. 10: Scanning near-field infrared microscopy on VO_2 film. Evidence of percolation progress of metallic domains (light colors) to completely insulating domains (dark blue) by increase in temperature. From Ref. [64].

avalanches found in the thermal hysteresis in VO_2 thin film [62]. They found a power law behavior in the avalanche size distribution signifying a possibility of percolation of metal-insulator islands as driven by temperature. Such an inhomogeneous distribution of metallic-insulating domains have been found earlier through scanning-tunneling microscope (STM) experiments. In 2007, Qazilbash *et al* [64] found similar evidence in VO_2 thin film by the scanning near-field infrared microscopy (see Fig. 10). Thus the hysteresis mechanism may lead to a different realm of physics and question about universality in the context of non-equilibrium phase transition and statistical mechanics.

0.10 Formalism for transport and thermodynamics.

We calculate the optical conductivity ($\sigma(\omega)$) via the Kubo-Greenwood [65–67] formula and get the following expression.

$$\sigma(\omega) = \frac{\sigma_0 t_*^2}{2\pi^2} \mathrm{Re} \int d\omega' \frac{n_F(\omega') - n_F(\omega+\omega')}{\omega} \left[\frac{G^*(\omega') - G(\omega+\omega')}{\gamma(\omega+\omega') - \gamma^*(\omega')} \right. \\ \left. - \frac{G(\omega') - G(\omega+\omega')}{\gamma(\omega+\omega') - \gamma(\omega')} \right] \tag{23}$$

where

$$\sigma_0 = 4e^2 a^2 n/\hbar \tag{24}$$

e, a, n, and $\hbar$ are electronic charge, lattice constant, electron density, and the reduced Planck's constant respectively, and

$$\gamma(\omega) = \omega^{+} - \epsilon_d - \Sigma(\omega) \quad .$$

Now $\omega \to 0$ limit gives the DC conductivity, whose inverse is the resistivity. We employ the equation of motion method (see Appendix A) and obtain the following expression for the internal energy (see Appendix B for the derivation).

$$E = \int d\omega \, n_F(\omega) \left[2\omega D(\omega) + \frac{1}{\pi} \mathrm{Im} \left(\Sigma(\omega) G(\omega) \right) \right] \tag{25}$$

where $D(\omega) = -\frac{1}{\pi}\mathrm{Im}G(\omega)$ and $n_F(\omega) = 1/(e^{\beta\omega} + 1)$ is the Fermi-Dirac function.

By taking the temperature derivative of the above expression, we calculate the specific heat, i.e.

$$C_V = \left(\frac{\partial E}{\partial T} \right)_V \quad . \tag{26}$$

0.11 An overview of the thesis chapters

In this thesis, our main objective is to develop and apply diagrammatic perturbation theory based quantum many body approaches to investigate the effects of strong correlation and its specific manifestation in the Mott transition physics in the Hubbard model framework. A brief description of each chapter and the main results are given below.

In Chapter 1, we develop a new implementation of the iterated perturbation theory (IPT), which has been developed earlier by Kotliar and Georges and their co-workers [45]. IPT is based on a second order perturbation theory ansatz about the Hartree limit. We show that our method has multiple advantages over previous implementations. For example, we obtain real frequency spectral functions and self-energies directly without recourse to the ill-defined problem of analytic continuation. This makes the algorithm more efficient and lets us handle the zero temperature features correctly. We find excellent (sometimes resolution-wise better) agreement with earlier results like the zero temperature scaling collapse of the spectral functions and the Mott transition. We find both interaction-driven hysteresis and temperature-driven (thermal) hysteresis in the system. The thermal hysteresis can be explained from the phase diagram on the temperature-interaction plane. We see universal crossing points in the specific heat and the optical conductivity. Such crossing points have been observed in many optical conductivity measurements and are known as the *isosbestic points*. We discuss a severe problem in the specific heat calculation which has been overlooked in earlier calculations, and argue that the non-conserving nature of IPT might be responsible for such unphysical results. Finally, we point out that our implementation is very robust and will be very useful for calculations employing IPT in multi-orbital Hubbard models for first principles approaches to SCES. Most of the results on transport and spectral properties have been presented in our recent published work [68].

In Chapter 2, we develop another formalism, known as the local moment approach (LMA), based on the perturbation about the unrestricted Hartree-Fock (UHF) limit for the Hubbard model. This is far more sophisticated than IPT approach since it incorporates spin-flip processes to all orders and builds in local-moments (the primary effect of strong interactions) from the outset. The LMA has been developed originally for the single-impurity Anderson model [55, 56] and has been subsequently applied to study heavy fermion systems through the periodic Anderson model (PAM) within DMFT [69–71]. In this chapter, we describe the mean-field results in detail and show that a metal-insulator transition exists even at the mean field level, but with the metal violating Fermi-liquid behavior. The diagrammatics of LMA is elaborated and the emergence of a low energy scale through the inclusion of spin-flip processes is demonstrated in the Fermi liquid regime. The whole formalism has been discussed in this chapter. The application of this formalism to the various regimes of the Hubbard model (zero and finite temperature, particle-hole symmetric and asymmetric cases) is carried out in the next four chapters. The need to structure this work into four different chapters is based on two criteria - (a) the different regimes pointed above demand distinct aspects of LMA to be implemented. (b) The physics issues in each parameter regime are quite unique to that regime, albeit interrelated. While the discussion of the aspects that are unique to each regime is the focus of each chapter, we do take particular care to collate the results of each chapter with the previous chapters and with other theoretical work.

In Chapter 3, we study universality and scaling in the ground state of the particle-hole symmetric Hubbard model. The Mott transition and its manifestation as a discontinuous first order phenomenon in spectra and optics forms our focus in this chapter. The disappearance of the low energy scale with increasing interactions and the approaching of Mott insulator is demonstrated. The destruction of the Mott insulator on the other hand, by closing of the gap and the concomitant appearance of a finite spectral density at the Fermi level with decreasing interaction strength is investigated. We find a single low-energy scale in the problem, given by $\omega_L = Zt_*$, where Z is the quasi-particle weight and t_* is the effective hopping integral. The strong coupling metallic regime in this problem is shown to occur in the proximity of the Mott transition on the Fermi liquid side. The spectral functions in the neighborhood of the Fermi level are shown to have a universal scaling form as functions of ω/ω_L. This scaling regime extends decades of above ω_L and in strong-coupling (close to the Mott transition), it appears to extend all the way up to the Hubbard band edges. The optical conductivity is also found to have a universal absorption peak position for different interaction strengths after scaling the frequency axis by ω_L.

In Chapter 4, we study the interplay between particle-hole (p-h) asymmetry and strong correlation effects using an implementation of the LMA for the p-h asymmetric case. The Luttinger's theorem is used as a constraint to ensure Fermi liquid behavior. Though we do study the scaling properties of the single and two particle quantities, our main focus is the role of asymmetry when combined with strong correlations. Any finite asymmetry is found to induce metallic behavior in the system, and an interaction-driven Mott transition does not occur. Increasing asymmetry is found to decrease the effect of strong correlations and the changes in the spectra and optical conductivity are elucidated.

Chapters 3 and 4 deal with the zero temperature properties of the symmetric and asymmetric Hubbard model. We now move on finite temperature transport and thermodynamics properties and the LMA formalism is developed further.

In Chapter 5, the finite temperature LMA is developed and applied to study the particle-hole symmetric Hubbard model, and thus represents an extension of chapter 3. The focus is on transport and thermodynamic properties across the Mott transition. The resistivity in the metallic regime shows high T^2 coefficient. Like the zero temperature result, the scaling behavior of the absorption peak with universal position optical conductivity is also observed at low finite temperature. In contrast to the results from IPT (Chapter 1), we find an excellent finite temperature scaling collapse in the spectral density. We do not find any anomalous or unphysical behavior in the specific heat. The Mott transition is shown to become continuous at finite temperatures.

In Chapter 6, we investigate the particle-hole asymmetric Hubbard model at finite temperature, and focus on the finite temperature properties of doped Mott insulators. We show that the proximity of the Mott insulator in the asymmetric case leads to a clear pseudogap in the vicinity of the Fermi level. An anomalous behavior in the resistivity due to the presence of this pseudogap is seen. For example, the resistivity shows a wide region of linear or 'quasi'-linear region that resembles the non-Fermi liquid behavior discussed in Sec. 0.3. We discuss microscopic origin of such 'Marginal Fermi liquid' behavior (proposed phenomenologically by C. M. Varma and co-workers [72]) and point out the relevance of our results to the high temperature cuprate superconductors. We report that a linear resistivity behavior in combination with a Fermi liquid ground state ($\rho(T) \sim AT^2$) has been obtained within our approach.

Chapter 7 represents a deviation from the diagrammatic perturbation theory approach since here we are interested in the non-equilibrium properties across the Mott transition. We propose a novel reasoning for why thermal hysteresis is not commonly observed in most ferromagnets. The 'phase diagram' from IPT gives an insight on how to describe the thermal hysteresis that has been found in materials like V_2O_3 [13] and VO_2 [62]. However, IPT solutions mathematically mimic two metastable states (metal and insulator) and give rise to metal-insulator coexistence regime. For a real system, such a coexistence regime may manifest itself in a spatial inhomogeneous network of metallic and insulating islands (as observed in recent experiments on VO_2 thin films [64]). Quantum many body calculations for such inhomogeneous systems are extremely expensive and even if carried out might not be able to provide insight into the physics of the disorder-driven dynamical Mott transition. For this reason, we adopt a phenomenological approach. Following the success of random-field Ising model (RFIM) [73, 74] in describing avalanche statistics for magnetic systems, we employ a scheme where the RFIM model is mapped onto a resistor-network that represents the real inhomogeneous metal-insulator systems. The metal-insulator island network is mapped through the final spin configuration of the RFIM, which we obtain through a zero temperature Monte-Carlo simulation. The resistor network is solved by standard sparse-matrix based linear algebra techniques to determine the effective resistance. As expected, we find hysteresis with avalanches which exhibit the finite size effects very similar to the experimental finding by Sharoni *et al* [62] on VO_2 thin films. We also find a comparable agreement in the power law exponent of the avalanche size distribution with that found by the same experimental group.

Finally I must say that the work presented in this thesis is a small attempt to probe the tip of the giant iceberg of electronic correlation problem in the ocean of condensed matter physics. Many interesting issues remain unexplored due to limitations of a Ph. D. duration. Nevertheless, I hope that my work has covered many significant aspects and methods within many-body perturbation theory and also a few issues of the non-equilibrium phenomena across the Mott transition.

Chapter 1

Iterated Perturbation Theory for half-filled Hubbard model (p-h symmetric HM)

1.1 Introduction

In ’70s Yosida and Yamada [75] used diagrammatic perturbation theory on half-filled single-impurity Anderson model (SIAM) and showed that only the second-order diagrams contribute significantly. Their approach was later carried forward with implementation on the HM primarily by Georges, Kotliar, Krauth and Rozenberg [45, 53, 54] within the DMFT framework and later by many other people. This approach in the context of DMFT is known as the iterated perturbation theory (IPT). Here we present an improved numerical implementation of this theory, that we employ to the half-filled single band Hubbard model. We demonstrate higher resolution of spectral and transport features and a reduced computational expense. Using this implementation, we study the issues of scaling and universality in spectral and transport properties of the particle-hole symmetric Hubbard model within DMFT. We compare some of our results with experiments, e.g. resistivity with pressure dependence in Selenium doped NiS_2 and with thermal hysteresis on V_2O_3. A systematic study of spectral weight transfer in optical conductivity is also carried out.

1.2 Formalism and implementation

We first rewrite the single band Hubbard model (HM) once again, that has been already discussed in the previous chapter in order to keep connections to the parameters that are often discussed in this chapter.

$$\hat{H} = -\sum_{<ij>\,\sigma} t_{ij}(c^{\dagger}_{i\sigma}c_{j\sigma} + \text{h.}c.) + \epsilon_d \sum_{i\sigma} c^{\dagger}_{i\sigma}c_{i\sigma} + U\sum_{i} \hat{n}_{i\uparrow}\hat{n}_{i\downarrow} \tag{12}$$

The ansatz for the dynamical part of the self-energy (apart from the static Hartree term) within IPT is just the second order term of the perturbative expansion in U about the Hartree limit, i.e.

$$\Sigma^{\text{IPT}}(\omega) = \frac{U}{2}\langle\hat{n}\rangle + \Sigma_2(\omega) \tag{1.1}$$

where

$$\Sigma_2(\omega) = \lim_{i\omega\to\omega^+} \frac{U^2}{\beta^2}\sum_{m,p} \mathcal{G}(i\omega + i\nu_m)\mathcal{G}(i\omega_p + i\nu_m)\mathcal{G}(i\omega_p) \tag{1.2}$$

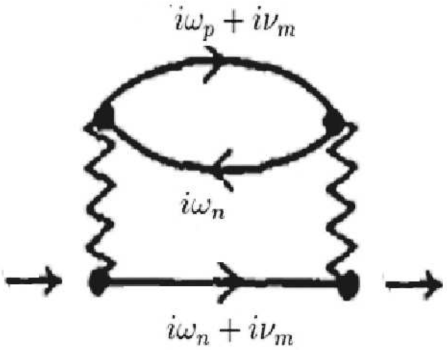

Fig. 1.1: Feynman diagram of the second order perturbation term: $\Sigma_2(\omega)$, in IPT approximation

and $i\omega$ and $i\nu$ denote odd and even Matsubara frequencies respectively (see Fig. 1.1). In the half-filling case, $\langle \hat{n} \rangle = 1$ and this assigns a particle-hole (p-h) symmetry in the lattice (one electron or hole per lattice site). One major advantage of this symmetry is that the orbital energy ϵ_d is always known for a given interaction strength U. By doing particle-hole transformation on the HM and then by imposing the particle-hole symmetry condition, one can find (see Appendix C for the derivation)

$$\epsilon_d = -U/2 \quad . \tag{1.3}$$

Using the spectral representation $\mathcal{G}(i\omega_n) = \int_{-\infty}^{\infty} d\omega' \, \frac{D_{\mathcal{G}}(\omega')}{i\omega_n - \omega'}$, (where $D_{\mathcal{G}}(\omega) = -\mathrm{Im}\,\mathcal{G}(\omega)/\pi$) and carrying out the Matsubara sums along with the trivial analytic continuation $i\omega_n \to \omega^+$, we get the following expressions for the imaginary part of the self-energy on the real frequency axis (Eq. (E.15) in Appendix E) :

$$\begin{aligned} D_\Sigma(\omega) &= -\frac{1}{\pi}\mathrm{Im}\Sigma(\omega) \\ &= U^2 \int_{-\infty}^{\infty} d\omega' D_{\mathcal{G}}(-\omega') \Big[n_F(\omega')\chi(\omega+\omega') + n_F(-\omega')\chi(-\omega-\omega') \Big] \end{aligned} \tag{1.4}$$

where

$$\chi(\omega) = \int_{-\infty}^{\infty} d\omega' D_{\mathcal{G}}(\omega+\omega') D_{\mathcal{G}}(\omega') n_F(-\omega-\omega') n_F(\omega') \tag{1.5}$$

with

$$\hat{n}_F(\omega) = \frac{1}{e^{\beta\omega}+1} \tag{1.6}$$

as the Fermi-Dirac distribution function. We get the real part by using Kramers-Kronig transformation:

$$\mathrm{Re}\,\Sigma(\omega) = \frac{1}{\pi}\mathcal{P}\int_{-\infty}^{\infty} d\omega' \, \frac{\mathrm{Im}\,\Sigma(\omega')}{\omega'-\omega}. \tag{1.7}$$

Eq. (18), (19), and (22) along with Eq. (1.4)- (1.7) constitute the necessary ingredients for the solution of the half-filled Hubbard model within DMFT. We remark here that the integrals above are all one-dimensional and hence do not present any excessive computational expense.

Numerical implementation of the above equations is straightforward in almost the whole metallic regime. However, the metallic regime in proximity to the Mott transition and the Mott insulating regime is trickier. We will illustrate this point and its resolution in detail here. The retarded host

Green's function may be separated into a singular and a regular part ($\mathcal{G}^{\rm reg}$):

$$\mathcal{G}(\omega) = \sum_i \frac{\alpha_i}{\omega - \omega_i + i\eta} + \mathcal{G}^{\rm reg}(\omega), \quad \eta \to 0+ \quad . \tag{1.8}$$

The sum in the above equation is over the poles ω_i or the singularities of the $\mathcal{G}(\omega)$ and α_i's are the corresponding weights or residues.

It is easily seen that if $\mathcal{G}(\omega)$ has to satisfy the self-consistent equations of DMFT [(18)- (22), (1.4)- (1.7)], the residue α_i of the singularities must satisfy self-consistent equations. For example, in the Mott insulator case where there is just one pole with residue α at the Fermi level (this follows from the singular behavior of the self-energy and host Green's function in the atomic limit ($t_* = 0$) [30, 45, 76]), we get a cubic equation (at $T = 0$), given by (Eq. (F.22) in Appendix F)

$$\alpha^{-1} = 1 + \frac{4M_2}{U^2\alpha^3} \tag{1.9}$$

where M_2 is the second moment of $D_0(\omega)$ [$M_2 = \int_{-\infty}^{\infty} d\omega\, \omega^2 D_0(\omega)$], $D_0(\omega)$ is the non-interacting lattice density of states (DoS). Solutions of this equation by Cardano's method [77] shows that out of three roots, the physically reasonable root (such that $\alpha \to 1$ as $U \to \infty$) exists only for $U > U_{c1} \simeq 3.67t_*$ for the HCL (see Fig. 1.2).For the Bethe lattice (BL), $U_{c1} \simeq 2.6t_*$. For a general U, we solve the above cubic equation numerically to get α. In the strongly correlated metallic regime, poles can arise in the host Green's function $\mathcal{G}(\omega)$ even though the spectral density of the interacting Green's function shows a FL behavior within a width of low energy scale (described

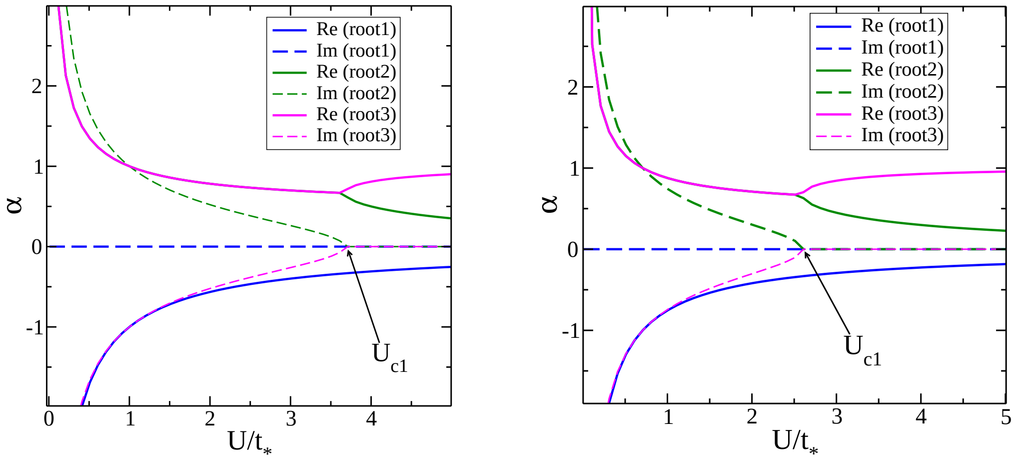

Fig. 1.2: Solving cubic equation (Eq. (1.9)) by Cardano's method. The physical root is the root 3 in the figures (pink lines, solid for the real part, dashed for the imaginary part). It is purely real after $U = U_{c1}$ (Left panel: $U_{c1} = 3.67t_*$ for the HCL, right panel: $U_{c1} = 2.6t_*$ for the BL) and approaches the strong-coupling ($U \to \infty$) limit ($\alpha \to 1$).

as ω_L later). Two poles occur symmetrically about the Fermi level at $\pm\omega_0$ proportional to the square-root quasiparticle weight Z (see Eq. (G.7) in Appendix G). The Mott transition from the metallic regime to the insulating regime occurs through the collapse of these two poles at the Fermi level into one single pole characteristic of the insulating regime (as described above). The poles of the $\mathcal{G}(\omega)$ lead to divergences at $\pm 3\omega_0$ in the $\Sigma(\omega)$ (through Eq. (1.4), see Fig. 1.3). Using such a pole structure of the Green's functions and the self-energy, the critical U at which the metal transforms into the insulator, i.e U_{c2} may be estimated as $4.77t_*$ (see Appendix G) for the HCL. We also find the same for the Bethe lattice ($U_{c2} = 3.28t_*$) which agrees with the numerical estimation in Ref. [54].

At finite temperatures, the singularity at the Fermi level must have a finite width. However, this width could be exponentially small in practice, and it is

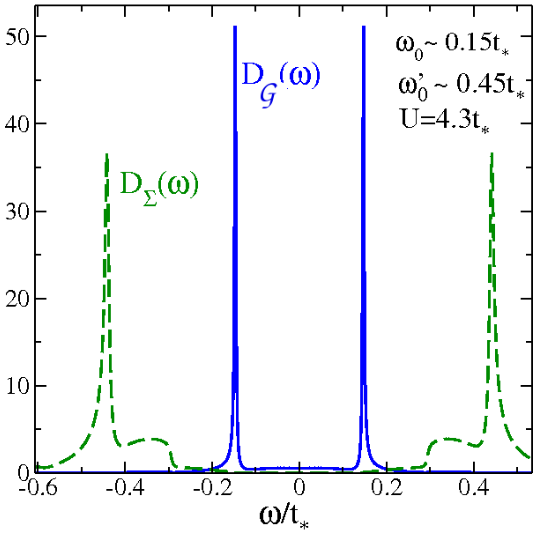

Fig. 1.3: The sharp resonance-like features that appear in the spectra of $\mathcal{G}$ and Σ near the Mott transition ($U = 4.3t_*$). These resonances can be approximated as Dirac-delta functions at the close vicinity of the transition. Singularities of $D_{\mathcal{G}}(\omega) = -\text{Im}\mathcal{G}(\omega)/\pi$ at $\omega = \pm\omega_0$ give rise to singularities of $D_{\Sigma}(\omega) = -\text{Im}\Sigma(\omega)/\pi$ at $\omega = \omega_0' = \pm 3\omega_0$.

next to impossible to capture such sharp resonance numerically. So we utilize the spectral weight sum rule to compute the weight of the singularity, i.e. α. The presence of this singularity is numerically detected by a significant deviation (in practice 2%) of the integrated spectral weight of $D_{\mathcal{G}}$ from unity. The sharp resonance at the Fermi level in $D_{\mathcal{G}}$ is then numerically cut off to get $\mathcal{D}_{\mathcal{G}}^{\text{reg}}$ and the weight α is obtained by $\alpha = 1 - \int_{-\infty}^{\infty} d\omega\, \mathcal{D}_{\mathcal{G}}^{\text{reg}}$. With the above separation of $D_{\mathcal{G}}$ into regular and singular parts, for the insulating phase, the self-energy expression reduces to

$$\Sigma(\omega) = \Sigma^{\text{reg}}(\omega) + \frac{U^2\alpha^3}{4\omega^+} \qquad (1.10)$$

where Σ^{reg} is obtained through the Kramers-Kronig transform of D_{Σ}^{reg} which is given by

$$\begin{aligned}
D_{\Sigma}^{\text{reg}}(\omega) = U^2 \Bigg[& \int_{-\infty}^{\infty} d\omega' \, D_{\mathcal{G}}^{\text{reg}}(-\omega') n_F(\omega') \chi^{\text{reg}}(\omega + \omega') \\
& + \frac{\alpha^2}{4} n_F(-\omega) D_{\mathcal{G}}^{\text{reg}}(\omega) + \frac{\alpha}{2} \chi^{\text{reg}}(\omega) \\
& + \int_{-\infty}^{\infty} d\omega' \, D_{\mathcal{G}}^{\text{reg}}(-\omega') n_F(-\omega') \chi^{\text{reg}}(-\omega - \omega') \\
& + \frac{\alpha^2}{4} n_F(\omega) D_{\mathcal{G}}^{\text{reg}}(\omega) + \frac{\alpha}{2} \chi^{\text{reg}}(-\omega) \Bigg]
\end{aligned} \tag{1.11}$$

and

$$\chi^{\text{reg}}(\omega) = \int_{-\infty}^{\infty} d\omega' \, D_{\mathcal{G}}^{\text{reg}}(\omega') D_{\mathcal{G}}^{\text{reg}}(\omega + \omega') n_F(\omega') n_F(-\omega - \omega') + \alpha D_{\mathcal{G}}^{\text{reg}}(\omega) n_F(-\omega). \tag{1.12}$$

A brief remark about the computational expense in implementing the above approach would be appropriate here. (1.9)- (1.12) are the rate limiting steps in the algorithm, since they scale as $\mathcal{O}(N^2)$ for a frequency grid with N points. We must mention that the use of Fast Fourier transforms would reduce this expense to $\mathcal{O}(N \ln N)$; however, the frequency grid would need to be very wide and homogeneous with a high density, thus leading to a high memory requirement and increased computational expense. In contrast, our approach requires a relatively sparse frequency grid, since we separate the sharp features analytically. Thus, without sacrificing resolution, we are able to achieve reasonable computational expense. Now we proceed to discuss our results.

1.3 Spectral properties

Since our implementation is new, we would like to benchmark it by comparing our results with other implementations. We begin with the local density of states (DoS) as given by $D(\omega) = -\mathrm{Im}\, G(\omega)/\pi$. In Fig. 1.4 we show the $D(\omega)$ computed at temperature $T = 0$ for various U's in the metallic regime. The left panel shows the spectral function on 'non-universal' scales, i.e. *vs.* ω/t_*, where the Hubbard bands are seen to form with increasing U, while the Abrikosov-Suhl resonance at the Fermi level gets narrower. The zero frequency value of the spectral function is also seen to be pinned at the non-interacting ($U = 0$) value. Such behavior finds a natural explanation in Fermi liquid (FL) behavior. A simple linear expansion of the self-energy as $\Sigma(\omega) = \Sigma(0) + \left(1 - \frac{1}{Z}\right)\omega + \mathcal{O}(\omega^2)$ when used in Eq. (19) gives $G(\omega) = G_{U=0}(\omega/\omega_L)$ where $\omega_L = Zt_*$ is the low energy Fermi liquid scale. Since the quasiparticle

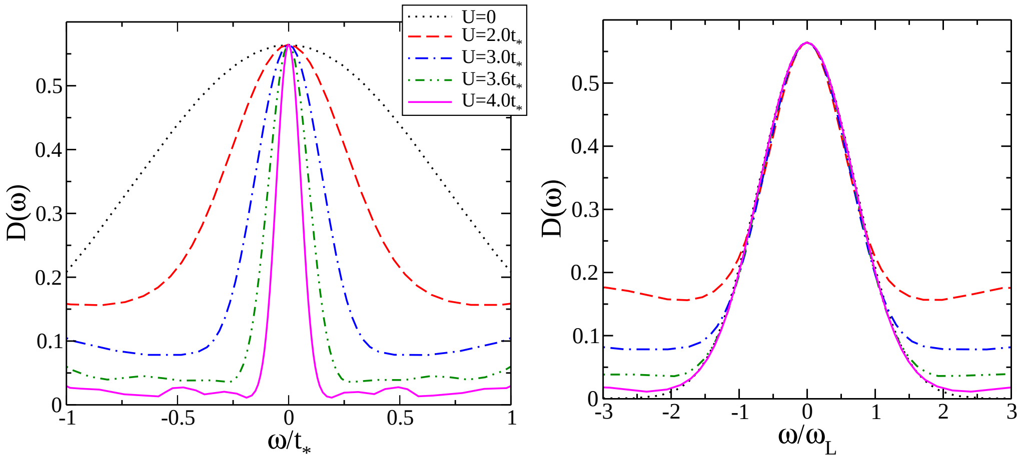

Fig. 1.4: Spectral functions for various U's showing quasiparticle resonances at Fermi level (left). A simple x-axis re-scaling by $\omega_L = Zt_*$ leads to a collapse of all of these onto the non-interacting ($U = 0$) spectral function in the neighborhood of the Fermi level thus signifying adiabatic continuity and FL behavior (right: follows same legends).

weight Z decreases with increasing U, thus signifying an increase in effective mass ($m_* = m/Z$), the full width at half-maximum (FWHM) for a hypercubic lattice that is given by $\Delta = 2\omega_L\sqrt{\ln(2)}$ would decrease with increasing U. Another inference from such low frequency scaling behavior is the universality of the low frequency part of the spectral function. On the right panel of Fig. 1.4, the same spectra as the left panel are plotted as a function of ω/ω_L, and they are all seen to collapse onto the non-interacting limit spectra in the neighborhood of the Fermi level. All of the above behavior is of course well known and well understood [54]. We nevertheless emphasize that the extent of the FL regime is very small in strong coupling, because as the right panel shows, the scaling collapse is valid for $\omega \lesssim \omega_L$, where ω_L is expected to decrease exponentially with increasing U. The approximation of IPT does not capture such exponential decrease of ω_L, instead predicting an algebraic decrease.

The left panel in Fig. 1.5 shows that the spectral function of the metallic phase shrinks down as U/t_* is increased and finally disappears at $U = U_{c2} \simeq 4.4t_*$ (for the HCL) by forming a gap at the Fermi level. This indicates a Mott transition to an insulator due to increase in interaction starting from a metallic (gapless) phase. The gap increases further as U/t_* is increased more. The right panel in Fig. 1.5 shows the change in spectral functions in the opposite situation, where we start from an insulating phase an gradually decrease interaction. As anticipated in our discussion in Sec. 1.2, we find a different transition point: U_{c1} ($U_{c1} \simeq 3.7t_*$ for the HCL), where the spectral gap closes and a metallic spectral density appears. Thus the presence of two different transition points U_{c1} and U_{c2}, that depends on the history of the driving interaction, signifies a presence of hysteresis in the system. The values of U_{c1} and U_{c2} remarkably agree with our analytical predictions discussed in Sec. 1.2. Due to presence of hysteresis, and even as that has been found in experiments as well (see discussions in Chapter 0), many authors believe that the transition is of first order. We have done finite temperature calculations as well, which shows that the difference between U_{c1} and U_{c2} decreases as one increases temperature and it vanishes at a critical temperature $T = T_c$. We describe this now in term of the phase diagram on the U-T plane.

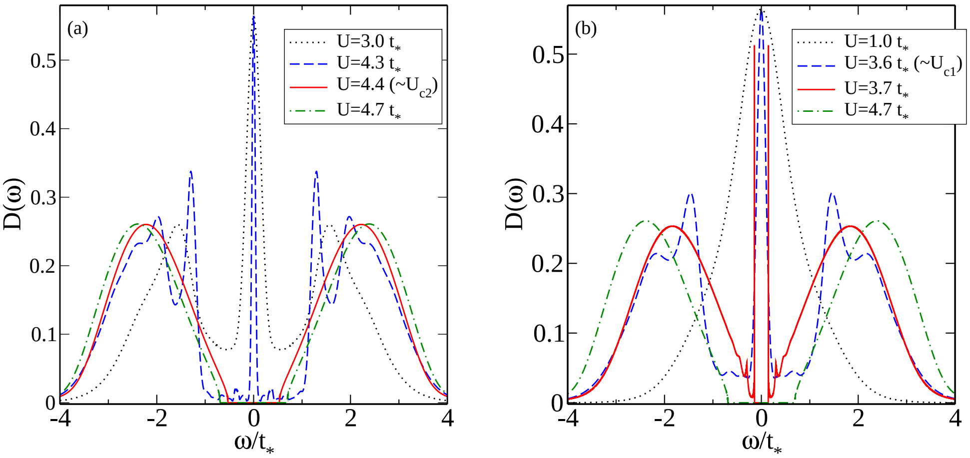

Fig. 1.5: Spectral function evolution as a function of U/t_* for the hypercubic lattice (HCL). Left panel shows that the quasiparticle resonance of the metallic phase decreases due to increase in U/t_* and finally vanishes by forming a gap at the Fermi level. Thus it signifies a metal-to-insulator transition and the transition point is named as U_{c2} ($U_{c2} \simeq 4.4t_*$ for the HCL). However, we get a different transition point when we decrease U/t_* starting from an gapped spectral density (insulating phase) and we call it U_{c1}. Presence of two different metal-insulator transition points shows a presence of hysteresis at zero temperature.

In the U-T plane, the metallic and insulating solutions are known to coexist in a certain region bounded by spinodal lines. The $T = 0$ bounds are denoted by U_{c1} and U_{c2}. This first order coexistence region may be simply found by computing the temperature or U dependence of the Fermi level density of states ($D(0) = -\mathrm{Im}\, G(0)/\pi$) for various values of U/t_* or T/t_*. The resulting phase diagram is shown below in Fig. 1.6. It agrees well with those reported previously [45, 54]. In addition, the resolution of the spectra here is seen to be far better than those obtained previously [45,54,78] through the analytic continuation of Matsubara frequency quantities.

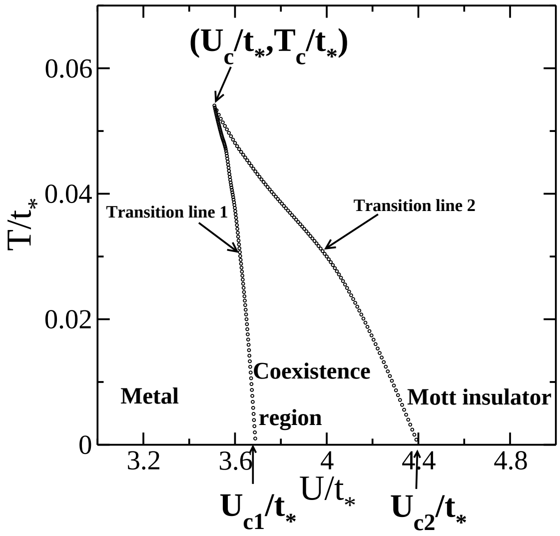

Fig. 1.6: Phase diagram on the U-T plane as calculated within IPT for the hypercubic lattice (HCL). The solid lines with zero temperature end points at U_{c1} and U_{c2} mark the spinodals of the coexistence region where the metallic and the insulating solutions coexist. ($U_c/t_*, T_c/t_*$) denote the critical point above which a second order metal-insulator crossover is observed.

The metallic region is a strongly renormalized FL, and thus the properties close to the Fermi level must be governed by a single low energy scale ω_L. For universality to hold in the strong coupling region, the spectral function must have the following form:

$$D(\omega; T) = f\left(\frac{T}{\omega_L}; \frac{\omega}{\omega_L}\right), \tag{1.13}$$

i.e. it must be a function purely of $\tilde{T} = T/\omega_L$ and $\tilde{\omega} = \omega/\omega_L$ [19]. In Fig. 1.7,

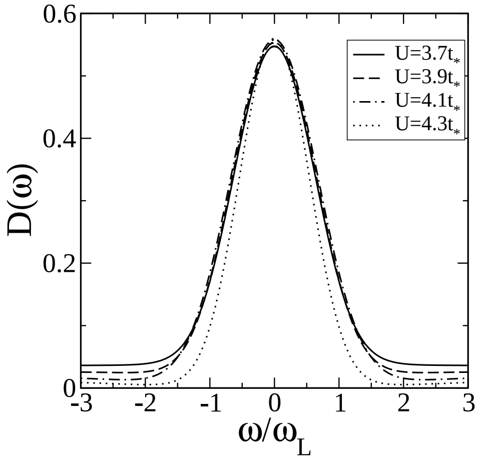

Fig. 1.7: Finite temperature scaling violated. Spectral functions plotted for various U's, keeping $\tilde{T} = T/\omega_L = 0.2$ fixed, do not collapse .

we show the spectra in strong coupling for fixed $\tilde{T} = 0.2$ and increasing U/t_*. We see that a scaling collapse does not occur implying that the above universal form does not describe the finite temperature IPT results. This non-universal behavior is an artefact of the specific iterated perturbation theory ansatz for the self-energy which is known to yield a non-universal form for its imaginary part [78], namely $\mathrm{Im}\,\Sigma_{\mathrm{IPT}}(\omega = 0) \propto U^2T^2/t_*^3$.

1.4 Transport properties

1.4.1 Resistivity

The dc resistivity is computed by taking $\omega \to 0$ limit on Eq. (23) and taking inverse of it. Again, the pathologies in the imaginary part of the self-energy are reflected in the low temperature FL region in the following way. Although the resistivity does have a T^2 form, the expected universal scaling form of $(T/\omega_L)^2$ is not obtained [78]. However, surprisingly, the 'coherence peak' position, which represents a crossover between low temperature coherent behavior to high temperature incoherent behavior does seem to be a universal feature in strong coupling as seen in Fig. 1.8 occurring at $\tilde{T} = 0.6$. The crosses represent the peak position, and as is seen in the right panel, these crosses line up at a single $\tilde{T}$. Thus the position of the coherence peak may be used to infer the low energy scale in a real material. In the inset of the left panel, we show the experimentally measured [79, 80] resistivity of $\mathrm{NiS}_{2-x}\mathrm{Se}_x$ as a function of pressure in Kbar (indicated as numbers). The resistivity for the lowest pressure rises dramatically with increasing T, before reaching a coherence maximum, and then decreasing slowly for higher temperatures. With increasing pressures, the initial rise becomes more gradual, and the coherence peak shifts to higher temperatures. An increase in pressure leads

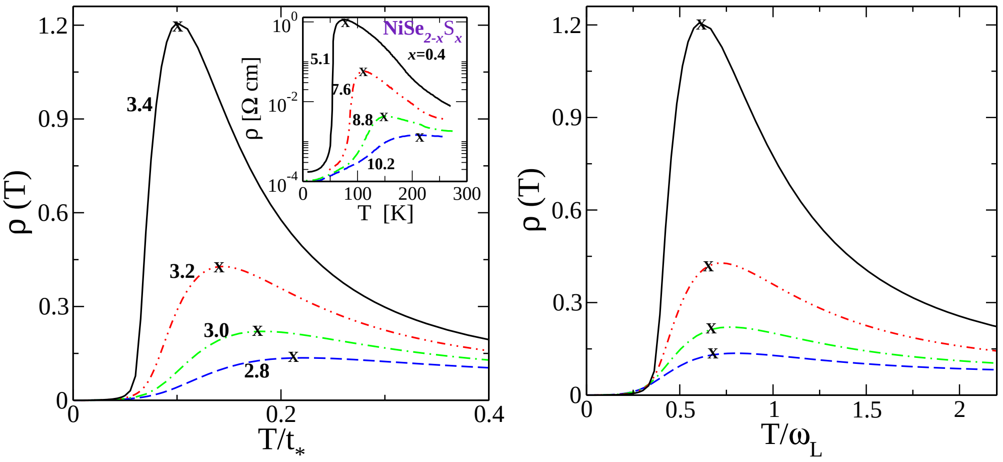

Fig. 1.8: Left panel: Theoretically computed resistivity as a function of temperature for various U/t_* values (indicated as numbers). The crosses indicate the position of the coherence peak. Left panel inset: Experimentally measured [79, 80] resistivity for $\mathrm{NiS}_{2-x}\mathrm{Se}_x$ as a function of pressure (indicated as numbers). Right panel: The same resistivity as in the left panel with the temperature rescaled by the low energy coherence scale $\omega_L = Zt_*$ showing that the coherence peak is indeed a universal feature of the strongly correlated metallic regime.

to a decrease in lattice spacing, thus increasing t_*, the hopping parameter, while the local Coulomb repulsion U remains unaffected. Thus increasing pressure can be interpreted as a decrease in the U/t_* ratio. A comparison of the inset with the main figure of the left panel clearly indicates qualitative agreement. The initial rise of $\rho(T)$ with T is much sharper in experiment than in theory, but the rest of the features, including a shift of the coherence peak to higher temperatures with increasing pressure, are indeed observed. We emphasize here that the agreement is only qualitative and as such, no attempt is made to obtain quantitative agreement.

We now study the resistivity hysteresis as obtained within IPT approximation.

1.4.2 Thermal hysteresis

Fig. 1.9 shows the thermal hysteresis in resistivity obtained through heating and cooling cycles for fixed U's ($t_* = 1$) in the coexistence region. The area enclosed by the hysteresis loop decreases as $U \to U_c$. A full cycle hysteresis is observed only in the region U_c ($\sim 3.5t_*$) $< U < U_{c1}$ ($\sim 3.7t_*$). For $U < U_c$, the metal-insulator transition is continuous and hence of second order while for $U > U_{c1}$ the transition is discontinuous but hysteresis is not obtained. The hysteresis can be qualitatively explained through the coexistence region in Fig. 1.6. For $U_c < U < U_{c1}$ the $T = 0$ ground state is a FL. As one increases T for a fixed U, and crosses the spinodal on the right (transition line 2), a first order transition to a paramagnetic insulating state occurs, which upon cooling does not transit to the paramagnetic insulating

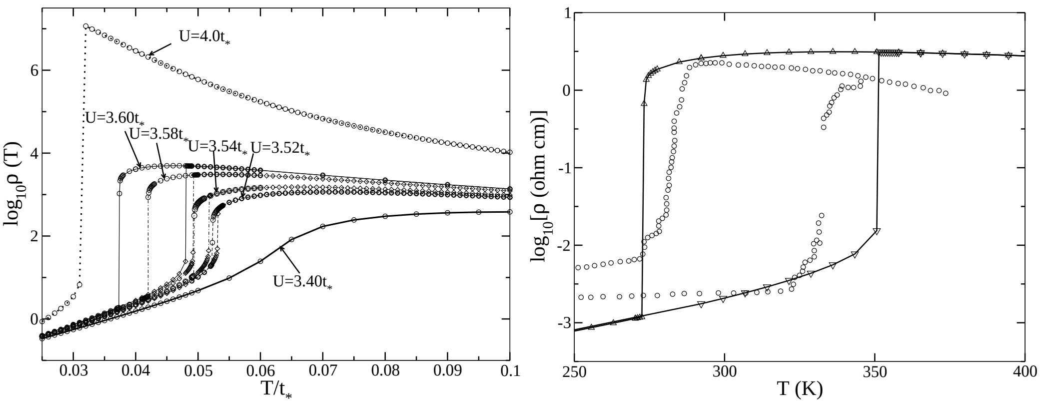

Fig. 1.9: Left panel: The resistivity on a log-scale exhibits thermal hysteresis as a function of temperature when $U_c < U < U_{c1}$ (see text for discussion). For $U = 3.4t_*$ second order transition is observed without hysteresis. For $U = 4.0t_*$ hysteresis is not observed though the metal-insulator transition is of first order. Right panel: Comparison of theoretically obtained thermal hysteresis ($U = 3.6t_*$) with experimental observations in V_2O_3 [13].

state until the left spinodal is crossed (transition line 1). Thus as one crosses the coexistence region and reenters via heating/cooling, thermal hysteresis would be obtained. The hysteretic behavior seen in the present theory is naturally very far removed from the rich experimentally observed hysteresis seen e.g. in V_2O_3. The coexistence of metallic and insulating islands has been experimentally observed in thin films [81], as well as in manganites [82], while within DMFT, where spatial inhomogeneities are completely ignored, the coexistence is just that of the metallic and insulating solutions. Experimentally, the resistivity does not increase monotonically with heating or cooling. Instead, multiple steps or avalanches are observed to accompany the hysteretic behavior. While such details are absent in the present theory, nevertheless, we carry out a direct comparison of our hysteresis result with the one found experimentally in doped V_2O_3 [13] (right panel of Fig. 1.9). The purpose of such a comparison being to assess if the half-filled Hubbard model can capture at least the qualitative aspects of real materials. If it does, then the hope would be that a realistic theory based on finite dimensions including spatial inhomogeneities would be able to capture the experimentally observed behavior quantitatively. The best fit of the hysteresis result for a specific interaction ($U = 3.6t_*$), yields $t_* \sim 7305$K (0.63eV). This agrees well with the independent band structure calculations for V_2O_3 [83] and is of the right magnitude.

We now focus on optical transport in the next subsection.

1.4.3 Optical conductivity:

As can be naturally expected, changes in interaction strength U/t_* and especially the Mott MIT affect dynamical or optical transport properties strongly. Fig. 1.10 shows the computed $T = 0$ optical conductivity $\sigma(\omega)$ as U/t_* increases from a low value of 1.0 to a moderately strong value of 3.0. The inset shows the corresponding spectral functions. Several very interesting features can be seen. As U increases, a strong absorption feature emerges at $\sim U/2$ for $U \gtrsim 2t_*$, while a second peak at $\sim U$ emerges beyond $3t_*$. For low values, none of these features may be distinguished. The first peak arises because of excitations between either of the Hubbard bands and the Fermi level, while the second peak represents excitations between the lower and upper Hubbard band. The zero frequency Drudé peak is also present, but is not visible, since it has a Dirac-delta function form. The changes in optical conductivity are naturally understood through the inset of Fig. 1.10. For low values of U/t_*, a single featureless spectral function is obtained, while the emergence

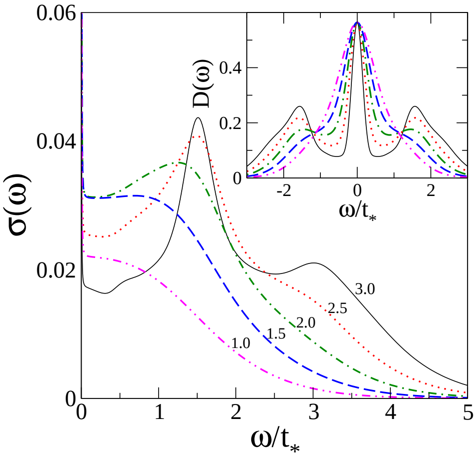

Fig. 1.10: The main panel shows the zero temperature optical conductivity for U/t_* values ranging from 1.0 to 3.0 (indicated by numbers). The inset shows the corresponding spectral functions.

of distinct Hubbard bands in the spectra mark the emergence of the first and second absorption peaks in the optical conductivity. At around the half bandwidth ($\omega \simeq 1.15t_*$) a universal crossing point is seen in the spectra.

The effect of Mott transition on the optical absorption is illustrated clearly in Fig. 1.11, which is similar to the previous figure, except that the values of U/t_* considered here increase from 3.0 to 5.0. The transition from the correlated metallic phase to the Mott insulator phase occurs at $U/t_* \simeq 4.5$, where, within IPT, a large gap $\sim U - 2t_*$ is known to form [45,54]. The main panel shows optical conductivity as a function of ω/t_*. In the metallic phase ($U < U_{c2}$), the first absorption peak is seen to get narrower and surprisingly gets red-shifted as the Mott transition is approached. The second absorption peak begins to dominate as $U \to U_{c2}$ and becomes the sole feature in the Mott insulating phase. The $U > U_{c2}$ optical conductivity is seen to possess a clear optical gap, which increases with increasing U and reflects the presence of the gap in the density of states (see inset).

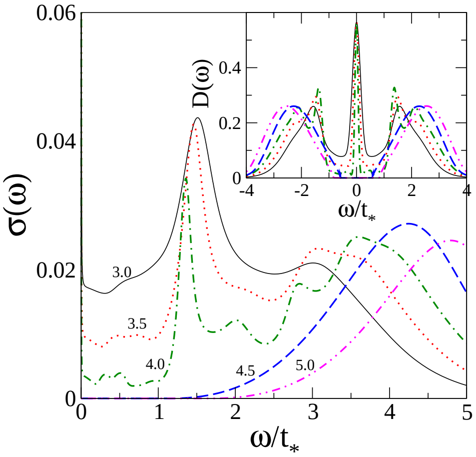

Fig. 1.11: The main panel shows the zero temperature optical conductivity for U/t_* values ranging from 3.0 to 5.0 (indicated by numbers). The inset shows the corresponding spectral functions.

The temperature evolution of the optical conductivities is equally interesting. In Fig. 1.12 we show the $\sigma(\omega;T)$ behavior for various T's for a moderately strong interaction strength of $U = 3.0t_*$. The inset again shows the corresponding spectral functions. The first absorption peak at lower temperatures loses spectral weight as temperature increases, which is gained by the second peak, and again an almost universal crossing point is seen, marking the frequency across which the transfer of spectral weight occurs. The Drudé peak at $\omega = 0$ diminishes in height, consistent with the dc conductivity values, and disappears completely at $T = 0.2$ by forming a shoulder-like feature at higher frequency $\omega \sim 2.5t_*$. An earlier investigation [84] (though it was not exactly calculated for the half-filled HM) claimed that the shoulder formation is actually shifting of Drudé peak (pseudo-Drudé peak) and the phase is metallic. However, here we argue that this arises due to the pseudogap formation in the DoS (see the left inset) and it is actually an insulating state since $d\rho(T)/dT < 0$ (see the right inset) and the phase lies in the crossover

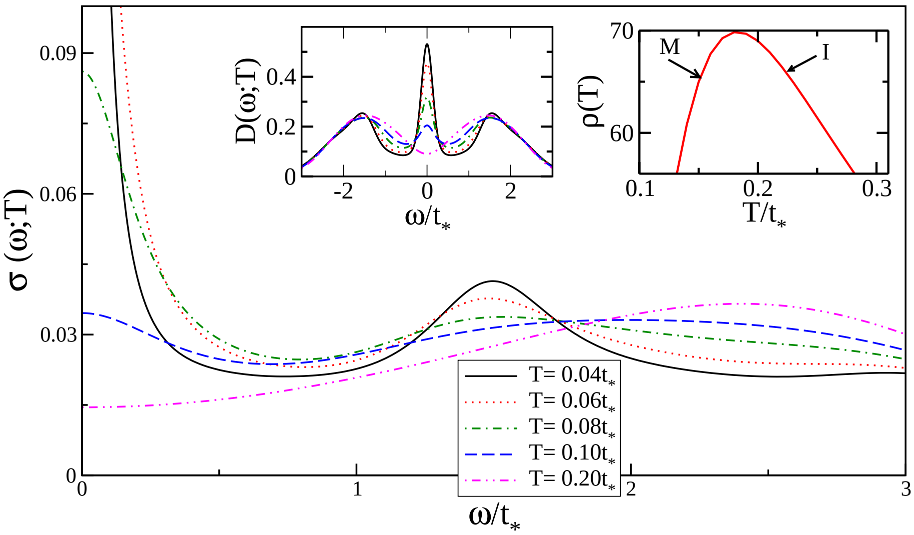

Fig. 1.12: The main panel shows the temperature evolution of optical conductivity for $U/t_* = 3.0$. Temperature varies from $T = 0.04t_*$ to $T = 0.2t_*$. The left inset shows the corresponding spectral functions and the right inset shows the resistivity at $T = 0.2t_*$. M marks for metallic ($d\rho/dT > 0$) and I marks for insulating ($d\rho/dT < 0$) behavior.

regime.

The universal crossing point, known as the *isosbestic point* in the metallic phase has been observed in several materials, e.g. V_2O_3 [85], $NiS_{2-x}Se_x$ [86], $La_{2-x}Sr_xCuO_4$ [87], $La_{1-x}Ca_xTiO_3$ [88]. Occurrence of isosbestic points is not well-explained. Nevertheless such a point is believed to have a close connection with f-sum rules and its location is associated to microscopic energy scales in correlated systems [89, 90]. Here, we see that the dynamics also exhibit a similar feature indicating an even more general basis for its existence. If we use our earlier estimation of t_* (0.6 eV) for V_2O_3 or the LDA-calculated value, we find that the isosbestic point arises at $\sim$ 0.9-1.0 eV which lies in the mid-infrared range, and which is close to that seen in a recent infra-red spectroscopy measurement [85] i.e. at 6000 cm^{-1} ($\sim$ 0.7 eV).

Finally we show the optical conductivity for the Mott insulating regime ($U/t_* = 4.7$) evolving with temperature in Fig. 1.13. A single absorption peak is seen at low temperatures, and as T increases, spectral weight is transferred from this peak to lower frequencies, and the absorption peak diminishes, and experiences a slight blue shift. The spectral function exhibits negligible change as a function of temperature and although, there is indeed, an exponentially small rise in the density of states in the neighborhood of the Fermi level, it visually appears to coincide with the $T = 0$ DoS.

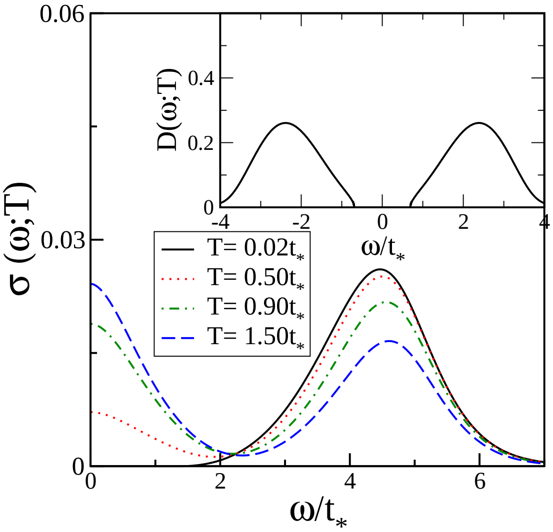

Fig. 1.13: The main panel shows optical conductivity for temperatures $T/t_* = 0.02, 0.5, 0.9$ and 1.5. The inset shows the corresponding spectral function which exhibits negligible changes as temperature is increased.

In the next section, we discuss the thermodynamic properties of both metallic and insulating phases.

1.5 Thermodynamic properties: internal energy and specific heat

We rewrite Eq. (25) from Chapter 0, that we use to calculate the internal energy:

$$E = \langle \hat{H}_{\mathrm{HM}} \rangle = \int d\omega n_F(\omega) \left[2\omega D(\omega) + \frac{1}{\pi} \mathrm{Im}\left(\Sigma(\omega) G(\omega)\right) \right] \tag{25}$$

This expression is quite remarkable in a sense that the internal energy has been written as a function of real frequency ω, and this is numerically more convenient to use compared to the expression obtained in terms of Matsubara frequencies [45,67,91] in earlier implementations. Fig. 1.14 shows the internal energies for the metallic ($U = 2.8t_*$) and insulating phase ($U = 4.7t_*$)

By numerically taking derivative w.r.t. temperature we find the specific heat also. Fig. 1.15 shows the linear temperature dependence of specific heat at low T for U/t_* ranging from 2.2 to 2.8. When we scale temperature by low-energy scale Δ, all low-temperature curves merge together. This universal behavior signifies the Fermi-liquid properties at low temperature (Fig. 1.15).

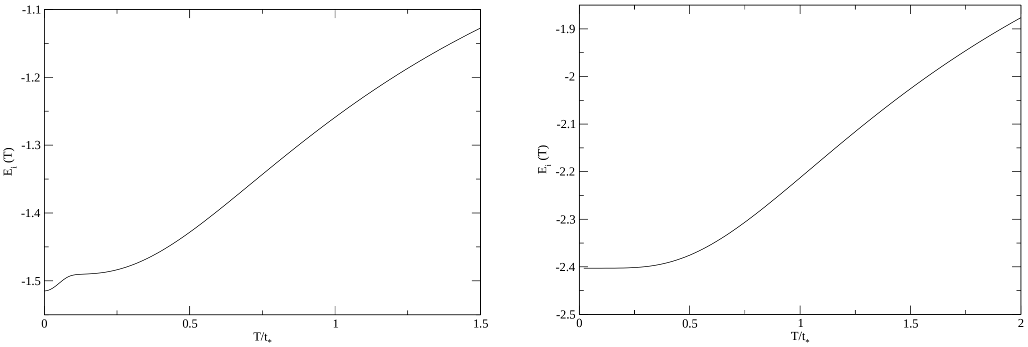

Fig. 1.14: Internal energy for $U = 2.8t_*$ (left panel) and $U = 4.7t_*$ (right panel)

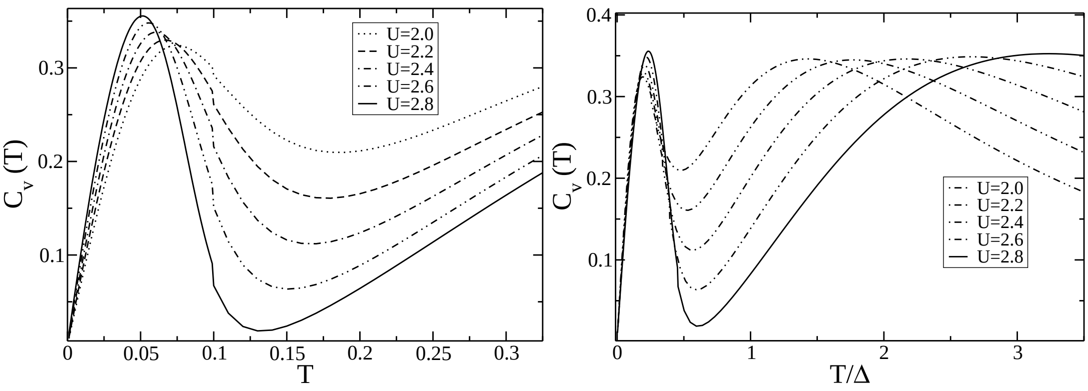

Fig. 1.15: Left panel: Specific heat with temperature for U/t_*=2.0, 2.2, 2.4, 2.6, 2.8. Right panel: The same after scaling the temperature axis by the FWHM of corresponding spectarl densities.

In insulating regime, as shown in Fig. 1.16, at temperature quite smaller than the spectral gap, we find the activation behavior: $C_v(T) \propto T\exp(-\Delta_g/T)$ (see Appendix H for a heuristic derivation). Though internal energy and

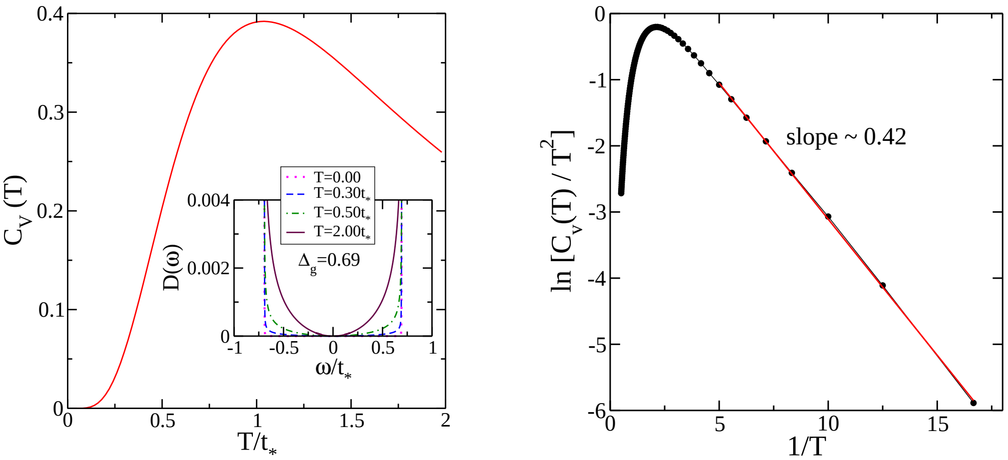

Fig. 1.16: Specific heat in insulating regime (U/t_*=4.7) $C_v(T) \propto T\exp(-\frac{\Delta_g}{T})$ where Δ_g is half of the spectral gap. The slope of the linear regime (highlighted) is $\sim 0.42t_*$ (right panel) which is slightly less than the gap of zero-temperature spectral function ($\Delta_g \sim 0.7t_*$).

specific heat behaves physically with consistence at low and high U regions, there is a serious drawback in the intermediates region. The internal energy shows a dip as we gradually increase T for $U > 2.8t_*$ in HCL. Since IPT, as a perturbation does not assure any conservation of physical properties (e.g. here energy), this may result in unphysical values in the internal energy and hence in the specific heat (see Fig. 1.17).

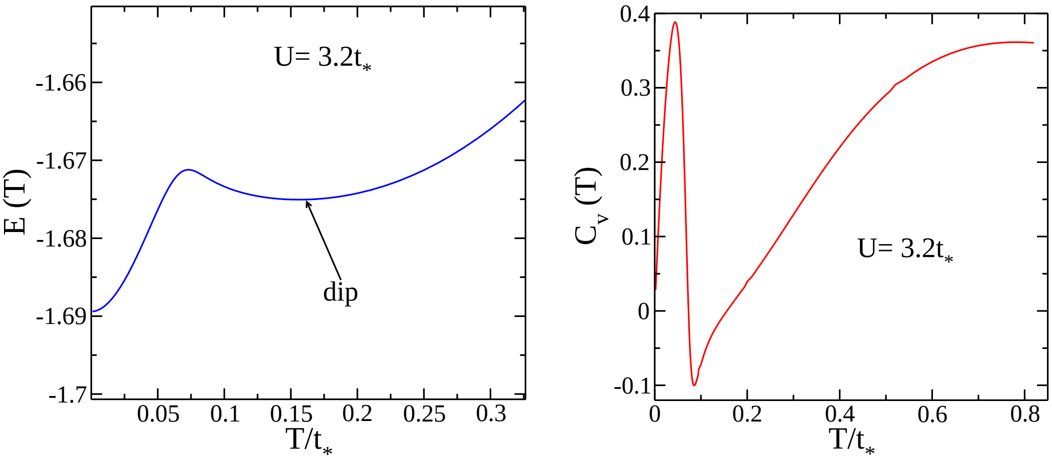

Fig. 1.17: Internal energy (left panel) and specific heat (right panel) for $U = 3.2t_*$. The dip in the internal energy produces negative value of specific heat.

1.6 Summary

A systematic study of the half-filled Hubbard model within dynamical mean field theory is carried out, with the focus being on universality, scaling and qualitative comparison to experiments. We reformulate a well-known and extensively employed impurity solver for the effective impurity problem that the lattice problem gets mapped onto within DMFT, namely the IPT, such that some of the problems with previous implementations have been overcome. We find that the coherence peak in the resistivity is a universal feature. A comparison with experimental measurements of resistivity in Se doped NiS_2

with varying pressure yields qualitatively excellent agreement. Thermal and pressure driven hysteresis is shown to be qualitatively explicable within this scenario, and again, a comparison of thermal hysteresis with experiments in V_2O_3 are seen to yield a reasonable number for the hopping integral. The transfer of spectral weight across the Mott transition and the isosbestic points have been highlighted in the study of optical conductivity. We conclude that the Hubbard model does indeed represent an appropriate phenomenological model that can qualitatively explain a large range of phenomena observed in transition metal oxides. This offers hope for more detailed material specific studies such as those employing LDA+DMFT [92–94] approaches to obtain quantitative agreement with experiments.

Chapter 2

Zero temperature local moment approach (LMA): Theory and formalism

2.1 Introduction

The requirement of a non-perturbative theory, specifically in the context of the single-impurity Anderson model (SIAM) sitting at the heart of any DMFT based calculation, that can capture single-particle dynamics at all energy scales has been a constant need for resolving the issues in correlated systems. IPT certainly fails to capture the strong-coupling limit due to its perturbative nature (second order in interaction strength U). Exact methods like quantum Monte Carlo (QMC) [51,52] cannot be employed directly at zero temperature and additionally are computationally very expensive. Other methods, such as exact diagonalization (ED) [45, 49] and NRG [95] produce discrete features that need broadening, the procedure for which remains *ad hoc*. ED is inefficient to capture the low-energy feature and NRG also suffers from inability to get correct high energy features, specifically the band edges of Hubbard bands [19,50], and continuous variation of finite temperature [95]. On the other hand, the local moment approach (LMA), developed by David Logan and his co-workers [55, 56] during the late nineties, showed a remarkable success in capturing both weak and strong coupling limits correctly in the SIAM. Later many works have been carried out successfully using LMA in the context of the periodic Anderson model (PAM) [69, 96] and the Hubbard model (HM) [97, 98]. In this sense, the LMA can be a useful method in the context of Mott transition. In our present work, many approaches have been followed from Ref. 98 and M. P. Eastwood's PhD thesis [99]. However, many issues in the HM context have remained unresolved, specifically regarding the Fermi liquid metal and its universal scaling behavior close to the Mott transition and and properties of the doped Mott insulator. For this reason, before we arrive the issues within particular contexts, we need to set up the basic formalism of LMA.

In this chapter, we discuss the zero temperature formalism of LMA, starting from a simple mean-field approximation, which is the unrestricted Hartree-Fock (UHF) approximation. We show that this approximation fails to give the correct physics since in certain cases, it does not preserve the Fermi liquid property even though it yields a metallic phase. We realize that the static nature of the mean-field approximation is responsible for such discrepancy and we develop a scheme as a remedy by introducing the spin-flip dynamics (through transverse spin-polarization propagators of infinite orders) in the self-energy approximation. We also find that by restoring the broken spin-symmetry in the UHF approximation, we get back a consistent Fermi liquid behavior below the Mott transition point. We discuss the special condition that occurs in the insulating case and the special care needed as a singularity arises in the spin-polarization propagator. Finally we discuss the numerical implementation with a flow diagram.

2.2 Starting point: unrestricted Hartree-Fock (UHF)

The simplest mean-field approximation one can formulate as a starting point is the unrestricted Hartree-Fock (UHF) approximation. In this approximation, each electron moves in a time-independent mean-field background of other electrons. UHF is a site and spin dependent approximation. Thus it allows for a possibility of breaking spin-symmetry and hence the formation of local moments in contrast to the conventional restricted Hartree Fock (RHF) approximation which does not have any spin-dependence. The value of the local moment is measured as $|\mu| = |\langle \hat{n}_\uparrow - \hat{n}_\downarrow \rangle|$, we label A and B for solutions $\mu = \pm|\mu|$ respectively. The mean-field or the UHF Hubbard model can be written as

$$\begin{aligned} \hat{H}^{\mathrm{MF}} = & - \sum_{<ij>\,\sigma} t_{ij}\,(c^\dagger_{i\sigma} c_{j\sigma} + \mathrm{h.c.}) + \epsilon_d \sum_{i\sigma} c^\dagger_{i\sigma} c_{i\sigma} \\ & + U \sum_{i\sigma} \langle \hat{n}_{i\bar{\sigma}} \rangle \hat{n}_{i\sigma} - U \sum_{i} \langle \hat{n}_\uparrow \rangle \langle \hat{n}_\downarrow \rangle \end{aligned} \tag{2.1}$$

In term of momentum ($\mathbf{k}$) space

$$\begin{aligned}\hat{H}^{\mathrm{MF}} &= \sum_{\mathbf{k}\,\sigma} \epsilon_{\mathbf{k}}\, c^{\dagger}_{\mathbf{k}\,\sigma} c_{\mathbf{k}\,\sigma} + \epsilon_d \sum_{\mathbf{k}\,\sigma} c^{\dagger}_{\mathbf{k}\,\sigma} c_{\mathbf{k}\,\sigma} + U\langle \hat{n}_{\bar{\sigma}}\rangle \sum_{\mathbf{k}\,\sigma} c^{\dagger}_{\mathbf{k}\,\sigma} c_{\mathbf{k}\,\sigma} + \text{constant} \\ &= \sum_{\mathbf{k}\,\sigma} \epsilon_{\mathbf{k}}\, \hat{n}_{\mathbf{k}\,\sigma} + \Sigma^0_{\sigma} \hat{n}_{\mathbf{k}\,\sigma} + \text{constant} \qquad (2.2)\end{aligned}$$

where

$$\Sigma^0_{\sigma} = \epsilon_d + U\langle \hat{n}_{\bar{\sigma}}\rangle \,. \qquad (2.3)$$

This is a diagonalizable form and in fact the Green's function is similar in form to a non-interacting propagator in a lattice with energy shifted by Σ^0_{σ}. We can write the total electronic density or filling $\langle \hat{n}\rangle$ and the average local moment μ (for A-type solution) as

$$\langle \hat{n}\rangle = \langle \hat{n}_{\uparrow}\rangle + \langle \hat{n}_{\downarrow}\rangle \qquad (2.4)$$

and

$$\mu = \langle \hat{n}_{\uparrow}\rangle - \langle \hat{n}_{\downarrow}\rangle \,. \qquad (2.5)$$

Now depending on the choice of solution A or B, we can write the general spin-dependent UHF self-energy as

$$\Sigma^0_{\alpha\sigma} = \epsilon_d + U\langle \hat{n}_{\alpha\bar{\sigma}}\rangle = \epsilon_d + \frac{U}{2}(\,\langle \hat{n}\rangle - \alpha\sigma\mu\,) \qquad (2.6)$$

where $\alpha = \pm 1$ for A and B-solutions respectively.

Hence the single-particle UHF Green's functions can be written as

$$\mathcal{G}_{A\sigma}(\omega) = \frac{1}{\omega^+ - \Sigma^0_{A\sigma} - S_\sigma(\omega)} = \frac{1}{\omega^+ - \epsilon_d - \frac{U}{2}(\,\langle \hat{n}\rangle - \sigma\mu\,) - S_\sigma(\omega)} \tag{2.7a}$$

$$\mathcal{G}_{B\sigma}(\omega) = \frac{1}{\omega^+ - \Sigma^0_{B\sigma} - S(\omega)} = \frac{1}{\omega^+ - \epsilon_d - \frac{U}{2}(\,\langle \hat{n}\rangle + \sigma\mu\,) - S_\sigma(\omega)} \tag{2.7b}$$

where $S_\sigma(\omega)$ is the medium self-energy or the Feenberg self-energy [99–101], which arises due to presence of nearest neighbor hopping in a lattice. $S_\sigma(\omega) = S_\sigma[\mathcal{G}_{A\uparrow}(\omega), \mathcal{G}_{B\downarrow}(\omega)]$ for the A-type solutions, i.e. a functional of the interacting Green's functions. For the paramagnetic case, it depends only on the spin-independent average Green's function, which is $\frac{1}{2}(\mathcal{G}_{A\sigma}(\omega) + \mathcal{G}_{A\bar{\sigma}}(\omega))$ in the UHF theory. Therefore for the paramagnetic case we can write

$$S_\sigma(\omega) = S(\omega) \tag{2.8}$$

Then from Eq. (2.7) we can see that

$$\mathcal{G}_{A\sigma}(\omega) = \mathcal{G}_{B\bar{\sigma}}(\omega) \tag{2.9}$$

and from Eq. (2.6)

$$\Sigma^0_{a\sigma}(\omega) = \Sigma^0_{B\bar{\sigma}}(\omega) \tag{2.10}$$

Therefore if we just work with one type solution (say, A-type) of Green's functions or self-energies, we can find the same for the other type using the above symmetries. Hence onward we shall drop the solution label index (in accord to our choice biased to A-type solutions) and we shall mention explicitly when needed. So let us rewrite the UHF self-energy and the UHF

Green's function:

$$\Sigma^0_\sigma = \epsilon_d + \frac{U}{2}(\,\langle\hat{n}\rangle - \sigma\,\mu) \tag{2.11}$$

$$\mathcal{G}_\sigma(\omega) = \frac{1}{\omega^+ - \epsilon + \sigma x - S(\omega)} \tag{2.12}$$

where we define

$$x \equiv \frac{1}{2}|\mu|U \tag{2.13}$$

and

$$\epsilon = \epsilon_d + \frac{U}{2}\langle\hat{n}\rangle \tag{2.14}$$

We shall see later that instead of U and $|\mu|$ independently, their product or x plays a crucial role in the implementation of the local moment approach (LMA).

Now if we want to calculate the total effective UHF Green's function for the paramagnetic case, we need to take average of spin-dependent Green's functions in Eq. (2.12), i.e.

$$G^0(\omega) = \frac{1}{2}[\mathcal{G}_\uparrow(\omega) + \mathcal{G}_\downarrow(\omega)] \tag{2.15}$$

Once we calculate $\mathcal{G}_\sigma(\omega)$, following Eq. (2.4) and Eq. (2.5) we can determine the density and the local moment from their imaginary parts, i.e.

$$\langle\hat{n}\rangle = \int_{-\infty}^{\infty} d\omega\,[\mathcal{D}_\uparrow(\omega) + \mathcal{D}_\downarrow(\omega)] \tag{2.16}$$

$$\mu = \int_{-\infty}^{\infty} d\omega \, [\mathcal{D}_{\uparrow}(\omega) - \mathcal{D}_{\downarrow}(\omega)] \tag{2.17}$$

where

$$\mathcal{D}_{\sigma}(\omega) = -\frac{1}{\pi} \mathrm{Im}\, \mathcal{G}_{\sigma}(\omega) \tag{2.18}$$

Hence we plug the magnitude of the local moment in Eq. (2.12) and find the UHF Green's functions again. If we repeat these two steps until we arrive self-consistency, we get the UHF Green's functions for a given U. However, in practice, instead of doing this iterative process, we select x and determine U from Eq. (2.13) after calculating μ by using Eq. (2.17). One important thing to remember is that $S(\omega)$ is also unknown from the beginning. We re-calculate it since $G^0(\omega)$ can be also written as

$$G^0(\omega) = \frac{1}{\gamma(\omega) - S(\omega)} \, . \tag{2.19}$$

Thus

$$S(\omega) = \gamma(\omega) - 1/G^0(\omega) = \omega - 1/\mathcal{H}[\gamma(\omega)] \tag{2.20}$$

where we have use the fact that $G^0(\omega)$ is the Hilbert transform of the lattice DoS $D_0(\omega)$ over $\gamma(\omega)$ (*Cf.* Eq. (19)):

$$\mathcal{H}[\gamma(\omega)] = \int_{-\infty}^{\infty} d\omega' \, \frac{D_0(\omega')}{\gamma(\omega) - \omega'} \tag{2.21}$$

Now $\gamma(\omega)$ can be calculated by equating Eq. (2.15) and Eq. (2.19), which leads to

$$\gamma(\omega) = \frac{2\gamma_{\uparrow}(\omega)\gamma_{\downarrow}(\omega) - [\gamma_{\uparrow}(\omega) + \gamma_{\downarrow}(\omega)]S(\omega)}{\gamma_{\uparrow}(\omega) + \gamma_{\downarrow}(\omega) - 2S(\omega)} \tag{2.22}$$

where

$$\gamma_\sigma(\omega) = \omega^+ - \epsilon + \sigma x \,. \tag{2.23}$$

2.2.1 p-h symmetric case

So far we have discussed formulation for a general filling or average electron occupation number $\langle \hat{n} \rangle$. Now we will focus on a special case: $\langle \hat{n} \rangle = 1$, which is the half-filling or the particle-hole symmetric case. p-h symmetric HM is interesting since only for this particular filling, we expect a Mott insulator. For any other filling, there will be always empty sites available for electrons to hop and hence they should always construct a metal. As we have mentioned in Chapter 1, the half-filled case yields a simple relation between the orbital energy and the interaction strength, viz. $\epsilon_d = -U/2$ (see Appendix C for a derivation). This makes $\epsilon = 0$ in Eq. (2.14), which implies that the spin-dependent UHF Self-energies and Green's functions in Eq. (2.11) and Eq. (2.12) reduce as

$$\Sigma_\sigma^0 = \frac{-\sigma}{2} U|\mu| = -\sigma x \tag{2.24}$$

$$\mathcal{G}_\sigma(\omega) = \frac{1}{\omega^+ + \sigma x - S(\omega)} \,. \tag{2.25}$$

Below we summarize the steps required for practical calculations within the UHF approximation (for simplicity we consider symmetric case here, i.e. $\epsilon = 0$). As a common practice, t_* is chosen to be 1.

Steps to determine UHF Green's functions and the corresponding U

(i) Choose an x and a guess function for $S(\omega)$.

(ii) Calculate $\mathcal{G}_\sigma$ from Eq. (2.12).

(iii) Calculate μ from Eq. (2.17).

(iv) Find total Green's function from Eq. (2.15).

(v) Calculate $S(\omega)$ from Eq. (2.20).

(vi) Go back to step (ii) and repeat next steps.

(vii) Stop after self-consistency is achieved in $S(\omega)$. Find related U from Eq. (2.13).

The UHF spectral densities for different U/t_* have been shown in Fig. 2.1. As one changes U, one finds three distinct regimes by looking at the spectral function and the local moment μ:

(I) $0 \leq U \leq U_m^0$ -metallic, $|\mu| << 1$;

(II) $U_m^0 \leq U \leq U_c^0$ -metallic, $|\mu| < 1$;

(III) $U > U_c^0$ -insulating, $|\mu| \sim 1$.

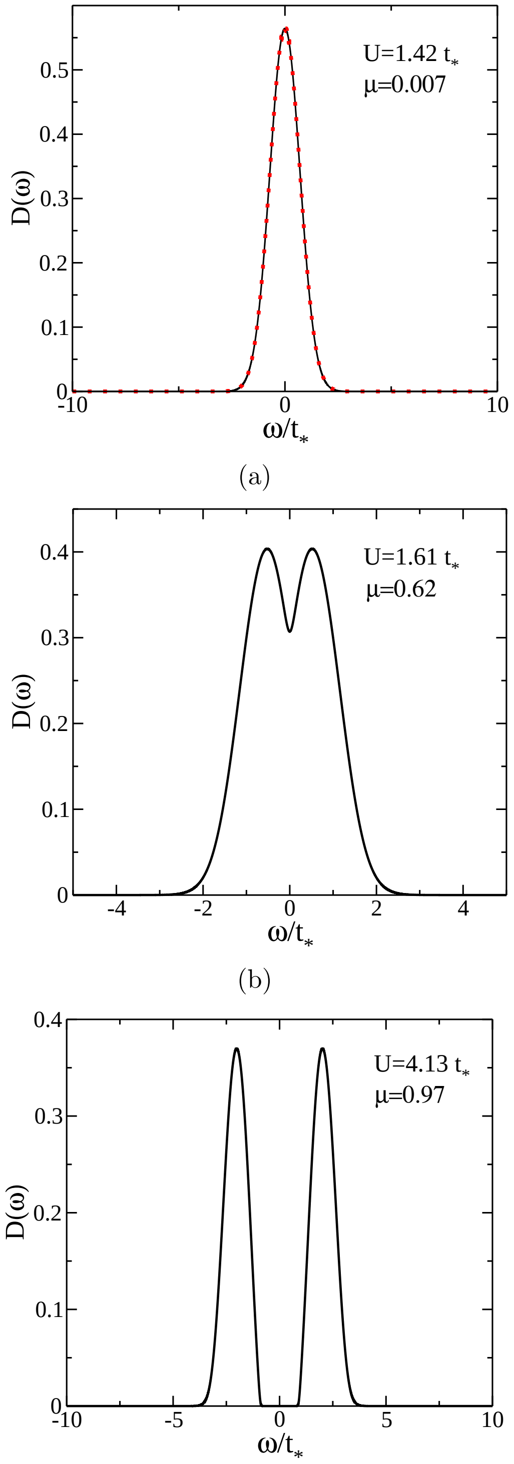

(a)

(b)

(c)

Fig. 2.1: Spectral functions for the hypercubic lattice for interaction strengths $U/t_* = 1.42\,, 1.61\,, 4.13 t_*$, that belong to different regimes. (a), (b), and (c) represent the regimes (I), (II), and (III) as described in the text. Red dotted line in (a) represents the non-interacting value which sits on top of the interacting curve. Local moments in (I) is insignificant ($\mu = 0.007$), in (II) is significant enough to show non-Fermi liquid behavior ($\mu = 0.62$), and in (II) reaches close to the value ($\mu = 0.97 \sim 1$) at strong-coupling limit ($U \to \infty$).

In the regime-I UHF practically becomes RHF (since no significant local moment forms) and the spectral density coincides with the non-interacting (red dotted curve in Fig. 2.1(a)) non-interacting DoS. In that sense, it is like a Fermi-liquid though it does not have any resonance feature, as we have already seen in the IPT metallic state, at $\omega = 0$. Here $\mathcal{G}_{\uparrow}(\omega)$ and $\mathcal{G}_{\downarrow}(\omega)$ are effectively equal and hence $G^0(\omega)$ too. Therefore no significant local moment does arise.

After a critical value U_m^0 ($U_m^0 \simeq 1.425t_*$ for the HCL and $U_m^0 \simeq 1.17t_*$ for the BL), the spectral densities deviate from the non-interacting value. Moreover, local moments with significant values start forming as we increase U/t_* further. This happens due to significant difference between two spin-dependent Green's functions, that reflect in the two peaks that appear at opposite sides of the Fermi level. However, the spectral density still remains finite at the Fermi level and hence the electronic property in this regime is expected to be metallic. The spectral density at the Fermi level appear as a valley between the two peaks, and decreases as interaction is increased further, finally it becomes zero at a critical value U_c^0 ($U_c^0 \simeq 1.82t_*$ for the HCL and $U_c^0 \simeq 1.33t_*$ for the BL).

For $U > U_c^0$, the system enters into the regime-III, where a clean gap is observed around the Fermi level. Thus the regime signifies insulating behavior. At large U/t_*, clear Hubbard bands are observed and they appear at $\omega = \pm U/2$, which is expected for the strong-coupling limit.

Now it is clear that the UHF results bear severe drawbacks, namely

(i) Before the system goes to a Mott transition, it passes through a non-Fermi liquid regime (regime-II), which is not physically acceptable.

(ii) The Fermi liquid regime (regime-I) does not have any Hubbard band feature(*Cf.* IPT results in Chapter 1).

(iii) The Hubbard bandwidth at the strong-coupling does not match with that found from the exact calculation [98].

Naturally in the UHF approximation the self-energies are static (frequency independent), which sounds very crude as an approximation. Therefore it is fair to ask: Is it possible to develop a many-body theory beyond the mean-field approximation or can the consideration of higher order diagrams in the perturbation theory give more sensible results, e.g. a Fermi liquid metal to a Mott insulator transition?

2.3 Inclusion of spin-flip scattering dynamics

The UHF approximation fails to capture the Fermi liquid (low energy scaling behavior) and we blame it on the static nature of the approximation. Therefore as a first possible improvement, we wish to see if we can find a remedy of the problems, that arise due to static nature of the self-energy approximation, by including the spin-flip dynamics along with it.

The transverse spin-polarization propagator or the polarization bubble is defined as [1]

$$\Pi^{\sigma\bar{\sigma}}_{ii}(t) \equiv i\langle\, \hat{T}\hat{S}^{\sigma}_{i}(t)\hat{S}^{\bar{\sigma}}_{i}(0)\,\rangle \tag{2.26}$$

---

[1] Note that σ or $\bar{\sigma} = -\sigma$ in the superscript of $\Pi^{\sigma\bar{\sigma}}_{ii}$ does not imply spin orientation (up or down). $\sigma = +/-$ stands for raising/lowering operator as defined in Eq. (2.26). However, these notations will be useful to write in a general form making connection to the spin index of spin-dependent self-energy and Green's function.

where $S_i^+ = c_{i\uparrow}^\dagger c_{i\downarrow}$ (raising operator); $S_i^- = c_{i\downarrow}^\dagger c_{i\uparrow}$ (lowering operator) We call it 'bare' polarization when there is no interaction line. We can construct higher order diagrams by putting more interaction lines in the 'bare' polarization bubble . If we consider all such diagrams, we find that they appear in a geometric progression (i.e in powers of ${}^0\Pi_{ii}^{\sigma\bar{\sigma}}(\omega)$), which can be summed as follows (see Fig. 2.2).

$$\Pi_{ii}^{\sigma\bar{\sigma}}(\omega) = \frac{{}^0\Pi_{ii}^{\sigma\bar{\sigma}}(\omega)}{1 - U\,{}^0\Pi_{ii}^{\sigma\bar{\sigma}}(\omega)} \tag{2.27}$$

This summation is known as the random-phase approximation (RPA).

The 'bare' polarization is the convolution of 'bare' propagators (here in our context, the UHF Green's functions).

$${}^0\Pi_{ii}^{\sigma\bar{\sigma}}(\omega) = \frac{i}{2\pi} \int_{-\infty}^{\infty} d\omega'\, \mathcal{G}_{i\bar{\sigma}}(\omega') \mathcal{G}_{i\sigma}(\omega' - \omega) \tag{2.28}$$

From Eq. (2.28), the imaginary part of the bare polarization is written as

$$\frac{1}{\pi}\mathrm{Im}\,{}^0\Pi_{ii}^{\sigma\bar{\sigma}}(\omega) = \theta(\omega) \int_0^{|\omega|} d\omega'\, \mathcal{D}_\downarrow(\omega')\mathcal{D}_\uparrow(\omega'-\omega) + \theta(-\omega) \int_{|-\omega|}^0 d\omega'\, \mathcal{D}_\downarrow(\omega')\mathcal{D}_\uparrow(\omega'-\omega) \tag{2.29}$$

In practice $\mathrm{Im}\,{}^0\Pi_{ii}^{\sigma\bar{\sigma}}(\omega)$ is calculated from Eq. (2.29) and its real part is calculated through Kramers-Kronig transformation, i.e.

$$\mathrm{Re}\,{}^0\Pi_{ii}^{\sigma\bar{\sigma}}(\omega) = \int_{-\infty}^{\infty} \frac{d\omega'}{\pi} \frac{\mathrm{Im}\,{}^0\Pi_{ii}^{\sigma\bar{\sigma}}(\omega')}{\omega' - \omega}\,. \tag{2.30}$$

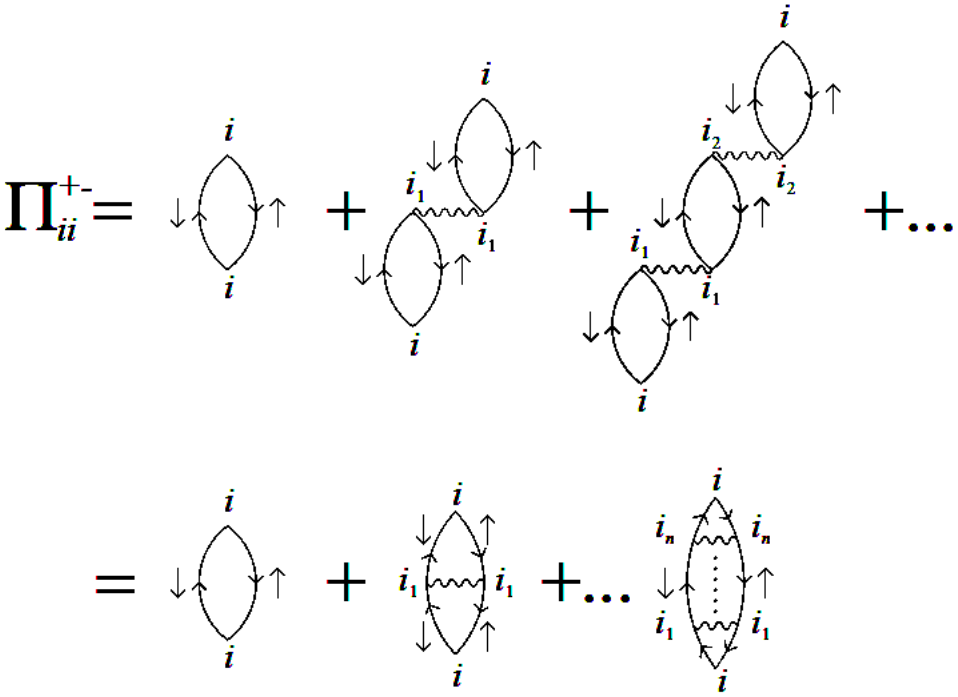

Fig. 2.2: Diagrammatic expansion of the full polarization bubble Π_{ii}^{+-}

2.3.1 Stability criterion

Using the Lehmann representation [91] the imaginary part of $\Pi_{ii}^{\sigma\bar{\sigma}}(\omega)$ can be written as

$$\frac{1}{\pi}\mathrm{Im}\Pi_{ii}^{\sigma\bar{\sigma}}(\omega) = \sum_n |\langle\psi_n^N|\hat{S}_i^{\sigma}|\psi_0^N\rangle|^2\delta(\omega + [E_n^N - E_0^N]) \\ + \sum_n |\langle\psi_n^N|\hat{S}_i^{-\sigma}|\psi_0^N\rangle|^2\delta(\omega - [E_n^N - E_0^N]) \geq 0 \qquad (2.31)$$

Also from Eq. (2.27), in terms of ${}^0\Pi_{ii}^{\sigma\bar{\sigma}}(\omega)$, $\mathrm{Im}\Pi_{ii}^{\sigma\bar{\sigma}}(\omega)$ can be expressed as

$$\mathrm{Im}\Pi_{ii}^{\sigma\bar{\sigma}}(\omega) = \frac{\mathrm{Im}^0\Pi_{ii}^{\sigma\bar{\sigma}}(\omega)}{[1 - U\mathrm{Re}^0\Pi_{ii}^{\sigma\bar{\sigma}}(\omega)]^2 + [U\mathrm{Im}^0\Pi_{ii}^{\sigma\bar{\sigma}}(\omega)]^2}\,. \qquad (2.32)$$

Since $\mathrm{Im}\Pi_{ii}^{\sigma\bar{\sigma}}(\omega) \geq 0$,

$$\mathrm{Re}\Pi_{ii}^{\sigma\bar{\sigma}}(\omega = 0) = \int_{-\infty}^{\infty} \frac{d\omega}{\pi} \frac{\mathrm{Im}\Pi_{ii}^{\sigma\bar{\sigma}}(\omega')}{|\omega'|} \geq 0 \tag{2.33}$$

Now using Eq. (2.27),

$$\mathrm{Re}\Pi_{ii}^{\sigma\bar{\sigma}}(0) = \frac{\mathrm{Re}^0\Pi_{ii}^{\sigma\bar{\sigma}}(0)}{1 - U\mathrm{Re}^0\Pi_{ii}^{\sigma\bar{\sigma}}(0)} \tag{2.34}$$

Therefore to retain the positive-semidefinite property of $\mathrm{Re}\Pi_{ii}^{\sigma\bar{\sigma}}(0)$ (from Eq. (2.33)) we need the following condition to be satisfied

$$1 - U\mathrm{Re}^0\Pi_{ii}^{\sigma\bar{\sigma}}(0) \geq 0$$

i.e.,

$$U\mathrm{Re}^0\Pi_{ii}^{\sigma\bar{\sigma}}(0) \leq 1 \tag{2.35}$$

When the equality holds, we find a pole in $\Pi_{ii}^{\sigma\bar{\sigma}}$ at $\omega = 0$

Now directly from Eq. (2.12)

$$\mathcal{G}_\uparrow(\omega) - \mathcal{G}_\downarrow(\omega) = -U|\mu|\mathcal{G}_\uparrow(\omega)\mathcal{G}_\downarrow(\omega) \tag{2.36}$$

and from Eq. (2.28) we find

$$U\mathrm{Re}^0\Pi^{+-}(0) = \frac{1}{|\mu|}\int_{-\infty}^{0} d\omega\, [\mathcal{D}_\uparrow(\omega) - \mathcal{D}_\downarrow(\omega)] \equiv \frac{|\mu^0|}{|\mu|} \tag{2.37}$$

where $|\mu^0|$ is pure static MF (UHF) local moment (i.e. self-consistent solution of Eq. (2.12) and Eq. (2.17)). Thus when the equality holds for stability criterion (Eq. (2.35)) $|\mu|$ takes its UHF-value (supposed to be solved self-consistently) from the gap equation. Away from UHF, within stable regime, $|\mu| > |\mu^0|$.

2.3.2 Self-energy

Incorporation of transverse spin-flip polarization with RPA sum, as shown in Fig. 2.2, gives rise to the following diagram for the dynamic self-energy. which readily translates into a convolution integral:

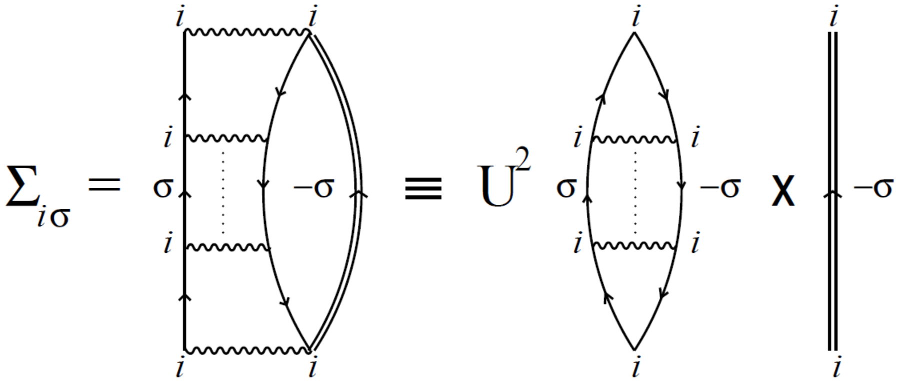

Fig. 2.3: Diagrammatic representation of the dynamic self-energy $\Sigma(\omega)$ in term of polarization bubbles and host Green's function

$$\Sigma_\sigma(\omega) = U^2 \int_{-\infty}^{\infty} \frac{d\omega'}{2\pi i} \mathcal{G}_{\bar{\sigma}}(\omega - \omega')\Pi^{\bar{\sigma}\sigma}(\omega') \tag{2.38}$$

where $\mathcal{G}(\omega)$ is now a self-consistent host Green's functioni (Note that we have dropped the subsciprts ii from $\Pi^{\bar{\sigma}\sigma}$ and we shall continue the notation now onwards except the cases where we need to specify them.).

Thus the total self-energy become

$$\begin{aligned}\Sigma_\sigma^{\mathrm{tot}}(\omega) &= \Sigma_\sigma^0 + \Sigma_\sigma(\omega) \\ &= \epsilon_d + \frac{U}{2}(\,\langle\hat{n}\rangle - \sigma\,\mu) + \Sigma_\sigma(\omega)\end{aligned} \tag{2.39}$$

Since the self-energy expression is spin-dependent, we always find two self-energies for the same site. At $T = 0$, from Eq. (2.38) the self-energy can be written as

$$\Sigma_\sigma(\omega) = U^2 \int_{-\infty}^{\infty} d\omega' \, \frac{1}{\pi}\mathrm{Im}\Pi^{+-}(\omega)[\theta(\omega')\mathcal{G}_{\bar{\sigma}}^{-}(\omega'+\omega)+\theta(-\omega')\mathcal{G}_{\bar{\sigma}}^{+}(\omega'+\omega)] \tag{2.40}$$

where

$$\mathcal{G}_\sigma^{\pm}(\omega) = \int_{-\infty}^{\infty} d\omega' \, \frac{\mathcal{D}_\sigma(\omega')\theta(\pm\omega')}{\omega - \omega' \pm i0^+} \tag{2.41}$$

such that $\mathcal{G}_\sigma(\omega) = \mathcal{G}_\sigma^{+}(\omega) + \mathcal{G}_\sigma^{-}(\omega)$.

2.3.3 Symmetry restoration

Though the UHF solutions are broken spin-symmetry solutions, as the original Hamiltonian is rotational (spin) invariant, the propagators should also be spin independent. This can be achieved by taking average of two spin-dependent Green's functions. Thus the Green's function for a paramagnetic system (spins unpolarized on average) is

$$\begin{aligned}G(\omega) &= \frac{1}{2}[G_\uparrow(\omega) + G_\downarrow(\omega)] \\ &= \frac{1}{2}\left[\frac{1}{\mathcal{G}_\uparrow^{-1}(\omega) - \Sigma_\uparrow^{\mathrm{tot}}(\omega)} + \frac{1}{\mathcal{G}_\downarrow^{-1}(\omega) - \Sigma_\downarrow^{\mathrm{tot}}(\omega)}\right]\end{aligned} \tag{2.42}$$

Also we can define a single spin-independent self-energy, $\Sigma(\omega)$ from the Dyson's Eq. :

$$G(\omega) = \frac{1}{\mathcal{G}^{-1}(\omega) - \Sigma(\omega)} \tag{22}$$

From Eq. (2.42) and Eq. (22) we get

$$\Sigma(\omega) = \frac{1}{2}(\Sigma^{\rm tot}_{\uparrow}(\omega) + \Sigma^{\rm tot}_{\downarrow}(\omega)) + \frac{[\frac{1}{2}(\Sigma^{\rm tot}_{\uparrow}(\omega) - \Sigma^{\rm tot}_{\downarrow}(\omega))]^2}{\mathcal{G}^{-1}(\omega) - \frac{1}{2}(\Sigma^{\rm tot}_{\uparrow}(\omega) + \Sigma^{\rm tot}_{\downarrow}(\omega))} \tag{2.43}$$

Now if we want to ensure the Fermi liquid behavior, we need to have $\mathrm{Im}\Sigma = 0$ at $\omega = 0$. If we consider only the static part in $\Sigma^{\rm tot}_{\sigma}(\omega)$, i.e. the MF self-energy Σ^0_{σ}, then from Eq. (2.43) the single self-energy becomes

$$\Sigma^{\rm MF}(\omega) = \frac{U\langle n\rangle}{2} + \frac{(\frac{1}{2}U|\mu|)^2}{\omega^+ - \epsilon - \frac{U\langle n\rangle}{2} - S(\omega)} \tag{2.44}$$

From Eq. (2.44), it is straightforward to see that $\mathrm{Im}\Sigma(0) = 0$ is ensured only when $\mu = 0$, which will lead to RHF result, i.e. to the non-interacting limit shifted by a constant term. Also for $\mu = 0$, both of the two self-energies coincide with the single self-energy and we are left with no dynamics at all. This also motivates us to look beyond the MF.

Now we shall seek if there is any hope to recover an FL behavior when we consider the RPA approximation in the dynamic part of two self-energies. Not only the imaginary part of the self-energy becomes zero, but also in case of an FL, it must have the following at low frequency.

$$\mathrm{Im}\Sigma^{\rm tot}_{\sigma}(\omega) \overset{\omega\to 0}{\sim} \omega^2 \tag{2.45}$$

This situation indeed arises from the fact that (from Eq. (2.29))

$$\frac{1}{\pi}\mathrm{Im}^0\Pi^{+-}(\omega) \overset{\omega\to 0}{\sim} |\omega|\mathcal{D}_\uparrow(0)\mathcal{D}_\downarrow(0) \tag{2.46}$$

Thus once the imaginary part of the self-energy is guaranteed, the only task that remains is to ensure the linear ω-dependence in the real part.

We can also express the real part of the self-energy as a low-ω expansion:

$$\mathrm{Re}\Sigma_\sigma^{\mathrm{tot}}(\omega) \sim \mathrm{Re}\Sigma_\sigma^{\mathrm{tot}}(0) - \left[\frac{1}{Z_\sigma} - 1\right]\omega \tag{2.47}$$

such that

$$Z_\sigma = \left[1 - \left.\frac{\partial(\mathrm{Re}\Sigma_\sigma^{\mathrm{tot}})}{\partial\omega}\right|_{\omega=0}\right]^{-1} \tag{2.48}$$

Now it can be shown that (see Appendix I) the necessary condition for

$$\mathrm{Im}\Sigma^{\mathrm{tot}}(\omega) \overset{\omega\to 0}{\sim} \omega^2 \tag{2.49}$$

is

$$\mathrm{Re}\Sigma_\uparrow^{\mathrm{tot}}(\omega=0) = \mathrm{Re}\Sigma_\downarrow^{\mathrm{tot}}(\omega=0) \tag{2.50}$$

In the same way the Kramer-Kronig transform on the imaginary part of the single self-energy will give rise to low-ω behavior in its real part:

$$\mathrm{Re}\Sigma(\omega) \overset{\omega\to 0}{\sim} \left(\frac{1}{Z} - 1\right)\omega \tag{2.51}$$

This has the same quasiparticle residue definition like $\Sigma_\sigma^{\mathrm{tot}}$'s

$$Z = \left[1 - \frac{\partial(\mathrm{Re}\Sigma(\omega))}{\partial\omega}\bigg|_{\omega=0} \right]^{-1} \tag{2.52}$$

And it can be easily shown that

$$1/Z = \frac{1}{2}(1/Z_\uparrow + 1/Z_\downarrow) \tag{2.53}$$

Now using Eq. (2.39) we can write the SR condition explicitly in term of the dynamic part (i.e. the RPA) of the self-energy as

$$\sum_\sigma \sigma\Sigma_\sigma(\omega) = |\mu|U \tag{2.54}$$

2.4 Low energy scale

In the FL behavior, we expect a low-energy FL scale to emerge, which turns out to be proportional to the quasiparticle weight Z. This scale decreases as interaction strength is increased and its disappearance at U_{c2} signifies the metal-to-insulator transition. As Z decreases, the width of the quasiparticle resonance decreases as well (*Cf.* IPT results in Chapter 1) and also ω_m, the position of the resonance in $\mathrm{Im}\Pi^{+-}(\omega)$ decreases accordingly. We shall see in the next chapter that Z is proportional to ω_m. Here we shall present a strong-coupling analytical argument of this for half-filled case.

$$\mathrm{Re}\Sigma_{\uparrow}(\omega) = U^2 \int_{-\infty}^{\infty} \frac{d\omega'}{\pi}\, \mathrm{Im}\Pi^{+-}(\omega')[\theta(\omega')\mathrm{Re}\mathcal{G}_{\downarrow}^{-}(\omega'+\omega)+\theta(-\omega')\mathrm{Re}\mathcal{G}_{\downarrow}^{+}(\omega'+\omega)] \tag{2.55}$$

At strong coupling ($U \to \infty$), we get contribution almost entirely from the positive frequency part of $\mathrm{Im}\Pi^{+-}(\omega)$ [55], i.e.

$$\int_0^{\infty} d\omega\, \frac{1}{\pi}\mathrm{Im}\Pi^{+-}(\omega) \overset{U\to\infty}{=} 1\,. \tag{2.56}$$

Therefore we can write

$$\begin{aligned}\mathrm{Re}\Sigma_{\uparrow}(\omega \to 0) &= U^2 \int_0^{\infty} d\omega'\, \delta(\omega' - \omega_m)\, \mathrm{Re}\mathcal{G}_{\downarrow}^{-}(\omega') \\ &= U^2 \mathrm{Re}\mathcal{G}_{\downarrow}^{-}(\omega_m)\end{aligned} \tag{2.57}$$

Now

$$\mathrm{Re}\mathcal{G}_{\downarrow}^{-}(\omega) = \int_{-\infty}^{0} d\omega'\, \frac{\mathcal{D}_{\downarrow}(\omega')}{\omega - \omega'}\,. \tag{2.58}$$

Therefore

$$\mathrm{Re}\mathcal{G}_{\downarrow}^{-}(\omega_m) = -\mathcal{D}_{\downarrow}(\omega')\ln|\omega_m - \omega'|\big|_{-\infty}^{0} + \int_0^{\infty} d\omega'\, \frac{d\mathcal{D}_{\downarrow}(\omega')}{d\omega'} \ln|\omega_m - \omega'|\,. \tag{2.59}$$

Note that the second term on the RHS has the form $\int d\omega\, f(\omega) \ln\omega$ ($f(\omega) \equiv$

$d\mathcal{D}_\downarrow(\omega')/d\omega'$) which can be expanded as

$$\begin{aligned}\int d\omega\, f(\omega)\ln\omega &= f(\omega)\omega(\ln\omega-1) - \int d\omega'\, f'(\omega)\omega(\ln\omega-1)\\ &= f(\omega)\omega(\ln\omega-1) - \int d\omega'\, f'(\omega)\omega[\omega(\ln\omega-1)-\omega]+\ldots\end{aligned} \tag{2.60}$$

Now all the term of the above expansion vanishes at the integration limit ($\omega = 0$ as it is always a multiplication factor and $\omega = \infty$ where $f(\omega)$ and all its derivatives vanish).

Thus the second term in Eq. (2.59) does not contribute at all and hence

$$\text{Re}\mathcal{G}^-_\downarrow(\omega_m) = -\mathcal{D}_\downarrow(\omega')\ln|\omega_m-\omega'|\Big|^0_{-\infty} = -\mathcal{D}_\downarrow(0)\ln|\omega_m|\,. \tag{2.61}$$

Again following the same previous argument $\mathcal{D}_\downarrow(\omega')$ vanishes at $\omega' \to \infty$. So finally

$$\text{Re}\Sigma_\uparrow(\omega\to 0) = -U^2\mathcal{D}_\downarrow(0)\ln|\omega_m+\omega| \tag{2.62}$$

Now

$$\begin{aligned}\mathcal{D}_\downarrow(0) &= -\frac{1}{\pi}\frac{\text{Im}S(0)}{x^2+(\text{Im}S(0))^2}\\ &= \frac{1}{\pi}\frac{\pi D(0)}{\pi^2(U\mu)^2D^2(0)/4+1}\\ &\simeq \frac{4}{\pi^2U^2\mu^2D^2(0)}\end{aligned} \tag{2.63}$$

where we use $\text{Im}S(0) = -1/(\pi D(0))$ (Eq. (J.10) in Appendix J).

Taking derivative w.r.t ω of the LHS of Eq. (2.62) we find

$$1 - \frac{1}{Z} = \frac{\partial \mathrm{Re}\Sigma(\omega)}{\partial\omega}\Big|_{\omega=0} = -U^2\mathcal{D}_{\downarrow}(0)\frac{1}{\omega_m} \tag{2.64}$$

Since $Z \ll 1$ we can rewrite the above Eq. and find from Eq. (2.63)

$$Z_{\uparrow} = -\frac{\omega_m}{U^2\mathcal{D}_{\uparrow}(0))} = \omega_m\frac{\pi^2\mu^2 D(0)}{4} \tag{2.65}$$

For the hypercubic lattice (HCL), non-interacting DoS

$$D_0(\omega) = \frac{1}{\sqrt{\pi}t_*}e^{-\omega^2/t_*^2}$$

Using above and the condition for pinning at the non-interacting limit at the Fermi level: $D(0) = D_0(0)$, we get

$$D(0) = \frac{1}{\sqrt{\pi}t_*} \tag{2.66}$$

For the symmetric case: $Z_{\uparrow} = Z_{\downarrow}$ and strong coupling limit ($U \to \infty$) for μ, i.e. $|\mu| \to 1$.

Then from Eq. (2.65) and Eq. (2.66), we have

$$Z = \frac{2Z_{\uparrow}Z_{\downarrow}}{Z_{\uparrow} + Z_{\downarrow}} = Z_{\uparrow} = \omega_m\frac{\pi\sqrt{\pi}\mu^2}{4t_*} \simeq 1.39\,\omega_m/t_*\,. \tag{2.67}$$

Thus, generalizing the strong-coupling limit, we may expect that the quaiparticle weight Z is indeed proportional to the spin-flip cost ω_m (see the next Chapter for the numerical verification).

2.5 Insulating phase: singularity in the $\boldsymbol{\Pi(\omega)}$

We can anticipate that the metallic phase that the quasiparticle weight Z should vanish at a critical value $U = U_{c2}$ (*Cf.* IPT results in Chapter 1) leading to a Mott transition. Beyond this point symmetry restoration is not possible and we reach the upper boundary of the stability criterion Eq. (2.35), i.e.

$$U\mathrm{Re}\Pi^{+-}(0) = 1\,. \tag{2.68}$$

In this situation, $|\mu^0|$ becomes equal to $|\mu|$ though the host Green's function is not the UHF Green's function since the Feenberg self-energy gets modified through DMFT iterations.

Eq. (2.68) eventually turns the $\mathrm{Im}\Pi^{+-}(\omega)$ into a Dirac-delta function from its resonance-like form in the metallic phase. As shown in Appendix K, we can write

$$\mathrm{Im}\Pi(\omega) = \pi Q\,\delta(\omega) \tag{2.69}$$

with

$$Q = \left[U^2\left|\frac{d\mathrm{Re}^0\Pi(\omega)}{d\omega}\right|_0\right]^{-1} \tag{2.70}$$

It has been argued by Eastwood [99] that

$$Q = |\mu|^2 \tag{2.71}$$

and indeed we see that in our numerical result (though a rigorous analytical proof is not yet at hand).

This singularity at $\omega = 0$ is consistent with the fact that arbitrary large numbers of spin-flip is possible without any cost of energy, i.e. $\omega = 0$ for a paramagnetic insulator since there is no spatial fluctuation at $d \to \infty$ limit and each site has a Ising-like spin equally surrounded by similar $\uparrow$ and $\downarrow$ spins without causing any difference in energy by fluctuations [99]. This results in a pole in $\Sigma(\omega)$ at $\omega = 0$ which signifies the presence of atomic limit like feature in our theory.

2.6 Numerical implementation

Now we briefly state the necessary steps for implementing our formalism in numerical computation. Again here for the sake of simplicity, we shall consider the *p*-*h* symmetric case. Extra care that is required for the asymmetric case (specifically satisfying the Luttinger theorem) will be mentioned in the relevant context. Below we chart the steps require to get Fermi liquid metallic phase with the help of symmetry restoration condition. As mentioned in the earlier section, symmetry restoration is not possible for the insulating case. Hence we drop the step (viii) and we determine U only from the UHF approximation. Apart from this, rest of the steps are the same as for the metallic case. However, since a pole arises in $\Pi^{+-}(\omega)$, which cannot be handled numerically, we cut the pole in our numerical calculation and add it separately via the following analytical expression after evaluating Q.

$$\Sigma_\sigma(\omega) = QU^2 \mathrm{Re}\mathcal{G}_\sigma(\omega) \tag{2.72}$$

where we use Eq. (2.40). Now we describe the same as above by a simple

Steps for LMA implementation for the p-h symmetric case

(i) Choose an x, a guess U, $\epsilon_d = -U/2$, and a guess $S(\omega)$. $t_* = 1$ is chosen as a common practice.

(ii) Calculate host Green's functions $\mathcal{G}_\sigma(\omega)$ from Eq. (2.12). At the first step, $\mathcal{G}_\sigma(\omega)$ will be just the UHF Green's functions .

(iii) Find μ from Eq. (2.17). Then from the definition of x, i.e. Eq. (2.13), calculate U.

(iv) Now the guess U should be less than the UHF U $(= 1/\mathrm{Re}{}^0\Pi^{+-}(0))$ to obey the stability condition: Eq. (2.35). If $U \geq 1/\mathrm{Re}{}^0\Pi^{+-}(0)$ decrease it to a value that satisfies Eq. (2.35).

(v) Find ${}^0\Pi^{+-}(\omega)$ from the convolution Eq. (2.28) using the already calculated $\mathcal{G}_\sigma(\omega)$ in (ii). In practice, use Eq. (2.29) to calculate $\mathrm{Im}{}^0\Pi^{+-}(\omega)$ and then do Kramers-Kronig transform to find $\mathrm{Re}{}^0\Pi^{+-}(\omega)$.

(vi) Find $\Pi^{+-}(\omega)$ from the RPA sum: Eq. (2.27). In practice, use Eq. (2.32) to calculate $\mathrm{Im}\Pi^{+-}(\omega)$ and then Eq. (**??**) to find $\mathrm{Re}\Pi^{+-}(\omega)$.

(vii) Calculate $\Sigma(\omega)$ from Eq. (2.39) and the convolution: Eq. (2.40). Again take the imaginary part of Eq. (2.40) and use Kramers-Kronig transform to determine the real part separately.

(viii) Check the symmetry restoration condition: Eq. (2.54). If it is not satisfied, change U and repeat steps (vi) to (viii) till it is satisfied. Note that in practice, we choose $\mu = \mu^0$ in Eq. (2.54).

(ix) Evaluate $\gamma_\sigma(\omega)$ from Eq. (2.23). (a) Determine $\gamma(\omega)$ in term of the guessed $S(\omega)$ using Eq. (2.22) and (b) hence update $S(\omega)$ by Hilbert transform over $\gamma(\omega)$: Eq. (2.20). Repeat (a) and (b) till consistency is achieved.

(x) Put the new $S(\omega)$ back to step (ii) and update $\mathcal{G}_\sigma(\omega)$. Now naturally this $\mathcal{G}_\sigma(\omega)$ will not be the UHF Green's functions that we have started with. Follow all the steps from (ii) to (x) until consistency arrives.

(xi) Calculate $G(\omega)$ from Dyson's Eq.: Eq. (22) and other physical properties in terms of $G(\omega)$ and $\Sigma(\omega)$.

flowchart below (Fig. 2.4). The iterative loop to reach self-consistent $S(\omega)$ in step (ix) is not shown intentionally to keep the structure look simple.

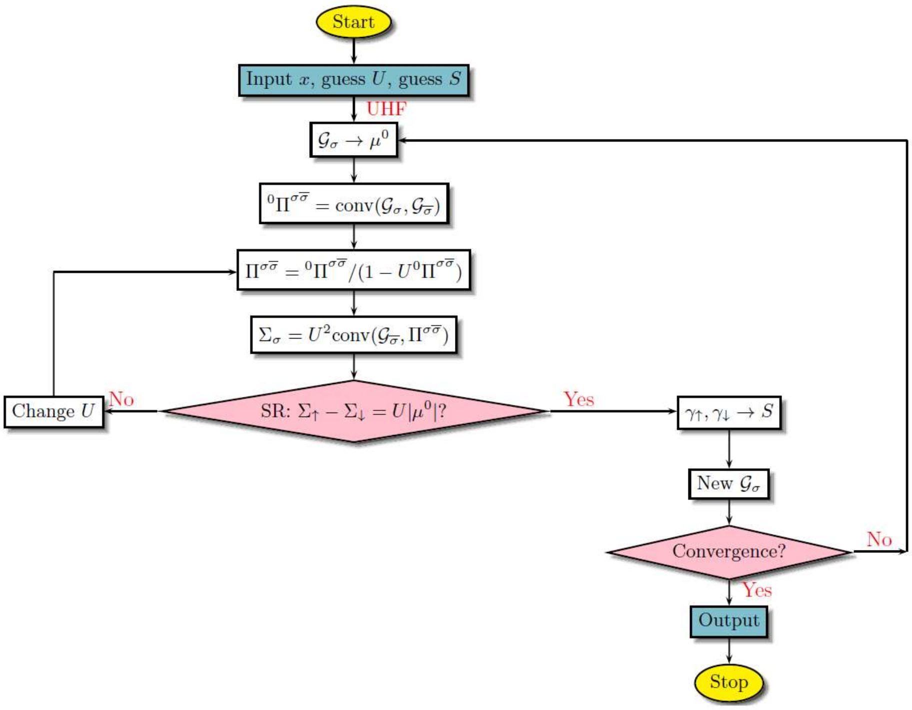

Fig. 2.4: Flowchart of basic LMA implementation

2.7 Summary

We describe and formulate a non-perturbative quantum many-body approach which may offer an alternative route to capture the Mott transition physics in the context of the Hubbard model. We started with a spin-symmetry broken mean-field solution, which is commonly known as the unrestricted Hartree-Fock (UHF) solution. Though UHF itself shows a metal-to-insulator transition depending on the interaction strength, it fails to assure a Fermi liquid state all the way in the metallic regime. The broken symmetry could be blamed for this failure and no way exists to restore the symmetry since the UHF approximation is a static approximation. Therefore we build spin-dependent dynamical self-energies, by considering higher order spin-flip diagrams (polarization bubbles with RPA sum) in our approximation and impose a symmetry restoration (SR) condition on them so that the final effective single self-energy shows Fermi liquid behavior. The SR condition also helps us to determine the correct value of interaction strength U since we always calculate the host Green's functions in term of a combination of U and local moment μ. We also notice that a stability criterion (Eq. (2.35)) is necessary to be while we restore symmetry by changing U. In addition to this, we find a linear relation between the Fermi liquid scale Z and the resonant frequency ω_m from the strong-coupling analysis, reflecting the fact that it is the spin-flip dynamics which gives rise to the low-energy scaling behavior.

In the insulating case, we do not require to restore the symmetry and we work with the U that we evaluate after calculating μ ($U = 2x/\mu$) from the host Green's functions. As a natural consequence a singularity arises in the RPA summed polarization bubble, $\Pi^{+-}(\omega)$. This reflects the physical fact that there is no spin-flip cost $\omega = 0$ for a paramagnetic insulator. We cut this pole in our numerical implementation and we add the analytical result separately in the convolution integration for the self-energy.

In the upcoming chapters, we discuss the results based on our formalism and as a first test, we look whether can obtain a Mott insulator by increasing interaction starting from a Fermi liquid (our symmetry restoration condition should ensure a Fermi liquid at low interaction strength). We also verify our analytical prediction such as the linear relation between ω_m and Z. We first implement for the zero temperature p-h symmetric case. Later we extend it to the asymmetric case and also to finite temperature. We compare our results with experiments wherever possible.

Chapter 3

LMA: Universality and scaling in the zero temperature dynamics of the p-h symmetric HM

3.1 Introduction

In chapter1, we have investigated the spectral and transport properties of the particle-hole symmetric Hubbard model using the iterated perturbation theory (IPT) as the impurity solver within DMFT. In this and the next three chapters, we treat the same model (without restriction to the particle-hole symmetric case), using the local moment approach (LMA) as the impurity solver. The formalism of the LMA has been outlined in the previous chapter. This chapter will utilize that formalism and deal with roughly the same issues as in the Chapter 1, which were the study of spectral dynamics, universality and scaling (especially in the proximity of the Mott transition), the $T = 0$ phase diagram, and the $T = 0$ optical conductivity. Since the LMA captures the strong coupling asymptotics of the single impurity Anderson model exactly, the use of LMA within DMFT for the Hubbard model can be expected to yield very good results, with the added advantage of obtaining real frequency quantities, at all temperatures and interaction strengths with very little computational expense (as compared to solvers such as quantum Monte Carlo (QMC) [51, 52]).

The chapter is structured as follows. In this chapter we mainly discuss our theoretical results on spectral and transport quantities for the zero temperature p-h symmetric Hubbard model. We first show Fermi liquid behavior in the metallic spectral densities along with universal scaling behavior in strong coupling (close to the Mott transition, $U \to U_{c2}$). Adiabatic continuity to the non-interacting limit is indeed found, but in contrast to the case of IPT (Chapter 1), the frequency interval over which the renormalized non-interacting limit (RNIL) overlaps the interacting spectra is extremely small. The strong frequency dependence of the imaginary part of the self energy close to the Fermi level readily explains this. We see that, apart from the quasiparticle residue, which is the low-energy scale for a Fermi liquid, the resonant frequency (spin-flip energy cost) for the $\mathrm{Im}\Pi^{+-}(\omega)$ discussed in the previous chapter, emerges as an alternative energy scale. As expected, we find an insulating phase at higher interaction strength U_{c2} reflecting a Mott transition. The value of the U_{c2} is extracted through an extrapolation of the low energy scale since very close to the transition, numerical difficulties prohibit us from achieving self-consistency. Similarly, while decreasing U from the Mott insulating side, we find that the metallic phase emerges at an interaction strength $U_{c1} < U_{c2}$. Thus there does exist a coexistence region within the LMA results, however, as compared to the IPT result, this region is much smaller. We discuss optical conductivity results for both metallic and insulating phases and show in the former, a universality in the absorption peak position after a scaling in the frequency axis.

3.2 Spectral density

3.2.1 Fermi liquid scaling

We first look at the low-energy behavior of the the spectral density $D(\omega) = -\frac{1}{\pi}\text{Im}G(\omega)$ for small interaction U and hence for small x . The left panel of Fig. 3.1 shows the presence of finite DoS at the Fermi level and hence the phase is metallic. The finite DoS appears via the quasiparticle or the Abrikosov-Suhl resonance which is similar to what we have already observed for the IPT approximation discussed in Chapter 1. As expected, all the resonance peaks are pinned at the same value at the Fermi level $\omega = 0$. The resonance shrinks gradually as we increase x or U. Thus as we have done in case of IPT in Chapter 1, we can associate a low-energy scale, $\omega_L = Zt_*$, determined by the quasiparticle residue Z, proportional to the width of the resonance. From the right panel of Fig. 3.1 we can see that all spectral densities become pinned at the Fermi level $(\omega = 0)$. The spectra seem to deviate

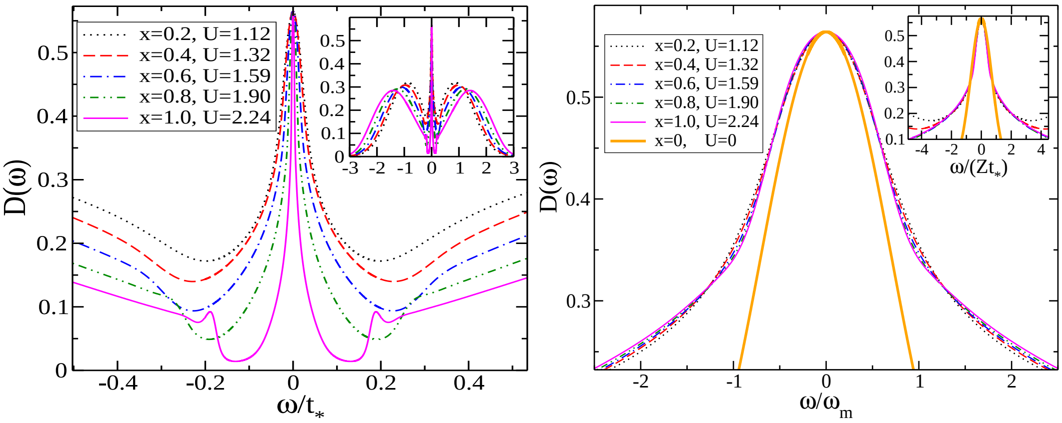

Fig. 3.1: Spectral densities and scaling collapse. Left panel shows the Abrikosov-Suhl resonance that appears at the Fermi level ($\omega = 0$). Inset shows the full spectra for the same. Right panel is the scaling collapse of spectral densities when the frequency axis is scaled by the low-energy scale ω_m. Inset is the same when scaled by quasiparticle weight Z. Note that, in both scaling, the collapse deviates from the non-interacting curve ($U = 0$) almost immediately away from the Fermi level.

from the non-interacting limit almost immediately away from the Fermi level. Thus, even though adiabatic continuity at the Fermi level is maintained, the renormalized non-interacting limit (RNIL) description is seen to be invalid. This can be explained if we look at the self-energy behavior at low-frequency. The RNIL assumes that contribution from $\mathrm{Im}\Sigma(\omega)$ is negligible compared to the contribution from $\mathrm{Re}\Sigma(\omega)$ at low ω since the former vanishes as $\omega \to 0$ with one power of ω ($\propto \omega^2$) higher than the latter ($\propto \omega$). This approximation does hold in our previous results within IPT over a large interval around the Fermi level. However, the contributions from both real and imaginary part of $\Sigma(\omega)$ become comparable when the coefficient of imaginary part becomes large enough. Fig. 3.2 shows that the slope change in $\mathrm{Im}\Sigma(\omega)$ away from $\omega = 0$ is faster in LMA (shown in the left panel) compared to that in IPT

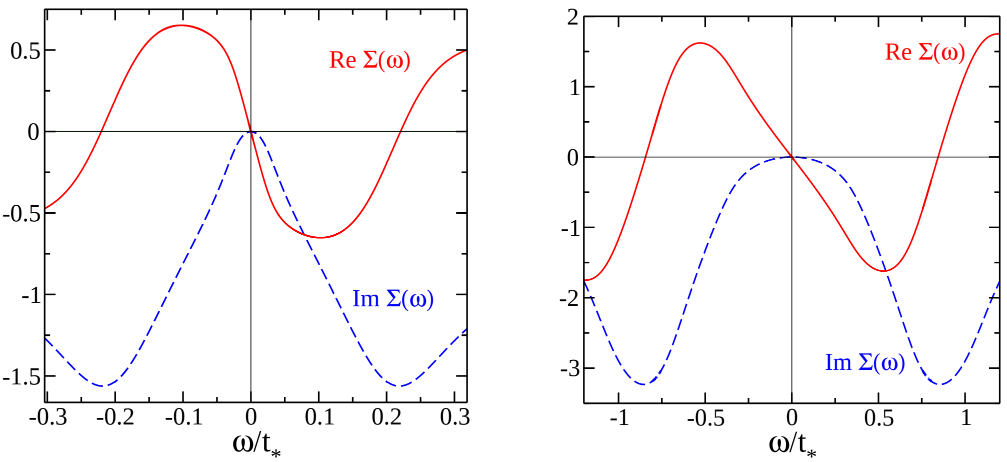

Fig. 3.2: Reason for non-collapse with the non-interacting DoS. Dashed lines (blue in color) and full lines (red in color) are the imaginary and real part of the self-energy respectively. The static part $\Sigma(0) = U/2$ has been subtracted from the real part. $\text{Im}\Sigma(\omega)$ grows far more rapidly from $\omega = 0$ in LMA (left panel) than that in IPT (right panel) suggesting that not only in the strong coupling regime, but also in the intermediate correlation regime, incoherent scattering effects become important at energies even slightly away from the Fermi level . The interaction strength for the LMA: $U = 1.12t_*$ ($x = 0.2t_*$) and for the IPT: $U = 3.0t_*$.

(shown in the right panel). Apart from the non-realizability of the renormalized non-interacting limit (RNIL), the scaling collapse is seen to be quite good implying that the imaginary and real parts of the self energy assume universal forms for strong coupling (see Fig. 3.3). We see the same scaling if we either scale by Z (found by differentiating the real part of the self-energy) or ω_m/t_*. The inset in Fig. 3.3 clearly shows the linearly proportional relation between the two scales. However, the slope (=1.6) varies $\sim$ 15% above our estimation (=1.39) (see Eq. (2.67)), which, we believe, is an underestimation due to the strong coupling $U \to \infty$ assumption.

3.2.2 Strong correlation universality

As can be anticipated from Fig. 3.1, the spectra seem to assume a universal form $D(\omega) = D(\omega/\omega_L)$ in strong coupling regime. And indeed close to the Mott transition, we find scaling collapse in the spectral densities for decades of ω_L (see Fig. 3.4: U ranging from $2.07t_*$ to $2.60t_*$), when the frequency axis is scaled by the same scale, i.e. ω_L . Moreover, this universal region extends to higher and higher frequencies as we increase U/t_* suggesting that in the limit $U \rightarrow U_{c2}^-$, the universal scaling region extends to $|\omega| \rightarrow \infty$. The universal scaling form is seen to be very different from the renormalized non-interacting limit suggesting very non-trivial tails of the spectral function for large ω/ω_L. These tails should manifest themselves in transport and other finite temperature/frequency properties that would be an interesting feature to look for in experiments.

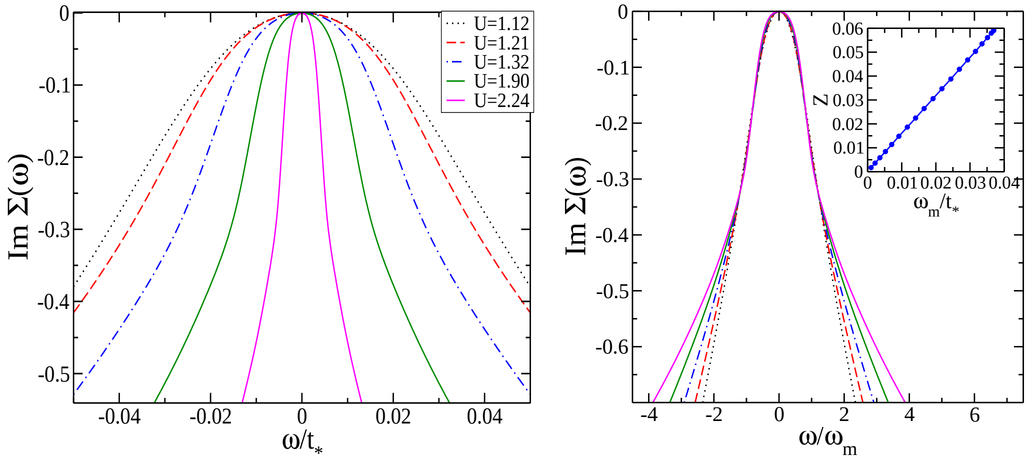

(a) (b)

Fig. 3.3: Good scaling collapse in the imaginary part of $\Sigma(\omega)$. (a) Before scaling. (b) After scaling ω/t_*-axis by ω_m/t_*. Inset shows a linear relation between Z and ω_m/t_*, as predicted in Eq. (2.67) in Chapter 2.

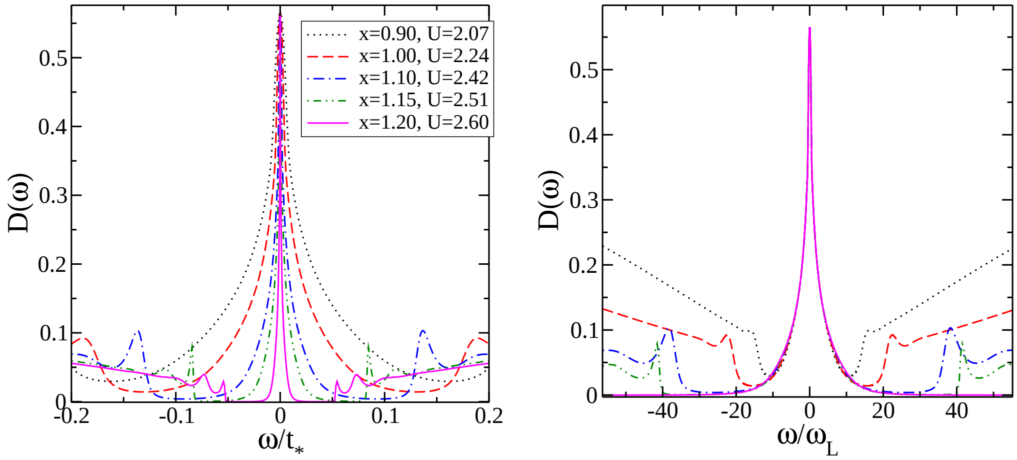

(a) (b)

Fig. 3.4: Scaling collapse at strong-coupling. (a) Before scaling. (b) After scaling ω/t_*-axis by ω_m/t_*. The universal scaling form is seen to be very different from the renormalized non-interacting limit suggesting very non-trivial tails of the spectral function. The scaling collapse is seen to be very good even upto $\omega \gtrsim 50\omega_L$ and does seem to extend to $|\omega| \to \infty$ in the limit $U \to U_{c2}$.

3.2.3 Mott transition

It is evident from Fig. 3.5 that the width of the resonance shrinks gradually as

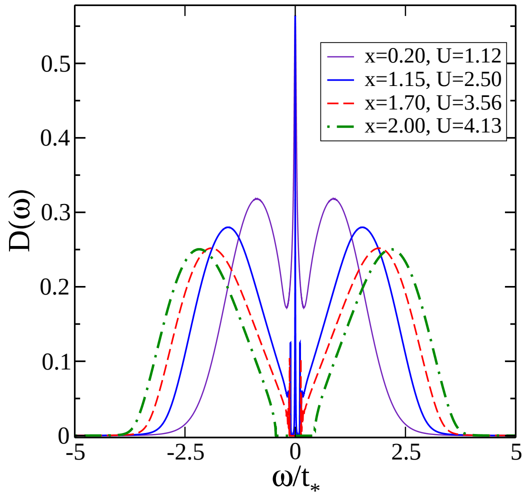

Fig. 3.5: Metal-to-insulator transition (MIT). Quasiparticle resonance narrows down with increasing U/t_*. It finally disappears and a clean gap forms at the Fermi level. Gap increases as U/t_* is increased further.

U/t_* is increased and similar to the IPT result, metal-to-insulator transition (MIT) occurs when $U \geq U_{c2}$. For the hypercubic lattice (HCL), we find approximately $x_{c2} = 1.3t_*$ and therefore $U_{c2} \simeq 2.8t_*$ (see Fig. 3.5). The estimation of U_{c2} is carried out through an extrapolation of the zero crossing of the low energy scale with increasing U, and hence as such may be a little vague. At $x = 1.3t_*\,(U \sim 2.8t_*)$, the ω_L scale does seem to vanish (see Fig. 3.7).

3.2.4 Destruction of Mott insulator and presence of hysteresis

In IPT, we have seen, in the zero temperature evolution of spectral densities with interaction strength, that there exist two transition points U_{c1} and U_{c2}

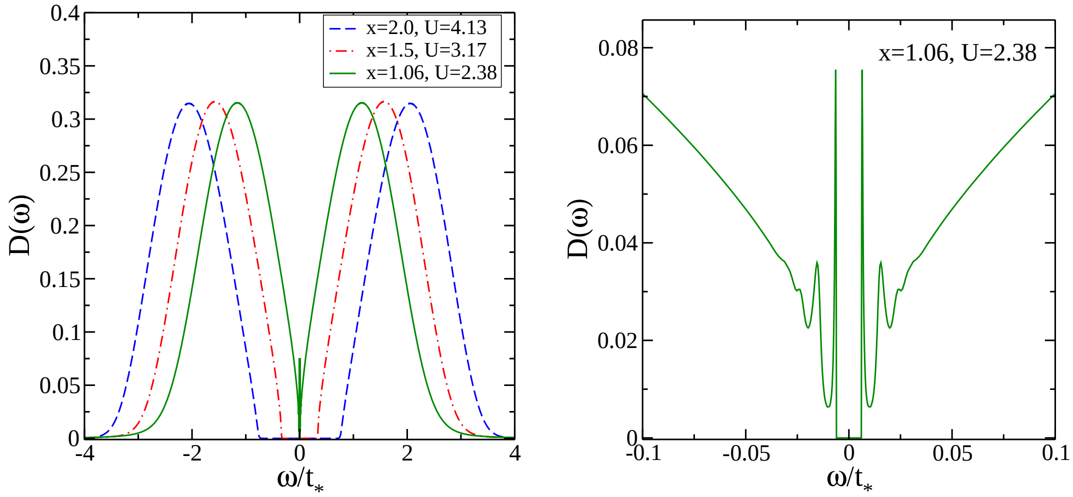

(a) (b)

Fig. 3.6: (a) Gap in the spectral density decreases as U/t_* is decreased from the insulating regime. The gap apparently closes at $U = 3.38t_*$ ($x = 1.6t_*$). (b) At $U = 3.38t_*$ the gap is still about to close, which means that the transition point U_{c1} is a little below $U = 3.38t_*$.

.

depending on whether we are changing U from the metallic or insulating side. Therefore it is natural to ask that if we start from an insulating regime and keep on decreasing x (hence U), do we get a insulator to metal transition at the same point that we have mentioned above? Fig. 3.6(a) shows that we find that the gap decreases as we decrease x from $2.0t_*$ ($U = 4.13t_*$) and it appears that the gap closes at $x = 1.06t_*$ ($U = 2.38t_*$). However, the gap

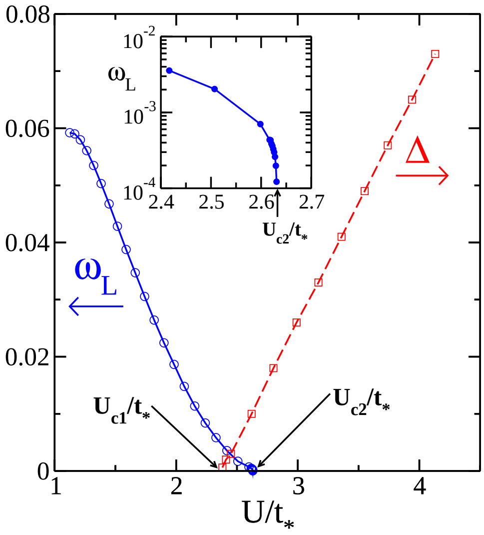

Fig. 3.7: Decay of the low-energy scale $\omega_L = Zt_*$ with increasing U/t_* (solid line). Inset shows the same in log-scale. ω_L seems to vanish at $U_{c2} = 2.64t_*$. Note that we have been able to reach a value of the low energy scale $\sim 10^{-4}t_*$, which requires very high precision calculations. The dashed line shows that the spectral gap Δ of the Mott insulator decreases linearly with decreasing U/t_* and closes at $U_{c1} = 2.36t_*$. The coexistence region is quite small compared to that in IPT. .

is truly not zero at $x = 1.06t_*$ as Fig. 3.6 shows in a zoomed view. For this reason we plot the gap (Δ) as a function of U/t_* in Fig. 3.7 (dashed line). We find that Δ linearly decreases with U/t_* and it appears that $U_{c1} \simeq 2.36t_*$. Thus similar to the IPT result, LMA also shows presence of a coexistence region (possibility of having both metallic and insulating solutions) and hence hysteresis driven by interaction. The U_{c1} and U_{c2} for the Bethe lattice, as reported by Eastwood [99] in his thesis, are $3.41t_*$ and $3.46t_*$ respectively (though his implementation of LMA seems to be different from ours). Thus both his and our finding of coexistence region, as estimated by $U_{c2} - U_{c1}$ ($0.28t_*$ for the HCL) is very less compared to that in IPT ($\sim 1.0t_*$).

3.3 Optical conductivity

3.3.1 Metallic regime

Fig. 3.8 shows the optical conductivity results at zero temperature. In general the optical conductivity seems to have two peaks. The lower peak is centred around the low energy scale ω_L, while the upper peak seems to be due to excitations from the lower to the upper Hubbard band, and hence should be non-universal. The left panel shows that apart from the Drude peak at

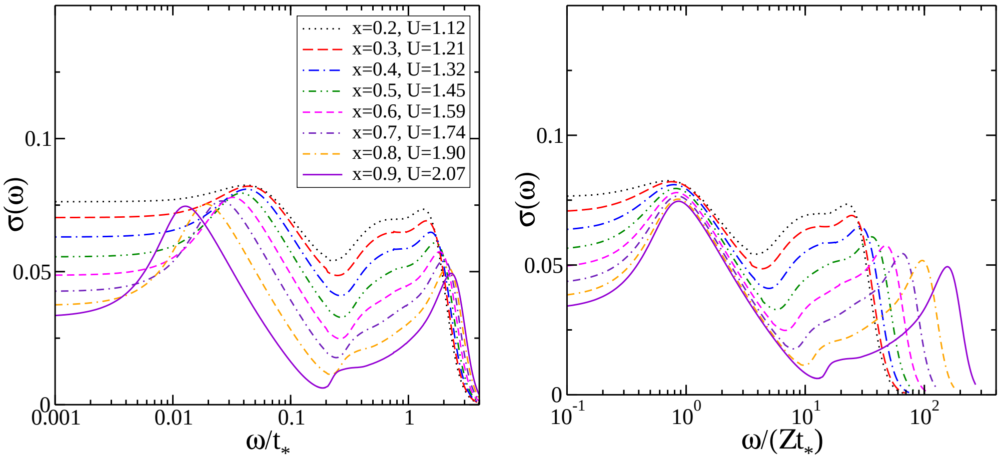

(a) (b)

Fig. 3.8: Optical conductivity in the metallic regime for different U/t_*. (a) Absorption peak starts forming as U/t_* is increased. (b) Peaks arise almost at the same position after scaling the frequency axis by Zt_*.

$\omega = 0$ an absorption peak, appears roughly at $\omega \sim Zt_*$ and becomes more prominent as we increase U/t_*. We can clearly see that the peak position, in unit of t_* gets a red-shift with increasing U/t_*. However, if we scale the frequency by Zt_* or ω_m, the peak position collapses to $\omega \sim \omega_L$. This signifies the presence of a universal low-energy scale $\omega_L = Zt_*$ in the optical conductivity. And as the right panel shows, the high frequency peak shifts to higher frequencies progressively with increasing U if seen as a function of the scaled frequency ω/ω_L. This implies that the second peak is non-universal and indeed from the left panel, it is easy to see that the peak position is roughly the U/t_* value itself signifying that this absorption peak is due to excitations between the LHB and the UHB.

3.3.2 MIT and Insulating regime

In the Mott insulator regime $U > U_{c2}$, the spectral density has a gap at the Fermi level, which manifests in an optical gap in the optical conductivity. The height of low frequency absorption peak, just mentioned above, does not change significantly (though small decrease noticeable) with increasing U/t_*, but a dip next to it increases gradually. The Drudé peak and the low frequency absorption peak finally vanishes with commencement of an optical gap (see Fig. 3.9 (a)) . As expected, the gap increases with further increase in U/t_* leading to a blue-shift of the higher frequency optical absorption peak. During this blue-shift, the peak height diminishes as well (see Fig. 3.9).

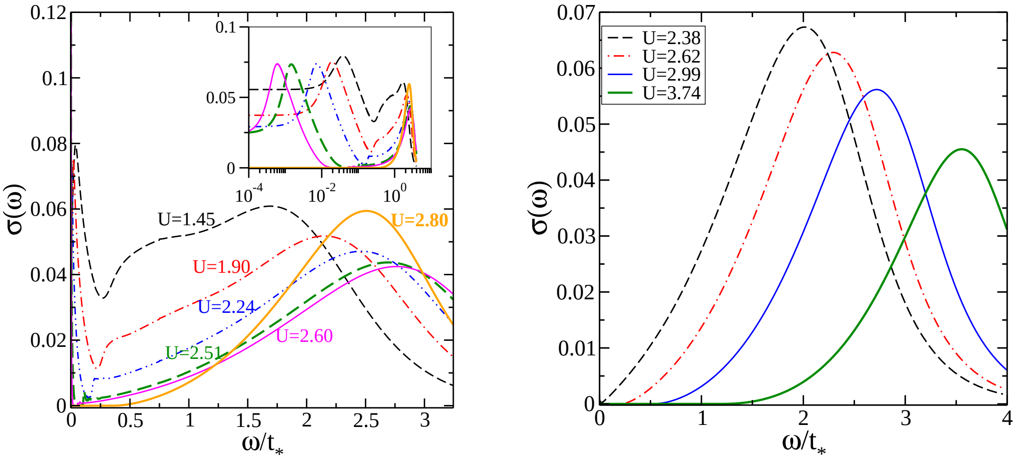

(a)

(b)

Fig. 3.9: (a) Optical conductivity for various U/t_* is shown. As $U/t_* =$ is increased, the low frequency absorption peak diminishes and close to the metal-insulator transition point ($U =$) an optical gap is about to form. A clean optical gap is observed for $U \gtrsim U_{c2}$). Inset shows the same in logarithmic scale. (b) Blue-shift of peak position and decrease of peak height as U/t_* is increased. Increase of the optical gap Δ_g with U/t_* is apparent (values mentioned inside the legend box).

3.4 Summary

Here we see that LMA does capture the Fermi liquid metal to Mott insulator transition. The adiabatic continuity to the non-interacting limit holds only very close to the Fermi level since the imaginary part of the self-energy significantly competes with its real part at very low frequency. As we expected, the position of the $\mathrm{Im}\Pi^{+-}(\omega)$ resonance, ω_m becomes proportional to the quasiparticle weight Z and hence either of these may be used to demonstrate scaling. However, the proportionality constant 15% more than our prediction (Eq. (2.67)) since we assume the strong coupling limit ($U \to \infty$) in our derivation. The strong coupling metallic spectra assume a universal scaling form as $U \rightarrow U_{c2}^{-}$ with the scaling region extending to $\omega \rightarrow \infty$.The optical conductivity results show that absorption peaks become more significant as we increase U/t_{*} and their positions collapse to a universal number $\omega \sim \omega_{L}$ close to the Mott transition. The signature of MIT is also found in the optical conductivity as U/t_{*} is increased beyond U_{c2} forming a clean optical gap. The gap increases as U/t_{*} is increased further and the absorption peak shifts towards the lower wavelength.

Chapter 4

LMA: Interplay between asymmetry and correlation in the dynamics of the p-h asymmetric HM

4.1 Introduction

The metal-to-insulator transition (MIT), as described in the previous chapter, happens due to the dominance of strong electronic interaction over the electron's hopping strength, i.e. $U/t_* \gtrsim 1$ according to our formalism. The hopping strength t_* is the matrix element of the one-electron operators, namely the kinetic energy and the periodic potential in the localized Wannier orbital basis. It is a measure of the bandwidth in the energy dispersion picture. Since the presence of Coulomb repulsion effectively tunes the bandwidth to Zt_*, such an MIT is referred to as the bandwidth controlled MIT (BC-MIT). BC-MIT occurs only at half-filling which is the p-h symmetric limit of the one-band Hubbard model.

The other way to achieve an MIT is by changing the filling. Since away from half-filling, the system is generally metallic, an MIT must occur as the filling is tuned to $n = 1$ (p-h symmetric) from $n \neq 1$. This transition is called filling-controlled MIT (FC-MIT). FC-MITs bear a special interest, specially in the context of high-T_c superconductors [20, 102] as these are obtained by doping a Mott insulator. In this chapter, we discuss the zero temperature physics associated with an FC-MIT. We make comparisons with IPT results at appropriate places.

4.2 Formalism

The formalism we use to describe the FC-MIT is a modification of the LMA+DMFT employed to understand BC-MIT in Chapter 3. The main modifications have been partly introduced in Ref. 69. Since the symmetry restoration condition (Eq. (2.54)) is generic, we use it in the p-h asymmetric case as well. In contrast to the symmetric case, we do not get a simple relation between the chemical potential and the interaction strength, namely $\epsilon_d \neq -U/2$ anymore. Also there is a shift $\delta\mu$ from the chemical potential μ, that we usually keep zero in the symmetric case. Therefore Eq. (2.12) is modified as

$$\mathcal{G}_\sigma(\omega) = \frac{1}{\omega^+ - \tilde{\epsilon} + \sigma x - S(\omega)} \tag{4.1}$$

where

$$\tilde{\epsilon} \equiv \epsilon - \delta\mu = \epsilon_d + Un/2 - \delta\mu \tag{4.2}$$

which is zero only in the half-filled case ($\epsilon = 0$, $\delta\mu = 0$).

Now there are two important algorithmic remarks that we make here:

(i) We keep x fixed and by SR condition (Eq. (2.54)) we determine the U. This step is common to both the half-filled and the away from half-filled case.

(ii) Once we find U, we calculate the $\Sigma(\omega)$ and $G(\omega)$ for a fixed $\tilde{\epsilon} = \epsilon_d + Un/2 - \delta\mu$, then we find the ϵ_d by self-consistently satisfying Luttinger's sum-rule discussed in Chapter 0 (Eq. (11)). For a comparison, we show IPT results in necessary places. For the IPT in *p*-*h* asymmetric case, we use the ansatz proposed by Kajueter and Kotliar [103, 104].

A parameter $\eta = 1 + 2\epsilon_d/U$ is defined as a measurement of *p*-*h* asymmetry that we often use in our calculations. Note that for the symmetric case, $\epsilon_d = -U/2$ and hence $\eta = 0$.

4.3 Spectral density

4.3.1 Empty orbital, mixed valence, and doubly occupied orbital states

Before we embark on the results, we first make a few qualitative remarks. When the electron density is not equal to one per site, i.e. away from the half-filling, there are always empty sites available for electrons to hop without encountering the Coulomb repulsion U. Therefore we can get Mott insulators only when the filling reaches the half-filled ($n = 1$) value. However, there can be special situations, namely $n = 2$ where electron's hopping is forbidden since orbitals at all sites are fully (doubly) occupied. This leads to an insulator, which is in fact a band insulator. Similarly for $n \rightarrow 0$ case, there will be only a few electrons will be left for conduction, or from the hole point of view, the sites will be fully occupied again and again a band insulator. Thus at zero temperature we can divide into five distinct regimes, viz. (i) empty orbital ($n \rightarrow 0$), (ii) mixed valence-I ($0 < n < 1$), (iii) symmetric metal or Mott insulator ($n = 1$), (iv) mixed valence-II ($1 < n < 2$), and (v) doubly occupied orbital ($n \rightarrow 2$). The regimes (iv) and (v) are p-h symmetric counterparts of (ii) and (i) respectively.

Fig. 4.1 and Fig. 4.2 show the evolution of spectral density towards the two extremes (regime (i) and regime (v)) for the hypercubic lattice, starting from a half-filled Fermi liquid metal ($n = 1$). In the first case, the lower Hubbard band starts moving towards the Fermi level ($n = 0.75$) with decreasing its height compared to the upper Hubbard band, then it coalesces with the quasiparticle resonance ($n = 0.42$) where resonance itself shifts away from the Fermi level. Gradually the lower Hubbard band and the qausiparticle features do not remain significant any more ($n = 0.14$) and the density just becomes a non-interacting one, situated above the Fermi level, thus being a band insulator with the band edge at the Fermi level. Similarly in the second case, the upper Hubbard band moves towards the Fermi level and finally the lower Hubbard band occupies the whole spectral region and the system becomes a empty orbital band insulator (regime (i)). Thus Fig. 4.1

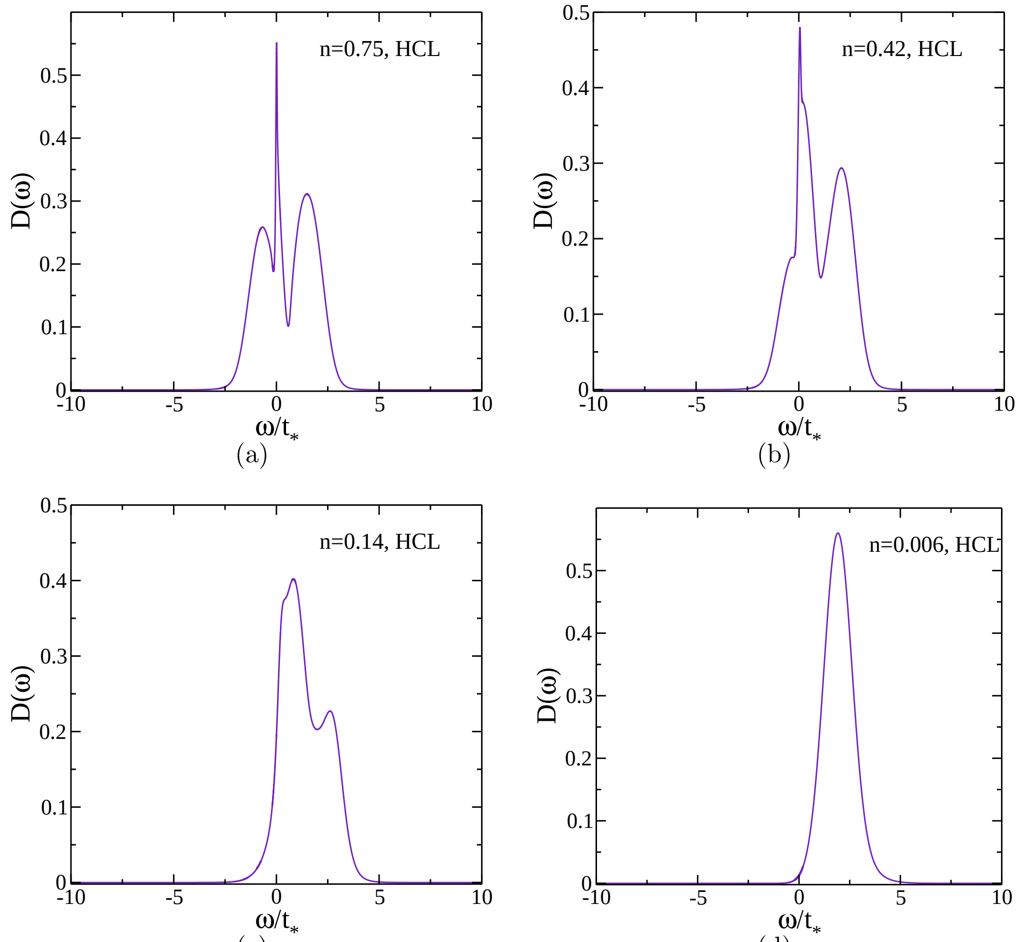

(a) (b)

(c) (d)

Fig. 4.1: Spectral densities for $x = 0.5t_*$ ($U \simeq 1.5t_*$) from $n < 1$ to $n \simeq 0$, for the hypercubic lattice (HCL). Parent (half-filled, i.e $n = 1$) phase is metallic. (a) At $n = 0.75$, the lower Hubbard band moves closer to the Fermi level with decreasing height compared to the upper one. (b) At $n = 0.42$, the lower Hubbard band and the resonance coalesce. (c) At $n = 0.14$, there are no distinct signatures of lower Hubbard band and the resonance. (d) At $n = 0.006$, almost the empty orbital regime is reached signifying a band insulator $n \to 0$.

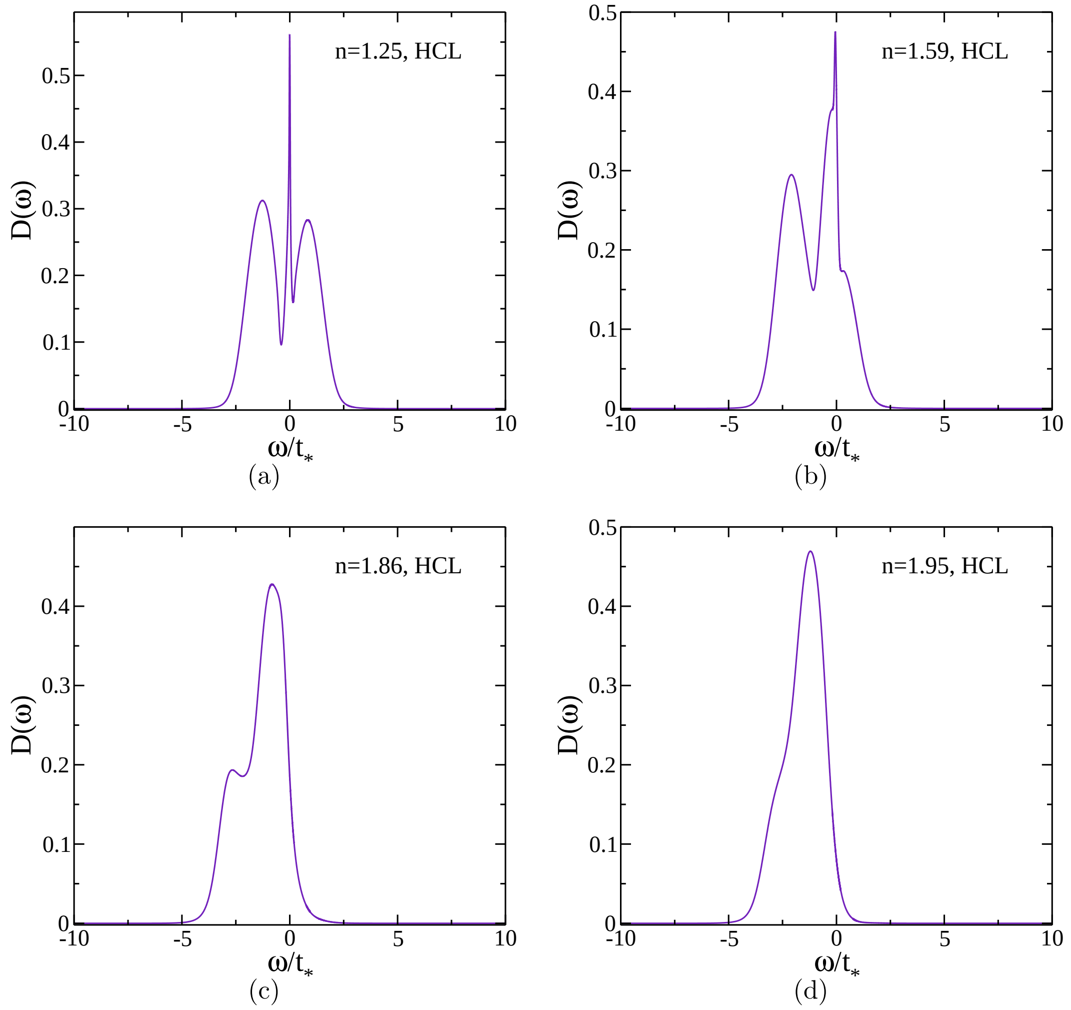

(a) (b)

(c) (d)

Fig. 4.2: Spectral densities for $x = 0.5t_*$ ($U \simeq 1.5t_*$) from $n > 1$ to $n \simeq 2$, for the hypercubic lattice (HCL). Parent (half-filled, i.e $n = 1$) phase is metallic. (a) As expected, at $n = 1.25$ the upper Hubbard band loses height and arrives closer to the Fermi level (*Cf.* Fig. 4.1 (a)). (b) At $n = 1.59$, the upper Hubbard band coalesce with the quasiparticle resonance(*Cf.* Fig. 4.1(b)). (c) No more Upper Hubbard band at $n = 1.86$ (*Cf.* Fig. 4.1 (c)). (d) At $n = 1.95$, the doubly occupied band-insulator approached (*Cf.* Fig. 4.1 (d)). Thus the spectral densities for $1 \leq n \leq 2$ show a hole counterpart of that for $0 \leq n \leq 1$.

and Fig. 4.2 reflect the the fact that for a particle with $1 \leq n \leq 2$ has its hole counter-part in $0 \leq n \leq 1$. For a parallel comparison, in Fig. 4.3, we

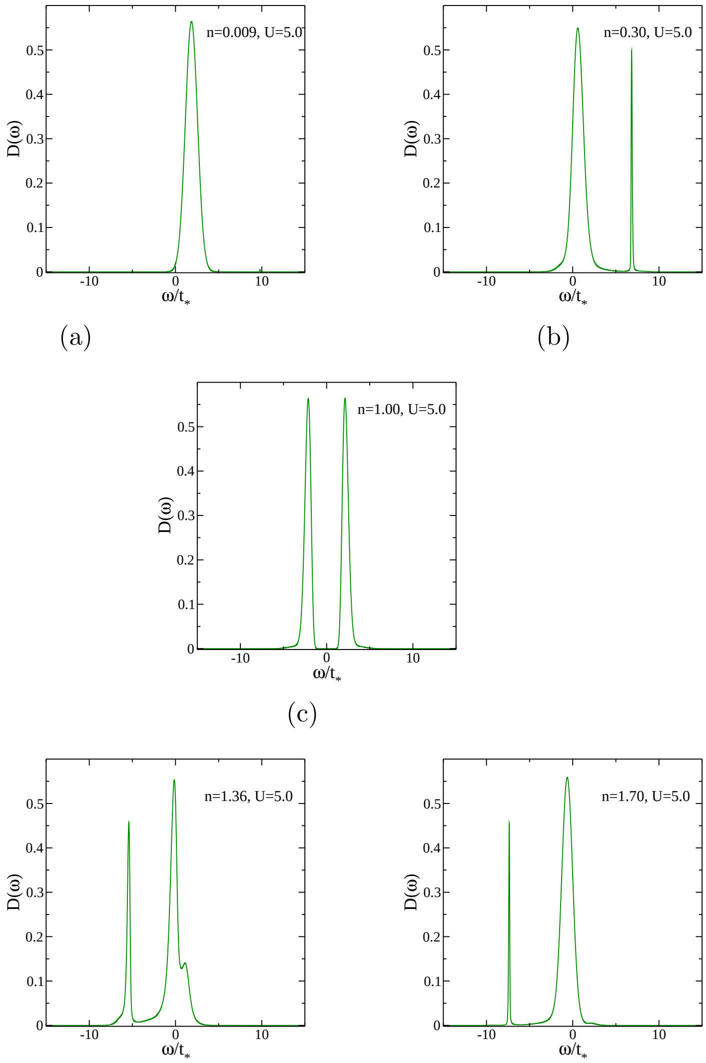

(a) (b)

(c)

(d) (e)

Fig. 4.3: Spectral densities in the asymmetric IPT. (a) $n = 0.009$: empty orbital band insulator. (b) $n = 0.30$: mixed valence-I. (c) $n = 1$ Mott insulator. (d) $n = 1.36$: mixed valence-II. (d) $n = 1.7$: close to doubly occupied band insulator (small finite density at the Fermi level and the presence of lower Hubbard band since $n = 2.0$ is not reached due to lack of numerical convergence.)

show that similar evolution of the spectral density with doping is observed in IPT. The half-filling c spectral density is an insulator since the interaction is high ($U = 5t_*$).

A schematic phase diagram on the filling-interaction plane at zero temperature should be as shown in Fig. 4.4.

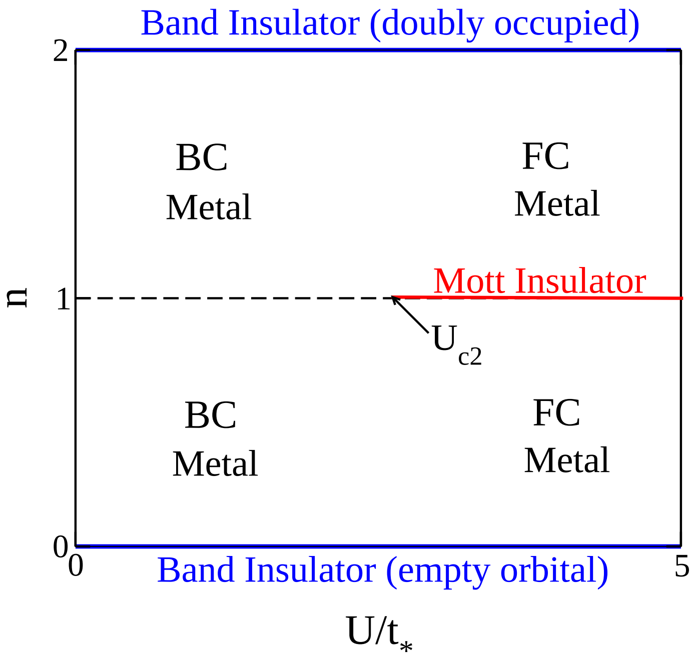

Fig. 4.4: Phase diagram on the filling-interaction (n-U) plane from the analogous result found in IPT. The region is bounded along the filling axis by empty orbital and doubly occupied band insulator lines. The metal emerging by doping a Mott insulator side is known as the filling controlled (FC) metal ($U > U_{c2}$) and remaining region is the band-width controlled (BC) metal since interaction is low. In case of LMA, $U_{c2} = U_c$, as discussed in Chapter 3.

4.3.2 Charge susceptibility

Another way to infer a Mott transition is to look at the charge compressibility or the charge susceptibility: $\kappa = -\partial n/\partial \epsilon_d$. Mott insulator has zero compressibility ($\kappa = 0$), which is a unique property that distinguishes a Mott insulator from an Anderson insulator [105]. Based on this distinguishing property, some authors often draws the liquid-gas analogy where the Mott insulator is termed as an incompressible *Mott liquid* and the associated metallic phase is called as a compressible *Mott gas* [106]. We first examine the IPT results for charge compressibility. Fig. 4.5 (c) and (d) show the charge susceptibility for the metallic ($U = 3.0t_*$) and insulating ($U = 5.0t_*$) phases respectively as calculated through IPT. Evidently $\kappa = 0$ in the latter case. Now we compare our LMA results for interaction strengths smaller ($U \sim 1.45t_*$) and

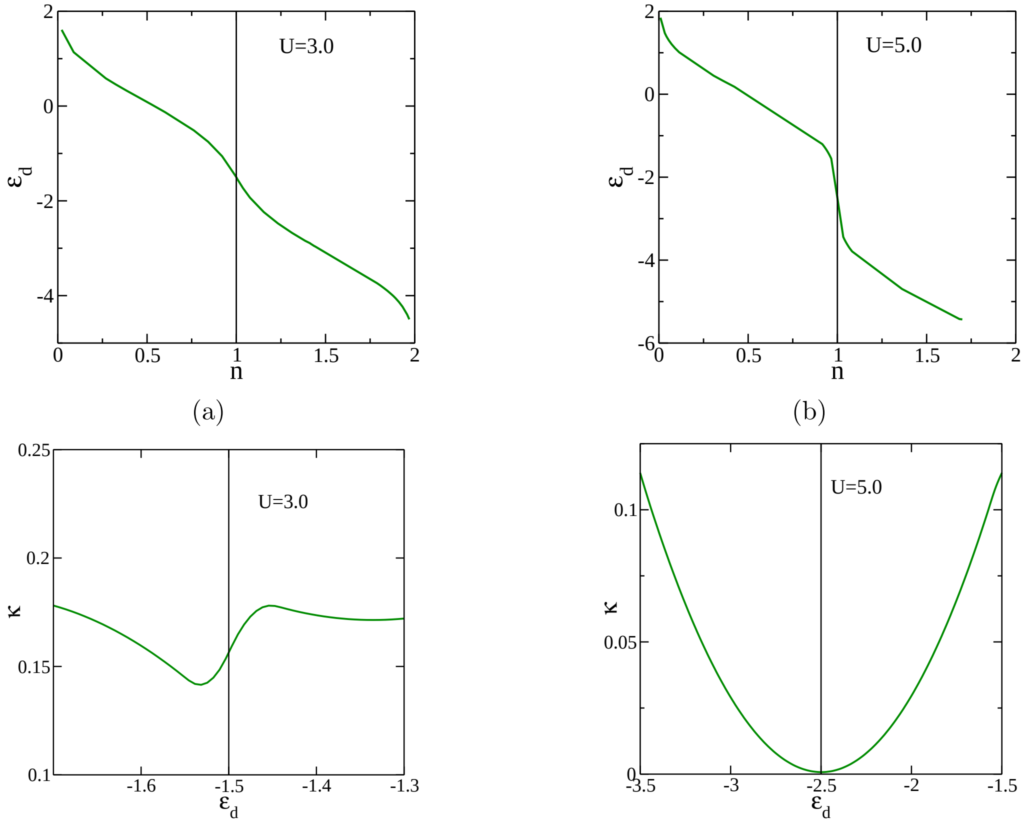

(a) (b)

(c) (d)

Fig. 4.5: (a) and (b) The orbital energy, ϵ_d as functions of filling n for $U = 3.0t_*$ (metal) and $U = 5.0t_*$ (insulator) respectively in IPT. (c) and (d) Charge susceptibility ($\kappa = -\partial n/\partial\epsilon_d$) calculated from numerical differentiation after using cubic spine interpolation. The vertical lines are guides to mark the value at half-filling.

close to the Mott transition ($U \sim 2.9t_*$)[1]. Fig. 4.6 (d) shows κ becomes minimum at the half-filled value ($n = 1$) but does not vanish like the case in IPT (see Fig. 4.5 (d)). The vanishing of charge susceptibility clearly indicates that zero temperature metal-to-insulator transition may not be second order in nature and the insulators and metals will be separated by phase

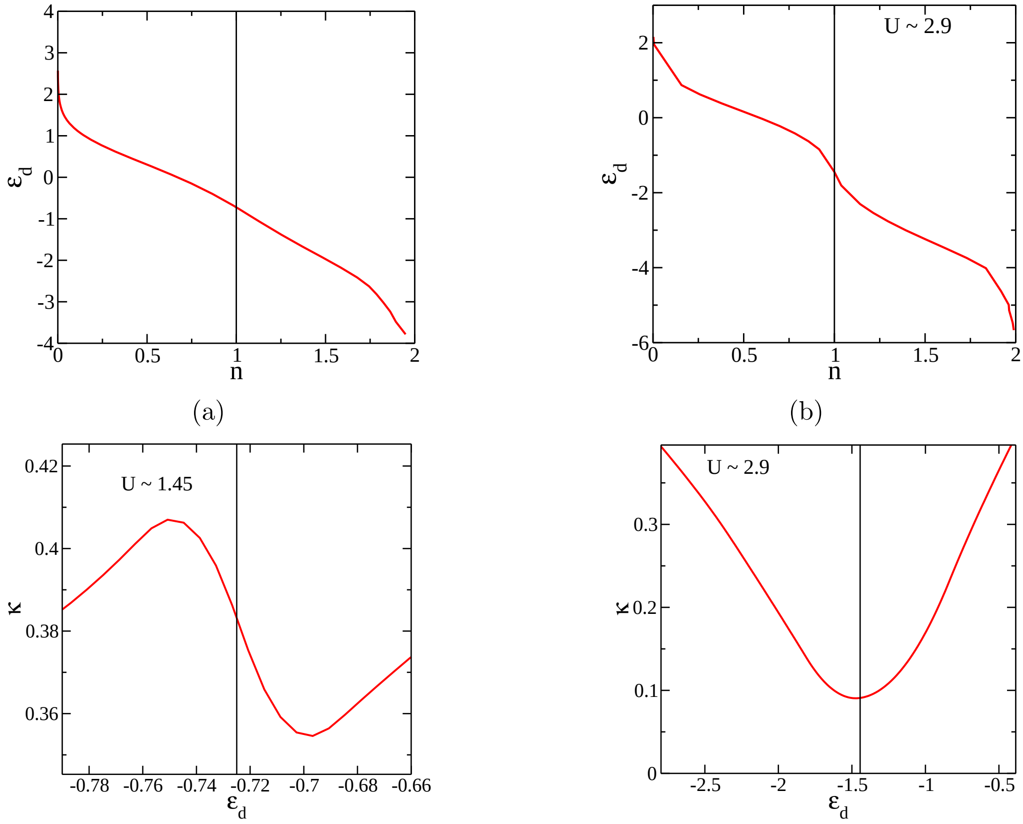

(a) (b)

(c) (d)

Fig. 4.6: (a) and (b) The orbital energy, ϵ_d as functions of filling n for $U \sim 1.45t_*$ (metal) and $U = 2.9t_*$ (Mott insulator close to the MIT at $n = 1$) respectively in IPT. (c) and (d) Charge susceptibility ($\kappa = -\partial n/\partial \epsilon_d$) calculated from numerical differentiation after using cubic spine interpolation. κ does not vanish at $n = 1$ for $U = 2.9t_*$ in contrast to the IPT result. The vertical lines are guides to mark the value at half-filling.

---

[1] The approximation sign is kept since U changes a little as we always find it through symmetry restoration in LMA

boundaries [107, 108]. Nevertheless, Furukawa and Imada find a diverging susceptibility just away from the Mott transition point in two dimensional Hubbard model [109, 110] and it is believed by many authors [105, 111] that zero temperature filling-controlled transition belongs to the second or continuous phase transition category. The zero charge susceptibility result agrees with the findings from many other methods, e.g. exact diagonalization (ED) and quantum Monte Carlo (QMC) in the context of DMFT [45]. Remarkably similar agreement has been found in recent compressibility experiments in interacting Fermionic optical lattice [112]. Though charge susceptibility does not vanish at the half-filling in case of LMA, the quasiparticle residue Z continuously vanishes for both IPT and LMA.

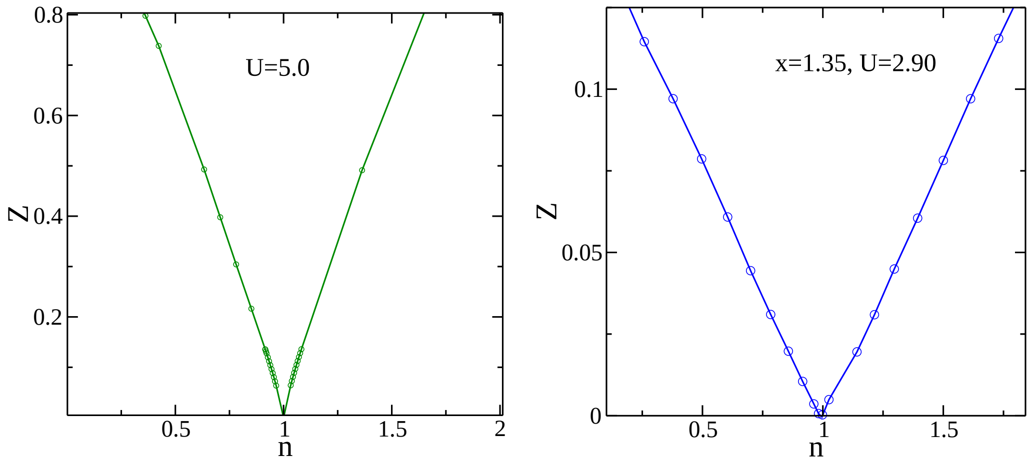

(a) (b)

Fig. 4.7: Disappearance of quasiparticle residue Z at half-filling ($n = 1$) in (a) IPT ($U = 5.0t_*$) and (b) LMA ($U = 2.9t_*$). Note the very different scales as found within IPT and LMA. The latter has been found in other contexts to produce the correct non-perturbative and even exponentially small scales.

4.3.3 Fermi liquid scaling

Similar to the symmetric case, we look for the Fermi liquid pinning since we expect the same as we have put the symmetry restoration condition for general filling at zero temperature. In Fig. 4.8, we can see that all the spectral function collapse well up to $\pm\omega \sim 0.5t_*$ after being scaled by the low-energy scale $\omega_L = Zt_*$. The collapse exists longer in the negative frequency side, which is due to the asymmetry in the p-h number.

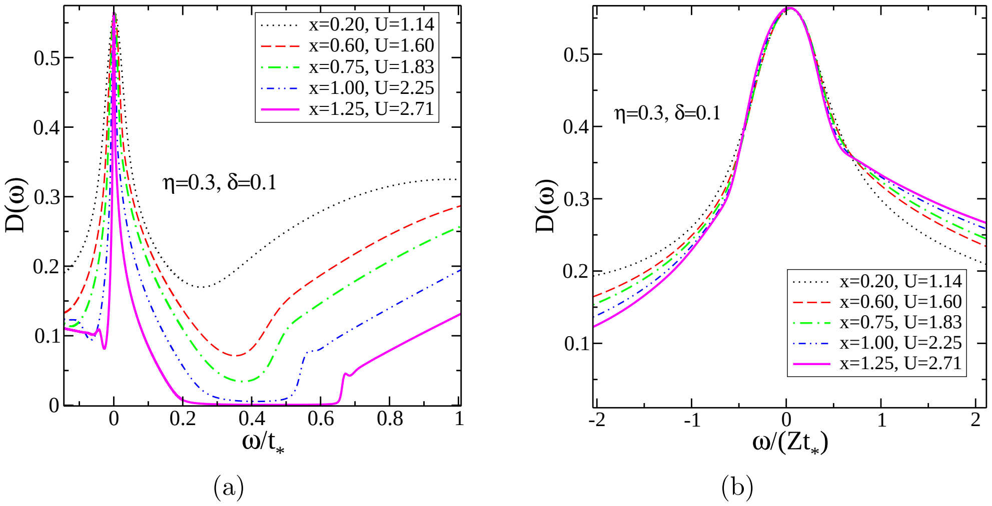

Fig. 4.8: Scaling collapse of the asymmetric (asymmetry parameter: $\eta = 0.3$, $\delta = 1 - n = 0.1$) spectral densities for different interaction strengths. (a) Before scaling. (b) After scaling by $\omega_L = Zt_*$.

4.3.4 Pseudogap formation

Fig. 4.8 also shows that after certain U/t_* ($\sim 2.7t_*$) a pseudogap starts to form near the Fermi level. The gap increases as we increase U/t_* further. We have noticed that pseudogap has the same width as the gap in the Mott insulator has in half-filling. It seems that the quasiparticle weight never

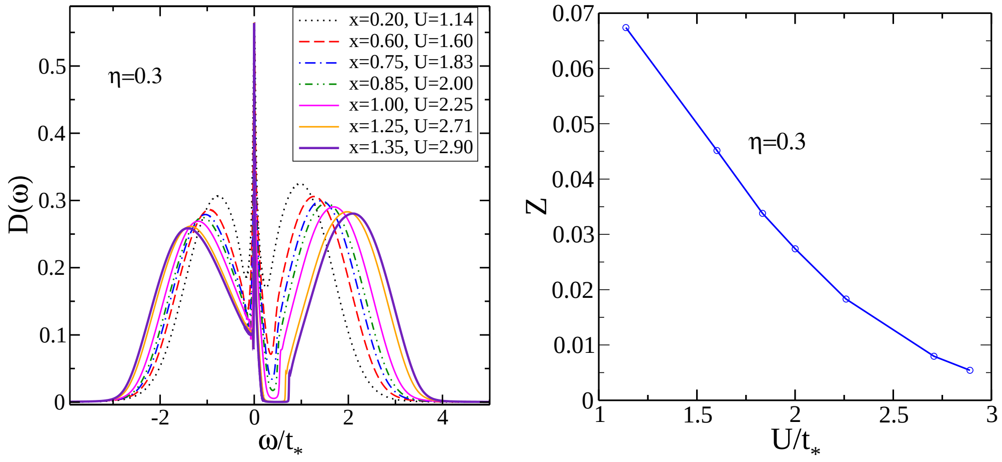

(a) (b)

Fig. 4.9: (a) Pseudogap formation near the Fermi level at large interaction strength, e.g. $U/t_* = 2.71$ and $U/t_* = 2.90$. (b) Quasiparticle residue Z as a function of U/t_*.

vanishes at any large finite U/t_* above U_{c2}/t_* and hence the pseudogap never touches (however close it may be) the Fermi level (see Fig. 4.9 (a)). This is expected because once we go away from half-filling, even by infinitesimal doping, we never expect a Mott transition. Though quasiparticle residue Z decreases with increasing U/t_*, tracing its behavior up to large U/t_* is numerically difficult in our present approach due to its limitation in self-consistent determination of the asymmetry parameter η and reaching a good convergence (see Fig. 4.9 (b)).

4.4 Strong coupling universality

Similar to the half-filled case, the scaling universality for strong interaction strength extends to very large frequencies beyond the low-energy Fermi liquid scale $\omega_L = Zt_*$ (see Fig. 4.10) and it appears that as we increase U/t_* further,

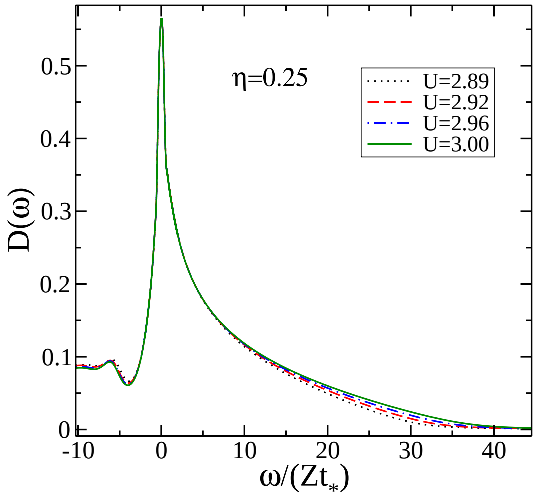

Fig. 4.10: Scaling universality at strong interaction values: $U/t_* = 2.89$, 2.92, 2.96, and 3.00. The universal region extends to very large values of ω/ω_L and the universal scaling form is seen to be very different from the renormalized non-interacting Gaussian form.

the scaling agreement extends further and at strong-coupling limit, we expect the scaling universality will extend all the way till the frequency reaches one of the Hubbard bands.

4.5 Optical conductivity

Following the same spirit of the symmetric case, we look for the universal scaling feature in the optical conductivity. As expected from the scaling in the spectral densities, we see that the absorption peak positions of the optical conductivity for different interaction and fixed doping, arise almost at the same reduced frequency $\omega/(Zt_*)$ (see Fig. 4.11). This universal feature of the absorption peaks implies that the universality is merely a a Fermi liquid, hence does not depend on doping as long as the phase remains a Fermi liquid. Another interesting feature is found when we look at the optical

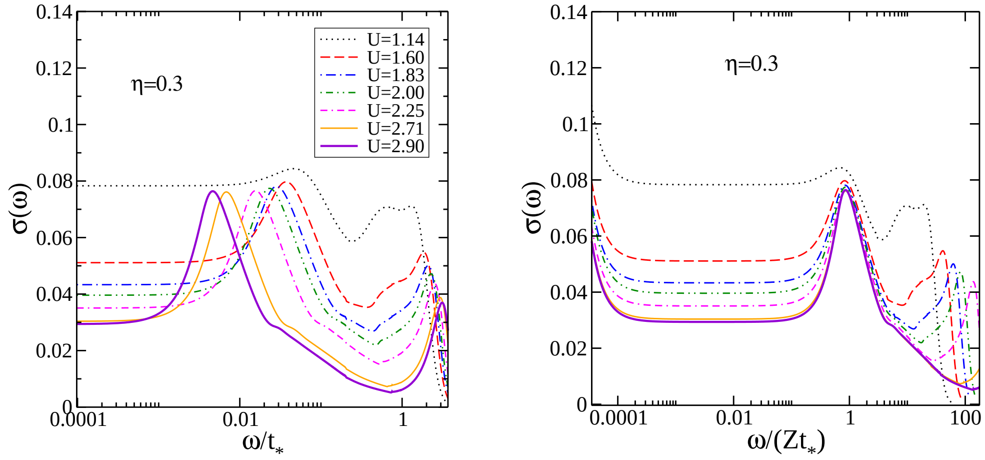

(a) (b)

Fig. 4.11: Scaling behavior in the optical conductivity for the asymmetry parameter $\eta = 0.3$ and different interaction strengths. (a) Before scaling the absorption peaks arise in different positions. (b) After scaling the frequency axis by $\omega_L = Zt_*$ the peaks almost appear at the same position.

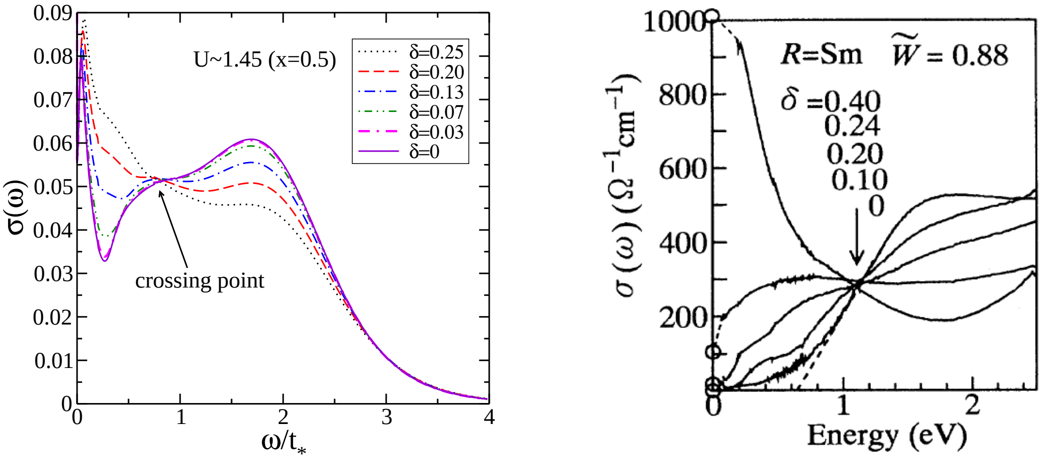

(a) (b)

Fig. 4.12: (a) LMA results for optical conductivity with various hole concentrations: $\delta = 1 - n$. (b) Optical conductivity for $Sm_{1-x}Ca_xTiO_3$ where $\tilde{W}$ is the bandwidth done by a tight-binding calculation, mentioned in Ref. 88, normalized to that of $LaTiO_3$.

conductivity as change the doping keeping the interaction fixed. As we see in Fig. 4.12, we find a universal crossing point, namely the *isosbestic point*, for different dopings $\delta = 1 - n$ ranging from 0 to 0.25. This behavior does indeed describe the experiments on compounds of the formulae $R_{1-x}Ca_xTiO_{3+y}$, R representing rare-earth metals, done by Katsufuji *et al* [88] (see Fig. 4.12(b)). Similar spectral weight transfer through an isosbestic point or a point-like region in the cuprates (e.g. $La_{2-x}Sr_xCuO_x$ [87] and $Pr_{2-x}Ce_xCuO_4$ [113]), Sr doped $LaCoO_3$ [114], and very recently in $NiS_{2-x}Se_x$ [86].

4.6 Summary

The role of p-h asymmetry in the Hubbard model has been a subject of interest since the discovery of high-T_c superconductors as these are doped Mott insulators. As the symmetry restoration condition of LMA is generic for arbitrary fillings, we apply it for the case away from half-filling as well. However, since we cannot get any direct relation between the orbital energy (or the chemical potential) and the interaction strength, we find it by changing the orbital energy and satisfying the Luttinger theorem (Eq. (11)) until we reach self-consistency. The schematic phase diagram on the filling-interaction plane is shown in Fig. 4.4, which shows that metallic regions are bounded by two band insulators: empty orbital ($n \to 0$) and doubly occupied ($n \to 2$) sites. The spectral densities show that there is a mirror symmetry between the region $0 \leq n \leq 1$ and $1 \leq n \leq 2$. We show this is true for both LMA and IPT spectral densities. The doped Mott insulator region is very hard to investigate since the scale becomes extremely small in the proximity of the

Mott insulator or in strong coupling at fixed asymmetry. Nevertheless, we have calculated spectral properties very close to the MIT in LMA and find that the charge susceptibility approaches zero at half-filling, which was also confirmed using IPT. We find that the Fermi liquid scaling collapse holds for the asymmetric case as well and a large universal region exists in strong coupling. We observe a pseudogap to arise in the vicinity of the Fermi level at higher interaction strength. Similar to symmetric case, we find an almost universal peak position in the optical absorption when we scale the frequency axis by the Fermi liquid low energy scale $\omega_L = Zt_*$. Remarkably we find a presence of universal crossing point, known as the isosbestic point, for different fillings and we find excellent qualitative agreement (though our case is zero temperature) with optical measurements in many real materials.

Chapter 5

LMA: Finite temperature transport and thermodynamics across the Mott transition

5.1 Introduction

In this chapter, the finite temperature LMA is developed and applied to the particle-hole symmetric Hubbard model and hence represents an extension of chapter 3. The focus is on transport and thermodynamic properties across the Mott transition. The resistivity in the metallic regime shows high T^2 coefficient. Like the zero temperature result, the scaling behavior of the absorption peak with universal position optical conductivity is also observed at low finite temperature. In contrast to the results from the IPT (Chapter 1), we find an excellent finite temperature scaling collapse in the spectral density. We do not find any anomalous or unphysical behavior in the specific heat.

5.2 Formalism

The $T = 0$ formalism may be extended to finite temperature through two major steps, namely

(i) The diagrams for the Green's functions and self-energies are the same as at $T = 0$, but now are formulated in terms of Matsubara frequencies $i\omega_n$ [67, 91] and then analytically continued ($i\omega_n \to \omega + i\eta$) as done in the case of finite T IPT calculations (see Chapter 1). However, the analytic continuation in the case of LMA however must be supplemented with a hard-core boson constraint which has been described in detail in Ref. 115. (ii) The integration sum $\int_{-\infty}^{\infty} d\omega/2\pi$ is replaced by the Matsubara sum $1/\beta \sum\limits_n$ where $\beta = 1/(k_BT)$ and the Fermi-Dirac distribution $n_F(\omega)$ that enters through the following identity wherever applicable.

$$\frac{1}{\beta}\lim_{\eta\to 0+}\sum_n e^{i\omega_n\eta}\frac{1}{i\omega_n - \omega} = n_F(\omega) \tag{5.1}$$

(iii) We do not employ symmetry restoration condition any more since that was solely meant for the ground state. Instead the interaction U found at $T = 0$ is fixed for all finite temperatures.

Below we shall write a few modified equations that we use in the finite temperature implementation. We skip the detailed derivations here. The calculations are straight-forward and can be found in Ref.115. We shall mention T dependence of the modified equations explicitly on the LHS, whereas it will remain implicit for the convenience of observation.

Eq. (2.16) and Eq. (2.17) are modified as

$$n(T) = \int_{-\infty}^{\infty} d\omega\, n_F(\omega)[\mathcal{D}_\uparrow(\omega) + \mathcal{D}_\downarrow(\omega)] \tag{5.2}$$

and

$$\mu(T) = \int_{-\infty}^{\infty} d\omega\, n_F(\omega)[\mathcal{D}_\uparrow(\omega) - \mathcal{D}_\downarrow(\omega)]\,. \tag{5.3}$$

Eq. (2.29) is modified as

$$\frac{1}{\pi}\mathrm{Im}^0\Pi^{+-}(\omega, T) = \int_{-\infty}^{\infty} d\omega' \mathcal{D}_\downarrow(\omega')\mathcal{D}_\uparrow(\omega' - \omega)[n_F(\omega' - \omega) - n_F(\omega')] \tag{5.4}$$

Imaginary part of Eq. (2.40) is modified as

$$\mathrm{Im}\Sigma_\sigma(\omega, T) = U^2 \int_{-\infty}^{\infty} \frac{d\omega'}{2\pi}\mathcal{D}_{\bar{\sigma}}(\omega + \omega')\mathrm{Im}\Pi^{\bar{\sigma}\sigma}(\omega')n_F(\mathrm{sgn}(\omega + \omega')) \tag{5.5}$$

5.3 Numerical implementation

Every finite temperature calculation requires a zero temperature converged solution as a starting point. The $T = 0$ calculation entails the symmetry restoration condition (Eq. (2.54)) for the metallic phase which fixes the value of U/t_* and leads to a Fermi liquid ground state. For the insulating phase, the U value is found through $U = 1/(\mathrm{Re}^0\Pi^{+-}(0))$ as done for the $T = 0$ insulating phase (see Eq. (2.68)). The zero temperature solution is used as input for finite temperature calculation at the lowest temperature. The temperature is increased in steps that are fractions of the relevant energy scale, such as the low energy scale Zt_* in the metallic phase or the spectral gap Δ_g, in the Mott insulating phase. The input for the $(n+1)^{\text{th}}$ step is taken as the converged solution of the n^{th} step.

At a given temperature, the DMFT self-consistency requires the calculation of ${}^0\Pi^{+-}(\omega)$, $\Pi^{+-}(\omega)$, and then $\Sigma_\sigma(\omega)$. We find that a stable algorithm which yields physically meaningful results requires us to use the $\text{Im}{}^0\Pi_{ii}^{\sigma\bar{\sigma}}(\omega, T=0)$. In the finite T calculation, we start with the symmetry restored U/t_* and then look for the evolution as the temperature is turned on. However, there is a numerical instability as soon as we turn on the temperature (even a very little). The metal instantly turns into an insulator. Although this might indeed be an actual prediction of the LMA, we believe it to be a numerical artefact. To get rid of this problem, which we believe to arise because of suddenly turning off the symmetry restoration condition check, we forcefully keep the ${}^0\Pi^{+-}(\omega)$ to be identical to its $T=0$ value. Such an *ad hoc* constraint is justified since we expect that it does not get modulated drastically at low temperature. However, more robust finite temperature algorithm is still an open challenge and it can be future extension of the work presented in the thesis.

5.4 Spectral density

5.4.1 Fermi liquid metal and universality at strong coupling

We anticipate that the spectral density $D(\omega) = -\frac{1}{\pi}\text{Im}G(\omega)$ has a universal scaling for $D(\omega/\omega_L, T/\omega_L)$ for $(\omega/\omega_L, T/\omega_L) \sim \mathcal{O}(1)$. Indeed we find good scaling collapse for a wide range of frequencies (see Fig. 5.1). This is in contrast to the violation of scaling behavior at finite temperature in the case of IPT (Chapter 1). This implies that LMA is not only capable of capturing the low temperature Fermi liquid behavior, but also a wide universal scaling behavior. Moreover, the universality regime extends to several decades above the low energy scale ($\omega \gg \omega_L$) for interaction strength close to the Mott insulator (here in Fig. 5.1 $U/t_* = 2.24$, 2.42, and 2.51). Thus it seems that the regime of scaling collapse extends more and more as one approaches higher U/t_* values (e.g. $U = 2.42t_*$ and $U = 2.51t_*$ share more universal regime compared $U < 2.42t_*$). If we generalize this, we can infer that in the strong-coupling limit (in our case, $U \to U_{c2}$), the scaling universality will exist all the way up to the Hubbard band edge.

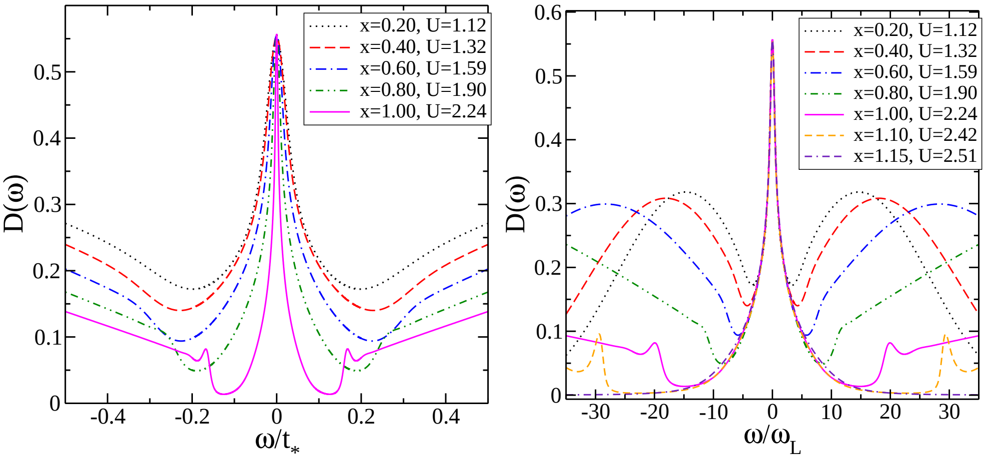

(a) (b)

Fig. 5.1: Spectral densities at temperature $T = 0.1\omega_L$ in the metallic phase where $\omega_L = Zt_* \propto \omega_m$. (a) Spectral densities for different U/t_* ($t_* = 1$). (b) The same spectra when ω is scaled by the corresponding ω_L's. All spectra collapse up to $\omega \sim 2\omega_L$ for the U values shown. The collapse extends to a few

5.4.2 Temperature evolution of spectra

Metallic regime

Next we investigate the temperature evolution of the spectra starting from a U-value that is well within the metallic regime at $T = 0$. As we see from Fig. 5.2 that, similar to the IPT result (Chapter 1), the quasiparticle resonance disappears forming a dip at the Fermi level ($\omega = 0$) for $T \gtrsim 2.50 Z t_*$ (see Fig. 5.2). As the temperature is increased further, spectral weight transfer from the Fermi level to the Hubbard bands continues, which deepens the dip with rising T.

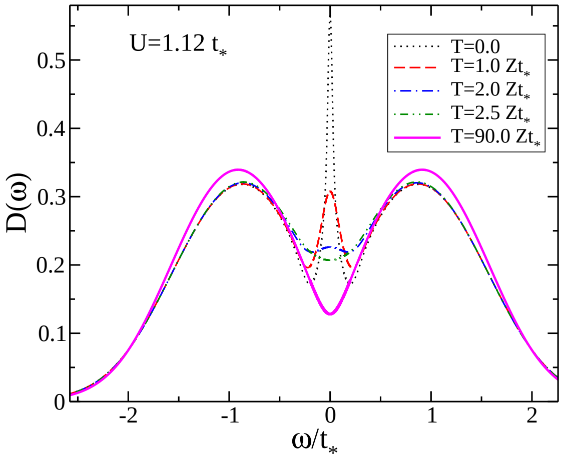

Fig. 5.2: Finite temperature evolution of the spectral density that has metallic phase ($U = 1.12 t_*$) at $T = 0$. Quasiparticle resonance disappears at $T = 2.5\,\omega_L$ ($\omega_L = Z t_*$) by forming a dip at the Fermi level. The dip increases with temperature.

Mott insulator regime

Similarly if we start from an insulating phase, the spectral gap starts being filled up. This filling-up occurs continuously and it is hard to infer metallic or insulating unless we look at the change of resistivity slope with temperature. The continuous temperature evolution of both metallic and insulating phase is similar in nature for $T > T_c$ in case of IPT. As our calculations show, at extremely high temperature, all the Hubbard band features melt down to a single featureless density at the Fermi level and we should get a high-temperature metallic state. However, such a state is not feasible in reality since at such a high temperature (considering t_* to be of the order of an eV) most of the materials melt down.

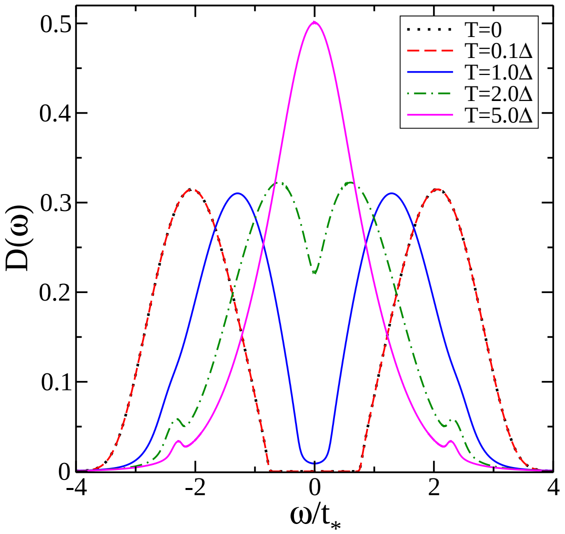

Fig. 5.3: Temperature (in unit of spectral gap Δ) evolution of an insulating phase ($U/t_* = 4.13$). The spectral gap ($\Delta = 1.46t_*$ at $T = 0$) is filled up continuously as temperature is raised. At high temperature (say, $T = 5t_*$), the Hubbard band feature completely disappears .

5.5 Transport and optical properties

5.5.1 Resistivity

Fig. 5.4 shows the behavior of resistivity as a function of temperature. The resistivity behavior at low temperature show T^2 behavior. The T^2 regime is very small and it decreases further as we increase the interaction strength U/t_*. On the other hand, the T^2-coefficients A appear to be very high ($\sim 10^5$) compared to that obtain in the IPT results (10^3). Since the regime of T^2 dependence decreases as U/t_* is increased, it is tempting to expect the peak position in the resistivity to become universal after scaling the temperature by corresponding low-energy scale $\omega_L = Zt_*$. However, in contrast to the IPT result, such a universality is absent (see Fig. 5.5). The resistivity for the insulating case shows activation behavior (first three curves from the top in

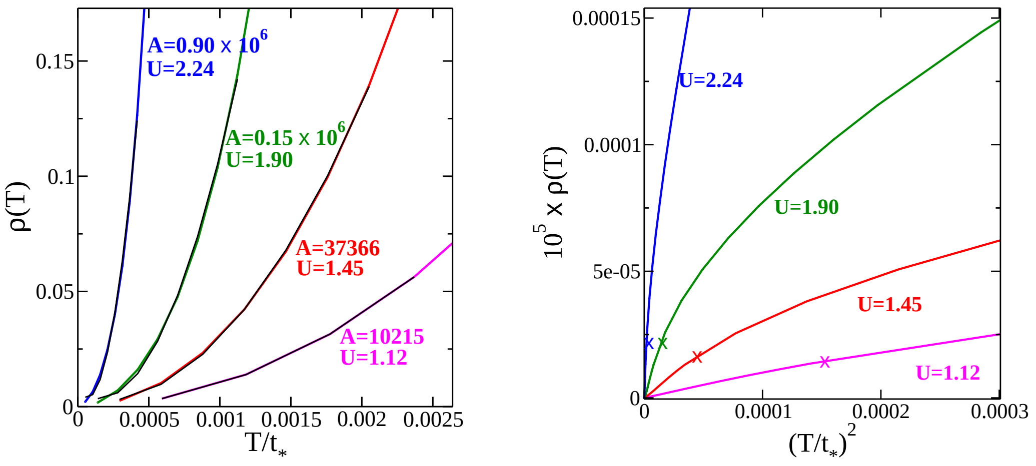

(a) (b)

Fig. 5.4: Fermi liquid signature in the resistivity in the metallic phase. (a) T^2-dependence of resistivity with high-value of coefficients A. (b) Same plotted with T^2 showing that linear (Fermi liquid) regime decreases with increase in interaction strength U/t_* ($t_* = 1$). Cross marks are guides to show the range of the T^2-regime.

Fig. 5.5 (a)), exponentially decreases with increase in temperature. It starts increasing again, i.e. becomes metallic at high temperature (not shown), since the gap in the spectral density is filled up sufficiently (see Fig. 5.3).

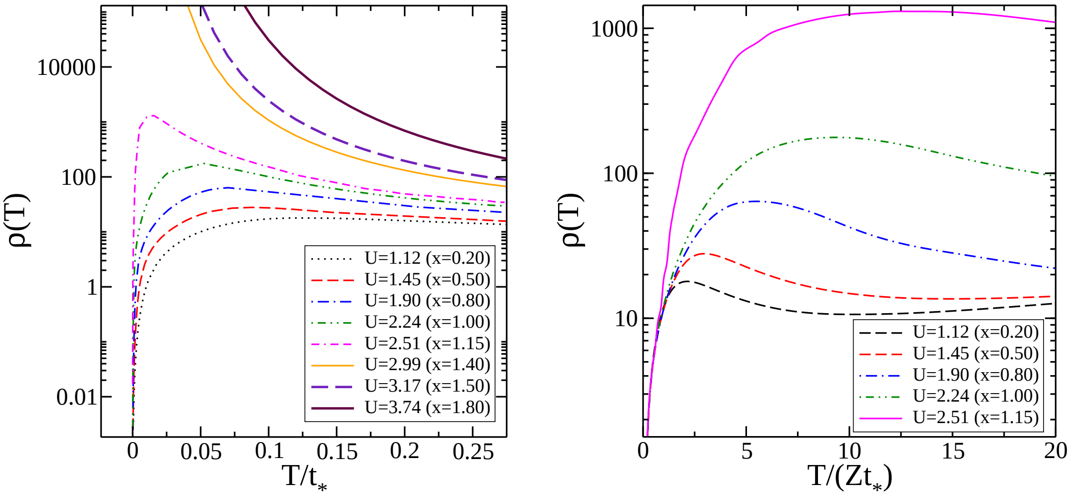

Fig. 5.5: Absence of universal peak position in resistivity curves after scaling the the temperature axis by Zt_*. (a) Resistivity as a function of T/t_* for various U/t_*'s (U/t_*= 1.12, 1.45, 1.90, 2.24, and 2.51 are for metallic phase and U/t_*= 2.99, 3.17, and 3.74 for insulating phase). (b) Resistivity values for the metallic case are plotted against $T/(Zt_*)$.

5.5.2 Optical conductivity

Metallic phase

The low frequency absorption peaks that we have observed in Fig. 3.8 in Chapter 3 disappear above $T \simeq 0.05Zt_*$ and therefore it does not seem relevant to look for scaling behavior at very low temperature. Towards ultra-violet regime, a semi *isosbestic point* or crossing point is observed (see Fig. 5.6(a)). This signifies a universal feature of strong electronic correlation [89]. Keeping the interaction fixed, if we look at the temperature effect, we find a long tail unaffected by temperature and running all the region starting from $\omega/t_* \sim 0.05$.

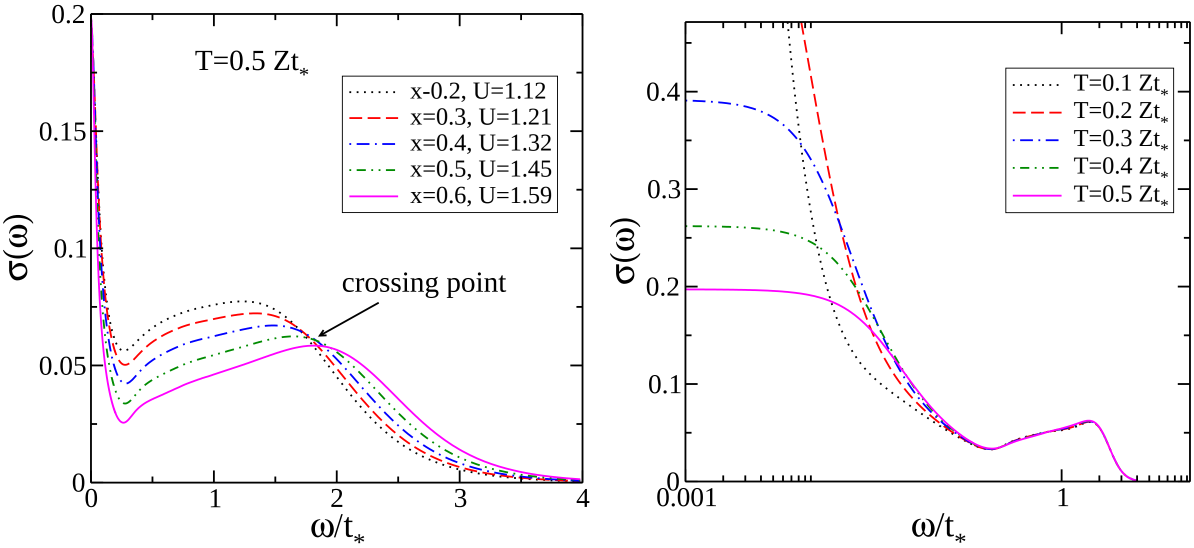

(a) (b)

Fig. 5.6: (a) Isosbestic point found in optical conductivity at $T/(Zt_*) = 0.5$. (b) Temperature independent long tail observed for $U/t_* = 1.45$ ($x = 0.5t_*$) at different temperatures.

Insulating phase

The transition from insulator to metal like behavior is also seen from the optical conductivity results. Fig. 5.7 shows that at very low temperature ($T = 0.1\Delta$, $\Delta = 1.46t_*$), an optical gap remains present. As the temperature is raised, the optical gap starts getting filled up by transfer of spectral weight from the absorption peak that arises around $4t_*$. During this transfer the absorption peaks experience a red-shift (i.e. move towards lower frequency) in contrast to the optical conductivity results in IPT (in IPT, the absorption peaks for the Mott insulator experience a blue-shift, see Fig. 1.13 in Chapter

1).

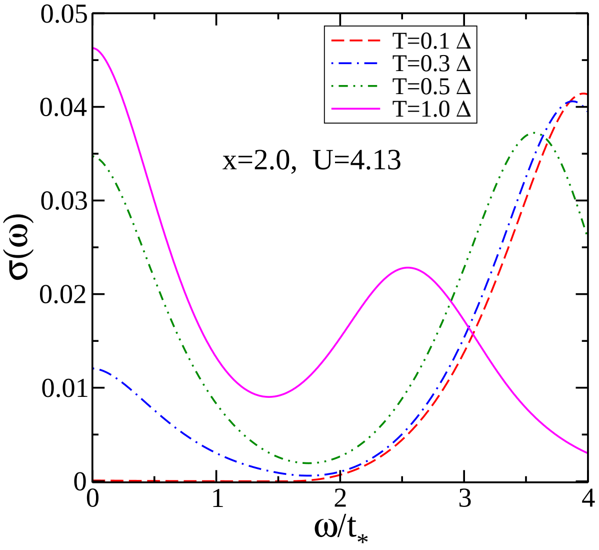

Fig. 5.7: Temperature evolution of optical conductivity in the insulating phase. Transfer of spectral weight occurs as temperature in the unit of spectral gap $\Delta = 1.46t_*$. Also a red-shift in the absorption peak is noticed during the spectral weight transfer.

5.6 Thermodynamic properties

We use the same expression for the expectation value of the Hamiltonian Eq. (25) in Chapter 0 in order to calculate the internal energy. From Fig. 5.8 we can notice that the internal energy monotonically increases with temperature and in this case at no condition any dip (i.e. negative slope) arises. Therefore we do not find any anomaly, in contrast to some cases in the IPT results. The specific heat shows linear behavior with T (see Fig. 5.9(a)) and hence signifies a Fermi liquid. Now if we scale the temperature axis by $\omega_L = Zt_*$, we find scaling collapse in the linear regime, which again affirms that ω_L is the associated low-energy Fermi liquid scale.

Moreover, though not accurately a point, a universal crossing region is observed around $T = 0.01t_*$. Unlike the IPT result, no second universal crossing point is found. However, the crossing region is shifted and becomes more point-like as we scale the temperature axis by ω_L. Not obtaining a sharp crossing point like the earlier finding in IPT, may be a numerical artefact.

5.7 Summary

In the finite temperature LMA, we apply the Matsubara formalism [67, 91] to compute the diagrams and using the spectral representation for the analytic continuation, we express the final results in terms of real frequencies. The symmetry restoration condition is not imposed in contrast to the zero temperature case. A numerical instability occurs in the $\mathrm{Im}^0\Pi^{+-}(\omega)$ that we calculate during the DMFT iterations. To avoid such an instability, the T-dependence in $\mathrm{Im}^0\Pi^{+-}(\omega)$ is ignored after computing it in the first iteration

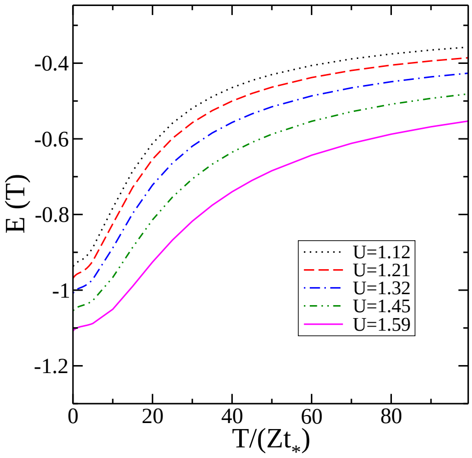

Fig. 5.8: Internal energy as a function of temperature for U/t_* ranging from. Unlike the IPT results no dip is observed in any case.

from $\mathcal{G}(\omega)$ (assuming a minor change to happen at finite temperature) and keeping it fixed through out rest of the iterations. This approximation leads to stable solutions and as a first check, it affirms the Fermi liquid nature, e.g. quasiparticle resonance and the scaling collapse, in the finite temperature spectral densities. This is a remarkable achievement since the finite T scaling is not captured in the IPT scenario.

We find continuous metal-to-insulator transition by observing a semigap to open at finite temperature. However, true demarcation between metal and insulator is inferred after looking at sign of the resistivity slope at that temperature. Similarly we observe insulator-to-metal transition at very high, physically unattainable temperature.

As expected, the resistivity in the metallic regime shows T^2 dependence

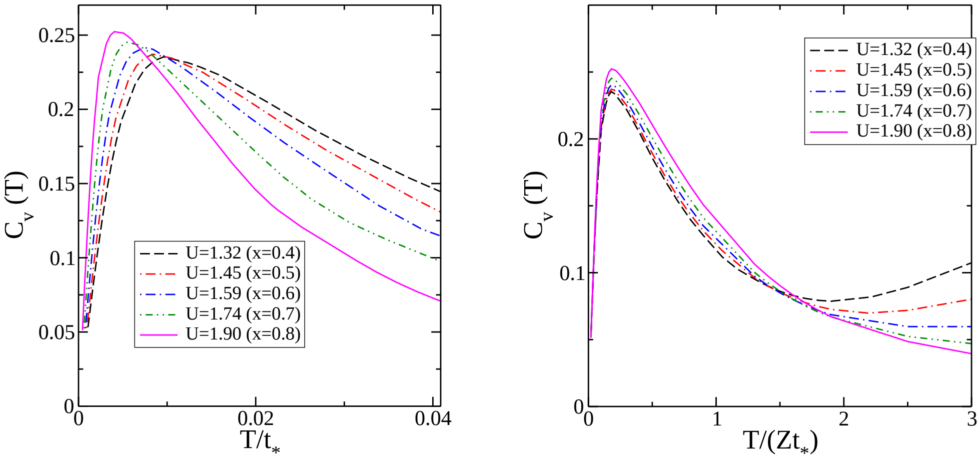

(a) (b)

Fig. 5.9: Specific heat as a function of temperature for different U/t_*. (a) Steep linear regimes signifying Fermi liquid behavior. A crossing region occurs around $T = 0.01t_*$. (b) Linear regimes collapse due to T/ω_L scaling of the x-axis. Also the crossing regimes shift near $T = 1.5\omega_L$.

with a very high value (as compared to IPT) of its coefficient. The resistivity peak scaling, as we addressed in the resistivity results from IPT, is not observed, indicating that this peak could be non-universal. As in the case of zero temperature, the optical conductivity shows universality in the absorption peak position once the frequency is scaled down by the associated low-energy scale ω_L. Universal crossing point, often termed as the *isosbestic point* has been found in the ultra-violet side of the optical conductivity of metals for different temperatures.

We find no dip in the internal energy as a function of temperature and hence no negative specific heat or other physical anomalies has been found in the specific heat. In that sense, LMA may offer more realistic calculations compared to IPT. The specific heat scaling has been observed similar to that we find in IPT. However, instead of two universal crossing points found in the IPT result, we find one low-temperature universal crossing zone which shifts after temperature being scaled down by ω_L.

Chapter 6

LMA: Anomalous transport in doped Mott insulator and the effects of transverse spin fluctuations

6.1 Introduction

As has been mentioned hitherto in this thesis, the high temperature superconducting cuprates are basically doped Mott insulators (Fig. 6.1 shows a schematic phase diagram showing that different phases emerge from doping (electron or hole) a Mott insulator, which has an antiferromagnetic (AF) ground state.) Since the problem of high temperature superconductivity has remained unsolved [20], the transport and thermodynamic properties of doped Mott insulators have generated a sustained interest over the past two

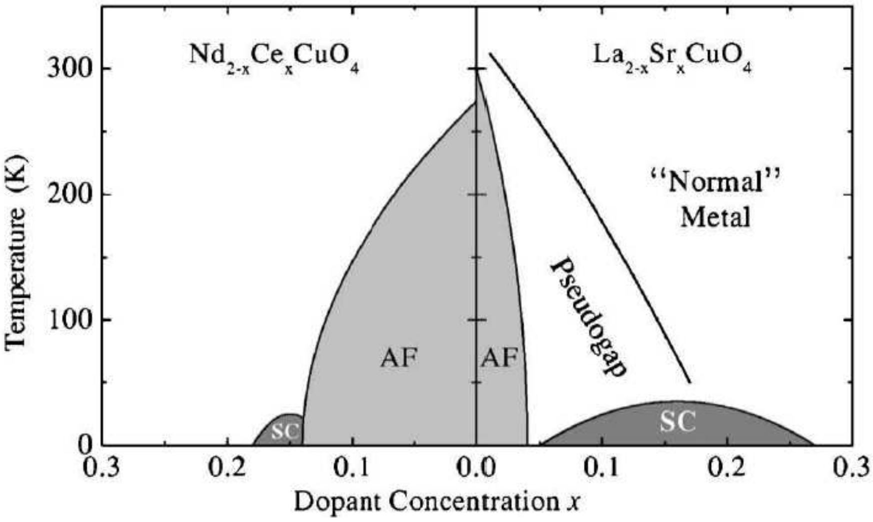

Fig. 6.1: Schematic phase diagram of high T_c superconductors showing emergence of different phases by doping holes (right side) or electrons (left side) an antiferromagnetic (AF) Mott insulator. Fig. reproduced from Ref. 116.

decades. Within the framework of this thesis, doped Mott insulators are described through the particle-hole asymmetric Hubbard model. In Chapter 4, we have examined the spectral functions, self-energies and optical conductivities as functions of interaction strength and doping at zero temperature. We have seen that the spectral functions develop a narrow resonance at the Fermi level, whose width is proportional to the quasiparticle weight and whose functional form is described by the renormalized non-interacting limit at the lowest frequencies ($\omega \ll \omega_L$). The single-particle dynamics has been found to be universal in strong coupling, namely the spectral functions and self-energies were functions purely of ω/ω_L in the strong coupling scaling regime. The clean gap for Mott insulators centred at the Fermi level shifts to above the Fermi level for any finite doping. In the imaginary part of the self-energy, a remarkable crossover from Fermi liquid ω^2 behavior to a linear

$\sim \omega$, often described as marginal Fermi liquid (MFL) behavior [72] , has been seen around $\omega \sim Zt_*$ in certain parameter regimes. Such a zero temperature behavior is naturally expected to lead to a crossover in resistivity from a low temperature T^2 form to a high temperature linear form. A finding like this would be exciting since that could provide clues to understanding the normal phase of high T_c cuprates where such linear resistivities have been seen extending over a decade of temperatures and a sizable range of dopings [117]. Phenomenological explanations such as the marginal Fermi liquid behavior have been proposed which do rationalize the linear scattering rates, but do not have a microscopic justification. The van-Hove singularity (vHs) has also been cited as a possible reason [118]. However, a compilation of experimental data shows that the vHs arises only for certain materials at certain dopings, while the linear resistivity is a very generic phenomenon. Recent theoretical results on the two-dimensional Hubbard model using functional renormalization group (FRG) calculations which include the spin-fluctuation vertex corrections find a strongly angle-dependent T-linear term in the resistivity [119].

This chapter is a finite temperature extension of the T=0 study of the asymmetric Hubbard model using LMA. Since LMA includes spin-flip processes to all orders through RPA, we expect that the results we get should be similar to the FRG calculations mentioned above. Of course the anisotropy cannot be captured, since we employ the DMFT framework, but it will be interesting to see if dimensionality has an effect at all on the linearity of the scattering rates or is the correct inclusion of spin fluctuation physics sufficient to get a T-linear resistivity. Within our DMFT+LMA framework, we do find a wide linear resistivity regime, hence we conclude that spin-fluctuation physics is the sole cause of marginal Fermi liquid like behavior. Additionally, we also expect (and indeed do find) a universality in the response functions such as the dc conductivity and the optical conductivity arising due to the universality in the single-particle dynamics in the strong correlation scaling regime of the doped Mott insulator.

The structure of the chapter is as follows. We first describe the properties of the spectral densities and the universal scaling regime associated with them. Then we look at the transport properties, where we find a wide region of T-linear and a very small region of T^2 dependence in the resistivity. We explain these feature in term of the marginal Fermi liquid (MFL), which is indeed observed in the imaginary part of the LMA self-energy. We compare our LMA results to the IPT results showing that the latter does not capture the T-linear dependence in the resistivity. Finally we discuss the universality issues in the optical conductivity and specific heat results as a thermodynamic quantity.

6.2 Spectral density

6.2.1 Quasiparticle resonance and pseudogap

From Fig. 6.2(a) we see that at low temperature (e.g. $T = 0.1\omega_L$) a quasiparticle resonance appears at the Fermi level and a pseudogap forms at higher U/t_*. At high temperature (e.g. $T = 5\omega_L$), the quasiparticle resonance disappears whereas the pseudogap remains almost unaffected (see Fig. 6.2(b)).

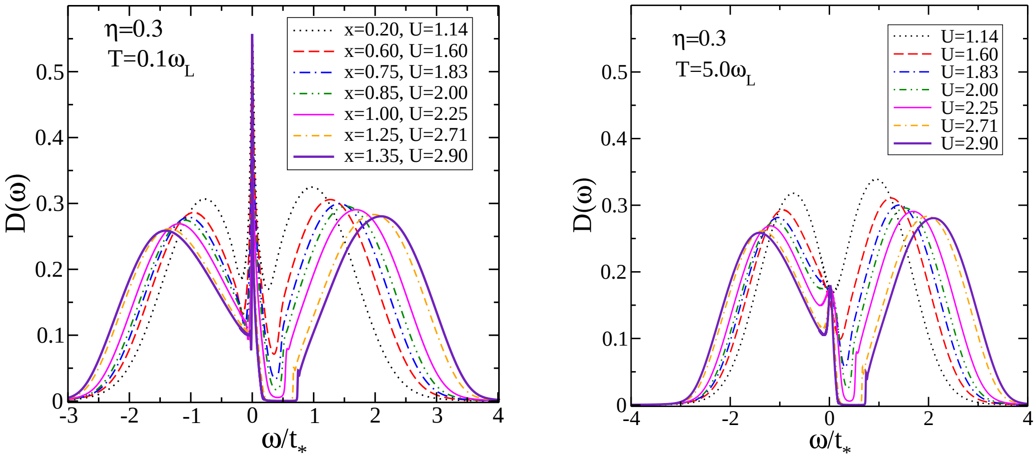

(a) (b)

Fig. 6.2: Finite temperature spectral densities for the asymmetric case ($\eta = 0.3$) for $U = 1.14$, 1.60, 1.83, 2.00, 2.25, 2.71, and 2.90 in the unit of t_*. (a) $T = 0.1\,\omega_L$ shows sharp resonance and pseudogap of $\sim 0.7t_*$ at $U = 2.90$ similar to the $T = 0$ results. (b) At sufficiently higher temperature, $T = 5.0\,\omega_L$, the resonance completely disappears, whereas the pseudogap does not alter noticeably.

Since the pseudogap does not form for all interaction strengths, we see different behaviors in temperature evolution in weakly correlated (small U/t_*) and strongly correlated (large U/t_*, close to the Mott insulator at half-filling) regime. For example, Fig. 6.3 (a) shows no pseudogap in the spectral densities for $U = 1.14t_*$, but the quasiparticle resonance gradually diminishes and finally form a dip or semigap at high temperature ($T \sim 5Zt_*$). On the other hand, at higher interaction strength, such as $U = 2.9t_*$, a pseudogap already has been formed at zero temperature and the gap size does not change significantly until we reach a temperature as high as $T = 100Zt_*$ (see Fig. 6.3 (b)).

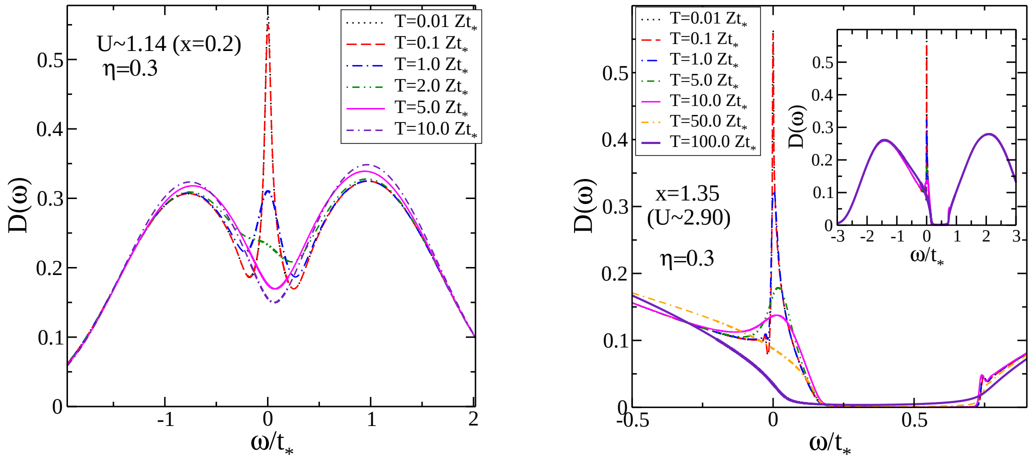

(a)

(b)

Fig. 6.3: Temperature evolution of spectral densities for the asymmetric case ($\eta = 0.3$) for different temperature in the unit of low-energy scale $\omega_L = Zt_*$. (a) At low interaction strength ($U \sim 1.14t_*$), pseudogaps do not appear. However, the quasiparticle resonance disappears at higher temperature ($T \sim 5Zt_*$) forming dips near the Fermi level. (b) At interaction strength close to the transition ($U \sim 2.90t_*$), a pseudogap is prominent and it size remains unaffected for a large range range of temperature (For $U \sim 2.90t_*$, the gap starts being filled up at $T \sim 100Zt_*$, which is physically unattainable in common experiments). Main shows the region close to the Fermi level. Inset shows the spectral functions containing the Hubbard bands.

6.2.2 Finite T scaling

Similar to zero temperature we verify if finite temperature scaling behavior for low temperature holds or not. We see that spectral densities for different interaction strengths and for a fixed asymmetry parameter η ($\eta = 0.3$) in Fig. 6.4), collapse to a universal curve. It is seen from the figure that the scaling collapse holds at least until $\omega \sim 10\omega_L$ (for $U \gtrsim 2.71t_*$), and the collapse improves as one progresses towards higher U/t_* suggesting that in the strong coupling regime, we should find a universal spectral function of the form $D(\omega/\omega_L;T/T_L)$.

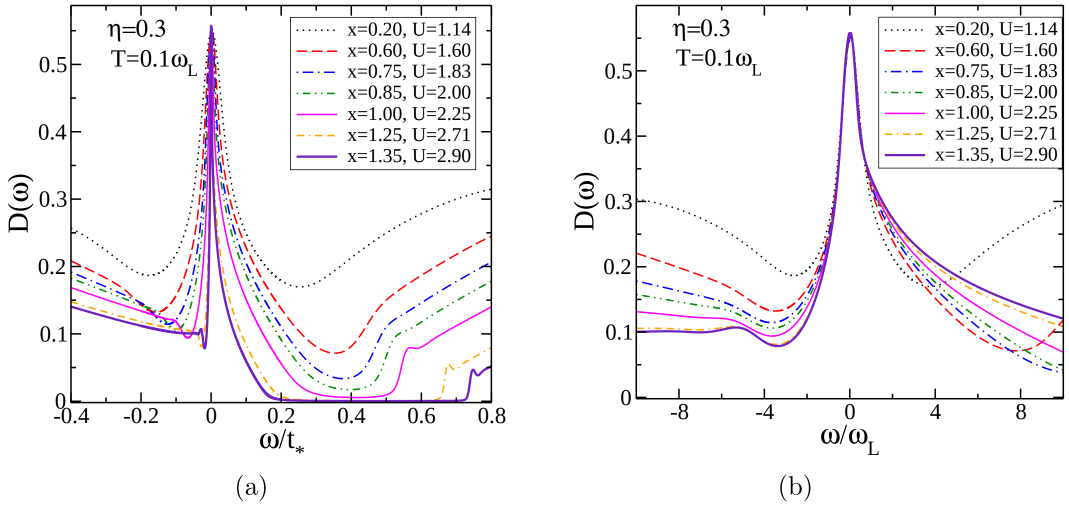

(a) (b)

Fig. 6.4: Scaling collapse of spectral densities at finite temperature for $\eta = 0.3$ and different U's in the unit of t_*. (a) Frequency axis unscaled. (b) Frequency axis scaled by the corresponding low energy scale $\omega_L = Zt_*$.

6.3 Transport and optical properties

6.3.1 Resistivity

The most surprising result that we obtain in this chapter is in the low-temperature behavior in the resistivity. The resistivity $\rho(T)$ for a fixed asymmetry parameter $\eta = 1 + 2\epsilon_d/U = 0.3$ and different interaction strengths, as shown in Fig. 6.5(a). The T^2 dependence is almost invisible whereas a linear-T behavior is found to exist up to $T \sim 0.12t_*$. On the other hand, it follows a linear behavior for a wide range of temperature. In Fig. 6.5(b) it seems that T^2 regime extends for higher U/t_* (see the position of the cross

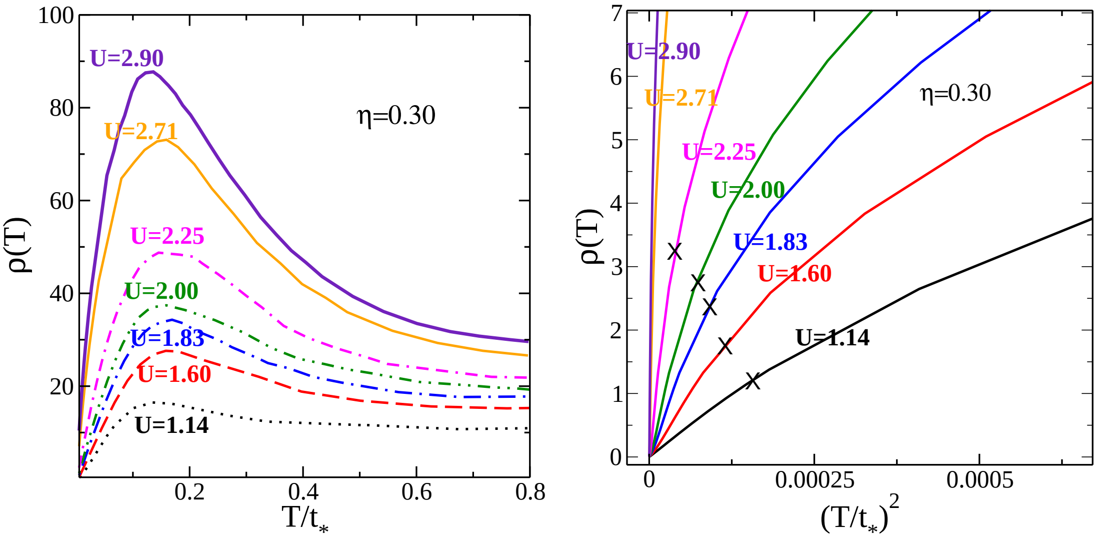

(a) (b)

Fig. 6.5: Resistivity $\rho(T)$ as a function of temperature for different U/t_* ($t_* = 1$) with asymmetry parameter $\eta = 0.3$ ($\delta = 1 - n \simeq 0.1$). (a) Linear increase of $\rho(T)$ up to $T \simeq 0.12$. After that $\rho(T)$ falls off with T. (b) $\rho(T)$ at very low temperature showing T^2 behavior. Cross marks are guides to see the range of T^2-behavior.

marks in the figure) whereas linear T-dependence behavior extends more for lower U/t_* (see Fig. 6.6). For fun, we just choose a $t_* \sim 0.6eV$ and scale the x-axis of Fig. 6.5(a). We find that some of the curves appear to have a linear regime extending all the way down to $50 - 100K$ from $T \sim 1000K$. Thus our approach can produce physically realistic values of the linear resistivity regime, which has been observed in many cuprate superconductors (see Fig. 3(b) in Chapter 0).

Next we look for the doping dependence of the resistivity profile as it is very much relevant to the cuprate experiments. Fig. 6.7 (a) shows that for small interaction strength ($U \simeq 1.5t_*$), linear regime in the resistivity is smaller and it extends further as doping is increased. This is expected since here we are decreasing doping starting from a metal, which is similar

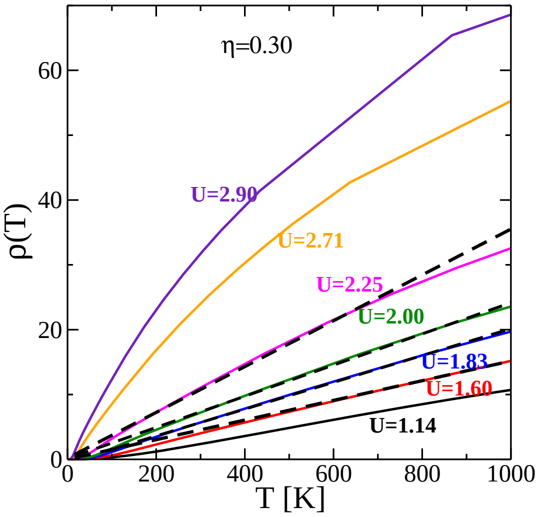

Fig. 6.6: Resistivity as a function of temperature for different interaction strengths U/t_* at fixed asymmetry parameter $\eta = 0.3$, showing a wide range of linear regime (up to order of 1000 K) for small and intermediate interaction strengths. The dashed lines are guides to see the range of linear regime.

to moving towards the superconducting dome from the right-side of the superconductivity phase diagram. There is a universality in the linear regime (where all curves collapse) at low temperature. We do similar resistivity calculation using IPT for the asymmetric Hubbard model. It turns out that it captures only the Fermi liquid (quadratic in T) part in the resistivity without a situation where a significantly wide linear temperature dependence can be observed (see Fig. 6.8) .

Such emergence of linear behavior in the resistivity signifies a possible existence of marginal Fermi liquid state, or more generally even though the ground state is a Fermi liquid, there is a smooth crossover from a true Fermi liquid to a marginal one. In the crossover regime, T dependence of $\rho(T)$ takes place with power varying from 2 to 1. According to Varma *et al*'s phenomenological hypothesis for a marginal Fermi liquid, in order to describe

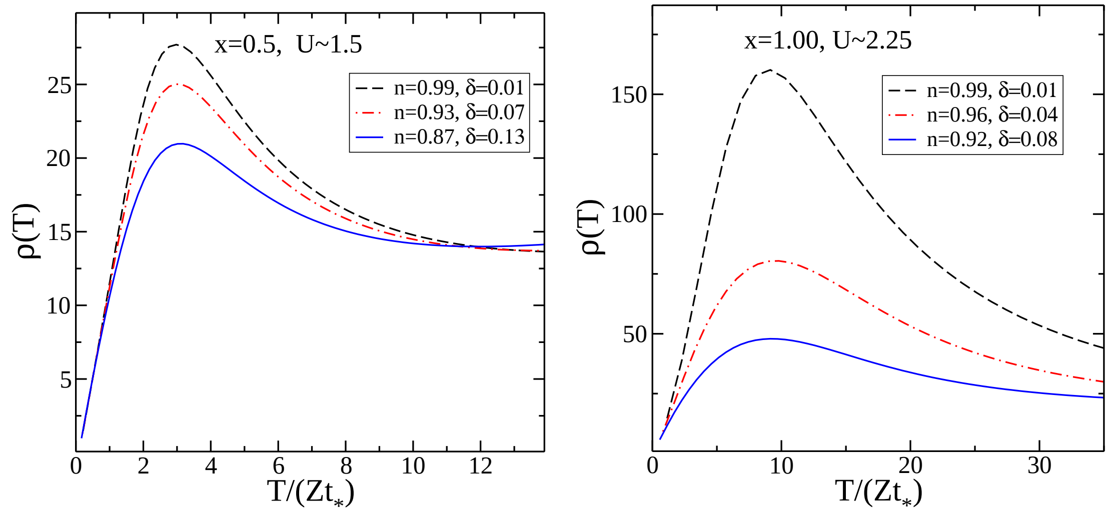

(a) (b)

Fig. 6.7: Resistivity $\rho(T)$ as a function of temperature for different hole doping concentrations. (a) Low interaction strength (b) Interaction strength close to the Mott transition at half-filling.

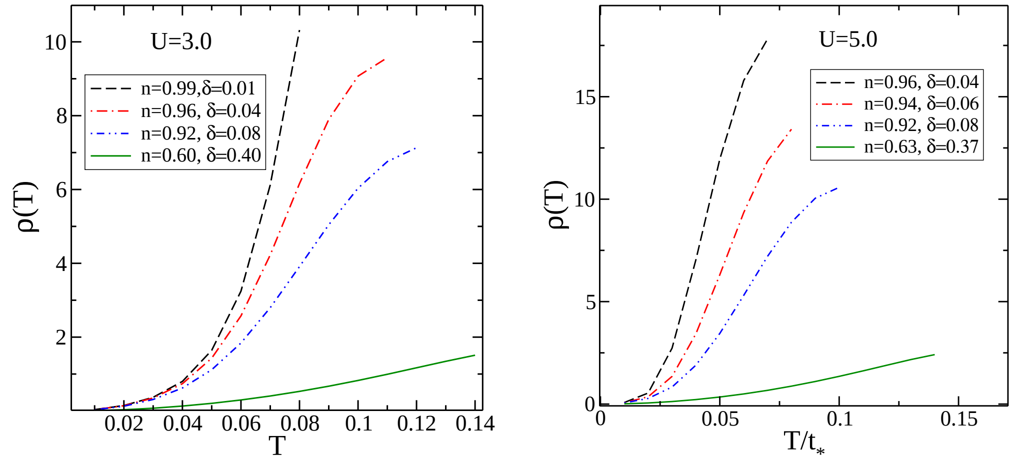

(a) (b)

Fig. 6.8: Resistivity $\rho(T)$ as a function of temperature for for different hole doping concentrations calculated from IPT. (a) Low interaction strength ($U = 3.0t_*$). (b) Interaction strength which has Mott insulating state at half-filling ($U = 5.0t_*$).

the “normal” state in cuprates, the self-energy takes the following form [72].

$$\Sigma(\mathbf{k},\omega) \sim g^2 N^2(0) \left[\omega \ln \frac{x}{\omega_c} - i\frac{\pi}{2} x \right] \tag{6.1}$$

where $N(0)$ is the single-particle density of states, g is a coupling

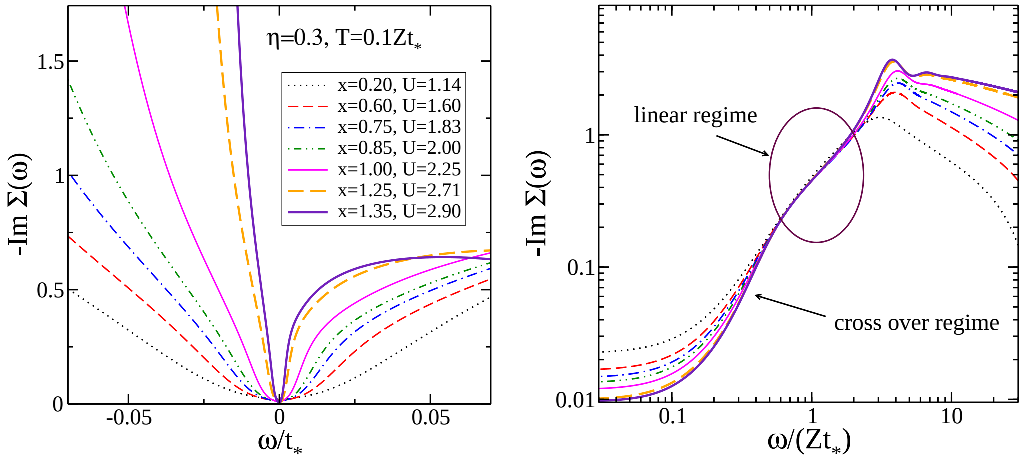

(a) (b)

Fig. 6.9: (a) Behavior of the imaginary part of the self-energy as a function of frequency at finite temperature $T = 0.1Zt_*$ and asymmetry $\eta = 0.3$ for various interaction strengths (see legends). There are small quadratic (Fermi liquid) regimes and wide linear regimes (marginal Fermi liquid) (b) The same in logarithmic scale. The slope is 1 in (i.e. linear) the encircled region signifying marginal Fermi liquid behavior. The linear regimes are universal as frequency axis is scaled by Zt_* and they emerge through a crossover from Fermi liquid or non-linear regimes. The slopeless regimes at very low frequency arise due to presence of finite imaginary part of the self-energy at finite temperature.

constant, and $x = \max(|\omega|, \mathrm{T})$. We must note that the momentum ($\mathbf{k}$) dependence has been ignored in this hypothesis. Therefore our DMFT approach could be relevant, as it has $\mathbf{k}$-independent self-energy too, to test whether the linear or quasi-linear behavior in the temperature dependence of resistivity near a doped Mott insulator arises due to linear behavior of $\mathrm{Im}\Sigma(\omega)$ as prescribed in Eq. (6.1). From Fig. 6.9 (a) we see that indeed $\mathrm{Im}\Sigma(\omega)$ has a linear regime just after a small quadratic regime that is expected from a Fermi liquid. The linear regime is more pronounced in one side of the Fermi liquid due to presence of asymmetry. Fig. 6.9 (b) depicts the same in logarithmic scale. The slope is unity at the linear regime (encircled in the figure) which appears after a crossover from a Fermi liquid regime (slope ~ 2). Moreover, as a surprise, the linear regime is universal as the frequency is scaled by $\omega_L = Zt_*$. Similarly when the frequency is small compared to temperature $\omega < T$, according to Eq. (6.1), $\mathrm{Im}\Sigma(\omega)$ should be linear in T. We verify this in Fig. 6.10, where we kept $\omega = 0$ so that it is always less than T, Fig. 6.10 (a) shows a linear-T behavior that extends up to $T \sim Zt_*$ (though there exists a very small T^2 regime that is not prominent in the figure). Fig. 6.10 (b) shows a log-scale analysis, when fitted with a power law, shows a crossover from T^2-regime (slope close to 2) a T-linear regime (slope close to 1). Similar crossover analysis of the resistivity on the log-scale is shown in Fig. 6.11. Thus our results establish a possible scenario where the spin-fluctuation dynamics can give rise to a marginal Fermi liquid which may be responsible for the linear temperature dependence in resistivity observed in the “normal” state of cuprate superconductors. One more interesting thing we observe is that when we scale $\rho(T)$ by the low energy scale $\omega_L = Zt_*$, all low-T curves collapse to a single curve. This certainly indicates a universal feature at low-T which does not depend on the interaction strength (see Fig. 6.11) and we believe that it arises due to the universality of the linear

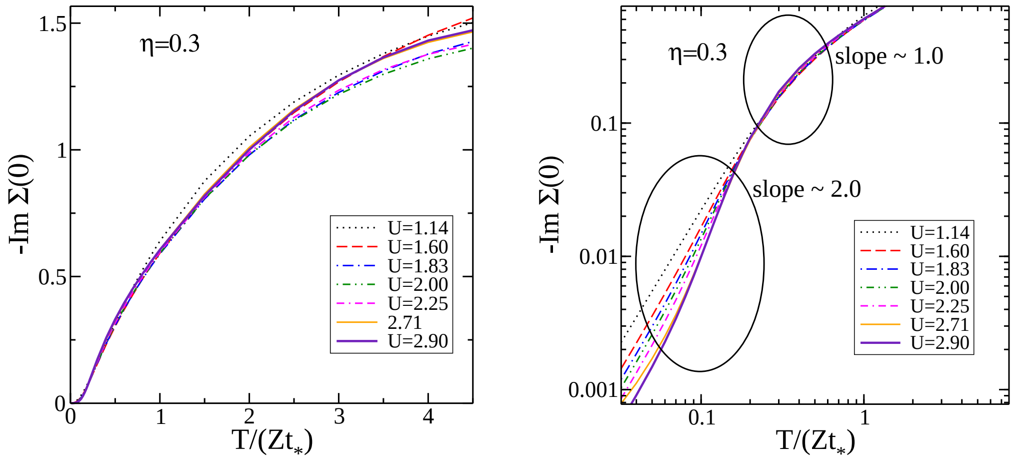

(a) (b)

Fig. 6.10: (a) Behavior of the imaginary part of self-energy $\Sigma(\omega)$ at the Fermi level ($\omega = 0$). At low temperature a linear regime observe (up to $T \sim Zt_*$). The T^2 behavior occurs at very low temperature (almost zero). (b) Plotting on the log-scale shows that there exist a cross-over from a T^2 regime (slope=1.92) to a linear-T regime (slope=1.01).

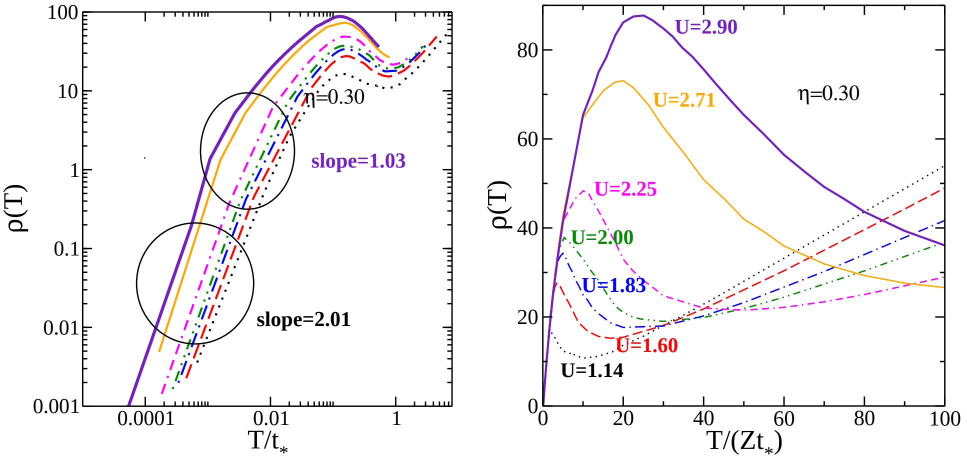

(a) (b)

Fig. 6.11: (a) Crossover from T^2 regime to a T-linear regime in the resistivity plotted as a function of temperature (in units of t_* for different interaction strengths and a fixed asymmetry $\eta = 0.30$. Legends are the same as shown in (b). (b) Low temperature scaling collapse of resistivity for $\eta = 0.3$ for various U/t_* ($t_* = 1$).

regime in $\text{Im}\Sigma(\omega)$ as shown in Fig. 6.9 (b). It is also seen that the resistivity peak shifts to higher multiples of ω_L with increasing U (see Fig. 6.11 (b)).

This result is in stark contrast to that found in IPT, where the resistivity peak became universal when plotted as a function of T/ω_L. As we had seen in chapter 4, the strong coupling scaling regime in the spectra extended a long way almost until the pseudogap adjacent to the Fermi level resonance. With increasing U, the lower and the upper gap edges get pushed out when the spectra are plotted as a function of ω/ω_L. So the pseudogap, which is a precursor of the Mott insulating gap in the symmetric case, is a non-universal feature as expected and is centred around $\sim 0.3 - 4t_*$. The resistivity peak, or the conductivity minimum can thus be understood as a lack of available states until the temperature becomes comparable to the upper gap edge. Thus the resistivity peak is related to the pseudogap scale and is hence non-universal as found.

6.3.2 Optical conductivity

We observe the long tail nature in the optical conductivity, like the symmetric case, in the optical conductivity for a fixed U/t_* ($U/t_* = 1.60$ in Fig. 6.12) and different temperatures. In several optical experiments in cuprates, such long tails have been found with $\sigma(\omega) \sim 1/\omega^p$ at large frequencies [120–122] with p varying from 0.3 to 1. Varma *et al* [72] also showed that a marginal Fermi liquid self-energy can give rise to a long tail with ω^{-p} behavior. Fig. 6.12 (a) shows that indeed such a long tail behavior is observed till very high frequency and the tails are universal similar to that we obtain for the symmetric case

(*Cf.* Fig. 5.6(b)). By plotting in the logarithmic scale, we find the exponent to be $p \simeq 0.55$ (see Fig. 6.12 (b)). Thus though the long tail feature follows a power law behavior, it is not clear whether this arises due to spin-fluctuations that has been incorporated in the LMA or the marginal nature of the self-energy.

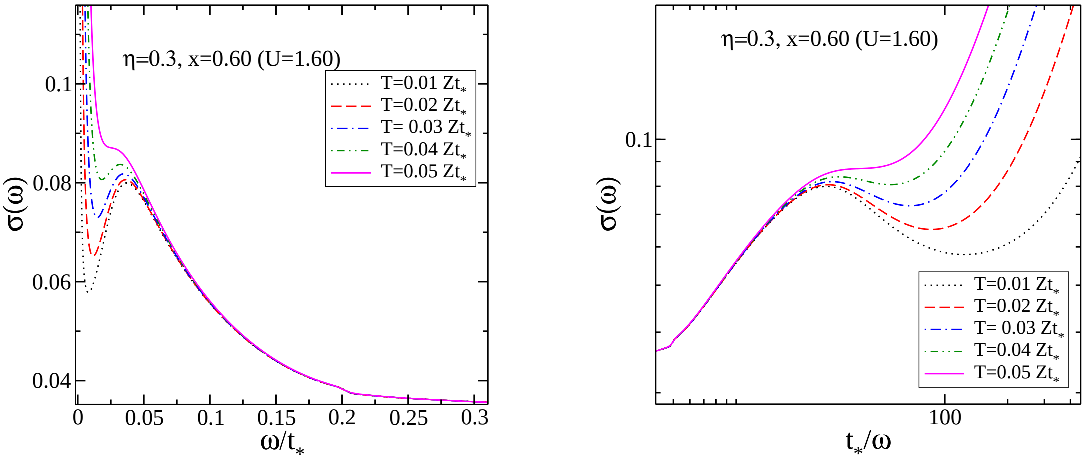

(a) (b)

Fig. 6.12: (a) Optical conductivity with frequency. Long universal tail is observed at high frequency. (b) Optical conductivity with inverse frequency in the logarithmic scale. The power law fit gives $p \simeq 0.55$ (see text).

6.4 Internal energy and specific heat

Again similar to the symmetric case, the internal energy shows monotonically increasing behavior as temperature is increased (see Fig. 6.13(a)). The specific heat shows linear behavior with temperature at low value (see Fig. 6.13(b)). However, the scaling collapse, when the specific heat is scaled by Zt_*, happens for a small region (up to $T \sim 0.1\, Zt_*$) compared to the symmetric case (see Fig. 6.13(c)). This is expected since the Fermi liquid regime is quite small in this case.

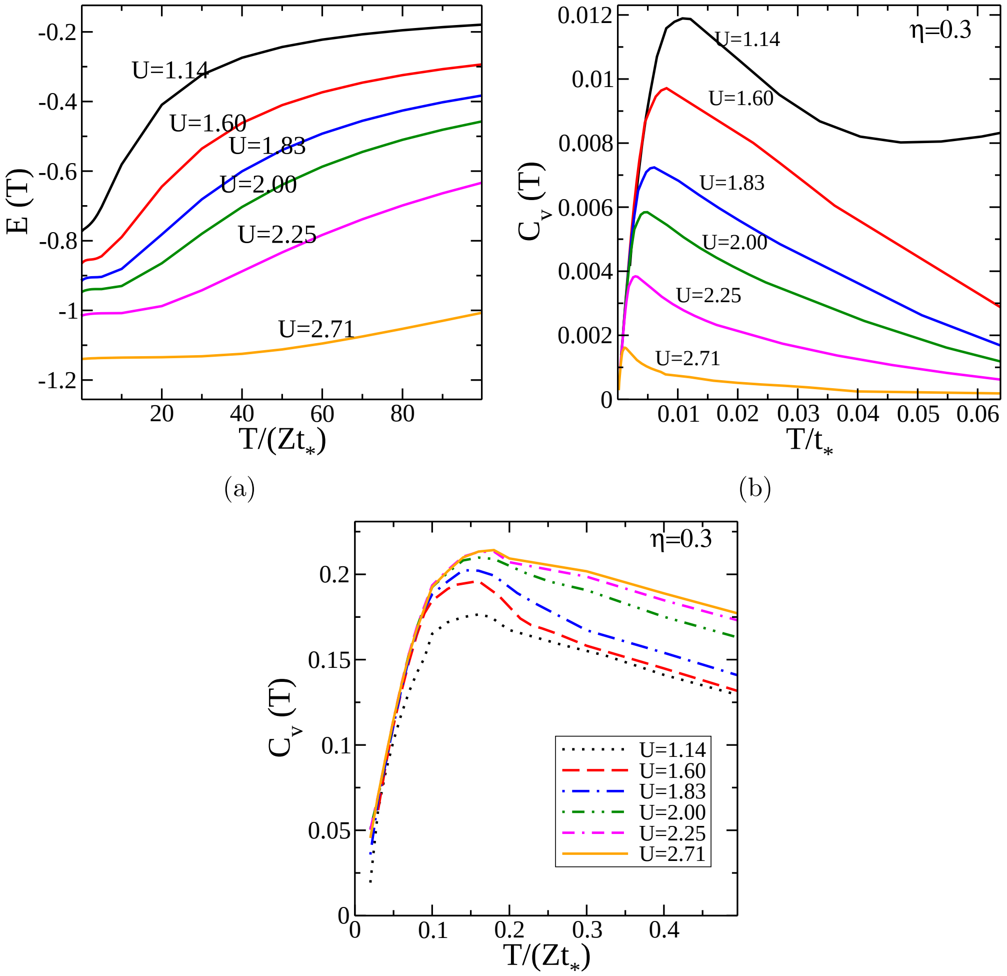

(a) (b)

(c)

Fig. 6.13: (a) Internal energy, (b) specific heat, and (c) scaled specific heat as functions of temperature for a fixed $\eta = 0.3$ and different U/t_* (=1.14, 1.60, 1.83, 2.00, 2.25, and 2.71). The scaling collapse exists up to $T \simeq 0.1Zt_*$.

6.5 Summary

In this chapter, we study the most celebrated regime of the infinite dimensional Hubbard model, where particle-hole symmetry has been broken and system is driven by temperature, interaction and asymmetry. We show that at interaction strength close to a Mott insulator at half-filling, a pseudogap is formed in the spectral density in the close vicinity of the Fermi level. The pseudogap sustains even at very high temperature, whereas the resonance at the Fermi level starts decreasing in height with temperature and finally disappears.

In the transport calculation, the resistivity shows a wide range of linear dependence on temperature for various interaction. The Fermi liquid T^2 behavior is also present, but that exists at extremely low temperature. We explain this behavior through a crossover from a small Fermi liquid regime to a marginal Fermi liquid (MFL) (as proposed by Varma *et al* [72] for the normal state of the high-T_c superconductors). This MFL behavior arises due to special functional dependence of the imaginary part of the self-energy on both frequency and temperature (Eq. (6.1)). Our DMFT calculation is quite relevant since Eq. (6.1) does not possess any momentum dependence like the case we have for infinite dimensions. We also see that, coming from a metallic side decreasing doping enhances the MFL regime, i.e. resistivity has larger linear regime at smaller doping. This is similar to the case of approaching from the overdoped Fermi liquid side to the optimal doped marginal Fermi liquid side in cuprates. In the optical conductivity, we observe a long tail showing $1/\omega^p$ power law decay, which can also arise due to the marginal nature of self-energy. We conclude by saying that the spin-flip scattering that is inherent in the LMA implementation could be responsible for the emerging MFL behavior.

Finally we show that internal energy has a monotonically increasing behavior similar to the symmetric result. However, we lack a good scaling collapse and universal crossing point due to presence of a very small Fermi liquid regime.

Chapter 7

Hysteresis and avalanches: inhomogeneous non-equilibrium Mott transition

7.1 Introduction

As mentioned in Chapter 0, the hysteresis found in the resistivity/conductance measurements in the metal-to-insulator transition (MIT) systems suggests a scenario of non-equilibrium phase transition[1]. Such a non-equilibrium phenomenon cannot be captured through the methods such as DMFT, employed in previous chapters, since it is basically an equilibrium approach. Moreover, IPT or LMA, in its present form, cannot capture the phase separated metallic and insulating domains, as shown in Fig. 10 in Chapter 0. However, in

---

[1] Note that *phase transitions* commonly refer to changes of phases within thermodynamic equilibrium.

this chapter, we propose a theoretical model, which macroscopically takes a non-quantum point of view in purpose to describe the non-equilibrium nature of the MIT. This is in the same spirit like the Ising model can be a suitable model to study the ferromagnetic to paramagnetic phase transition even though magnetism is quantum by its origin.

7.2 General theory of hysteresis

Hysteresis can occur during a phase transition when the free energy of the associated system develops many multiple valleys or local minima (see Fig. 7.1). The system may get stuck in one of these local minima and hence it reaches a stable state for a time span smaller compared to the time required to reach the actual equilibrium, which is the true global minimum. Such a short-time, compared to true equilibration time, could be long enough as an experimental measurement depending on the time scale of the dynamics of the system. Such a *quasi*-equilibrium state is known as a *metastable* state. In that sense, hysteresis can occur only in the case of discontinuous or first-order transition since a continuous phase transition never allows multiple solutions for the minimization. It is worth mentioning that hysteresis can arise even without system encountering metastable states, e.g. in case where the system is driven through an irreversible process due to dissipation or an extra phase is generated after a complete cycle or in case where the system has a unidirectional property (e.g. diodes or other rectifiers, Schmitt triggers).

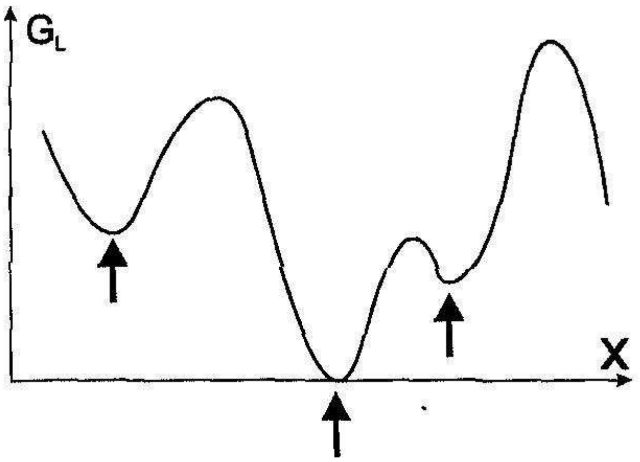

Fig. 7.1: Free energy with multiple local minima parametrized by X. Courtesy: *Hysteresis in Magnetism* by Bertotti [63].

7.3 Role of inhomogeneity

Inhomogeneity can arise in a sample in two ways. First, a sample can have several phase separated regions or domains. This may happen when some of the domains stick to their metastable states and hence cannot undergo a phase transition. The second kind of inhomogeneity is caused due to impurities or disorder, which are omnipresent in any real material. Such disorder in general is random and *quenched*, i.e. the distribution is temperature independent. In the other case, i.e. for *annealed* disorder, the systems get enough time to equilibrate and follow a grand-canonical distribution, which is temperature dependent (for detailed discussion see Ref. 123). The presence of quenched disorder can be a possible reason for observing *athermal* transition (thermal fluctuations do not affect significantly) in many non-equilibrium experiments, typically in acoustic emission in martensite transitions [124, 125] and in magnetic hysteresis experiments [124, 126].

7.4 Theoretical model for magnetic hysteresis and avalanches

Not only the hysteresis itself, the avalanches or the Barkhausen noise in ferromagnets signify non-equilibrium dynamics of domain flipping (see Fig. 9) in the course of driving an external magnetic field. In previous approaches, the Preisach model and Stoner-Wohlfarth [127] model served as mathematical models and have successfully been applied to hysteresis in real materials. Moreover, the Preisach model can also produce avalanches. However, these models fail to capture the rate dependent and non-equilibrium stochastic features in the hysteresis phenomena. Micromagnetic models based on energetics of magnetic materials [63, 128] is also one of them. In 1990, Alessandro, Beatrice, Bertotti, and Montorsi proposed a random energy model with a pinning field, widely known as the ABBM model [129, 130] in the framework of Langevin theory that involves domain wall dynamics. The ABBM model quite successfully describes the Barkhausen noise and shows power law behavior in the noise spectrum.

Despite these stochastic dynamic models, a microscopic spin model has been needed since spins are the microscopic entities that lead to magnetism and magnetic domains. The random-field Ising model (RFIM) is such a model that has been widely studied in the context of spin glass system [131]. Sethna and his co-workers [73, 74, 132] have successfully and extensively used this model to investigate the noise/avalanche study in ferromagnets and in many other systems. The RFIM Hamiltonian is written as

$$\mathcal{H} = -\sum_{<ij>} J_{ij}\, S_i S_j - \sum_i (H + h_i) S_i \tag{7.1}$$

where J_{ij} is the exchange interaction between spins at site i and j. H is a homogeneous external magnetic field and h_i is the random disorder at site i. The disorder distribution is usually chosen to be normal, i.e. one with a Gaussian probability: $P(h) = \exp(-h^2/2\Delta^2)/(\sqrt{2\pi}\Delta)$. The standard deviation, Δ serves as a strength or measurement of the disorder. The critical behavior of the RFIM has been investigated from two directions: (i) The renormalization group (RG) approach [133, 134] and (ii) numerical methods using Monte Carlo algorithm [73,135]. In both methods a power law behavior has been found in the avalanche distribution and the associated exponents have been studied in different dimensions (mostly 3d). The effect of random field can be understood qualitatively from a mean-field picture though the RG study predicts $d = 6$ to be the upper critical dimension. In the mean-field picture, each spin S_i feels an effective or local field $H_{\text{eff}} = -(J\sum_{<ij>} S_j + H + h_i)$. The external field is ramped from large negative value to a large positive value. The spin initially takes the sign of the local field and as the external field is ramped further it causes the spin to flip when H_{eff} changes sign. Now due to the presence of nearest neighbor interactions among the spins, a flipping spin can cause one or more neighbor spins to flip as well and hence it leads to an avalanche of spin flips.

For small values of disorder Δ, the first few spin flips are prone to cause a large avalanche whose size is comparable to system size. On the other hand, large Δ may let some of the spins “pinned” to their site unless the external field crosses a critical value. Thus in the first case, we see one single large avalanche to cause magnetization reversal whereas in the second case, the magnetization will change smoothly with small avalanches. These two regimes are separated by a critical disorder Δ_c and at this value, we expect a true power law divergence in the avalanche size distribution (see Fig. 7.2).

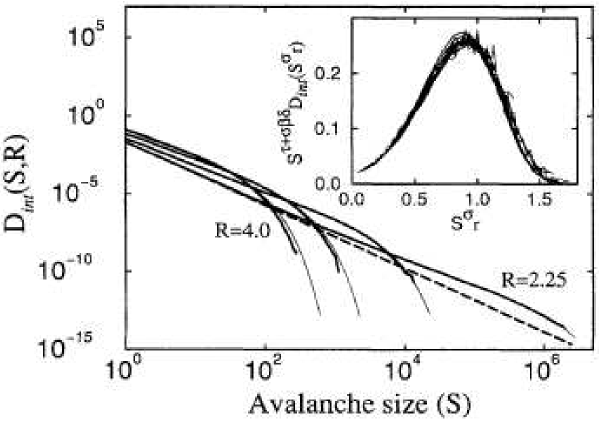

Fig. 7.2: Avalanche size distribution curves of the RFIM in 3d (from Ref.73). For disorder $R < 2.25$ ($J = 1$), we see a true power law behavior (linear on log-log plot) for all sizes. Critical disorder for 3d has been estimated (extrapolated dashed line) to be $R_c = 2.16$. The inset shows the scaling collapse by choosing proper scaling variables (not discussed in the text). Note that we use Δ to denote disorder instead of R for a specific reason.

7.5 Geometry of metastable ‘phase diagram’ and thermal hysteresis

We notice that the hysteresis that we often encounter happens due to change in the external magnetic field. Thermal hysteresis in ferromagnets may be a rare phenomenon in ferromagnets, whereas in contrast, we find both thermal and field hysteresis in MIT systems with IPT and also in experiments on V_2O_3 , VO_2 , and several manganites [136]. Here we propose that such a contrast can be explained by simply looking at the shape of the metastable 'phase diagrams'. We should be careful that they are not phase diagrams in true sense (hence we are keeping the phrase within a quotation mark) as phase diagrams are normally constructed for the equilibrium states.

We look at the temperature-field 'phase diagram' that contains two spinodal lines (transition line 1 and 2) around the metal-insulator coexistence regime (see Fig. 7.3, left panel). We can easily understand the reason of

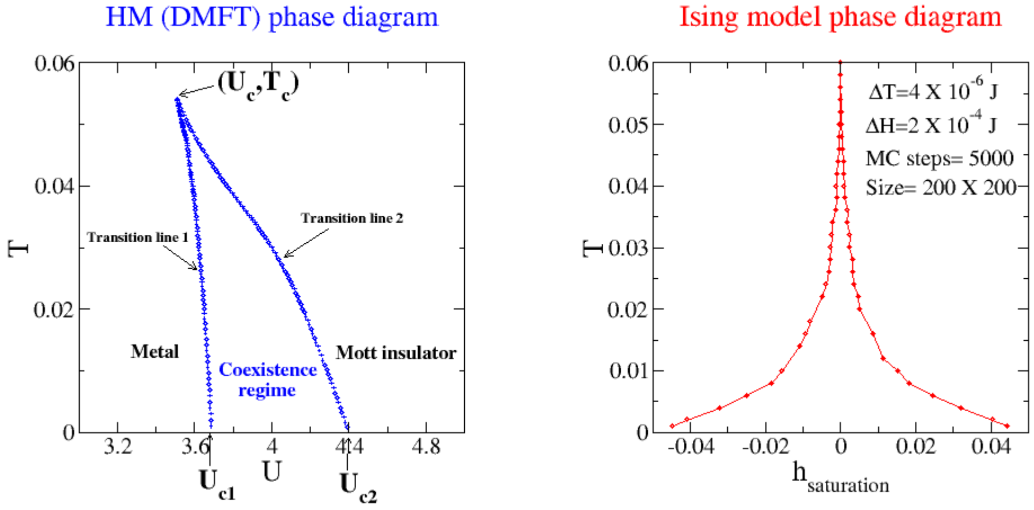

(a) (b)

Fig. 7.3: The phase diagram of (a) the Hubbard model (HM) from DMFT calculation using IPT as an impurity solve and (b) the Ising model from Monte Carlo calculation. The shape of the phase diagram explains why thermal hysteresis is generally not observed in ferromagnets (see text for details).

occurrence of thermal hysteresis in the MIT system, generally not found in ferromagnets, if we carefully examine the shape or geometry of the spinodal lines. Hysteresis happens when the system is driven by a field or temperature and it crosses two spinodal lines or phase transition lines. When the driving force is increased the system enters into the coexistence regime after crossing the transition line 1. The coexistence regime is defined as the region where system can have two metastable solutions (metallic/insulating for the MIT systems, positive/negative magnetization for the Ising ferromagnets) of the free energy. Therefore the system remains in the metastable metallic or negative magnetization state (local minimum of the free energy) even there exists a stable insulating/positive magnetization in the coexistence regime unless the thermal fluctuation helps the system to cross the barrier and to reach the actual equilibrium solution (global minimum) of the free energy. In the same way, when the system is driven by decreasing the field from the higher end (insulating/positive magnetization) it enters into the coexistence regime by crossing the transition line 2 and it denies the transition (which would happen when the system acquires the global minimum) and decides to get stuck into the insulating/positive magnetization metastable state. Thus the coexistence regime plays a crucial role to the system to choose different metastable states while the driving 'force' is applied in different directions and hence hysteresis arises.

Now we generalize this fact by saying that hysteresis occurs only when the system finds two different entries to the coexistence regime in the course of being driven by increasing and decreasing the field. In other word, crossing of two transition lines or spinodal lines, which make the boundary of the coexistence regime, is essential for occurrence of hysteresis. We can see from

Fig. 7.3 that crossing two spinodal lines can happen for both MIT and ferromagnets when the system is driven by an external field (pressure/interaction and magnetic field respectively). However, while changing the temperature may cause hysteresis in the former only since the system crosses only one and same spinodal lines in the latter when temperature is increased or decreased. Thus we can see that shape of the coexistence regime is responsible for the absence of thermal hysteresis in ferromagnets and the presence of the same in MIT systems, e.g. V_2O_3 and VO_2 .

Though temperature and external field are different variables of any thermodynamic system, in non-equilibrium and for an athermal transition, both can be treated with equal footing. In other words, we will argue that temperature takes on the role of a field and the thermal fluctuations expected due to finite temperature are negligible. This concept is essential to build up our theoretical formulation in the forthcoming section.

7.6 Can we address critical phenomena and hysteresis together?

Hysteresis is generally associated with first order or abrupt phase transition. However, disorder can introduce a critical fluctuation near a critical disorder strength [74]. This large fluctuation results in divergence in the correlation length which can set in a power law behavior in the distribution of avalanche size. So even though the hysteresis deals with the first order phase transition, presence of disorder can lead the system to another regime of criticality and

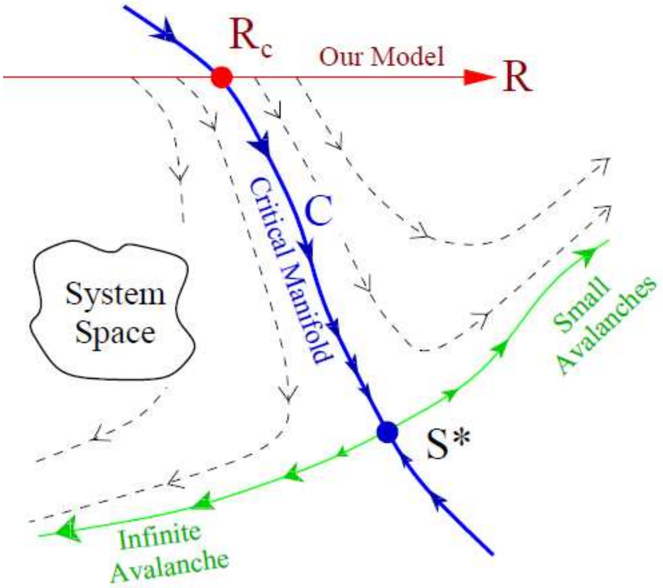

Fig. 7.4: Renormalization group (RG) flow diagram for the RFIM. The fixed point S^* separates the phases with infinite avalanches and small step-like avalanches and hence it is sitting at the critical disorder value R_c. Image is reproduced from Ref. 74.

we can expect usual scaling and power law and finally look for the universality class the system may belong to.

Perković, Dahmen and Sethna [73] simulated the RFIM by using Monte Carlo (MC) method with a Gaussian distribution for the disorder of width R. They found the critical disorder value $R_c = 2.16$ for 3D (in the unit of J, i.e. $J = 1$). Above R_c, the power law is obeyed 50 % above R_c. Sethna group [74] argued for the phase transition (though may not be envisaged as a change in order parameter) in term of renormalization group (RG) flow diagram (see Fig. 7.4). There is a critical manifold which flows toward the fixed point and separate the phases having infinite, system-spanning and small finite avalanches.

7.7 Percolation picture: resistor network model

The metal to insulator transition, as a function of field or temperature, can be viewed as a percolation of physical domains of one over the other. Evidence of such physical domains had been found earlier in manganites [82, 136] and recently on VO_2 thin film.

Now the percolation theory has been well studied in last few decades which can be physically imagined as punching holes in a conducting sheet and the holes grow up or percolate with time. This percolation dynamics is useful in proposing the phenomenon in our context since it also produces power law behavior as it has been studied through a random resistor network model (RRN) [137, 138]. However, a simple percolation theory may not be successful, as it is based on probability of conduction paths, to describe domain flipping and pinning depending on the associated free energy barrier. Nevertheless, we wish to built a similar resistor network model which denies any explicit randomness in the resistances in the network. The randomness enters through the random field h_i of the RFIM once we map the up/down spins to high/low resistances. We put a contrast ratio C in order to define the high (insulating) R_{ins} and low (metallic) resistances R_{met}, i.e.

$$C = R_{\text{ins}}/R_{\text{met}} \tag{7.2}$$

Thus it seems legitimate to expect a power law in the MIT system, as experimentally found in VO_2 thin film by the Sharoni group [62].

Moreover, we may expect two different kind of transitions when the contrast ratio is very high ($C \gg 1$) and very low ($C \ll 1$). When $C \gg 1$, we can expect insulating domains to grow up over the metallic regime and we should expect several small jumps or avalanches to happen in the resistivity or conductivity measurement. On the contrary, at low contrast ratio ($C \ll 1$) which occurs near the critical point, the percolation picture holds no longer and one small avalanche may be expected (since the hysteresis loop becomes narrower). However, it is not clear that resistivity will increase in the same way as magnetization does in ferromagnets since the resistances are intensive or non-additive quantity in contrast to magnetization. Therefore, it may differ in the exponent in the power law (if observed) from the same in ferromagnets. This is the sole purpose of doing this model separately from the studied RFIM and RRN since the exponents do no match close to the mentioned experiment. Also we believe, the exponent may vary as we change the contrast ratio or disorder strength and thus our approach should propose different exponents which may vary with different samples.

7.8 Theoretical model for metal-insulator systems: RFIM mapped to a resistor network

Here use propose a mapping, as earlier used by Erica *et al* [139], where a RFIM is mapped to a resistor-network with resistance anisotropy that arises due to different orientations of nematic ordering of electrons observed in high-T_c cuprates. Such a mapping can be generalized to any material having two distinct phases and having quenched disorders, e.g. metal-insulator systems, martensitic transition systems etc.

Since a direct mapping of a lattice-gas [140] model to an Ising Hamiltonian exists, it could be possible to think of a lattice-gas model for the metal-insulator system[2] (discussed in the next section). Similarly using RG scaling arguments, Kirkpatrick and Belitz have shown that Anderson-Mott MIT [141] can be mapped to RFIM problem. Recently Papanikolau *et al* [142] have used a method where they mapped the metal-insulator conductivities in terms of Ising spin variables and then solving the conductivity by applying Kirchhoff's law or by Franck-Lobb algorithm.

7.9 Lattice-gas model

To look for a connection between the metal-insulator, we propose a lattice-gas model [140, 143]. Let us imagine a specific sample undergoing a Mott transition as a function of temperature. The bulk of the sample would in general have a network of coexisting metallic and insulating islands. We discretize this sample into a lattice of cells, and define a variable n_i for any cell i, which takes the values 1 and 0 depending upon whether the cell comprises a metallic or an insulating phase respectively. In such a coarse-grained description, there are four possible configurations for the n_i variables of any two nearest neighbor cells. They are $(n_i,\ n_j)$ = (1, 1), (1, 0), (0, 1) and (0, 0). Among these, we argue that only the (1, 1) combination leads to a lowering of the energy, while the other three neither raise nor lower the total energy of the system. The proximity of two metallic cells ((1, 1)

---

[2] Suggested by D. E. Logan (Oxford).

combination) leads to a tunnelling of electrons from one cell to the other thus leading to a kinetic energy or a delocalization energy gain. It is easy to see that such a gain does not occur for any other combination. Thus we may write the lattice-gas Hamiltonian for this discretized system in the grand canonical ensemble as

$$H = -K \sum_{<ij>} n_i n_j - \mu \sum_i n_i \tag{7.3}$$

Here K and μ represent the K.E. gain and chemical potential respectively. The latter is, in general, pressure/temperature dependent and should be interpreted as the gain in total energy upon flipping an insulating cell to a metallic cell. Now, a simple bilinear transformation such as $S_i = 2(n_i - 1/2)$ leads to a change of variables and yields an Ising model in a magnetic field:

$$H = -J \sum_{<ij>} S_i S_j - H \sum_i S_i + h_0 \tag{7.4}$$

where the exchange coupling $J = K/4$, the field $H = (zK + \mu)/2$ and the constant $h_0 = -Kz/4 - \mu N/2$. The numbers z and N are the coordination number and total number of cells respectively. In real materials, disorder exists in various forms such as substitutional defects or vacancies, impurities, grain boundaries, etc. Such disorder is usually quenched and acts as nucleation centers for the metastable phases giving rise to coexistence of the stable and the metastable phases across the first order transition. In the lattice gas description, disorder would play a role in randomizing the delocalization energy gain as well as the chemical potential. Thus, in general, K

must be K_{ij} and μ must be μ_i reflecting the dependence on the inhomogeneous quenched disorder. This would manifest in the Ising model as random exchange and random field. If we ignore the randomness in the exchange term, we get the well-known RFIM as a phenomenological model of a first order metal-insulator transition in the presence of quenched disorder

$$H = -J \sum_{<ij>} S_i S_j - \sum_i (H + h_i) S_i \tag{7.1}$$

In the above, h_i is a small random field that is, in practice, picked from a Gaussian distribution centered at zero and having a width that represents the disorder strength in the material. Given a specific K and μ, we should be able to, through a simple Monte-Carlo simulation of the RFIM for example, describe the positions of the metallic and insulating phases for a given disorder configuration. With the metal-insulator network thus determined, a mapping to a bimodal resistor network and its solution through Kirchhoffs equations would yield the macroscopic transport properties of this inhomogeneous system. In order to understand the parameters of the RFIM, we need to make connection to a microscopic model.

Sharoni *et al* found a power law distribution , $p(A) \propto A^{-\alpha}$ for avalanche size A averaged over several hysteresis loops (see Fig. 7.5, linear in logarithmic scale). By using the maximum likelihood method [144, 145] they found $\alpha = 2.48 \pm 0.05$. This power law behavior certainly provokes us to think of a percolation process of one domain over the other. Evidence of such a percolation has been observed in early VO_2 thin-film experiments [64]. Sharoni group also found a linear relation when they plotted the largest avalanche (jump) against the inverse of device length (see Fig. 7.9(b)) . This may imply that observable avalanches in hysteresis may occur due to a finite size effect (in the thermodynamic limit we should expect smooth curves). They did numerical simulation for their experimental finding by using an effective medium approximation. However, neither they found an agreeable inverse device length scaling nor a good power law fit for the jump distribution. Therefore we may need to look for a different numerical scheme which we have proposed earlier.

7.10 The resistor network

Now we describe the way we construct the resistor network and implement to the numerical computation. Let us consider that the lattice size is $L_x \times L_y$ with four resistors at each lattice point. Here for our convenience, we

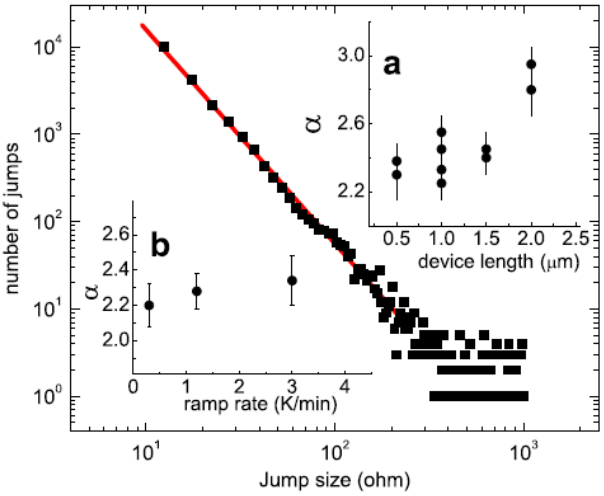

Fig. 7.5: Power law behavior in the resistance jump observed in VO_2 thin films as mentioned in Ref. 62. Inset shows the power law exponent α dependence on the device length size.

distinguish two kinds of resistor, horizontal (R_H) and vertical (R_V). Thus a (i, j) site is connected to 2 R_H's and 2 R_V's. Similarly the sites in the neighborhood ($(i-1, j)$, $(i+1, j)$, $(i, j-1)$, and $(i, j+1)$ sites) consists of 2 horizontal and 2 vertical resistors. Thus eventually between any two lattice points two resistors sit together in a series connection, i.e.

(i) $R_{H\,i\pm1,j}$ and $R_{H\,i,j}$ sit between sites $(i\pm1, j)$ and (i, j) where $i \in [1, L_x - 1]$ and $j \in [1, L_y]$.

(ii) $R_{V\,i,j\pm1}$ and $R_{V\,i,j}$ sit between sites $(i, j\pm1)$ and (i, j) where $i \in [2, L_y - 1]$ and $j \in [1, L_x - 1]$.

$i = 1$ and $i = L_x$ have connections to leads and for convenience, we consider that the left lead has a bias V while the right lead is grounded. So $i = 0$ points are not parts of the lattice, but merely connections to the bias. Now according to Kirchhoff's current law, the total current in a junction should be zero. For example, current at site (i, j), with coordination number, $z = 4$

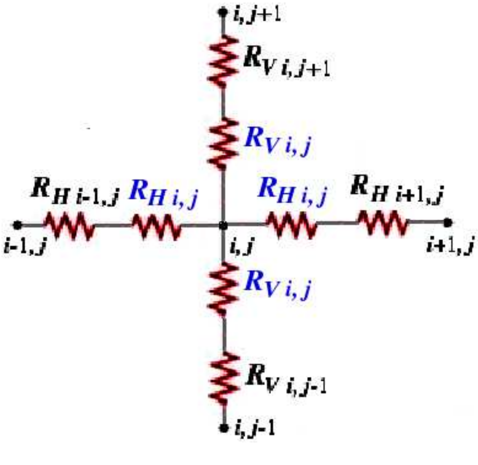

Fig. 7.6: Schematic diagram of a junction with $z = 4$.

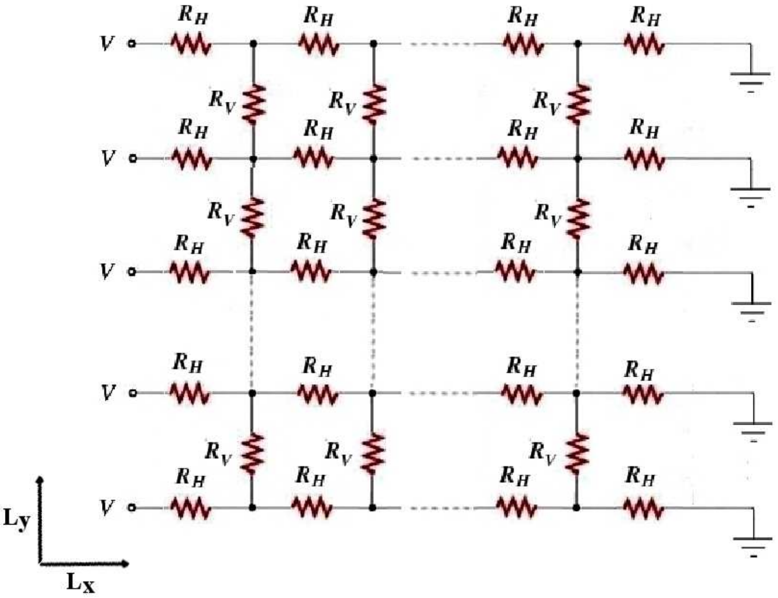

Fig. 7.7: Schematic diagram of a resistor network. Note that, though the resistors are labelled by the same name (R_H for horizontal, R_V for vertical) their value varies from site to site in the 2-dimensional network.

(number of resistors connected to the site, see Fig. 7.6):

$$I_{ij} = \frac{V_{i-1,j} - V_{i,j}}{R_{H\,i,j} + R_{H\,i-1,j}} + \frac{V_{i+1,j} - V_{i,j}}{R_{H\,i,j} + R_{H\,i+1,j}} + \frac{V_{i,j-1} - V_{i,j}}{R_{V\,i,j} + R_{V\,i,j-1}} + \frac{V_{i,j+1} - V_{i,j}}{R_{V\,i,j} + R_{V\,i,j+1}} = 0\,. \tag{7.5}$$

Similarly Kirchhoff's equations for other coordination numbers ($z = 2$ at corners, $z = 3$ at non-corner edges). We shall write all such equations now.

i. **Left bottom corner point ($i = 1,\ j = 1$)**

$$\frac{V - V_{1,1}}{R_{H\,1,1}} + \frac{V_{2,1} - V_{1,1}}{R_{H\,1,1} + R_{H\,2,1}} + \frac{V_{1,2} - V_{1,1}}{R_{V\,1,1} + R_{V\,1,2}} = 0 \tag{7.6}$$

ii. **Left non-corner edge point** ($i = 1,\ j = 2$ **to** $L_y - 1$)

$$\frac{V - V_{1,j}}{R_{H\,1,j}} + \frac{V_{2,j} - V_{1,j}}{R_{H\,1,j} + R_{H\,2,j}} + \frac{V_{1,j-1} - V_{1,j}}{R_{V\,1,j} + R_{V\,1,j-1}} + \frac{V_{1,j+1} - V_{1,j}}{R_{V\,1,j} + R_{V\,1,j+1}} = 0 \tag{7.7}$$

iii. **Left top corner point** ($i = 1,\ j = L_y$)

$$\frac{V - V_{1,L_y}}{R_{H\,1,L_y}} + \frac{V_{2,L_y} - V_{1,L_y}}{R_{H\,1,L_y} + R_{H\,2,L_y}} + \frac{V_{1,L_y-1} - V_{1,L_y}}{R_{V\,1,L_y} + R_{V\,1,L_y-1}} = 0 \tag{7.8}$$

iv. **Bottom non-corner edge point** ($i = 2$ **to** $L_x,\ j = 1$)

$$\frac{V_{i-1,1} - V_{i,1}}{R_{H\,i,1} + R_{H\,i-1,1}} + \frac{V_{i+1,1} - V_{i,1}}{R_{H\,i,1} + R_{H\,i+1,1}} + \frac{V_{i,2} - V_{i,1}}{R_{V\,i,1} + R_{V\,i,2}} = 0 \tag{7.9}$$

v. **Top non-corner edge point** ($i = 2$ **to** $L_x,\ j = L_y$)

$$\frac{V_{i-1,L_y} - V_{i,L_y}}{R_{H\,i,L_y} + R_{H\,i-1,L_y}} + \frac{V_{i+1,1} - V_{i,L_y}}{R_{H\,i,L_y} + R_{H\,i+1,L_y}} + \frac{V_{i,L_y-1} - V_{i,L_y}}{R_{V\,i,L_y} + R_{V\,i,L_y-1}} = 0 \tag{7.10}$$

vi. **Right top corner point** ($i = L_x,\ j = L_y$)

$$\frac{V_{L_x-1,L_y} - V_{L_x,L_y}}{R_{H\,L_x,L_y} + R_{H\,L_x-1,L_y}} + \frac{-V_{L_x,L_y}}{R_{H\,L_x,L_y}} + \frac{V_{L_x,L_y-1} - V_{L_x,L_y}}{R_{V\,L_x,L_y} + R_{V\,L_x,L_y-1}} = 0 \tag{7.11}$$

vii. **Right non-corner edge point** ($i = L_x,\ j = 2$ **to** $L_y - 1$)

$$\frac{V_{L_x-1,j} - V_{L_x,j}}{R_{H\,L_x,j} + R_{H\,L_x-1,j}} + \frac{-V_{L_x,j}}{R_{H\,L_x,j}} + \frac{V_{L_x,j-1} - V_{L_x,j}}{R_{V\,L_x,j} + R_{V\,L_x,j-1}} + \frac{V_{L_x,j+1} - V_{L_x,j}}{R_{V\,L_x,j} + R_{V\,L_x,j+1}} = 0 \tag{7.12}$$

viii. **Right bottom corner point** $(i = L_x,\ j = 1)$

$$\frac{V_{L_x-1,1} - V_{L_x,1}}{R_{H\,L_x,1} + R_{H\,L_x-1,1}} + \frac{-V_{L_x,1}}{R_{H\,L_x,1}} + \frac{V_{L_x,2} - V_{L_x,1}}{R_{V\,L_x,1} + R_{V\,L_x,2}} = 0 \tag{7.13}$$

ix. **Non-border inner point** $(i = 2$ **to** $L_x - 1,\ j = 2$ **to** $L_y - 1)$

$$\frac{V_{i-1,j} - V_{i,j}}{R_{H\,i,j} + R_{H\,i-1,j}} + \frac{V_{i+1,j} - V_{i,j}}{R_{H\,i,j} + R_{H\,i+1,j}} + \frac{V_{i,j-1} - V_{i,j}}{R_{V\,i,j} + R_{V\,i,j-1}} + \frac{V_{i,j+1} - V_{i,j}}{R_{V\,i,j} + R_{V\,i,j+1}} = 0 \tag{7.14}$$

We can rearrange the above equations by collecting the coefficients of V_{ij} with new notations: $\widetilde{R}_{H/V}(i \pm 1, j \pm 1) = R_{H/V}(i,j) + R_{H/V}(i \pm 1, j \pm 1)$

i. **Left bottom corner point** $(i = 1,\ j = 1)$

$$\left[\frac{1}{R_{H\,1,1}} + \frac{1}{\widetilde{R}_{H\,2,1}} + \frac{1}{\widetilde{R}_{V\,1,2}}\right] V_{1,1} - \frac{1}{\widetilde{R}_{H\,2,1}} V_{2,1} - \frac{1}{\widetilde{R}_{V\,1,2}} V_{1,2} = \frac{V}{R_{H\,1,1}} \tag{7.15}$$

ii. **Left non-corner edge point** $(i = 1,\ j = 2$ **to** $L_y - 1)$

$$\begin{aligned} &\left[\frac{1}{R_{H\,1,j}} + \frac{1}{\widetilde{R}_{H\,2,j}} + \frac{1}{\widetilde{R}_{V\,1,j-1}} + \frac{1}{\widetilde{R}_{V\,1,j+1}}\right] V_{1,j} \\ &- \frac{1}{\widetilde{R}_{H\,2,j}} V_{2,j} - \frac{1}{\widetilde{R}_{V\,1,j-1}} V_{1,j-1} - \frac{1}{\widetilde{R}_{V\,1,j+1}} V_{1,j+1} = \frac{V}{R_{H\,1,j}} \end{aligned} \tag{7.16}$$

iii. **Left top corner point** $(i = 1,\ j = L_y)$

$$\begin{aligned} &\left[\frac{1}{R_{H\,1,L_y}} + \frac{1}{\widetilde{R}_{H\,2,L_y}} + \frac{1}{\widetilde{R}_{V\,1,L_y-1}}\right] V_{1,L_y} \\ &- \frac{1}{\widetilde{R}_{H\,2,L_y}} V_{2,L_y} - \frac{1}{\widetilde{R}_{V\,1,L_y-1}} V_{1,L_y-1} = \frac{V}{R_{H\,1,L_y}} \end{aligned} \tag{7.17}$$

iv. **Bottom non-corner edge point** ($i = 2$ **to** L_x, $j = 1$)

$$\begin{aligned}&\left[\frac{1}{\widetilde{R}_{H\,i-1,1}}+\frac{1}{\widetilde{R}_{H\,i+1,1}}+\frac{1}{\widetilde{R}_{V\,i,2}}\right]V_{i,1}\\&\quad-\frac{1}{\widetilde{R}_{H\,i-1,1}}V_{i-1,1}-\frac{1}{\widetilde{R}_{H\,i+1,1}}V_{i+1,1}-\frac{1}{\widetilde{R}_{V\,i,2}}V_{i,2}=0\end{aligned}\tag{7.18}$$

v. **Top non-corner edge point** ($i = 2$ **to** L_x, $j = L_y$)

$$\begin{aligned}&\left[\frac{1}{\widetilde{R}_{H\,i-1,L_y}}+\frac{1}{\widetilde{R}_{H\,i+1,L_y}}+\frac{1}{\widetilde{R}_{V\,i,L_y-1}}\right]V_{i,L_y}\\&\quad-\frac{1}{\widetilde{R}_{H\,i-1,L_y}}V_{i-1,L_y}-\frac{1}{\widetilde{R}_{H\,i+1,L_y}}V_{i+1,1}-\frac{1}{\widetilde{R}_{V\,i,L_y-1}}V_{i,L_y-1}=0\end{aligned}\tag{7.19}$$

vi. **Right top corner point** ($i = L_x$, $j = L_y$)

$$\begin{aligned}&\left[\frac{1}{\widetilde{R}_{H\,L_x-1,L_y}}+\frac{1}{R_{H\,L_x,L_y}}+\frac{1}{\widetilde{R}_{V\,L_x,L_y-1}}\right]V_{L_x,L_y}\\&\quad-\frac{1}{\widetilde{R}_{H\,L_x-1,L_y}}V_{L_x-1,L_y}-\frac{1}{\widetilde{R}_{V\,L_x,L_y-1}}V_{L_x,L_y-1}=0\end{aligned}\tag{7.20}$$

vii. **Right non-corner edge point** ($i = L_x$, $j = 2$ **to** $L_y - 1$)

$$\begin{aligned}&\left[\frac{1}{\widetilde{R}_{H\,L_x-1,j}}+\frac{1}{R_{H\,L_x,j}}+\frac{1}{\widetilde{R}_{V\,L_x,j-1}}+\frac{1}{\widetilde{R}_{V\,L_x,j+1}}\right]V_{L_x,j}\\&\quad-\frac{1}{\widetilde{R}_{H\,L_x-1,j}}V_{L_x-1,j}-\frac{1}{\widetilde{R}_{V\,L_x,j-1}}V_{L_x,j-1}-\frac{1}{\widetilde{R}_{V\,L_x,j+1}}V_{L_x,j+1}=0\end{aligned}\tag{7.21}$$

viii. **Right bottom corner point ($i = L_x$, $j = 1$)**

$$\begin{aligned}&\left[\frac{1}{\widetilde{R}_{H\,L_x-1,1}} + \frac{1}{R_{H\,L_x,1}} + \frac{1}{\widetilde{R}_{V\,L_x,2}}\right] V_{L_x,1} \\ &- \frac{1}{\widetilde{R}_{H\,L_x-1,1}} V_{L_x-1,1} - \frac{1}{\widetilde{R}_{V\,L_x,2}} V_{L_x,2} = 0 \end{aligned} \tag{7.22}$$

ix. **Non-border inner point ($i = 2$ to $L_x - 1$, $j = 2$ to $L_y - 1$)**

$$\begin{aligned}&\left[\frac{1}{\widetilde{R}_{H\,i-1,j}} + \frac{1}{\widetilde{R}_{H\,i+1,j}} + \frac{1}{\widetilde{R}_{V\,i,j-1}} + \frac{1}{\widetilde{R}_{V\,i,j+1}}\right] V_{i,j} \\ &- \frac{1}{\widetilde{R}_{H\,i-1,j}} V_{i-1,j} - \frac{1}{\widetilde{R}_{H\,i+1,j}} V_{i+1,j} - \frac{1}{\widetilde{R}_{V\,i,j-1}} V_{i,j-1} - \frac{1}{\widetilde{R}_{V\,i,j+1}} V_{i,j+1} = 0 \end{aligned} \tag{7.23}$$

Thus we see can set up a vector $\mathbf{V}(i\,, i = 1 \text{ to } L_xL_y)$ and find the components by solving the following matrix eq.

$$\mathbf{GV} = \mathbf{I} \tag{7.24}$$

Where G matrix contains the coefficient which has the dimension of 1/resistance and hence can be called as the *conductance matrix*.

Here j's are rows and i's are columns if we write in a matrix form.

Now we notice that only a few components (maximum 5) contribute to the Eq.s (7.15)-(7.23). Therefore the **G** matrix contains a very few non-zero elements compared to its full dimension $(L_xL_y)^2$, i.e. the matrix is *sparse*. Hence instead of required $\sim 5\,(L_xL_y)^2$ number of processes for the full matrix, we store only the nonzero elements in a *compact row storage* format and use the Intel Math Kernel Library direct sparse solver routine to find the elements of **V**.

The mapping to the linear array can be done with a new index p such that $p = i + (j-1)L_x$, $i \in [1, L_x]$, $j \in [1, L_y]$[3]. Thus we can fill up the lattice by running p from 1 to $N = L_x L_y$ and we fill up first visiting all the columns for the same row, i.e. first run i from 1 to L_x and then update each row by adding 1 to the previous row (we can do the other way as well). If filling is done in this way, then for a given p and j,

$$i = p - (j-1)L_x \tag{7.25}$$

.

We can keep the row (j) fixed while running i by defining

$$j = \lfloor (p-1)/L_x \rfloor + 1\,. \tag{7.26}$$

where $\lfloor x \rfloor$ denotes the floor function of x.

Now we should note that **G** is a $N \times N$ square matrix and **V** is a $1 \times N$ column matrix ($N = L_x L_y$) with no zero elements in general. Therefore the row of **V** will have a nonzero coefficient in the diagonal part of **G** with the same row. Thus we, in practice, visit all the lattice sites since all of them will have nonzero diagonal coefficient of potential in matrix **G**. In the course of

---

[3] Note that in the lattice geometry, i and j indices represent (x, y) coordinates respectively. Therefore in the lattice space, $R_{i,j}$ represents resistances related to the column number i and row number j. However, in a typical *Fortran* program, i and j in a matrix array $R(i, j)$ represent row and column ranks respectively, which have an opposite sense to the lattice representation described here.

this visit, we look for the nearest neighbor sites which will appear as nonzero off-diagonal element in the same row (the row of the central lattice point). The row of the neighborhood point potential (i.e. the rank in the linear array of **V**) will be the column of nonzero off-diagonal elements. This is due to the fact that in the multiplication of matrices **A** and **B**, the column index of **A** must match with the row index of **B**. Thus if **B** is a single column matrix, its row position is enough to determine the multiplying coefficient associated with it.

7.11 Results

We shall try to address three important findings that have been observed in the experiment on VO_2 thin film, viz.

(i) Sample size dependence of the avalanche size.

(ii) Power law behavior of the avalanche size distribution.

(iii) Size dependence of the power law exponent.

In addition to this, we report two other interesting theoretical predictions that need experimental verifications:

(v) Effect of the disorder strength on the avalanche size.

(vi) Effect of the disorder strength on the power law exponent.

7.11.1 Finite size effect

We examine for the system size dependence effect on the avalanche sizes. We can see from Fig. 7.8, as we increase the lattice size from 100 × 100 to 1000 × 100, the avalanche sizes decrease on average and it seems that, at thermodynamic limit, the hysteresis curve becomes completely smooth. Each calculation has been done for a random Gaussian disorder of width

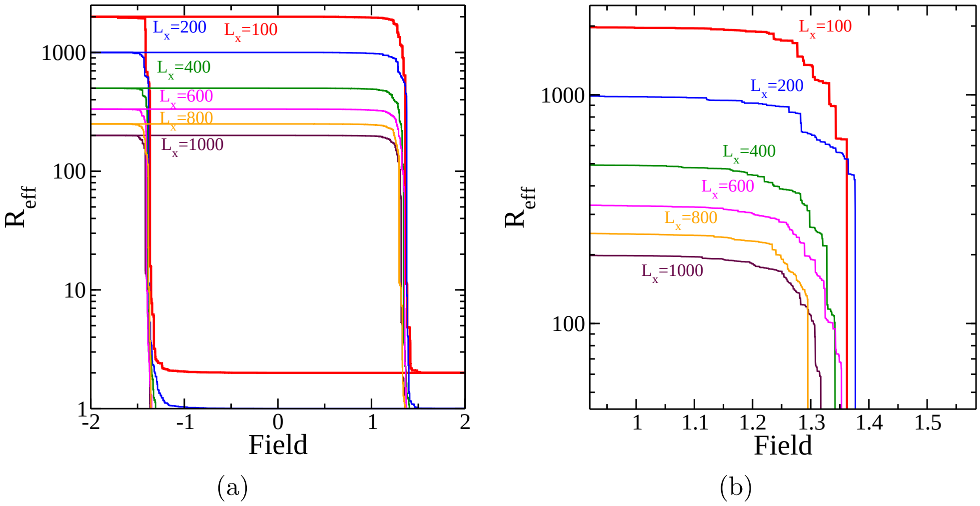

(a) (b)

Fig. 7.8: Lattice size dependence of the avalanches. (a) Hysteresis height changes with changes in the lattice length L_x ($L_y = 100$ is fixed). (b) Close-up view to see that average avalanche size decreases as the system size becomes bigger.

$\Delta = 1.0J$ and the contrast ratio, $C = R_{\text{ins}}/R_{\text{met}} = 1000$. We also notice that the hysteresis height decreases with increase in L_x (Fig. 7.8(a)). Exactly the opposite situation happens when L_y is increased and hysteresis height does not change at all for any square lattice, i.e. $L_x = Ly$ (results not shown here) since the effective resistance of the completely insulating phase (highest resistance in the hysteresis plot) roughly follows the formula

$$R_{\text{eff}} = 2C\, R_{\text{met}} L_x / L_y \tag{7.27}$$

where C is the contrast ratio as mentioned before. We plot the largest avalanche size against L_x (see Fig. 7.9(a)). The inset shows almost a linear dependence when it is plotted against inverse. Such a linear behavior remarkably agrees with the result found by Sharoni *et al* on VO_2 thin films (Fig. 7.9(b)). With a similar quest, we also look at the maximum avalanche size dependence on the device width. It appears that the maximum avalanche size on average does not change significantly (except the size at $L_y = 600$, which we consider to be a point with statistically large deviation). Thus changing width may have a very less influence on the disorder effect (see Fig. 7.10). The influence of changing width on the power law will be discussed in a forthcoming section.

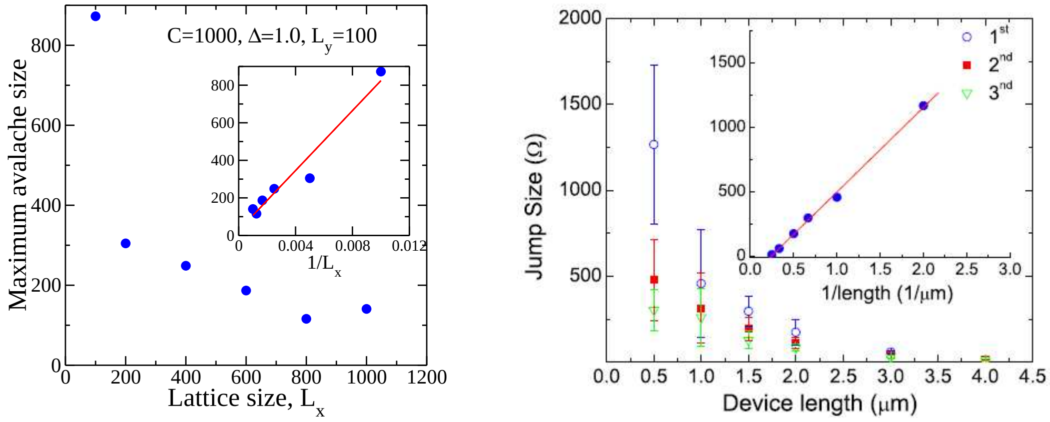

(a)

(b)

Fig. 7.9: Maximum avalanche size dependence on the system length. Insets show a linear dependence when plotted against the inverse length plot. (a) Theoretical plot for contrast ratio, $C = 1000$ and disorder strength $\Delta = 1.0J$ ($J = 1$, $L_y = 100$). (b) Similar plot for the VO_2 thin film experiment by Sharoni *et al* [62].

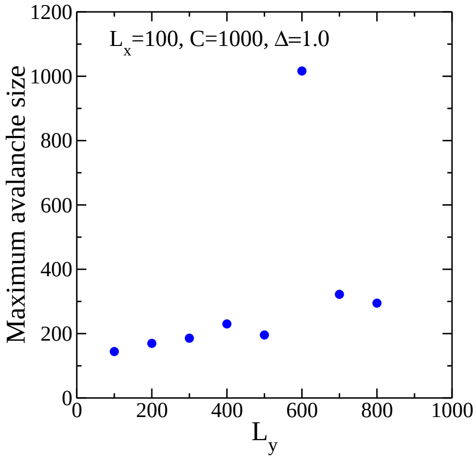

Fig. 7.10: Maximum avalanche size as a function of system width L_y. The size does not get affected significantly by change in the width (though shows an increasing nature) except $L_y = 600$ having a large deviation.

7.11.2 Avalanche size distribution

To investigate whether the avalanche size follows a power law we plot the

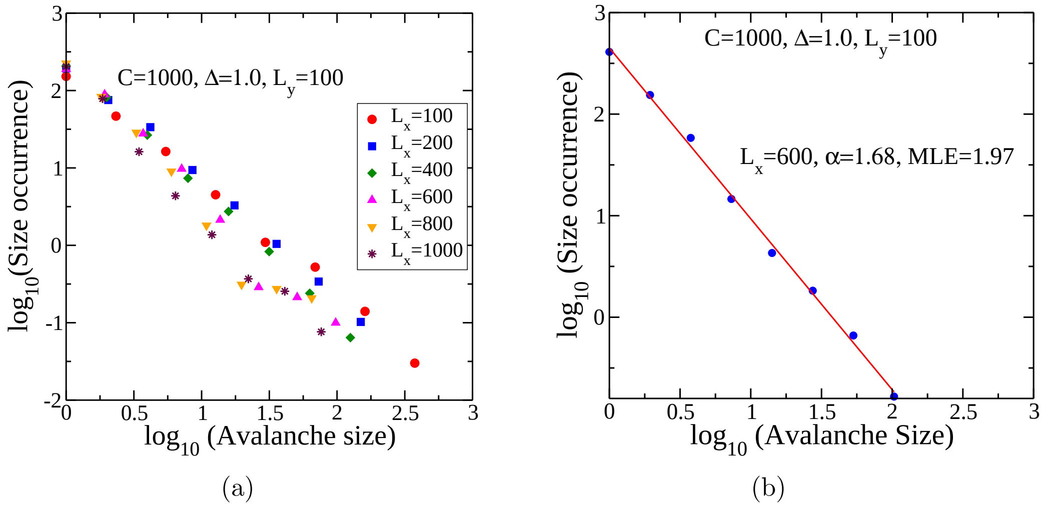

(a) (b)

Fig. 7.11: (a) Double-log distribution plots of avalanches for different lengths, L_x ranging from 100 to 1000 keeping $L_y = 100$, $\Delta = 1.0$, and $C = 1000$ fixed. (b) Linear regression line for $L_x = 600$. The slope yields $\alpha = 1.68$ whereas maximum likelihood estimation (MLE) is a little higher ($\alpha = 1.97$).

logarithmically binned data (for the method see Appendix L) for the resistance hysteresis for different sizes. Fig. 7.11 (a) shows the avalanche size distribution on double-log scale for different length L_x and for fixed width $L_y = 100$, disorder strength $\Delta = 1.0$ and $C = 1000$. We find a good linear regression plot showing a power law behavior and the power law exponent α is obtain from the slope of the regression line. For example, for system size with $L_x = 600$ and $L_y = 100$ (see Fig. 7.11 (b)) gives $\alpha = 1.68$, which is less than that obtained in the VO_2 experimental data. We also estimate α using the maximum likelihood estimation (MLE) and we find it to have a little higher value ($\alpha = 1.97$).

7.11.3 Size dependence of power law exponent

Since we vary the system length L_x, we desire to see the third point that has been mentioned in the beginning of this section. Fig. 7.12(a) shows that the power law exponent on average increases with the length L_x. This also bears a striking resemblance with the behavior found in the experiment (Fig. 7.12(b)). The power law exponent variation shows a feeble dependence on system width L_y. Fig. 7.13 shows the exponent α varies a little around a mean value $\alpha_{\text{mean}} = 1.36$.

7.11.4 Effect of disorder

The effect of disorder is important since the strength of the disorder decides the pinning of domains and hence size of the avalanches. First of all, as we expect for the RFIM, the average avalanche size decreases with increasing

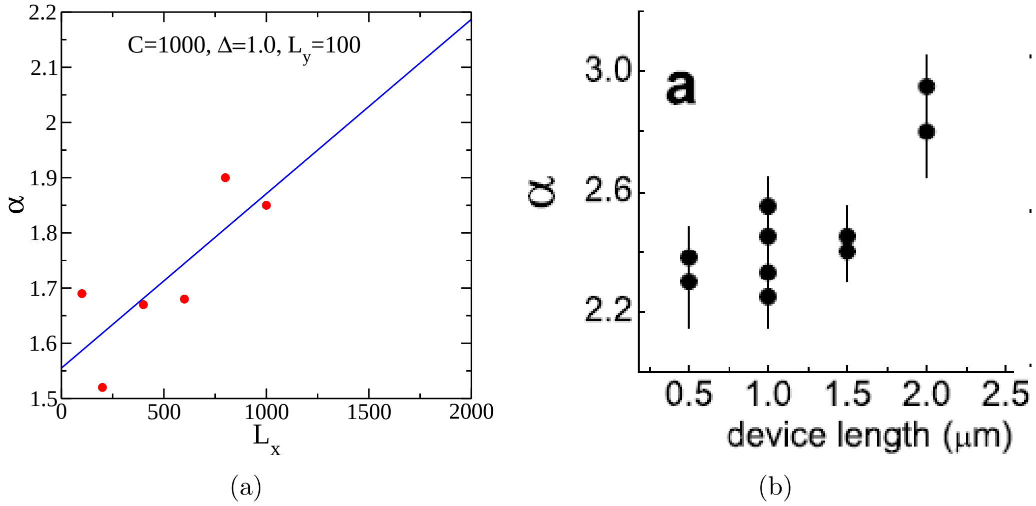

(a) (b)

Fig. 7.12: (a) Dependence of the power law exponent α with the system length. (b) Similar behavior observed in the experiment on VO_2 thin films mentioned in Ref. 62.

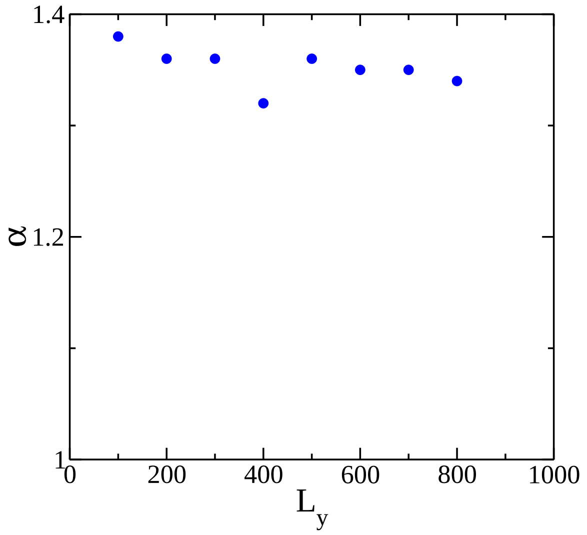

Fig. 7.13: Power law exponent α as a function of system width L_y. α changes very little (around an average value 1.36) with L_y.

disorder Δ. (see Fig. 7.14) . We observe power law with cut-offs that range

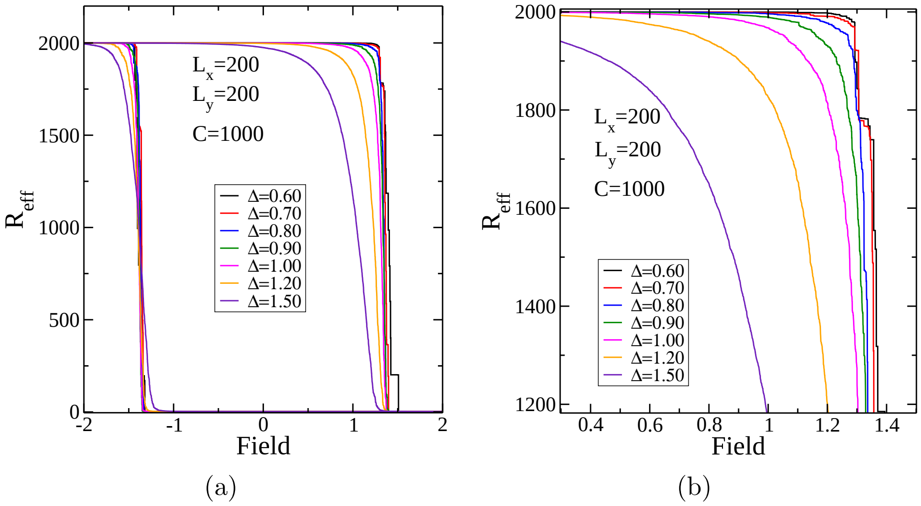

(a) (b)

Fig. 7.14: (a) Resistance hysteresis at different disorders Δ for a system size 200. (b) Zoomed in view of the same clearly shows that avalanche size becomes smaller as disorder is increased and the step like curve finally turn into a smooth one.

over one or two decades (see Fig. 7.15(a)). The cutoff apparently diverges around $\Delta = 0.8$, which seems to be the critical disorder Δ_c. This behavior is exactly similar to that in the pure RFIM in 3d (Fig. 7.2). Thus following the arguments by Perković *et al*, we see a wide critical region instead of a single critical point at Δ_c. Nevertheless, the power law exponent increases as disorder is increased (see Fig. 7.15(b)).

However, we should remember one important fact that magnetization is an extensive quantity whereas resistances in a network are not. Furthermore, though debatable, it is believed that, in the 2d RFIM, the critical disorder strength is $\Delta_c = 0$, i.e. only a clean sample should show true power law behavior [123, 146].

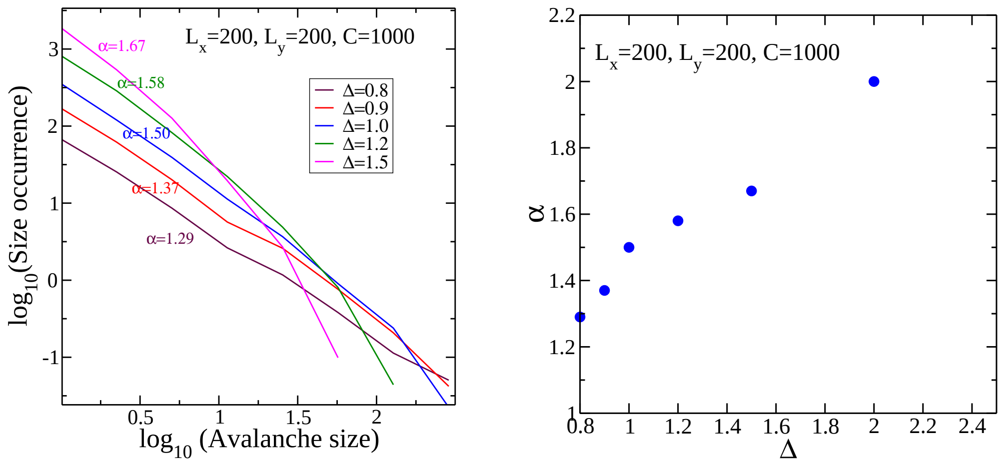

(a) (b)

Fig. 7.15: (a) The power law behavior with cutoffs at different disorders. The power law regime (linear in the log-scale) sustains up to one or two decades signifying a wide region of criticality (*Cf.* Fig. 7.2). (b) Change of critical exponent α with disorder Δ.

7.11.5 Effect of contrast ratio

The final issue that we want to examine is the effect of the contrast ratio, C on the statistics of resistance avalanches. In a typical temperature driven Mott transition C changes as a function of temperature. Specifically, close to the second order critical point T_c, it is almost impossible to distinguish a metallic and an insulating phase by looking at their resistivity or conductivity values. The hysteresis loop almost shrinks to zero as T approaches T_c. In that sense, a pure percolation picture is not applicable at $T \lesssim T_c$ and also the avalanche statistics may not make sense since the first-order transition no longer persists. In addition to this, critical fluctuations near T_c may overwhelm the the critical behavior due to disorder. However, from the energetics point of view, we can always get two metastable states once we get a finite contrast ratio, however small the contrast ratio is. In fact, we

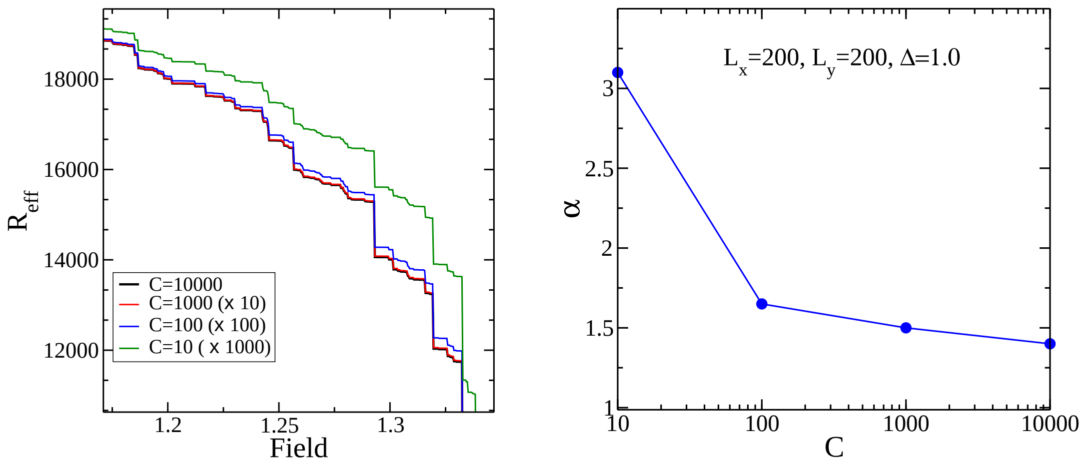

(a) (b)

Fig. 7.16: Dependence of the power law exponent α on the contrast ratio C for the lattice size 200×200 and disorder $\Delta = 1.0$. (a) The hysteresis plot shows no significant change in the nature of avalanche sizes. For comparison with effective resistance with $C = 10000$, effective resistances with $C = 10$, 100, and 1000 are multiplied by factors 1000, 100, 10 respectively (following the formula Eq. (7.27)). (b) α increases as C is decreased.

find no significant change in the avalanche size once we scale up the effective resistances to fit with the value of that for $C = 10000$ (see Fig. 7.16 (a)) . Also it turns out that we get higher critical exponents as we go for smaller contrasts ratio (see Fig. 7.16 (b)).

7.12 Estimation of power law exponents

If a distribution shows a power law behavior: $P(x) \sim x^{\alpha}$ for sample point variable x, then by taking logarithm on both sides, we can determine the exponent α. However, a direct linear binning in order to get the distribution leads to incorrect results since the sample point fluctuations can be enormous at the large value regime. Therefore we first obtain the size distribution by using a logarithmic binning and then we do the double-log plotting. The methodical detail has been discussed in Appendix L. However, in some cases, for better estimation of the power law exponent we use maximum likelihood estimation (MLE) in some cases [144, 145, 147, 148]. In most cases of our results, α from the MLE is little higher than than obtained from logarithmic binning but does not significantly alter the stochastic behavior. We use the C++ codes developed by Wim Otte and Matlab codes developed by Aaron Clauset, Cosma R. Shalizi, and M. E. J. Newman, which are freely available online (`http://tuvalu.santafe.edu/~aaronc/powerlaws/`).

7.13 Summary

In this chapter, we develop a classical theory which attempts to capture certain aspects of the inhomogeneous Mott transition that lie beyond the mean-field nature of DMFT discussed in all previous chapters. In this theory, a disordered magnetic Hamiltonian, namely the random field Ising model (RFIM) is mapped on to resistor network which corresponds to an inhomogeneous metal-insulator system of our interest. Being motivated by the experimental work done by Sharoni and co-workers on VO_2 thin films [62], we first compare our results with their experimental findings and we find excellent agreement with most of their results. However, we find that the measured power law exponent is higher than that obtained from our calculations within so far varied parameter regime. Nevertheless, we have shown in this chapter that the exponent is dependent strongly on several parameters, such as the sample geometry, disorder strength, contrast ratio and it is possible that the experimental system may correspond to very high disorder of our theory, which is intuitive from Fig. 7.15. Thus we find a suitable scenario from our theory, based on zero temperature RFIM, which can explain the statistical behavior of the resistance hysteresis found of the 2d inhomogeneous metal-insulator systems (as our present model is 2-dimensional too) driven by temperature keeping the athermal condition. Our other findings require further verification through experiments on the same or similar materials.

Thesis summary

The dynamical mean field theory (DMFT) is a very useful framework to study the electronic correlation physics in a lattice system. Within the DMFT framework, many techniques, e.g. exact diagonalization (ED), numerical renormalization group (NRG), quantum Monte Carlo (QMC) etc. have been applied in order to solve the mapped single impurity model (SIAM) problem in DMFT. All of these methods have theoretical advantages and disadvantages. Methods such as QMC are believed to be exact, but are highly expensive in terms of computational time and many of them are not capable of producing conclusive results at all energy scales. Furthermore, a supposedly exact method like QMC suffers from a 'sign' problem and also cannot produce zero temperature result. This is where diagrammatic perturbation theory based approaches help. With appropriate benchmarking these approaches can be put to very good use. The iterated perturbation theory (IPT) is one such method, that is less expensive but because of being a second order perturbation approximation, fails to capture the exponentially small scale of the SIAM. However, we develop a numerical implementation of the IPT method, which is a direct real-frequency formalism (hence free of the analytic continuation problems) and a method to capture the sharp poles

that arises in the spectra close to the Mott transition. We have also used IPT results (by our new scheme) as a comparative and benchmarking reference for the more sophisticated approach developed and applied in this thesis, namely the local moment approach (LMA). The LMA for the single band Hubbard model (both for half-filling and away from half-filling) has been investigated as a serious alternative to IPT considering its earlier successes in the SIAM and periodic Anderson model (PAM).

As a first benchmark, we have found the Mott transition by using LMA. We have also observed two transition points, namely U_{c2} and U_{c1}, similar to that obtained from IPT and many other methods, while increasing and decreasing interaction from the metallic and insulating phases respectively. The value of U_{c2} and U_{c1} have been inferred from the vanishing of quasiparticle weight and the closing of insulating gap in the spectral function respectively. We have reported some new universal behavior obtained from LMA calculations. For example, a universal peak position in the optical conductivity and a strong coupling scaling regime which goes far beyond the low-energy Fermi liquid scale and enhances more for the interaction strength close to the Mott transition point. We have studied the doped metal and Mott insulator case and compared spectral results to that in IPT.

The most striking results from our LMA calculation is the wide range of linear temperature dependence of the resistivity in the particle-hole asymmetric case. To explain our results, we have investigated the behavior of the self-energy and have found that it shows the marginal Fermi liquid behavior, as proposed by Varma *et al* in 1989 in order to explain the “normal” state of the high temperature superconductors.

Last but not the least, in our final research work, we have taken a diversion from the diagrammatic many-body theory in order to study the statistical behavior of the inhomogeneous Mott transition, after being motivated by the the recent resistance hysteresis and avalanches (step-like jumps along the hysteresis curve) experiments done by Sharoni *et al*(2008) on VO_2 thin films. To describe the statistical results of their experiment, namely a power law behavior in the avalanche size distribution, we have proposed a random field Ising model (RFIM) mapped to a resistor network. We have used Monte Carlo simulation for the RFIM and solved the resistor network through Kirchhoff's current equations. We have found remarkable agreement with the experimental results, such as the dependence of the maximum avalanche size and the power law exponent on the system size. However, we have found a smaller exponent compared to that has been reported in the experiment. We have speculated on the sources and parameters that may give rise to a higher value of the exponent.

Finally looking at my future research, I must mention that all that I have done in my thesis is just a beginning. We need to do benchmarking with results with other similar methods. We should develop more analytic handling of our theory. Our approach can be applied to negative-U Hubbard model or other extended Hubbard models. Our methods can be combined to realistic local density approximation (LDA) based band structure calculations. We may need to find a stronger connection of the local spin-flip scattering physics to the experiments on cuprates. For the last part of work, we must confess that a microscopic non-equilibrium quantum theory may be looked for the physical prediction of the non-equilibrium phenomena of Mott transition systems. A renormalization group study of the disorder effect (similar to the work has been done for the 2d non-interacting electron systems in the context of quantum Hall effect) can be useful in support of our theoretical result.

Appendix A

Equation of motion method

A.1 Equation of motion for fermions at $T = 0$ (real time)

We define

$$\begin{aligned} \langle\langle \hat{A}(\tau); \hat{B}(\tau') \rangle\rangle &\equiv -i\theta(\tau - \tau')\langle [\hat{A}(\tau), \hat{B}(\tau')]_+ \rangle \\ &= G^{AB}(\tau - \tau') \qquad\qquad \text{[retarded Green's function]} \end{aligned} \tag{A.1}$$

Let $\tau' = 0$, $\tau = t$. Then we can rewrite

$$\begin{aligned} \langle\langle \hat{A}(t); \hat{B} \rangle\rangle &\equiv -i\theta(t)\langle [\hat{A}(t), \hat{B}]_+ \rangle \\ &= G^{AB}(t) \end{aligned} \tag{A.2}$$

$$\begin{aligned} \Rightarrow \frac{d}{dt}\langle\langle \hat{A}(t); \hat{B} \rangle\rangle &= -i\frac{d\theta(t)}{dt}\langle [\hat{A}(t), \hat{B}]_+ \rangle - i\theta(t)\frac{d}{dt}\langle [\hat{A}(t), \hat{B}]_+ \rangle \\ &= -i\delta(t)\langle [\hat{A}(t), \hat{B}]_+ \rangle - i\theta(t)\langle \frac{d\hat{A}(t)}{dt}\hat{B} + \hat{B}\frac{d\hat{A}(t)}{dt} \rangle \\ &- i\delta(t)\langle [\hat{A}(t), \hat{B}]_+ \rangle + \theta(t)\langle [\hat{H}, \hat{A}(t)]\hat{B} + \hat{B}[\hat{H}, \hat{A}(t)] \rangle \\ &\qquad\qquad \left[\text{Using } \frac{d\hat{X}}{dt} = \frac{i}{\hbar}[\hat{H}, \hat{X}(t)] \text{ with } \hbar = 1\right] \\ &= -i\delta(t)\langle [\hat{A}(t), \hat{B}]_+ \rangle + \theta(t)\langle [\,[\hat{H}, \hat{A}(t)],\ \hat{B}]_+\,] \rangle \\ &= -i\delta(t)\langle [\hat{A}(t), \hat{B}]_+ \rangle - i(-i\theta(t)\langle [\,[\hat{A}(t), \hat{H}],\ \hat{B}]_+\,] \rangle) \\ &= -i\delta(t)\langle [\hat{A}(t), \hat{B}]_+ \rangle - i\langle\langle [\,[\hat{A}(t), \hat{H}];\ \hat{B}] \rangle\rangle \end{aligned} \tag{A.3}$$

Now by Fourier's transform of Eq. (A.3) into $\omega^+ \equiv \omega + i\eta$; $\eta \to 0$-space, we get

$$\begin{aligned} -i\omega \int dt\, e^{i(\omega+i\eta)t} \frac{d}{dt}\langle\langle \hat{A}(t); \hat{B}\rangle\rangle &= -i \int dt\, e^{i\omega^+ t}\delta(t)\langle [\hat{A}(t), \hat{B}]_+\rangle \\ &\quad - i \int dt\, e^{i\omega^+ t}\langle\langle [\,[\hat{A}(t), \hat{H}];\ \hat{B}]\rangle\rangle \\ \Rightarrow -i\omega \int dt\, \langle\langle \hat{A}; \hat{B}\rangle\rangle_{\omega^+} &= -i\langle [\hat{A}, \hat{B}]_+\rangle - i\langle\langle [\hat{A}, \hat{H}]\,; \hat{B}]\rangle\rangle_{\omega^+} \end{aligned}$$

Here we have used

$$\begin{aligned} \int dt\, e^{i(\omega+i\eta)t}\langle\langle \hat{A}(t); \hat{B}\rangle\rangle &= \frac{e^{i\omega t - \eta t}}{i\omega}\langle\langle \hat{A}(t); \hat{B}\rangle\rangle\Big|_{t=-\infty}^{t=\infty} - \int dt\, \frac{e^{i\omega t}}{i\omega}\frac{d}{dt}\langle\langle \hat{A}(t); \hat{B}\rangle\rangle \\ &= -\int dt\, \frac{e^{i\omega t}}{i\omega}\frac{d}{dt}\langle\langle \hat{A}(t); \hat{B}\rangle\rangle \end{aligned}$$

[1^{st} term vanishes at $t = \infty$ due to the factor ηt in the exponential.
The lower limit $(-\infty)$ does not contribute since there is a $\theta(t)$.]
(A.4)

N. B. Here any operator $\hat{X}$ is a short-cut of $\hat{X}(0)$ and remember that we have chosen $\tau = 0$ for our convenience. Therefore $[\hat{A}, \hat{B}]$ will imply any equal-time commutation of $\hat{A}$ and $\hat{B}$.
Thus suppressing the η-part from ω^+ can write

$$\boxed{\omega\langle\langle \hat{A}; \hat{B}\rangle\rangle_\omega = \langle [\hat{A}, \hat{B}]_+\rangle + \langle\langle [\hat{A}, \hat{H}]\,; \hat{B}]\rangle\rangle_\omega} \tag{A.5}$$

and similarly from $\langle\langle \hat{A}; \hat{B}(t)\rangle\rangle$

$$\boxed{\omega\langle\langle \hat{A}; \hat{B}\rangle\rangle_\omega = \langle [\hat{A}, \hat{B}]_+\rangle + \langle\langle \hat{A};\ [\hat{H}, \hat{B}]\rangle\rangle_\omega \quad .} \tag{A.6}$$

Eq. (A.5) and Eq. (A.6) are known as the equations for fermions at zero temperature.

A.2 Equation of motion for boson and fermions at $T > 0$ (imaginary time)

We now formulate a generic equation of motion at finite temperature for both bosons and fermions. In the compact notation form, which often consists of ± or ∓ signs, where the upper sign will denote for bosons and the lower sign will hold for fermions.

$$\begin{aligned}\langle\langle \hat{A}(\tau); \hat{B}(\tau')\rangle\rangle &\equiv -\langle[\hat{T}\hat{A}(\tau)\,\hat{B}(\tau')]_{\mp}\rangle \\ &= G^{AB}(\tau-\tau') \qquad \text{[full imaginary time G.F.]} \end{aligned} \tag{A.7}$$

Here $\hat{T}$ is the time-order operator which behaves as follows.

$$\hat{T}\hat{A}(\tau)\hat{B}(\tau') = \begin{cases} \hat{A}(\tau)\hat{B}(\tau') & \text{if } \tau > \tau' \\ \pm\hat{B}(\tau')\hat{A}(\tau) & \text{if } \tau < \tau' \end{cases} \tag{A.8}$$

Let $\tau' = 0$, $\tau = \tau$. Then we can re-write

$$\begin{aligned}\langle\langle \hat{A}(\tau); \hat{B}\rangle\rangle &= -\langle \hat{T}\hat{A}(\tau)\hat{B}\rangle \\ &= -[\theta(\tau)\langle\hat{A}(\tau)\hat{B}\rangle \pm \theta(-\tau)\langle\hat{B}\hat{A}(\tau)\rangle] \end{aligned} \tag{A.9}$$

Now the imaginary time evolution for the Heisenberg operator can be written as

$$\hat{O}(\tau) = e^{\hat{K}\tau/\hbar}\hat{O}(0)e^{-\hat{K}\tau/\hbar} \tag{A.10}$$

where

$$\hat{K} = \hat{H} - \mu N \tag{A.11}$$

This leads to the following Eq. of motion

$$\frac{d\hat{O}(\tau)}{d\tau} = \frac{1}{\hbar}[\hat{K}, \hat{O}(\tau)] \tag{A.12}$$

Again as before we are going to take $\hbar = 1$ to keep the notations look simpler.

We get

$$\begin{aligned}
\frac{d}{d\tau}\langle\langle\hat{A}(\tau);\hat{B}\rangle\rangle =& -\left[\frac{d\theta(\tau)}{d\tau}\langle\hat{A}(\tau)\hat{B}\rangle \pm \frac{d\theta(-\tau)}{d\tau}\langle\hat{B}\hat{A}(\tau)\rangle\right. \\
&\left. + \theta(\tau)\frac{d}{d\tau}\langle\hat{A}(\tau)\,\hat{B}\rangle \pm \theta(-\tau)\frac{d}{d\tau}\langle\hat{B}\,\hat{A}(\tau)\rangle\right] \\
=& -\left[\delta(\tau)\langle\hat{A}(\tau)\hat{B}\rangle \mp \delta(-\tau)\langle\hat{B}\hat{A}(\tau)\rangle\right. \\
&\left. + \theta(\tau)\langle\,[\hat{K},\hat{A}(\tau)]\hat{B}\,\rangle \pm \theta(-\tau)\langle\,\hat{B}[\hat{K},\hat{A}(\tau)]\,\rangle\right] \\
=& -\delta(\tau)\langle[\hat{A}(\tau),\hat{B}]_{\mp}\rangle - \langle\,\hat{T}\,[\hat{K},\hat{A}(\tau)]\hat{B}\,\rangle \\
=& -\delta(\tau)\langle[\hat{A}(\tau),\hat{B}]_{\mp}\rangle - \langle\langle\,[\hat{A}(\tau),\hat{K}];\hat{B}\,\rangle\rangle
\end{aligned} \tag{A.13}$$

Now in term of Matsubara frequency, $\omega_n = 2n\pi/\beta$ for bosons and $\omega_n = (2n+1)\pi/\beta$ for fermions, we get using above

$$\begin{aligned}
\int_0^\beta d\tau\; e^{i\omega_n\tau}\frac{d}{d\tau}\langle\langle\hat{A}(\tau);\hat{B}\rangle\rangle =& \int_0^\beta d\tau\, e^{i\omega_n\tau}\delta(\tau)\langle[\hat{A}(\tau),\hat{B}]_{\mp}\rangle \\
&- \int_0^\beta d\tau\, e^{i\omega_n\tau}\langle\langle\,[\hat{A}(\tau),\hat{K}];\hat{B}\,\rangle\rangle \\
\Rightarrow -i\omega_n\langle\langle\hat{A};\hat{B}\rangle\rangle_{\omega_n} =& \langle[\hat{A},\hat{B}]_{\mp}\rangle - \langle\langle\,[\hat{A}(\tau),\hat{K}];\hat{B}\,\rangle\rangle_{\omega_n}
\end{aligned} \tag{A.14}$$

Here we have used the following

$$\int_0^\beta d\tau\, e^{i\omega_n\tau}\langle\langle\hat{A}(\tau);\hat{B}\rangle\rangle = \frac{e^{i\omega_n\tau}}{i\omega_n}\langle\langle\hat{A}(\tau);\hat{B}\rangle\rangle\Big|_{\tau=0}^{\tau=\beta} - \int d\tau\,\frac{e^{i\omega_n\tau}}{i\omega_n}\frac{d}{d\tau}\langle\langle\hat{A}(\tau);\hat{B}\rangle\rangle \tag{A.15}$$

For bosons

$$\begin{aligned}
e^{i\omega_n\tau}\langle\langle\hat{A}(\tau);\hat{B}\rangle\rangle\Big|_{\tau=0}^{\tau=\beta} =& e^{i\omega_n\beta}\langle\langle\hat{A}(\beta);\hat{B}\rangle\rangle - \langle\langle\hat{A};\hat{B}\rangle\rangle \\
=& 0 \\
[\because e^{i\omega_n\beta} = e^{i2n\pi} = 1 &\text{ and } \langle\langle\hat{A}(\beta);\hat{B}(0)\rangle\rangle = \langle\langle\hat{A}(0);\hat{B}(0)\rangle\rangle]
\end{aligned} \tag{A.16}$$

For fermions

$$\begin{aligned} e^{i\omega_n\tau}\langle\langle\hat{A}(\tau);\hat{B}\rangle\rangle\Big|_{\tau=0}^{\tau=\beta} &= e^{i\omega_n\beta}\langle\langle\hat{A}(\beta);\hat{B}\rangle\rangle - \langle\langle\hat{A};\hat{B}\rangle\rangle \\ &= 0 \\ [\because e^{i\omega_n\beta} = e^{i(2n+1)\pi} &= -1 \text{ and } \langle\langle\hat{A}(\beta);\hat{B}(0)\rangle\rangle = -\langle\langle\hat{A}(0);\hat{B}(0)\rangle\rangle] \end{aligned} \tag{A.17}$$

Thus

$$\int_0^\beta d\tau\, e^{i\omega_n\tau}\langle\langle\hat{A}(\tau);\hat{B}\rangle\rangle = -\int d\tau\,\frac{e^{i\omega_n\tau}}{i\omega_n}\frac{d}{d\tau}\langle\langle\hat{A}(\tau);\hat{B}\rangle\rangle \tag{A.18}$$

and finally

$$\boxed{i\omega_n\langle\langle\hat{A};\hat{B}\rangle\rangle_{i\omega_n} = \langle[\hat{A},\hat{B}]_\mp\rangle + \langle\langle[\hat{A},\hat{K}]\,;\hat{B}]\rangle\rangle_{i\omega_n}} \tag{A.19}$$

In a similar way from $\langle\langle\hat{A};\hat{B}(\tau)\rangle\rangle$

$$\boxed{i\omega_n\langle\langle\hat{A};\hat{B}\rangle\rangle_{i\omega_n} = \langle[\hat{A},\hat{B}]_\mp\rangle + \langle\langle\hat{A};\,[\hat{K},\hat{B}]\rangle\rangle_{i\omega_n}} \tag{A.20}$$

Eq. (A.19) and Eq. (A.20) are known as the equation of motions in Matsubara (finite temperature) formalism.

Appendix B

Calculation of internal energy for the Hubbard model

$$\hat{H} = -\sum_{\langle ij\rangle,\sigma} t_{ij}(c^{\dagger}_{i\sigma}c_{j\sigma} + \text{h.}c.) + \epsilon_d \sum_{i\sigma} c^{\dagger}_{i\sigma}c_{i\sigma} + U\sum_{i} n_{i\uparrow}n_{i\downarrow} \tag{B.1}$$

In momentum space,

$$\begin{aligned}\hat{H} &= \sum_{\mathbf{k}\sigma} \epsilon_{\mathbf{k}} c^{\dagger}_{\mathbf{k}\sigma}c_{\mathbf{k}\sigma} + U\sum_{\mathbf{kpq}} c^{\dagger}_{\mathbf{k}\uparrow}c_{\mathbf{k-q}\uparrow}c^{\dagger}_{\mathbf{p}\downarrow}c_{\mathbf{p+q}\downarrow} \\ &= \sum_{\mathbf{k}\sigma} \epsilon_{\mathbf{k}} c^{\dagger}_{\mathbf{k}\sigma}c_{\mathbf{k}\sigma} + \frac{U}{2}\sum_{\mathbf{kpq}\sigma} c^{\dagger}_{\mathbf{k}\sigma}c_{\mathbf{k-q}\sigma}c^{\dagger}_{\mathbf{p}\bar{\sigma}}c_{\mathbf{p+q}\bar{\sigma}} \end{aligned} \tag{B.2}$$

where we have absorbed ϵ_d within $\epsilon_{\mathbf{k}}$

To find the expectation value of $\hat{C} = \hat{A}\hat{B}$, we use

$$\begin{aligned}\langle\hat{C}\rangle = \langle\hat{A}\hat{B}\rangle &= \lim_{\tau\to\tau'+}\langle\hat{A}(\tau)\hat{B}(\tau')\rangle = -\lim_{\tau\to\tau'+}\langle\hat{T}\hat{B}(\tau')\hat{A}(\tau)\rangle \\ &= \lim_{\tau\to\tau'+}\langle\langle\hat{B}(\tau');\hat{A}(\tau)\rangle\rangle = G^{BA}(\tau',\tau'+)\end{aligned} \tag{B.3}$$

Therefore

$$\langle\hat{H}\rangle = \frac{1}{\beta}\lim_{\eta\to 0+}\sum_{n} e^{i\omega_n\eta}\left[\sum_{\mathbf{k}\sigma}\epsilon_{\mathbf{k}}\langle\langle c_{\mathbf{k}\sigma};c^{\dagger}_{\mathbf{k}\sigma}\rangle\rangle + \frac{U}{2}\sum_{\mathbf{kpq}\sigma}\langle\langle c_{\mathbf{k-q}\sigma}c^{\dagger}_{\mathbf{p}\bar{\sigma}}c_{\mathbf{p+q}\bar{\sigma}};c^{\dagger}_{\mathbf{k}\sigma}\rangle\rangle\right]$$

Here we have absorbed ϵ_d within $\epsilon_{\mathbf{k}}$

So from the first equation of motion in terms of Matsubara frequencies (Eq. (A.19)) we get

$$i\omega_n\langle\langle c_{\mathbf{k}\sigma}; c^\dagger_{\mathbf{k}\sigma}\rangle\rangle = \langle[c_{\mathbf{k}\sigma}, c^\dagger_{\mathbf{k}\sigma}]_+\rangle + \langle\langle[c_{\mathbf{k}\sigma}, H]; c^\dagger_{\mathbf{k}\sigma}\rangle\rangle$$

$$\Rightarrow i\omega_n G_{\mathbf{k}\sigma}(i\omega_n) = 1 + \langle\langle[c_{\mathbf{k}\sigma}, H]; c^\dagger_{\mathbf{k}\sigma}\rangle\rangle$$

Now

$$\begin{aligned}
[c_{\mathbf{k}\sigma}, H] &= \epsilon_{\mathbf{k}} c_{\mathbf{k}\sigma} + \frac{U}{2}\sum_{\mathbf{k}'\mathbf{p}\mathbf{q}\sigma'}[c_{\mathbf{k}\sigma},\, c^\dagger_{\mathbf{k}'\sigma'}c_{\mathbf{k}-\mathbf{q}\sigma'}c^\dagger_{\mathbf{p}\bar{\sigma}'}c_{\mathbf{p}+\mathbf{q}\bar{\sigma}'}] \\
&= \epsilon_{\mathbf{k}} c_{\mathbf{k}\sigma} + U\sum_{\mathbf{p}\mathbf{q}\sigma} c_{\mathbf{k}-\mathbf{q}\sigma}c^\dagger_{\mathbf{p}\bar{\sigma}}c_{\mathbf{p}+\mathbf{q}\bar{\sigma}} \qquad (B.4)
\end{aligned}$$

$$\Rightarrow i\omega_n G_{\mathbf{k}\sigma} = 1 + \epsilon_{\mathbf{k}} G_{\mathbf{k}\sigma} + U\sum_{\mathbf{p}\mathbf{q}\sigma}\langle\langle c_{\mathbf{k}-\mathbf{q}\sigma}c^\dagger_{\mathbf{p}\bar{\sigma}}c_{\mathbf{p}+\mathbf{q}\bar{\sigma}}; c^\dagger_{\mathbf{k}\sigma}\rangle\rangle \qquad (B.5)$$

since

$$\begin{aligned}
&\frac{U}{2}\sum_{\mathbf{k}'\mathbf{p}\mathbf{q}\sigma'}[c_{\mathbf{k}\sigma},\, c^\dagger_{\mathbf{k}'\sigma'}c_{\mathbf{k}'-\mathbf{q}\sigma'}c^\dagger_{\mathbf{p}\bar{\sigma}'}c_{\mathbf{p}+\mathbf{q}\bar{\sigma}'}] \\
&= \frac{U}{2}\sum_{\mathbf{k}'\mathbf{p}\mathbf{q}\sigma'}\{c_{\mathbf{k}\sigma},\, c^\dagger_{\mathbf{k}'\sigma'}\}c_{\mathbf{k}'-\mathbf{q}\sigma'}c^\dagger_{\mathbf{p}\bar{\sigma}'}c_{\mathbf{p}+\mathbf{q}\bar{\sigma}'} - \frac{U}{2}\sum_{\mathbf{k}'\mathbf{p}\mathbf{q}\sigma'}c^\dagger_{\mathbf{k}'\sigma'}\{c_{\mathbf{k}\sigma},\, c_{\mathbf{k}'-\mathbf{q}\sigma'}c^\dagger_{\mathbf{p}\bar{\sigma}'}c_{\mathbf{p}+\mathbf{q}\bar{\sigma}'}\} \\
&= \frac{U}{2}\sum_{\mathbf{k}'\mathbf{p}\mathbf{q}\sigma'}\{c_{\mathbf{k}\sigma},\, c^\dagger_{\mathbf{k}'\sigma'}\}c_{\mathbf{k}'-\mathbf{q}\sigma'}c^\dagger_{\mathbf{p}\bar{\sigma}'}c_{\mathbf{p}+\mathbf{q}\bar{\sigma}'} + \frac{U}{2}\sum_{\mathbf{k}'\mathbf{p}\mathbf{q}\sigma'}c^\dagger_{\mathbf{k}'\sigma'}\{c_{\mathbf{k}\sigma},\, c^\dagger_{\mathbf{p}\bar{\sigma}'}\}c_{\mathbf{k}'-\mathbf{q}\sigma'}c_{\mathbf{p}+\mathbf{q}\bar{\sigma}'} \\
&= \frac{U}{2}\sum_{\mathbf{p}\mathbf{q}\sigma}c_{\mathbf{k}-\mathbf{q}\sigma}c^\dagger_{\mathbf{p}\bar{\sigma}}c_{\mathbf{p}+\mathbf{q}\bar{\sigma}} + \frac{U}{2}\sum_{\mathbf{k}'\mathbf{q}\sigma}c^\dagger_{\mathbf{k}'\bar{\sigma}}c_{\mathbf{k}-\mathbf{q}\bar{\sigma}}c_{\mathbf{k}+\mathbf{q}\sigma} \\
&= \frac{U}{2}\sum_{\mathbf{p}\mathbf{q}\sigma}c_{\mathbf{k}-\mathbf{q}\sigma}c^\dagger_{\mathbf{p}\bar{\sigma}}c_{\mathbf{p}+\mathbf{q}\bar{\sigma}} + \frac{U}{2}\sum_{\mathbf{p}\mathbf{q}\sigma}c^\dagger_{\mathbf{p}\bar{\sigma}}c_{\mathbf{p}+\mathbf{q}\bar{\sigma}}c_{\mathbf{k}-\mathbf{q}\sigma}
\end{aligned}$$

[Transform in 2nd term: $\mathbf{k}' \to \mathbf{p}$, $\mathbf{q} \to -\mathbf{q}$]

$$= U\sum_{\mathbf{p}\mathbf{q}\sigma}c_{\mathbf{k}-\mathbf{q}\sigma}c^\dagger_{\mathbf{p}\bar{\sigma}}c_{\mathbf{p}+\mathbf{q}\bar{\sigma}}$$

[Sign change occurs twice in rearranging 2nd term]

(B.6)

Thus

$$U\sum_{\mathbf{kpq}}\langle\langle c_{\mathbf{k-q}\sigma}c^{\dagger}_{\mathbf{p}\bar{\sigma}}c_{\mathbf{p+q}\bar{\sigma}};c^{\dagger}_{\mathbf{k}\sigma}\rangle\rangle=\sum_{\mathbf{k}}(i\omega_n-\epsilon_{\mathbf{k}})G_{\mathbf{k}\sigma}(i\omega_n)-\sum_{\mathbf{k}}1 \tag{B.7}$$

Therefore

$$\begin{aligned}&\frac{1}{\beta}\lim_{\eta\to0+}\sum_n e^{i\omega_n\eta}\,\frac{U}{2}\sum_{\mathbf{kpq}}\langle\langle c_{\mathbf{k-q}\sigma}c^{\dagger}_{\mathbf{p}\sigma}c_{\mathbf{p+q}\bar{\sigma}};c^{\dagger}_{\mathbf{k}\sigma}\rangle\rangle\\&=\frac{1}{\beta}\lim_{\eta\to0+}\sum_n e^{i\omega_n\eta}\sum_{\mathbf{k}}\frac{1}{2}(i\omega_n-\epsilon_{\mathbf{k}})\,G_{\mathbf{k}\sigma}(i\omega_n)\end{aligned} \tag{B.8}$$

since

$$\lim_{\eta\to0+}\sum_n e^{i\omega_n\eta}=0 \tag{B.9}$$

[See Ref. 91 or Ref. 67 to verify this identity.]
Thus

$$\begin{aligned}\langle\hat{H}\rangle&=\frac{1}{\beta}\lim_{\eta\to0+}\sum_n e^{i\omega_n\eta}\sum_{\mathbf{k}\sigma}\left[\epsilon_{\mathbf{k}}+\frac{1}{2}(i\omega_n-\epsilon_{\mathbf{k}})\right]G_{\mathbf{k}\sigma}(i\omega_n)\\&=\frac{1}{2}\frac{1}{\beta}\lim_{\eta\to0+}\sum_n e^{i\omega_n\eta}\sum_{\mathbf{k}\sigma}\frac{i\omega_n+\epsilon_{\mathbf{k}}}{i\omega_n-\epsilon_{\mathbf{k}}-\Sigma_{\mathbf{k}\sigma}(i\omega_n)}\end{aligned} \tag{B.10}$$

since

$$G_{\mathbf{k}\sigma}(i\omega_n)=\frac{1}{i\omega_n-\epsilon_{\mathbf{k}}-\Sigma_{\mathbf{k}\sigma}(i\omega_n)} \tag{B.11}$$

Thus

$$\begin{aligned}\langle\hat{H}\rangle&=\frac{1}{2}\frac{1}{\beta}\lim_{\eta\to0+}\sum_n e^{i\omega_n\eta}\sum_{\mathbf{k}\sigma}\frac{i\omega_n-\epsilon_{\mathbf{k}}-\Sigma_{\mathbf{k}\sigma}(i\omega_n)+(2\epsilon_{\mathbf{k}}+\Sigma_{\mathbf{k}\sigma}(i\omega_n))}{i\omega_n-\epsilon_{\mathbf{k}}-\Sigma_{\mathbf{k}\sigma}(i\omega_n)}\\&=\frac{1}{2}\frac{1}{\beta}\lim_{\eta\to0+}\sum_n e^{i\omega_n\eta}\sum_{\mathbf{k}\sigma}\left[1+\frac{2\epsilon_{\mathbf{k}}+\Sigma_{\mathbf{k}\sigma}(i\omega_n)}{i\omega_n-\epsilon_{\mathbf{k}}-\Sigma_{\mathbf{k}\sigma}(i\omega_n)}\right]\\&=\frac{1}{2}\frac{1}{\beta}\lim_{\eta\to0+}\sum_n e^{i\omega_n\eta}\sum_{\mathbf{k}\sigma}\frac{2\epsilon_{\mathbf{k}}+\Sigma_{\mathbf{k}\sigma}(i\omega_n)}{i\omega_n-\epsilon_{\mathbf{k}}-\Sigma_{\mathbf{k}\sigma}(i\omega_n)}\qquad\text{[used Eq. (B.9)]}\\&=\frac{1}{\beta}\lim_{\eta\to0+}\sum_n e^{i\omega_n\eta}\sum_{\mathbf{k}\sigma}\left[\epsilon_{\mathbf{k}}G_{\mathbf{k}\sigma}(i\omega_n)+\frac{1}{2}\Sigma_{\mathbf{k}\sigma}(i\omega_n)G_{\mathbf{k}\sigma}(i\omega_n)\right]\end{aligned} \tag{B.12}$$

We shall work for the paramagnetic case, i.e. $G_{\mathbf{k}\sigma}=G_{\mathbf{k}\bar{\sigma}}=G_{\mathbf{k}}$.

Therefore

$$
\begin{aligned}
\text{1st term} &= \frac{1}{\beta}\lim_{\eta\to 0+}\sum_{n} e^{i\omega_n\eta}\sum_{\mathbf{k}\sigma}\epsilon_{\mathbf{k}}G_{\mathbf{k}\sigma}(i\omega_n)\\
&= 2\frac{1}{\beta}\lim_{\eta\to 0+}\sum_{n\sigma} e^{i\omega_n\eta}\int d\epsilon\,\epsilon D_0(\epsilon)G(i\omega_n,\epsilon)\quad [D_0 \text{ is non-interacting DoS}]\\
&\qquad\qquad\qquad \left[\because \sum_{\mathbf{k}} f(\mathbf{k}) = \sum_{\mathbf{k}}\int d\epsilon\,\delta(\epsilon-\epsilon_{\mathbf{k}})f(\epsilon) = \int d\epsilon\, D_0(\epsilon)f(\epsilon)\right]\\
&= 2\frac{1}{\beta}\lim_{\eta\to 0+}\sum_{n\sigma} e^{i\omega_n\eta}\int d\epsilon\,\epsilon D_0(\epsilon)\int d\omega\,\frac{D(\omega,\epsilon)}{i\omega_n-\omega}\\
&= 2\int d\epsilon\,\epsilon\int d\omega\, n_F(\omega)D_0(\epsilon)D(\omega,\epsilon)\qquad \left[\because \frac{1}{\beta}\lim_{\eta\to 0+}\sum_{n} e^{i\omega_n\eta}\frac{1}{i\omega_n-\omega} = n_F(\omega)\right]\\
&= 2\int d\omega\, n_F(\omega)\int d\epsilon\,\epsilon D_0(\epsilon)[-\frac{1}{\pi}\mathrm{Im}G(\omega,\epsilon)]\\
&= 2\int d\omega\, n_F(\omega)\left[-\frac{1}{\pi}\mathrm{Im}\int\frac{d\epsilon\,\epsilon D_0(\epsilon)}{\gamma(\omega)-\epsilon}\right]\\
&\qquad\qquad\qquad\qquad\qquad\qquad [\text{where } \gamma = \omega^{+}-\epsilon_d-\Sigma(\omega)]\\
&= 2\int d\omega\, n_F(\omega)\left[-\frac{1}{\pi}\mathrm{Im}\int d\epsilon\,\frac{\gamma(\omega)-[\gamma(\omega)-\epsilon]}{\gamma(\omega)-\epsilon}D_0(\epsilon)\gamma(\omega)\right]\\
&= 2\int d\omega n_F(\omega)\left[-\frac{1}{\pi}\mathrm{Im}\left\{-\int d\epsilon\, D_0(\epsilon)+\gamma(\omega)\int\frac{d\epsilon D_0(\epsilon)}{\gamma(\omega)-\epsilon}\right\}\right]\\
&= 2\int d\omega\, n_F(\omega)\left[-\frac{1}{\pi}\mathrm{Im}\{\gamma(\omega)G(\omega)\}\right] \qquad\qquad \text{(B.13)}
\end{aligned}
$$

$$
\begin{aligned}
\text{2nd term} &= \frac{1}{\beta}\lim_{\eta\to 0+}\sum_n e^{i\omega_n\eta}\sum_{\mathbf{k}\sigma}\frac{1}{2}\Sigma_{\mathbf{k},\sigma}(i\omega_n)G_{\mathbf{k}\sigma}(i\omega_n) \\
&= \frac{1}{\beta}\lim_{\eta\to 0+}\sum_n e^{i\omega_n\eta}\int d\epsilon\, d\omega_1\, d\omega_2\, D_0(\epsilon)\frac{D_\Sigma(\omega_1)}{i\omega_n-\omega_1}\frac{D(\omega_2,\epsilon)}{i\omega_n-\omega_2} \\
&\qquad \text{(using paramagnetic assumption)} \\
&= \frac{1}{\beta}\lim_{\eta\to 0+}\int\sum_n d\epsilon\, d\omega_1\, d\omega_2\,\frac{1}{\omega_1-\omega_2}\left(\frac{e^{i\omega_n\eta}}{i\omega_n-\omega_1}-\frac{e^{i\omega_n\eta}}{i\omega_n-\omega_2}\right) \\
&\qquad\qquad \times\left(D_0(\epsilon)D_\Sigma(\omega_1)D(\omega_2,\epsilon)\right) \\
&= \int d\epsilon\, d\omega_1\, d\omega_2\, D_0(\epsilon)D_\Sigma(\omega_1)D(\omega_2,\epsilon)\frac{n_F(\omega_1)-n_F(\omega_2)}{\omega_1-\omega_2} \\
&\qquad\qquad\qquad\qquad \left[\because \frac{1}{\beta}\lim_{\eta\to 0+}\sum_n e^{i\omega_n\eta}\frac{1}{i\omega_n-\omega}=n_F(\omega)\right] \\
&= \int d\omega_1\, d\omega_2\, D_\Sigma(\omega_1)D(\omega_2)\frac{n_F(\omega_1)-n_F(\omega_2)}{\omega_1-\omega_2}
\end{aligned}
\tag{B.14}
$$

Thus

$$
\langle\hat{H}\rangle = 2\int d\omega\, n_F(\omega)\left[-\frac{1}{\pi}\mathrm{Im}(\gamma(\omega)G(\omega))\right]+\int d\omega_1\, d\omega_2\, D_\Sigma(\omega_1)D(\omega_2)\frac{n_F(\omega_1)-n_F(\omega_2)}{\omega_1-\omega_2}
\tag{B.15}
$$

Now

$$
\begin{aligned}
&\int d\omega_1\, d\omega_2\, D_\Sigma(\omega_1)D(\omega_2)\frac{n_F(\omega_1)-n_F(\omega_2)}{\omega_1-\omega_2} \\
&= \int d\omega_1\, d\omega_2\,(-\frac{1}{\pi}\mathrm{Im}\Sigma(\omega_1))(-\frac{1}{\pi}\mathrm{Im}G(\omega_2))\times\frac{n_F(\omega_1)-n_F(\omega_2)}{\omega_1-\omega_2} \\
&= -\int d\omega_1\frac{1}{\pi}(\mathrm{Im}\Sigma(\omega_1))n_F(\omega_1)\frac{1}{\pi}\int d\omega_2\frac{\mathrm{Im}G(\omega_2)}{\omega_2-\omega_1} \\
&\quad -\int d\omega_2\frac{1}{\pi}\int d\omega_1\frac{\mathrm{Im}\Sigma(\omega_1)}{\omega_1-\omega_2}(\frac{1}{\pi}\mathrm{Im}G(\omega_2)n_F(\omega_2)) \\
&= -\frac{1}{\pi}\int d\omega n_F(\omega)\Big[\mathrm{Im}\Sigma(\omega)\mathrm{Re}G(\omega)+\mathrm{Re}\Sigma(\omega)\mathrm{Im}G(\omega)\Big] \\
&\text{[by Kramers-Kronig relation } \mathrm{Re}f(z')=\tfrac{1}{\pi}\mathcal{P}\textstyle\int dz\,\dfrac{\mathrm{Im}f(z)}{z-z'}] \\
&= -\frac{1}{\pi}\int d\omega n_F(\omega)\mathrm{Im}\left(\Sigma(\omega)G(\omega)\right)
\end{aligned}
\tag{B.16}
$$

$$
\begin{aligned}
\langle\hat{H}\rangle &= \int d\omega n_F(\omega)(-\frac{1}{\pi}\mathrm{Im})\Big[2\gamma(\omega)G(\omega)+\Sigma(\omega)G(\omega)\Big] \\
&= \int d\omega n_F(\omega)(-\frac{1}{\pi}\mathrm{Im})\Big[2\gamma(\omega)+\Sigma(\omega)\Big]G(\omega) \\
&= \int d\omega n_F(\omega)(-\frac{1}{\pi}\mathrm{Im})\Big[2\omega^+-2\epsilon_d-2\Sigma(\omega)+\Sigma(\omega)\Big]G(\omega) \\
&= \int d\omega n_F(\omega)(-\frac{1}{\pi}\mathrm{Im})\Big[2\omega^+-2\epsilon_d-\Sigma(\omega)\Big]G(\omega) \qquad \text{(B.17)}
\end{aligned}
$$

Thus

$$
\boxed{\langle\hat{H}\rangle = \int d\omega\, n_F(\omega)\Big[2\omega D(\omega)+\frac{1}{\pi}\mathrm{Im}\left(\Sigma(\omega)G(\omega)\right)\Big] \quad .} \qquad \text{(B.18)}
$$

In case of singularity in self-energy (IPT):

When singularity arises in the self-energy, e.g. in the insulating state in IPT, we can write the self-energy by splitting them into its regular (denoted by superscript R) and singular part (denoted by superscript S), i.e.

$$
\Sigma(\omega) = \Sigma^R(\omega) + \Sigma^S(\omega) \qquad \text{(B.19)}
$$

In IPT

$$
\Sigma^S(\omega) = \frac{U^2\alpha^3}{4\omega^+} \qquad \text{(B.20)}
$$

Thus

$$
\int d\omega n_F(\omega)\frac{1}{\pi}\mathrm{Im}\left(\Sigma(\omega)G(\omega)\right) = \int d\omega n_F(\omega)\frac{1}{\pi}\mathrm{Im}\left(\Sigma^R(\omega)G(\omega)+\Sigma^S(\omega)G(\omega)\right)
$$

Now

$$
\begin{aligned}
&\frac{1}{\pi}\mathrm{Im}\int d\omega\, n_F(\omega)\Sigma^S(\omega)G(\omega)n_F(\omega) \\
&\qquad\qquad = \frac{U^2\alpha^3}{4\pi}\mathrm{Im}\int d\omega n_F(\omega)\frac{G(\omega)}{\omega^+} \\
&\qquad\qquad = \frac{U^2\alpha^3}{4\pi}\int d\omega n_F(\omega)\left[\mathrm{Im}G(\omega)\mathrm{Re}(\frac{1}{\omega^+}) + \mathrm{Re}G(\omega)\mathrm{Im}(\frac{1}{\omega^+})\right] \\
&\qquad\qquad = \frac{U^2\alpha^3}{4\pi}\int d\omega n_F(\omega)\left[\mathrm{Im}G(\omega)\mathcal{P}(\frac{1}{\omega}) - \mathrm{Re}G\pi\delta(\omega)\right] \\
&\qquad\qquad\qquad\qquad\qquad\qquad [\text{using}\frac{1}{\omega^+} = \mathcal{P}(\frac{1}{\omega}) - i\pi\delta(\omega)] \\
&\qquad\qquad = \frac{U^2\alpha^3}{4\pi}\left[\int d\omega n_F(\omega)\frac{\mathrm{Im}G(\omega)}{\omega} - \pi n_F(0)\mathrm{Re}G(0)\right] \\
&\qquad\qquad = \frac{U^2\alpha^3}{4}\left[-\int d\omega n_F(\omega)\frac{D_G(\omega)}{\omega} - n_F(0)\mathrm{Re}G(0)\right] \\
&\qquad\qquad = -\frac{U^2\alpha^3}{4}\left[\mathrm{KK}_{n_F G}(0) + \frac{1}{2}\mathrm{Re}G(0)\right] \qquad \text{(B.21)}
\end{aligned}
$$

where $\mathrm{KK}_{n_F G}(\omega)$ implies the Kramers-Kronig transform of $n_F(\omega')G(\omega')$ at frequency ω, i.e.

$$\mathrm{KK}_{n_F G}(\omega) \equiv \mathcal{P}\int d\omega' \frac{n_F(\omega')G(\omega')}{\omega - \omega'} \quad . \qquad \text{(B.22)}$$

Appendix C

p-h transformation on Hubbard model

Hubbard model (HM) Hamiltonian in terms of particle operators

$$\hat{H} = -\sum_{<ij>,\sigma} t_{ij}(\hat{c}^{\dagger}_{i\sigma}\hat{c}_{j\sigma} + \hat{c}^{\dagger}_{j\sigma}\hat{c}_{i\sigma}) + \frac{U}{2}\sum_{i\sigma}\hat{n}_{i\sigma}\hat{n}_{i\bar{\sigma}} + \epsilon_d \sum_{i\sigma}\hat{n}_{i\sigma} \tag{C.1}$$

Now particle-hole (p-h) transformation implies

$$\boxed{\hat{c}_{i\sigma} \rightarrow \hat{d}^{\dagger}_{i\sigma};\ \hat{c}^{\dagger}_{i\sigma} \rightarrow \hat{d}_{i\sigma};\ t_{ij} \rightarrow -t_{ij}} \tag{C.2}$$

Thus the HM in hole picture becomes

$$\hat{H}^h = +\sum_{<ij>,\sigma} t_{ij}(\hat{d}_{i\sigma}\hat{d}^{\dagger}_{j\sigma} + \hat{d}_{j\sigma}\hat{d}^{\dagger}_{i\sigma}) + \frac{U}{2}\sum_{i\sigma}\hat{d}_{i\sigma}\hat{d}^{\dagger}_{i\sigma}d_{i\bar{\sigma}}\hat{d}^{\dagger}_{i\bar{\sigma}} + \epsilon_d \sum_{i\sigma}\hat{d}_{i\sigma}\hat{d}^{\dagger}_{i\sigma} \tag{C.3}$$

Now the hole operators follow the same anti-commutation like the particles, i.e.

$$[d_{i\sigma}, d^{\dagger}_{j\sigma}]_{+} = \delta_{ij} \tag{C.4}$$

$$\Rightarrow d_{i\sigma}d^{\dagger}_{j\sigma} = -d^{\dagger}_{j\sigma}d_{i\sigma} \quad \text{for} \quad i \neq j \tag{C.5}$$

$$d_{i\sigma}d^{\dagger}_{i\sigma} = 1 - d^{\dagger}_{i\sigma}d_{i\sigma} \quad \text{when } i = j \tag{C.6}$$

Using above we get

$$\hat{H}^h = -\sum_{<ij>,\,\sigma} t_{ij}(\hat{d}^\dagger_{i\sigma}\hat{d}_{j\sigma} + \hat{d}^\dagger_{j\sigma}\hat{d}_{i\sigma}) + \frac{U}{2}\sum_{i\sigma}[1-\hat{d}^\dagger_{i\sigma}\hat{d}_{i\sigma}][1-\hat{d}^\dagger_{i\bar{\sigma}}\hat{d}_{i\bar{\sigma}}] \\ +\epsilon_d\sum_{i\sigma}[1-\hat{d}^\dagger_{i\sigma}\hat{d}_{i\sigma}]$$

$$= \underbrace{-\sum_{<ij>,\,\sigma} t_{ij}(\hat{d}^\dagger_{i\sigma}\hat{d}_{j\sigma} + \hat{d}^\dagger_{j\sigma}\hat{d}_{i\sigma}) + \frac{U}{2}\sum_{i\sigma}\hat{d}^\dagger_{i\sigma}\hat{d}_{i\sigma}\hat{d}^\dagger_{i\bar{\sigma}}\hat{d}_{i\bar{\sigma}} + \sum_{i\sigma}\epsilon_d\hat{d}^\dagger_{i\sigma}\hat{d}_{i\sigma}}_{\text{original form}} \\ +\frac{U}{2}\sum_{i\sigma}1 - \frac{U}{2}\sum_{i\sigma}[\hat{d}^\dagger_{i\sigma}\hat{d}_{i\sigma} + \hat{d}^\dagger_{i\bar{\sigma}}\hat{d}_{i\bar{\sigma}}] + \epsilon_d\sum_{i\sigma}1 - 2\epsilon_d\sum_{i\sigma}\hat{d}^\dagger_{i\sigma}\hat{d}_{i\sigma}$$

$$= (\text{original form}) + \frac{U}{2}.2L - U\sum_{i\sigma}\hat{d}^\dagger_{i\sigma}\hat{d}_{i\sigma} + \epsilon_d.2L - 2\epsilon_d\sum_{i\sigma}\hat{d}^\dagger_{i\sigma}\hat{d}_{i\sigma} \qquad \text{(C.7)}$$

Since the Hamiltonian is invariant under p-h exchange in the half-filled (equal number of p and h) case,

$$\langle\hat{H}\rangle = \langle\hat{H}^h\rangle \qquad \text{(C.8)}$$

This leads to

$$\boxed{\epsilon_d = -\frac{U}{2}} \qquad \text{(C.9)}$$

where we have equated coefficients of 1 and $\langle\hat{n}_{i\sigma}\rangle = \langle\hat{n}^h_{i\sigma}\rangle$ (independently) in Eq. (C.1) with that in Eq. (C.7). (In both cases, we get the same result.)

Appendix D

Atomic limit of the Hubbard model

The Hubbard Hamiltonian is

$$\hat{H} = -\sum_{<ij>\,\sigma} t_{ij}(c^{\dagger}_{i\sigma}c_{j\sigma} + \mathrm{h}.c.) + \epsilon_d \sum_{i\sigma} c^{\dagger}_{i\sigma}c_{i\sigma} + U\sum_{i} \hat{n}_{i\uparrow}\hat{n}_{i\downarrow}$$

We know,

$$[c_{i\sigma}, c^{\dagger}_{j\sigma}]_{+} = \delta_{ij} \tag{D.1}$$

and

$$\begin{aligned}[c_{i\sigma}, \hat{H}] = &-\sum_{<kl>\sigma'} t_{kl}\Big[[c_{i\sigma}, c^{\dagger}_{k\sigma'}c_{l\sigma'}] + [c_{i\sigma}, c^{\dagger}_{l\sigma'}c_{k\sigma'}]\Big] + \sum_{k\sigma'}[c_{i\sigma}, c^{\dagger}_{k\sigma'}c_{k\sigma'}] \\ &+ \frac{U}{2}\sum_{k}[c_{i\sigma}, \hat{n}_{k\sigma'}\hat{n}_{k\bar{\sigma}'}]\,. \end{aligned} \tag{D.2}$$

$$\begin{aligned}[c_{i\sigma}, c^{\dagger}_{k\sigma'}c_{l\sigma'}] &= [c_{i\sigma}, c^{\dagger}_{k\sigma'}]_{+}\, c_{l\sigma'} - c^{\dagger}_{k\sigma'}\,[c_{i\sigma}, c_{l\sigma'}]_{+} \\ &= \delta_{ik}\delta_{\sigma\sigma'}c_{l\sigma'}\,. \end{aligned} \tag{D.3}$$

Similarly,

$$[c_{i\sigma}, c^{\dagger}_{k\sigma'}c_{k\sigma'}] = \delta_{ik}\delta_{\sigma\sigma'}c_{k\sigma'} \tag{D.4}$$

$$\begin{aligned}
[c_{i\sigma}, \hat{n}_{k\sigma'}\hat{n}_{k\bar{\sigma}'}] &= [c_{i\sigma}, \hat{n}_{k\sigma'}]n_{k\bar{\sigma}'} + \hat{n}_{k\sigma'}[c_{i\sigma}, \hat{n}_{k\bar{\sigma}'}] \\
&= [c_{i\sigma}, c^{\dagger}_{k\sigma'}c_{k\sigma'}]\hat{n}_{k\bar{\sigma}'} + \hat{n}_{k\bar{\sigma}'}[c_{i\sigma}, c^{\dagger}_{k\bar{\sigma}'}c_{k\bar{\sigma}'}] \\
&= \Bigg[[c_{i\sigma}, c^{\dagger}_{k\sigma'}]_+\, c_{k\sigma'} - c^{\dagger}_{k\sigma'}[c_{i\sigma}, c_{k\sigma'}]_+\Bigg]\hat{n}_{k\bar{\sigma}'} \\
&\quad + n_{k\bar{\sigma}}\Bigg[[c_{i\sigma}, c^{\dagger}_{k\bar{\sigma}'}]_+\, c_{k\bar{\sigma}'} - c^{\dagger}_{k\bar{\sigma}'}[c_{i\sigma}, c_{k\bar{\sigma}'}]_+\Bigg] \\
&= \hat{n}_{k\bar{\sigma}'}\delta_{ik}\delta_{\sigma\sigma'}\, c_{k\sigma'} + \hat{n}_{k\sigma'}\delta_{ik}\delta_{\sigma\bar{\sigma}'}\, c_{k\bar{\sigma}'} \qquad \text{(D.5)}
\end{aligned}$$

Thus

$$[c_{i\sigma}, \hat{H}] = -2\sum_{l} t_{il}c_{l\sigma} + \epsilon_d c_{i\sigma} + U\hat{n}_{i\bar{\sigma}}c_{i\sigma} \qquad \text{(D.6)}$$

N. B. All the commutations/anti-commutations so far are for equal time operators.

$$\langle\langle [c_{i\sigma}, \hat{H}]; c^{\dagger}_{j\sigma}\rangle\rangle = -2\sum_{l} t_{il}\langle\langle c_{l\sigma}; c^{\dagger}_{j\sigma}\rangle\rangle + \epsilon_d\langle\langle c_{i\sigma}; c^{\dagger}_{j\sigma}\rangle\rangle + U\langle\langle \hat{n}_{i\bar{\sigma}}c_{i\sigma}; c^{\dagger}_{j\sigma}\rangle\rangle \qquad \text{(D.7)}$$

So considering $\hat{A} \equiv c_{i\sigma}$ and $\hat{B} \equiv c^{\dagger}_{j\sigma}$ for the first equation of motion (EoM) in Eq. (A.5), we get

$$\begin{aligned}
\omega G_{ij\,\sigma} \equiv \omega\langle\langle c_{i\sigma}; c^{\dagger}_{j\sigma}\rangle\rangle &= \langle [c_{i\sigma}, c^{\dagger}_{j\sigma}]_+\rangle + \langle\langle [c_{i\sigma}, \hat{H}]; c^{\dagger}_{j\sigma}\rangle\rangle \\
&= \delta_{ij} - 2\sum_{l} t_{il}G_{lj\,\sigma} + \epsilon_d G_{ij\,\sigma} + U\langle\langle \hat{n}_{i\bar{\sigma}}c_{i\sigma}; c^{\dagger}_{j\sigma}\rangle\rangle \qquad \text{(D.8)}
\end{aligned}$$

At the atomic limit, $t_{ij} = 0$

$$\omega G_{ij\,\sigma}(\omega) = \delta_{ij} + \epsilon_d G_{ij\,\sigma} + U\langle\langle \hat{n}_{i\bar{\sigma}}c_{i\sigma}; c^{\dagger}_{j\sigma}\rangle\rangle \qquad \text{(D.9)}$$

Therefore

$$(\omega - \epsilon_d)G_{ii\,\sigma}(\omega) = 1 + U\langle\langle \hat{n}_{i\bar{\sigma}}c_{i\sigma}; c^{\dagger}_{i\sigma}\rangle\rangle \qquad \text{(D.10)}$$

$$G_{i\,i\sigma}(\omega) = \frac{1 + U\langle\langle \hat{n}_{i\bar{\sigma}}c_{i\sigma}; c^{\dagger}_{i\sigma}\rangle\rangle}{\omega^{+} - \epsilon_d} \qquad \text{(D.11)}$$

Now the 2^{nd} term in numerator of the RHS can be evaluated again by EoM. This time $\hat{A} \equiv \hat{n}_{i\bar{\sigma}}c_{i\sigma}$ and $\hat{B} \equiv c^{\dagger}_{i\sigma}$.

So

$$\begin{aligned}\omega^+\langle\langle \hat{n}_{i\bar{\sigma}}c_{i\sigma}; c^\dagger_{i\sigma}\rangle\rangle &= \langle \hat{n}_{i\bar{\sigma}}\rangle\langle [c_{i\sigma}, c^\dagger_{i\sigma}]_+\rangle + \langle\langle \hat{n}_{i\bar{\sigma}}[c_{i\sigma}, \hat{H}]; c^\dagger_{i\sigma}\rangle\rangle \\ &= \langle \hat{n}_{i\bar{\sigma}}\rangle + [(-2\sum_l t_{il} + \epsilon_d + U)\langle\langle \hat{n}_{i\bar{\sigma}}c_{i\sigma}; c^\dagger_{i\sigma}\rangle\rangle] \quad . \end{aligned} \tag{D.12}$$

To expand the commutation above, we have used Eq. (D.6).

Now again by taking the atomic limit $t_{ij} = 0$ in the Eq. above, we find

$$\boxed{\langle\langle \hat{n}_{i\bar{\sigma}}c_{i\sigma}; c^\dagger_{i\sigma}\rangle\rangle = \frac{\langle \hat{n}_{i\bar{\sigma}}\rangle}{\omega^+ - \epsilon_d - U} \quad .} \tag{D.13}$$

So from Eq. (D.11) the site-diagonal Green's function can be written for the atomic limit (suppressing the *ii* subscript)

$$\begin{aligned} G_\sigma(\omega) &= \frac{1}{\omega^+ - \epsilon_d}[1 + U\frac{\langle \hat{n}_{i\bar{\sigma}}\rangle}{\omega^+ - \epsilon_d - U}] \\ &= \frac{\omega^+ - \epsilon_d - U + U\langle \hat{n}_{i\bar{\sigma}}\rangle}{(\omega - \epsilon_d)(\omega^+ - \epsilon_d - U)} \\ &= \frac{(\omega - \epsilon_d)\langle \hat{n}_{i\bar{\sigma}}\rangle + (\omega - \epsilon_d - U)(1 - \langle \hat{n}_{i\bar{\sigma}}\rangle)}{(\omega - \epsilon_d)(\omega^+ - \epsilon_d - U)} \quad . \end{aligned} \tag{D.14}$$

Thus

$$\boxed{G_\sigma(\omega) = \frac{\langle \hat{n}_{i\bar{\sigma}}\rangle}{\omega^+ - \epsilon_d - U} + \frac{1 - \langle \hat{n}_{i\bar{\sigma}}\rangle}{\omega^+ - \epsilon_d} \quad .} \tag{D.15}$$

Now for the half-filled case $\langle \hat{n}_{i\bar{\sigma}}\rangle = 1/2$ and $\epsilon_d = -U/2$.

Therefore at half-filling

$$\boxed{G_\sigma(\omega) = \frac{1}{2}\left[\frac{1}{\omega^+ - U/2} + \frac{1}{\omega^+ + U/2}\right] = \frac{1}{\omega^+ - \dfrac{U^2}{4\omega^+}} \quad .} \tag{D.16}$$

Thus

$$\Sigma(\omega) = \frac{U^2}{4\omega^+} \quad . \tag{D.17}$$

which has a pole at $\omega = 0$.

Appendix E

IPT self-energy calculation

The IPT self-energy is

$$\Sigma_2(\omega) = \lim_{i\omega\to\omega^+} \frac{U^2}{\beta^2} \sum_{m,p} \mathcal{G}(i\omega + i\nu_m)\mathcal{G}(i\omega_p + i\nu_m)\mathcal{G}(i\omega_p) \tag{E.1}$$

Plugging the spectral representation form $\mathcal{G}(i\omega_n) = \int_{-\infty}^{\infty} d\omega' \, \frac{D_{\mathcal{G}}(\omega')}{i\omega_n - \omega'}$ in above, we get

$$\begin{aligned}
\Sigma_2(i\omega_n) &= U^2 \int \prod_{i=1}^{3} d\epsilon_i \, D_{\mathcal{G}}(\epsilon_i) \frac{1}{\beta^2} \sum_{m,p} \frac{1}{i\omega_n + i\nu_m - \epsilon_1} \frac{1}{i\omega_p + i\nu_m - \epsilon_2} \frac{1}{i\omega_p - \epsilon_3} \\
&= U^2 \int \prod_{i=1}^{3} d\epsilon_i \, D_{\mathcal{G}}(\epsilon_i) \frac{1}{\beta^2} \sum_{m,p} \frac{1}{i\omega_n + i\nu_m - \epsilon_1} \left[\frac{1}{i\omega_p - \epsilon_3} - \frac{1}{i\omega_p + i\nu_m - \epsilon_2} \right] \\
&\qquad \times \frac{1}{i\nu_m - \epsilon_2 + \epsilon_3} \\
&= U^2 \int \prod_{i=1}^{3} d\epsilon_i \, D_{\mathcal{G}}(\epsilon_i) \frac{1}{\beta} \sum_{m} \frac{1}{i\omega_n + i\nu_m - \epsilon_1} \Big[n_F(\epsilon_3) - n_F(\epsilon_2) \Big] \frac{1}{i\nu_m - \epsilon_2 + \epsilon_3} \\
&= U^2 \int \prod_{i=1}^{3} d\epsilon_i \, D_{\mathcal{G}}(\epsilon_i) \Big[n_F(\epsilon_3) - n_F(\epsilon_2) \Big] \\
&\qquad \times \frac{1}{\beta} \sum_{m} \left[\frac{1}{i\nu_m - \epsilon_2 + \epsilon_3} - \frac{1}{i\omega_n + i\nu_m - \epsilon_1} \right] \frac{1}{i\omega_n - \epsilon_1 + \epsilon_2 - \epsilon_3}
\end{aligned}$$

$$= U^2 \int \prod_{i=1}^{3} d\epsilon_i \, D_{\mathcal{G}}(\epsilon_i) \frac{[n_F(\epsilon_3) - n_F(\epsilon_2)][n_B(\epsilon_2 - \epsilon_3) + n_F(\epsilon_1)]}{i\omega_n - \epsilon_1 + \epsilon_2 - \epsilon_3} \tag{E.2}$$

Here we have done the 2^{nd} sum in the following way.

$$\begin{aligned} \frac{1}{\beta} \sum_m \frac{1}{i\omega_n - i\nu_m - \epsilon_1} &= n_B(\epsilon_1 - i\omega_n) \\ &= \frac{1}{e^{\beta\epsilon_1} e^{-i\omega_n} - 1} \\ &= \frac{1}{e^{\beta\epsilon_1} e^{-i(2n+1)\pi} - 1} \\ &= \frac{1}{-e^{\beta\epsilon_1} - 1} \\ &= -n_F(\epsilon_1) \end{aligned} \tag{E.3}$$

Now

$$\begin{aligned} [n_F(\epsilon_3) - n_F(\epsilon_2)][n_B(\epsilon_2 - \epsilon_3)] &= [\frac{1}{e^{\beta\epsilon_3} + 1} - \frac{1}{e^{\beta\epsilon_2} + 1}] \frac{1}{e^{\beta(\epsilon_2 - \epsilon_3)} - 1} \\ &= n_F(\epsilon_3) n_F(\epsilon_2) \frac{e^{\beta\epsilon_2} - e^{\beta\epsilon_3}}{e^{\beta(\epsilon_2 - \epsilon_3)} - 1} \\ &= n_F(\epsilon_3) n_F(\epsilon_2) \frac{e^{\beta(\epsilon_2 - \epsilon_3)} - 1}{e^{\beta(\epsilon_2 - \epsilon_3)} - 1} e^{\beta\epsilon_3} \\ &= n_F(-\epsilon_3) n_F(\epsilon_2) \end{aligned} \tag{E.4}$$

$$\because n_F(-x) = \frac{1}{e^{-\beta x} + 1} = \frac{e^{\beta x}}{e^{\beta x} + 1} = e^{\beta x} n_F(x) \tag{E.5}$$

$$\begin{aligned} \therefore \, & [n_F(\epsilon_3) - n_F(\epsilon_2)][n_B(\epsilon_2 - \epsilon_3) + n_F(\epsilon_1)] \\ &= n_F(-\epsilon_3) n_F(\epsilon_2) + [n_F(\epsilon_3) - n_F(\epsilon_2)] n_F(\epsilon_1) \\ &= n_F(-\epsilon_3) n_F(\epsilon_2) + [e^{\beta\epsilon_2} - e^{\beta\epsilon_3}] n_F(\epsilon_3) n_F(\epsilon_2) n_F(\epsilon_1) \\ &= n_F(-\epsilon_3) n_F(\epsilon_2) + n_F(\epsilon_3) n_F(-\epsilon_2) n_F(\epsilon_1) \\ &\quad - n_F(-\epsilon_3) n_F(\epsilon_2) n_F(\epsilon_1) \end{aligned} \tag{E.6}$$

$$\begin{aligned}&= n_F(-\epsilon_3)n_F(\epsilon_2)[1-n_F(\epsilon_1)] + n_F(\epsilon_3)n_F(-\epsilon_2)n_F(\epsilon_1)\\ &= n_F(-\epsilon_1)n_F(\epsilon_2)n_F(-\epsilon_3) + n_F(\epsilon_1)n_F(-\epsilon_2)n_F(\epsilon_3)\end{aligned} \tag{E.7}$$

where we use

$$1 - n_F(x) = 1 - \frac{1}{e^{\beta x}+1} = e^{\beta x} n_F(x) = n_F(-x) \tag{E.8}$$

to get the last line.

Thus finally

$$\Sigma_2(i\omega_n) = U^2 \int \prod_{i=1}^{3} d\epsilon_i\, D_{\mathcal{G}}(\epsilon_i) \frac{n_F(-\epsilon_1)n_F(\epsilon_2)n_F(-\epsilon_3) + n_F(\epsilon_1)n_F(-\epsilon_2)n_F(\epsilon_3)}{i\omega_n - \epsilon_1 + \epsilon_2 - \epsilon_3} \tag{E.9}$$

By analytic continuation: $i\omega_n \to \omega^+$ we have

$$\Sigma_2(\omega) = U^2 \int \prod_{i=1}^{3} d\epsilon_i\, D_{\mathcal{G}}(\epsilon_i) \frac{n_F(-\epsilon_1)n_F(\epsilon_2)n_F(-\epsilon_3) + n_F(\epsilon_1)n_F(-\epsilon_2)n_F(\epsilon_3)}{\omega^+ - \epsilon_1 + \epsilon_2 - \epsilon_3} \tag{E.10}$$

Therefore

$$\begin{aligned}D_\Sigma(\omega) &= -\frac{1}{\pi}\mathrm{Im}\Sigma_2(\omega)\\ &= U^2 \int \prod_{i=1}^{3} d\epsilon_i\, D_{\mathcal{G}}(\epsilon_i)[n_F(-\epsilon_1)n_F(\epsilon_2)n_F(-\epsilon_3) + n_F(\epsilon_1)n_F(-\epsilon_2)n_F(\epsilon_3)]\\ &\qquad \times \delta(\omega - \epsilon_1 + \epsilon_2 - \epsilon_3)\\ &= U^2 \int \prod_{i=1}^{2} d\epsilon_i\, D_{\mathcal{G}}(\epsilon_i) D_{\mathcal{G}}(\omega - \epsilon_1 + \epsilon_2)\Big[n_F(-\epsilon_1)n_F(\epsilon_2)n_F(-\omega + \epsilon_1 - \epsilon_2)\\ &\quad + n_F(\epsilon_1)n_F(-\epsilon_2)n_F(\omega - \epsilon_1 + \epsilon_2)\Big]\\ &= U^2 \int d\epsilon_1\, D_{\mathcal{G}}(-\epsilon_1)\\ &\quad \times \Big[n_F(\epsilon_1)\int d\epsilon_2\, D_{\mathcal{G}}(\omega + \epsilon_1 + \epsilon_2) D_{\mathcal{G}}(\epsilon_2) n_F(\epsilon_2) n_F(-\omega - \epsilon_1 - \epsilon_2)\\ &\quad + n_F(-\epsilon_1)\int d\epsilon_2\, D_{\mathcal{G}}(\omega + \epsilon_1 + \epsilon_2) D_{\mathcal{G}}(\epsilon_2) n_F(-\epsilon_2) n_F(\omega + \epsilon_1 + \epsilon_2)\Big]\\ &\qquad\qquad [\text{by replacing: } \epsilon_1 \to -\epsilon_1]\end{aligned} \tag{E.11}$$

In a simpler form (suppressing $\mathcal{G}$ in subscript of $D_{\mathcal{G}}$),

$$D_\Sigma(\omega) = U^2 \int d\omega'\, D(-\epsilon) \Big[n_F(\omega')\chi_1(\omega+\omega') + n_F(-\omega')\chi_2(\omega+\omega') \Big]$$

where

$$\chi_1(\epsilon) = \int d\epsilon'\, D(\epsilon')n_F(\epsilon')D(\epsilon+\epsilon')n_F(-\epsilon-\epsilon') \tag{E.12}$$

$$\chi_2(\epsilon) = \int d\epsilon'\, D(\epsilon')n_F(-\epsilon')D(\epsilon+\epsilon')n_F(\epsilon+\epsilon') \tag{E.13}$$

Now

$$\begin{aligned}
\chi_1(-\epsilon) &= \int d\epsilon'\, D(\epsilon')n_F(\epsilon')D(-\epsilon+\epsilon')n_F(\epsilon-\epsilon') \\
&= \int d(\epsilon+\epsilon')\, D(\epsilon+\epsilon')n_F(\epsilon+\epsilon')D(-\epsilon+\epsilon+\epsilon')n_F(\epsilon-\epsilon-\epsilon') \\
&\qquad\qquad\qquad\qquad [\text{by } \epsilon' \to \epsilon+\epsilon' \text{ replacement}] \\
&= \int d\epsilon' D(\epsilon+\epsilon')n_F(\epsilon+\epsilon')D(\epsilon')n_F(-\epsilon') \\
&= \chi_2(\epsilon)
\end{aligned} \tag{E.14}$$

Thus

$$\begin{aligned}
D_\Sigma(\omega) &= U^2 \int d\omega' D_{\mathcal{G}}(-\omega') \Big[n_F(\omega')\chi_1(\omega+\omega') + n_F(-\omega')\chi_2(\omega+\omega') \Big] \\
&= U^2 \int d\omega' D_{\mathcal{G}}(-\omega') \Big[n_F(\omega')\chi_1(\omega+\omega') + n_F(-\omega')\chi_1(-\omega-\omega') \Big]
\end{aligned} \tag{E.15}$$

$$= U^2 \int d\omega' D_{\mathcal{G}}(-\omega') \Big[n_\chi(\omega,\omega') + n_\chi(-\omega,-\omega') \Big] \tag{E.16}$$

Now χ_1 can be written as convolution integration:

$$\chi_1 = \mathrm{conv}(Dn_F, D\bar{n}_F)$$

where

$$\mathrm{conv}(A,B) = \int d\epsilon' A(\epsilon')B(\epsilon+\epsilon')$$

and

$$\bar{A} \Rightarrow A(-\epsilon)$$

in the convolution. Thus after performing the convolution integration we can easily get the self energy as below:

$$\Sigma_2(\omega) = \mathrm{Re}\Sigma_2(\omega) - i\pi D_\Sigma(\omega) \tag{E.17}$$

where the real part of the self energy is obtained by Kramers-Kronig transformation of D_Σ, i.e.

$$\mathrm{Re}\Sigma_2(\omega) = -\mathcal{P}\int_{-\infty}^{\infty} \frac{d\omega' D_\Sigma(\omega')}{\omega' - \omega} \quad . \tag{E.18}$$

Appendix F

Expression for regular and singular part in self-energy in IPT

[This is a continuation of the previous appendix (Appendix E). Some of the terms used here have been defined there.]

We write the spectral density $D(\epsilon) = -\frac{1}{\pi}\mathrm{Im}\,\mathcal{G}(\epsilon)$ in terms of the regular part $D^R(\epsilon)$ and the singular part $D^S(\epsilon) = \alpha\,\delta(\epsilon)$ (α is the residue or the weight factor of the δ-function), i.e.

$$D(\epsilon) = D^R(\epsilon) + \alpha\delta(\epsilon) \tag{F.1}$$

$$\chi_1(\epsilon) = \int d\epsilon'\, D(\epsilon')D(\epsilon+\epsilon')n_F(\epsilon')n_F(-\epsilon-\epsilon') \tag{F.2}$$

$$\chi_2(\epsilon) = \int d\epsilon'\, D(\epsilon')D(\epsilon+\epsilon')n_F(-\epsilon')n_F(\epsilon+\epsilon') \tag{F.3}$$

Now

$$\chi_1(\epsilon) = \chi_1^R(\epsilon) + \chi_1^S(\epsilon) \tag{F.4}$$

$$
\begin{aligned}
\chi_1^R(\epsilon) &= \int d\epsilon'\, D^R(\epsilon')D^R(\epsilon+\epsilon')n_F(\epsilon')n_F(-\epsilon-\epsilon') \\
&\quad + \alpha \int d\epsilon'\, D^R(\epsilon')n_F(\epsilon')\delta(\epsilon+\epsilon')n_F(-\epsilon-\epsilon') \\
&\quad + \alpha \int d\epsilon'\, \delta(\epsilon')n_F(\epsilon')D^R(\epsilon+\epsilon')n_F(-\epsilon-\epsilon') \\
&= \mathrm{conv}(D^R n_F, D^R \bar{n_F}) + \alpha D^R(-\epsilon)n_F(-\epsilon)n_F(0) \\
&\quad + \alpha n_F(0)D^R(\epsilon)n_F(-\epsilon)
\end{aligned}
$$

$\because n_F(0) = \frac{1}{2}$

$$
\therefore \chi^R(\epsilon) = \mathrm{conv}(D^R n_F, D^R \bar{n_F}) + \frac{\alpha}{2}[D^R(-\epsilon) + D^R(\epsilon)]n_F(-\epsilon) \tag{F.5}
$$

For p-h symmetric case (i.e., $D(-\omega) = D(\omega)$)

$$
\boxed{\chi^R(\epsilon) = \mathrm{conv}(D^R n_F, D^R \bar{n_F}) + \alpha D^R(\epsilon)n_F(-\epsilon)} \tag{F.6}
$$

$$
\begin{aligned}
\chi_1^S &= \alpha^2 \int d\epsilon'\, \delta(\epsilon')n_F(\epsilon')\delta(\epsilon+\epsilon')n_F(-\epsilon-\epsilon') \\
&= \alpha^2 n_F(0)n_F(-\epsilon)\delta(\epsilon)
\end{aligned} \tag{F.7}
$$

i.e.,

$$
\boxed{\chi_1^S(\epsilon) = \frac{\alpha^2}{2}n_F(-\epsilon)\delta(\epsilon)} \tag{F.8}
$$

Now

$$
D_\Sigma(\omega) = U^2 \int d\omega' D(-\omega')[n_F(\omega')\chi_1(\omega+\omega') + n_F(-\omega')\chi_1(-\omega-\omega')] \tag{F.9}
$$

Regular part of

$$
D_\Sigma^1(\omega) \equiv U^2 \int d\omega' D(-\omega')n_F(\omega')\chi_1(\omega+\omega') \tag{F.10}
$$

is

$$
\begin{aligned}
D_\Sigma^{1R}(\omega) &= U^2 \int d\omega'\, D^R(-\omega') n_F(\omega') \chi_1^R(\omega+\omega') \\
&\quad + \frac{U^2\alpha^2}{2} \int d\omega'\, D^R(-\omega') n_F(\omega') n_F(-\omega-\omega') \delta(\omega+\omega') \\
&\quad + U^2\alpha \int d\omega'\, \delta(-\omega') n_F(\omega') \chi_1^R(\omega+\omega') \\
&= U^2 \mathrm{conv}(\bar{D}^R n_F, \chi_1^R) + \frac{U^2\alpha^2}{2} n_F(0) n_F(-\omega) D^R(\omega) + U^2 \alpha n_F(0) \chi_1^R(\omega) \\
&= U^2 \left[\mathrm{conv}(\bar{D}^R n_F, \chi_1^R) + \frac{\alpha^2}{4} n_F(-\omega) D^R(\omega) + \frac{\alpha}{2} \chi_1^R(\omega) \right] \qquad \text{(F.11)}
\end{aligned}
$$

And regular part of

$$
D_\Sigma^2(\omega) \equiv U^2 \int d\omega' D(-\omega') n_F(-\omega') \chi_1(-\omega-\omega') \qquad \text{(F.12)}
$$

is

$$
\begin{aligned}
D_\Sigma^{2R}(\omega) &= U^2 \int d\omega'\, D^R(-\omega') n_F(-\omega') \chi_1^R(-\omega-\omega') \\
&\quad + \frac{U^2\alpha^2}{2} \int d\omega'\, D^R(-\omega') n_F(-\omega') n_F(\omega+\omega') \delta(-\omega-\omega') \\
&\quad + U^2\alpha \int d\omega'\, \delta(-\omega') n_F(-\omega') \chi_1^R(-\omega-\omega') \\
&= U^2 \mathrm{conv}(\bar{D}^R \bar{n}_F, \bar{\chi}_1^R) + \frac{U^2\alpha^2}{2} n_F(0) n_F(\omega) D^R(\omega) + U^2 \alpha n_F(0) \chi_1^R(-\omega) \\
&= U^2 \left[\mathrm{conv}(\bar{D}^R \bar{n}_F, \bar{\chi}_1^R) + \frac{\alpha^2}{4} n_F(\omega) D^R(\omega) + \frac{\alpha}{2} \chi_1^R(-\omega) \right] \qquad \text{(F.13)}
\end{aligned}
$$

Now

$$\begin{aligned}
D^S_\Sigma(\omega) &= U^2 \int d\omega'\, D^S(-\omega') \Big[n_F(\omega')\chi^S_1(\omega+\omega') + n_F(-\omega')\chi^S_1(-\omega-\omega') \Big] \\
&= U^2 \int d\omega'\, \alpha\, \delta(-\omega') \\
&\times \Big[n_F(\omega') \frac{\alpha^2}{2} n_F(-\omega-\omega')\delta(\omega+\omega') + n_F(-\omega')\frac{\alpha^2}{2} n_F(\omega+\omega')\delta(-\omega-\omega') \Big] \\
&= \frac{U^2\alpha^2}{2}\delta(-\omega)\Big[n_F(-\omega)n_F(0) + n_F(\omega)n_F(0) \Big] \\
&= \frac{U^2\alpha^3}{4}[n_F(-\omega)+n_F(\omega)]\delta(\omega) \qquad \text{(F.14)}
\end{aligned}$$

$$\because n_F(-\omega)+n_F(\omega) = 1 \quad , \qquad \text{(F.15)}$$

$$\boxed{D^S_\Sigma(\omega) = \frac{U^2\alpha^3}{4}\delta(\omega)} \quad . \qquad \text{(F.16)}$$

Therefore

$$\begin{aligned}
\Sigma(\omega) &= \int d\omega' \frac{D_\Sigma}{\omega-\omega'} \\
&= \frac{U^2\alpha^3}{4}\int d\omega' \frac{\delta(\omega')}{\omega-\omega'} \\
&= \frac{U^2\alpha^3}{4\omega^+} \quad . \qquad \text{(F.17)}
\end{aligned}$$

Here we have considered the major contribution coming from the singular part of the self-energy spectral density D_Σ.
Now

$$\begin{aligned}
G(\omega) &= \int d\epsilon\, \frac{D_0(\epsilon)}{\gamma(\omega)-\epsilon} \\
&= \frac{1}{\gamma(\omega)}\int d\epsilon\, D_0(\epsilon)(1-\epsilon/\gamma(\omega))^{-1} \\
&= \frac{1}{\gamma(\omega)}\int d\epsilon\, D_0(\epsilon)[1+\frac{\epsilon}{\gamma(\omega)}+\frac{\epsilon^2}{\gamma^2(\omega)}+\cdots] \\
&= \frac{1}{\gamma(\omega)}\Big[1+\frac{M_2}{\gamma^2(\omega)}\Big] \quad . \qquad \text{(F.18)}
\end{aligned}$$

where $M_2 = \int d\epsilon\, \epsilon^2 D_0(\epsilon)$.

The Dyson's equation:

$$\begin{aligned}
\mathcal{G}^{-1}(\omega) &= G^{-1}(\omega) + \Sigma(\omega) \\
&= \gamma(\omega)\left[1 + \frac{M_2}{\gamma(\omega)^2}\right]^{-1} + \Sigma(\omega) \\
&\simeq \gamma(\omega)\left[1 - \frac{M_2}{\gamma(\omega)^2}\right] + \Sigma(\omega) \\
&= \gamma(\omega) - \frac{M_2}{\gamma(\omega)} + \Sigma(\omega) \\
&= \omega^+ - \frac{M_2}{\omega - \Sigma(\omega)} \quad . \qquad \text{(F.19)}
\end{aligned}$$

As $\omega \to 0$,

$$\begin{aligned}
\mathcal{G}^{-1} &= \omega^+ + \frac{M_2}{\Sigma(\omega)} \\
&= \omega^+ + \frac{M_2 4\omega^+}{U^2\alpha^3} \qquad \text{(F.20)}
\end{aligned}$$

Now

$$\mathcal{G}(\omega) = \alpha \int d\epsilon \, \frac{\delta(\epsilon)}{\omega - \epsilon} = \frac{\alpha}{\omega^+} \quad . \qquad \text{(F.21)}$$

$$\therefore \boxed{\frac{1}{\alpha} = 1 + \frac{4M_2}{U^2\alpha^3}} \quad . \qquad \text{(F.22)}$$

Appendix G

Analytical calculation of U_{c1} and U_{c2} at $T = 0$ in IPT

In this chapter, we demonstrate that a pole structure ansatz for the Green's functions and self energy combined with the IPT equations yields U_{c1} and U_{c2}, the bounds of the U interval where the metallic and insulating solutions coexist at zero temperature.
If $\mathcal{G}$ has simple poles at $\pm\omega_0$ with equal residue $\alpha/2$ (due to symmetry), then the singular part of $\mathcal{G}$ may be expressed as

$$\mathcal{G}(\omega) = \frac{\alpha}{2}\left[\frac{1}{\omega-\omega_0} + \frac{1}{\omega+\omega_0}\right] = \alpha\frac{\omega}{\omega^2-\omega_0^2}\,. \tag{G.1}$$

Now using the Dyson's equation ($\mathcal{G}^{-1} = G^{-1} + \Sigma$) and the moment expansion of the Hilbert transform, we get

$$\Sigma(\omega) = \frac{1}{\alpha}\frac{\omega^2-\omega_0^2}{\omega} - \omega + \Sigma(\omega) - \frac{M_2}{\omega-\Sigma(\omega)}\,.$$

where M_2 is the second moment of the non-interacting density of states $D_0(\omega)$. Thus

$$\Sigma(\omega) = \omega - \frac{M_2}{\frac{1}{\alpha}\frac{\omega^2-\omega_0^2}{\omega} - \omega}\,. \tag{G.2}$$

Therefore poles occur at

$$\omega_0' = \pm\frac{\omega_0}{\sqrt{1-\alpha}}\,. \tag{G.3}$$

Using the structure of $\mathcal{G}$ in the IPT equations, it is easy to see that poles at $\pm\omega_0$ in $\mathcal{G}$ will give rise to poles in the self energy at $\pm\omega_0$ and $\pm3\omega_0$. Only the latter are physically acceptable, since the former leads to a self-consistent value of the residue α equal to 0. So when $\omega_0' = \pm 3\omega_0$, α turns out to be $8/9$. The singular part (by using the same formalism to get Eq. (F.18), but for two poles at $3\omega_0$ now) and the FL part of the self energy may be expressed in a combined way as

$$\Sigma(\omega) = \frac{U^2\alpha^3}{8}\left[\frac{1}{\omega - 3\omega_0} + \frac{1}{\omega + 3\omega_0}\right] - \left(1 - \frac{1}{Z}\right)\omega\,. \tag{G.4}$$

This gives

$$\Sigma(\omega_0) = -\frac{U^2\alpha^3}{32\omega_0} - \left(1 - \frac{1}{Z}\right)\omega_0\,. \tag{G.5}$$

Now $\mathcal{G}^{-1}(\omega_0) = 0$. So the Dyson equation (Eq. (22)) gives

$$\Sigma(\omega_0) = -G^{-1}(\omega_0) = -\gamma(\omega_0) - \frac{M_2}{\gamma(\omega_0)} = -\omega_0 + \Sigma(\omega_0) - \frac{M_2}{\omega_0 - \Sigma(\omega_0)} \tag{G.6}$$

and hence, after rearranging we get

$$\omega_0^2 = Z\left(M_2 - \frac{U^2\alpha^3}{32}\right). \tag{G.7}$$

The above result shows that the pole position is proportional to the square root of the quasiparticle weight. The transition from the metallic to the insulating regime occurs when $\omega_0 = 0$. This occurs when $M_2 = \frac{U^2\alpha^3}{32}$, i.e. for HCL, with $\alpha = 8/9$,

$$\frac{U_{c2}}{t_*} = \frac{4}{\alpha^{3/2}} = \frac{27}{4\sqrt{2}}\,. \tag{G.8}$$

To get U_{c1}, we refer back to Eq. (1.9) which holds in the insulating phase. This self consistent equation for the pole residue in the insulating phase α has real roots only when $U^2 \geq 27M_2$, i.e. for HCL

$$U_{c1} = \frac{3\sqrt{3}}{\sqrt{2}}t_*\,. \tag{G.9}$$

The above analysis shows that we can analytically estimate U_{c1} and U_{c2} within the same framework.

Appendix H

DC conductivity and specific heat for the insulating case (IPT)

The DC conductivity can be written in the following form

$$\sigma_{\rm DC} = \sigma_0 \int_{\Delta_g}^{\infty} d\omega (-\frac{dn_F}{d\omega}) f(\omega) \tag{H.1}$$

where $f(\omega)$ contains real or imaginary part of Green's functions and/or self-energies (e.g. for Bethe lattice, $f(\omega) = D^2(\omega)$).

Here we look at the region where $\Delta_g << T$ ($k_B = 1$). So it is legitimate to take the limit $T \to 0$.
Now

$$n_F(\omega) = \frac{1}{e^{\beta\omega} + 1} \tag{H.2}$$

So

$$\frac{dn_F}{d\omega} = -\frac{1}{(e^{\beta\omega} + 1)^2} \beta e^{\beta\omega}$$

As $\beta \to 0$ (i.e. $T \to 0$),

$$\frac{dn_F}{d\omega} = -\beta e^{-\beta\omega} \tag{H.3}$$

Now for a quantity

$$Q = \int d\omega e^{-\beta\omega} f(\omega) \tag{H.4}$$

Using by parts we can re-write

$$
\begin{aligned}
Q &= -\frac{1}{\beta}e^{-\beta\omega}f(\omega) - \int d\omega(-\frac{1}{\beta}e^{-\beta\omega})f'(\omega) \\
&= -\frac{1}{\beta}e^{-\beta\omega}f(\omega) + (+\frac{1}{\beta})(-\frac{1}{\beta}e^{-\beta\omega})f'(\omega) - \frac{1}{\beta}\int d\omega(-\frac{1}{\beta}e^{-\beta\omega})f''(\omega) \\
&= -\frac{1}{\beta}e^{-\beta\omega}\left[f(\omega) + \frac{1}{\beta^2}f''(\omega) + \cdots\right]_{\Delta_g}^{\infty} \qquad \text{(H.5)}
\end{aligned}
$$

[only even ordered derivative contributes for a symmetric DoS]

Now the most significant contribution comes from the 3rd term in the bracket at very low T.

Therefore as $\beta \to \infty$

$$Q \simeq -\frac{1}{\beta^3}f''(\omega) \qquad \text{(H.6)}$$

Thus

$$
\begin{aligned}
\sigma &= \sigma_0(+\beta)(-\frac{1}{\beta})\frac{1}{\beta^2}e^{-\beta\omega})f(\omega)|_{\Delta_g}^{\infty} \\
&= \sigma_0\frac{1}{\beta^2}e^{-\beta\Delta_g}f(\Delta_g) \qquad \text{(H.7)}
\end{aligned}
$$

So

$$\sigma = \sigma_0 T^2 e^{-\Delta_g/(k_B T)}f(\Delta_g) \qquad \text{(H.8)}$$

[Here we assumed that $f(\omega)$ changes negligibly at $T \to 0$]

Similarly the internal energy can be written in the same form

$$E = \int d\omega\, n_F(\omega)g(\omega) \qquad \text{(H.9)}$$

As $\beta \to \infty$,

$$\frac{dn_F}{dT} = -\frac{1}{(e^{\beta\omega}+1)^2}\omega e^{\beta\omega} = -\omega e^{-\beta\omega} \qquad \text{(H.10)}$$

$$C_v(T) = \frac{dE}{dT} = -\int d\omega\, e^{-\beta\omega}f(\omega) \qquad \text{(H.11)}$$

where $f(\omega) = \omega g(\omega)$.

Again following the same procedure we get

$$C_v(T) = \frac{1}{\beta}e^{-\beta\omega}\left[f(\omega) + \frac{1}{\beta}f'(\omega) + \frac{1}{\beta^2}f''(\omega) + \cdots\right]_{\Delta_g}^{\infty} \tag{H.12}$$

Here significant contribution comes from the 2nd term.

Thus as $T \to 0$,

$$C_v(T) = T^2 e^{-\Delta_g/(k_B T)} f'(\Delta_g) \quad . \tag{H.13}$$

Appendix I

Derivation of symmetry restoration condition in LMA

We rewrite Eq. (2.42):

$$
\begin{aligned}
G(\omega) &= \frac{1}{2}\left[\frac{1}{\mathcal{G}^{-1}(\omega)-\Sigma_\uparrow^{\rm tot}(\omega)}+\frac{1}{\mathcal{G}^{-1}(\omega)-\Sigma_\downarrow^{\rm tot}(\omega)}\right]\\
&= \frac{\mathcal{G}^{-1}-\frac{1}{2}(\Sigma_\uparrow^{\rm tot}+\Sigma_\downarrow^{\rm tot})}{(\mathcal{G}^{-1})^2+\Sigma_\uparrow^{\rm tot}\Sigma_\downarrow^{\rm tot}-\mathcal{G}^{-1}(\Sigma_\uparrow^{\rm tot}+\Sigma_\downarrow^{\rm tot})}\\
&\qquad\text{[hence onward we drop } (\omega) \text{ for better visibility]}\\
&= \frac{\mathcal{G}^{-1}-\frac{1}{2}(\Sigma_\uparrow^{\rm tot}+\Sigma_\downarrow^{\rm tot})}{[\mathcal{G}^{-1}-\frac{1}{2}(\Sigma_\uparrow^{\rm tot}+\Sigma_\downarrow^{\rm tot})]^2-(\Sigma_\uparrow^{\rm tot}-\Sigma_\downarrow^{\rm tot})^2/4}\\
&= \frac{1}{\mathcal{G}^{-1}-\frac{1}{2}(\Sigma_\uparrow^{\rm tot}+\Sigma_\downarrow^{\rm tot})-\dfrac{(\Sigma_\uparrow^{\rm tot}-\Sigma_\downarrow^{\rm tot})^2/4}{\mathcal{G}^{-1}-\dfrac{1}{2}(\Sigma_\uparrow^{\rm tot}+\Sigma_\downarrow^{\rm tot})}}
\end{aligned}
\tag{I.1}
$$

Therefore from Dyson's Eq. ($G^{-1}=\mathcal{G}^{-1}-\Sigma$),

$$
\Sigma(\omega)=\frac{1}{2}[\Sigma_\uparrow^{\rm tot}(\omega)+\Sigma_\downarrow^{\rm tot}(\omega)]+\frac{[\Sigma_\uparrow^{\rm tot}(\omega)-\Sigma_\downarrow^{\rm tot}(\omega)]^2/4}{\mathcal{G}^{-1}(\omega)-\frac{1}{2}[\Sigma_\uparrow^{\rm tot}(\omega)+\Sigma_\downarrow^{\rm tot}(\omega)]}
\tag{I.2}
$$

Now once we ensure the imaginary part of $\Sigma(\omega)\sim\omega^2$, we are done.

$$
\begin{aligned}
{\rm Im}\Sigma(\omega) &= \frac{1}{2}[{\rm Im}(\Sigma_\uparrow^{\rm tot}(\omega)+\Sigma_\downarrow^{\rm tot}(\omega))]+{\rm Im}\frac{A^2}{B}\\
&= \frac{1}{2}[{\rm Im}(\Sigma_\uparrow^{\rm tot}(\omega)+\Sigma_\downarrow^{\rm tot}(\omega)\,)]-\frac{{\rm Re}A^2\,{\rm Im}B}{|B|^2}+\frac{{\rm Im}A^2\,{\rm Re}B}{|B|^2}
\end{aligned}
\tag{I.3}
$$

where

$$A \equiv [\Sigma_{\uparrow}^{\text{tot}}(\omega) - \Sigma_{\downarrow}^{\text{tot}}(\omega)]/2 \tag{I.4}$$

and

$$B \equiv \mathcal{G}^{-1}(\omega) - \frac{1}{2}[\Sigma_{\uparrow}^{\text{tot}}(\omega) + \Sigma_{\downarrow}^{\text{tot}}(\omega)] \tag{I.5}$$

Now we wish to make a few more definitions at $\omega \to 0$ limit:

$$\text{Im}\Sigma_{\sigma}^{\text{tot}} \sim \omega^2 \equiv P_\sigma \omega^2 \tag{I.6}$$

$$\text{Re}\Sigma_{\sigma}^{\text{tot}} \sim \text{Re}\Sigma_{\sigma}^{\text{tot}}(0) + (1 - 1/Z_\sigma)\omega \equiv M_\sigma + N_\sigma \omega \tag{I.7}$$

$$M \equiv (M_\uparrow + M_\downarrow)/2 \tag{I.8}$$

$$N \equiv (N_\uparrow + N_\downarrow)/2 \tag{I.9}$$

$$P \equiv (P_\uparrow + P_\downarrow)/2 \tag{I.10}$$

$$\Delta M \equiv (M_\uparrow - M_\downarrow)/2 \tag{I.11}$$

$$\Delta P \equiv (P_\uparrow - P_\downarrow)/2 \tag{I.12}$$

$$\Delta N \equiv (N_\uparrow - N_\downarrow)/2 \tag{I.13}$$

$$S^R \equiv \text{Re}S(\omega) \tag{I.14}$$

$$S^I \equiv \text{Im}S(\omega) \tag{I.15}$$

Now

$$\begin{aligned} A^2 &= (\Delta M + \Delta N\omega - i\,\Delta P\omega^2)^2 \\ &= (\Delta M + \Delta N\omega)^2 - (\Delta P)^2\omega^4 + 2i\,(\Delta M + \Delta N\omega)\Delta P\omega^2 \\ &= (\Delta M)^2 + 2\Delta M\Delta N\omega + (\Delta N)^2\omega^2 + 2i\,\Delta M\Delta P\omega^2 \end{aligned} \tag{I.16}$$

and

$$B = \omega - S^R - (M + N\omega) - i\,(S^I + P\omega^2) \quad [\because \mathcal{G}^{-1}(\omega) = \omega - S(\omega)] \tag{I.17}$$

Now we want to care two things:

1. Keep the lowest power of ω in the denominator, so that we get the most significant contribution overall.

2. Make sure that denominator is finite so that divergent terms do not arise.

Lowest power term in denominator, i.e. $|B|^2$ is constant ($\mathcal{O}(1)$). This confirms the condition 2 as well. If we keep the term up to $\mathcal{O}(\omega^2)$ in the numerator, we find using Eq.s (I.3), (I.16), and (I.17),

$$\begin{aligned}\mathrm{Im}\Sigma(\omega) = {} & P\omega^2 + [\,(\Delta M)^2 + 2\Delta M \Delta N \omega + (\Delta N)^2\omega^2\,]S^I\mathcal{O}(1) + (\Delta M)^2 P\omega^2 \\ & - 2\Delta M \Delta P[S^R + M]\omega^2\mathcal{O}(1)\end{aligned} \tag{I.18}$$

Note here in $S^{R/I}$ we have considered Taylor series expansion up to $\mathcal{O}(\omega^2)$ considering multiplication with other terms.

Thus from Eq. (I.18), to get purely $\mathrm{Im}\Sigma(\omega) \sim \omega^2$, we may need

$$\boxed{\Delta M = 0} \tag{I.19}$$

i.e.

$$M_\uparrow = M_\downarrow \tag{I.20}$$

which means

$$\boxed{\mathrm{Re}\Sigma^{\mathrm{tot}}_\uparrow(0) = \mathrm{Re}\Sigma^{\mathrm{tot}}_\downarrow(0)} \tag{I.21}$$

Appendix J

Behavior of $S(\omega)$ at $\omega = 0$ in LMA

From Dyson's equation,

$$\mathcal{G}^{-1}(\omega) = G^{-1}(\omega) + \Sigma(\omega) \tag{J.1}$$

i.e.

$$\omega^{+} - S(\omega) = G^{-1}(\omega) + \Sigma(\omega) \quad . \tag{J.2}$$

Therefore

$$S(\omega) = \omega^{+} - G^{-1}(\omega) - \Sigma(\omega) \quad . \tag{J.3}$$

Now once we restore symmetry, we have

$$\begin{aligned}\Sigma(0) &= \frac{1}{2}[\Sigma_{\uparrow}^{\text{tot}}(0) + \Sigma_{\downarrow}^{\text{tot}}(0)] \\ &= \frac{1}{2}[-x + \Sigma_{\uparrow}(0) + x + \Sigma_{\downarrow}(0)] \\ &= \frac{1}{2}[\Sigma_{\uparrow}(0) + \Sigma_{\downarrow}(0)] \quad .\end{aligned} \tag{J.4}$$

Thus

$$\begin{aligned}\mathrm{Re}\Sigma(0) &= \frac{1}{2}[\mathrm{Re}\Sigma_{\uparrow}(0) + \mathrm{Re}\Sigma_{\downarrow}(0)] \\ &= 2[x + \mathrm{Re}\Sigma_{\uparrow}(0)]\end{aligned} \tag{J.5}$$

[used symmetry restoration condition above: $\mathrm{Re}\Sigma_{\uparrow}(0) - \mathrm{Re}\Sigma_{\downarrow}(0) = 2x$]

and

$$\mathrm{Im}\Sigma(0) = 0 \qquad [\ \because \mathrm{Im}\Sigma(\omega) \sim \omega^2 \text{ at } \omega \to 0\ ] \tag{J.6}$$

Now

$$\mathrm{Re}S(0) = -\mathrm{Re}G^{-1}(0) + 2[x + \mathrm{Re}\Sigma_{\uparrow}(0)] \tag{J.7}$$

and

$$\begin{aligned}
\mathrm{Im}S(0) &= -\mathrm{Im}G^{-1}(0) \\
&= \frac{1}{|G(0)|^2}\mathrm{Im}G(0) \\
&= -\frac{1}{\pi}\frac{\pi^2}{[\mathrm{Re}G(0)]^2 + [\mathrm{Im}G(0)]^2}[-\frac{1}{\pi}\mathrm{Im}G(0)] \\
&= -\frac{1}{\pi}\frac{D(0)}{[\mathrm{Re}G(0)]^2/\pi^2 + D^2(0)}
\end{aligned} \tag{J.8}$$

Now in the *p*-*h* symmetric case,

$$\mathrm{Re}G(\omega) = -\mathrm{Re}G(-\omega) \tag{J.9}$$

Therefore $\mathrm{Re}G(0) = 0$ and hence from Eq. (J.8)

$$\boxed{\mathrm{Im}S(0) = -\frac{1}{\pi D(0)}} \tag{J.10}$$

Appendix K

Estimating the pole in $\Pi^{+-}(\omega)$ in LMA

The full transverse polarization $\Pi^{+-}(\omega)$ is calculated from the RPA sum of bare polarization ${}^{0}\Pi^{+-}(\omega)$:

$$\begin{aligned}\Pi &= \frac{{}^{0}\Pi}{1 - U{}^{0}\Pi} \\ &= \frac{(\mathrm{Re}{}^{0}\Pi + i\,\mathrm{Im}{}^{0}\Pi)[(1 - U\mathrm{Re}{}^{0}\Pi) + i\,U\mathrm{Im}{}^{0}\Pi]}{(1 - U\mathrm{Re}{}^{0}\Pi)^2 + (U\mathrm{Im}{}^{0}\Pi)^2}\end{aligned} \tag{K.1}$$

[ω dependence and $+-$ superscript in above equation have been suppressed for clarity.]
So

$$\mathrm{Im}\Pi = \frac{\mathrm{Im}{}^{0}\Pi\ \mathrm{Re}(1 - U{}^{0}\Pi) + \mathrm{Re}{}^{0}\Pi\ U\mathrm{Im}{}^{0}\Pi}{(1 - U\mathrm{Re}{}^{0}\Pi)^2 + (U\mathrm{Im}{}^{0}\Pi)^2} \tag{K.2}$$

Thus writing explicitly as a function of ω, we get

$$\boxed{\mathrm{Im}\Pi(\omega) = \frac{\mathrm{Im}{}^{0}\Pi(\omega)}{(1 - U\mathrm{Re}{}^{0}\Pi(\omega))^2 + (U\mathrm{Im}{}^{0}\Pi(\omega))^2}} \tag{K.3}$$

We seek whether a pole can arise in $\Pi(\omega)$, we can express above Eq. further as

$$\mathrm{Im}\Pi(\omega) = \frac{1}{U}\frac{U\mathrm{Im}{}^{0}\Pi(\omega)}{(1 - U\mathrm{Re}{}^{0}\Pi(\omega))^2 + (U\mathrm{Im}{}^{0}\Pi(\omega))^2} \tag{K.4}$$

Now $\mathrm{Im}^0\Pi(\omega) \simeq \pi|\omega|\mathcal{D}_\uparrow(0)\mathcal{D}_\downarrow(0) \to 0$ as $\omega \to 0$. Considering $U\mathrm{Im}^0\Pi(\omega)$ as ϵ we have

$$\begin{aligned}\frac{1}{\pi}\lim_{\omega\to 0}\mathrm{Im}\Pi(\omega) &= \frac{1}{\pi}\lim_{\epsilon\to 0}\frac{1}{U}\frac{\epsilon}{(1-U\mathrm{Re}^0\Pi(\omega))^2+\epsilon^2} \\ &= \frac{1}{U}\delta(1-U\mathrm{Re}^0\Pi(\omega)) \\ &= \frac{\delta(\omega-\omega_0)}{U^2\left|\frac{d\mathrm{Re}^0\Pi(\omega)}{d\omega}\right|_{\omega_0}} \qquad \text{(K.5)}\end{aligned}$$

If $\omega_0 = 0$, then

$$\frac{1}{\pi}\mathrm{Im}\Pi(\omega) = Q\delta(\omega)\,, \qquad \text{(K.6)}$$

where

$$\boxed{Q = \left[U^2\left|\frac{d\mathrm{Re}^0\Pi(\omega)}{d\omega}\right|_0\right]^{-1}\quad .} \qquad \text{(K.7)}$$

Appendix L

Plotting distribution of sample points using logarithmic binning

Introduction

Logarithmic binning is one of the methods to examine power law behavior in statistical data. Suppose we expect a power law distribution for data variable x as

$$P(x) \sim x^{-\alpha} \quad . \tag{L.1}$$

Then if we plot $\log P(x)$ vs. $\log x$, the slope should give the value of the power law exponent, i.e. α.

Basic feature

Let us assume that we have a set of data points $\{x\}$, which we want to bin logarithmically and therefore we wish to set up a grid on x-axis with n number of bins and bin-width b.
Thus

$$\log x_{i+1} = \log x_i + b \qquad i \text{ goes 1 to } n \tag{L.2}$$

Therefore

$$b = \log \frac{x_{i+1}}{x_i} \tag{L.3}$$

$$\Rightarrow x_{i+1} = e^b x_i \equiv \Delta x_i \tag{L.4}$$

(*N. B.:* For the sake of convenience, we have used the natural base e above.

However, one can replace e by other bases like 10, 2, etc. whenever it is required.)
Thus on x-grid, width w_i changes with index i

$$w_i = x_{i+1} - x_i = (\Delta - 1)x_i \tag{L.5}$$

This is the remarkable difference from the conventional linear binning. In log-binning the width is dynamic (i-dependent) whereas in linear binning it is always constant.

Binning procedure

Goal

So we need to plot n histograms h_i ($i \in [1, n]$). h_i should represent data points that fall between x_i and x_{i+1}. So our job will be only to count how many data points from the set $\{x\}$ fall in the interval $[\log x_i, \log x_{i+1})$ (we call it *floor*) or $(\log x_i, \log x_{i+1}]$ (we call it *ceiling*) and then we denote it by h_i.

Inputs

We shall take the following as inputs:

(i) Number of bins: n

(ii) $x_{\min}$: generally 1 or the minimum from the data

(iii) $x_{\max}$: some maximum range or the maximum of the data

Counting

Set $x_1 = x_{\min}$ and $x_{n+1} = x_{\max}$

Method 1: Now the bin size in the log-scale can be found from Eq. (L.3)

$$\boxed{b = \frac{1}{n} \log \frac{x_{n+1}}{x_1}} \tag{L.6}$$

Now if our data value is X, we can find its bin index by finding the following floor or ceiling value.

$$\boxed{i = \lfloor \frac{1}{b} \log \frac{x_{n+1}}{X} \rfloor \qquad (\text{or} \quad = \lceil \frac{1}{b} \log \frac{x_{n+1}}{X} \rceil)} \tag{L.7}$$

We count how many data points belong to the same i (using `count=count+1` algorithm) and determine the corresponding h_i.

Method 2: We can also do the similar counting by directly checking how many data points fall between the interval, i.e. whether $\log x_i \leq \log X < \log x_{i+1}$ (or $\log x_i < \log X \leq \log x_{i+1}$).

Plotting

In the histogram plot we wish to plot h_i Vs $\bar{x}_i$ where $\bar{x}_i$ is the mean-value of x_i and x_{i+1}, i.e.

$$\bar{x}_i = \frac{1}{2}(x_i + x_{i+1}) \tag{L.8}$$

Once we set up x_1, we can iteratively produce x_2, x_3, $\ldots$, x_n iteratively from Eq. (L.4).

One more extra care: We can notice that the width $w \propto x$ and we expect $P(x) \propto x^{\alpha}$. Since the histogram depends both on the width and also the distribution,

$$h(x) \propto x.x^{\alpha} \propto x^{\alpha+1} \tag{L.9}$$

So we need to scale down $h(x)$ by its width $w(x)$, i.e. we need to plot h_i/w_i vs. $\bar{x}_i$ in our numerical computation.

Addendum

IPT and LMA: a comparison of results

Features	**IPT**	**LMA**
Metal-insulator transition	observed	observed
Metal-insulator coexistence regime	larger	much smaller
Fermi liquid scaling to non-interacting limit	all the way till $\omega \lesssim \omega_L$	only for $\omega << \omega_L$
Strong correlation universality in spectra	not observed	observed
Finite temperature scaling	poor	good
Universality in the resistivity peak position	observed	not observed
Specific heat	unphysical anomaly observed	physically consistent
Linear resistivity in p-h asymmetric case	not observed	observed

Bibliography

[1] P. W. Anderson, *Phys. Rev.* **130**, 439 (1963).

[2] K. S. Novoselov, A. K. Geim, *et al.*, Nature **438**, 197 (2005).

[3] M. Z. Hasan and C. L. Kane, *Rev. Mod. Phys.* **82**, 3045 (2010).

[4] S. Sachdev and M. Muller, *J. Phys.: Condens. Matter* **21**, 164216 (2009).

[5] C. Kittel, *Introduction to Solid State Physics*, 7 ed. (John Wiley & Sons, New York, 1996).

[6] P. Drudé, *Ann. der Phys.* **306 (3)**, 566 (1900).

[7] P. Drudé, *Ann. der Phys.* **308 (11)**, 369 (1900).

[8] N. W. Ashcroft and N. D. Mermin, *Solid State Physics* (Harcourt, Orlando, 1976).

[9] W. Kohn and L. J. Sham, *Phys. Rev.* A **140**, 1133 (1965).

[10] J. H. de Boer and E. J. W. Verwey, *Proc. Phys. Soc* **49**, 59 (1937).

[11] N. F. Mott and R. Peierls, *Proc. Phys. Soc* **49**, 72 (1937).

[12] N. F. Mott, *Proc. Phys. Soc* A **62**, 416 (1949).

[13] H. Kuwamoto, J. M. Honig, and J. Appel, Phys. Rev. B **22**, 2626 (1980).

[14] D. B. McWhan *et al.*, *Phys. Rev. Lett.* **27**, 941 (1971).

[15] J. Kondo, *Prog. Theo. Phys.* **32**, 37 (1964).

[16] C. Petrillo *et al.*, *Phys. Rev.* B **74**, 085404 (2006).

[17] K. Wakabayashi and K. Harigaya, *J. Phys. Soc. Japan* **72**, 998 (2003).

[18] D. K. Campbell, D. Baeriswyl, and S. Mazumdar, *Synthetic Metals* **17**, 197 (1987).

[19] A. C. Hewson, *The Kondo Problem to Heavy Fermions* (Cambridge University Press, Cambridge, 1993).

[20] E. Dagotto, *Rev. Mod. Phys.* **66**, 763 (1994).

[21] P. Gegenwart *et al.*, *Phys. Rev. Lett.* **81**, 1501 (1998).

[22] P. Gegenwart *et al.*, *Phys. Rev. Lett.* **89**, 056402 (2002).

[23] L. Landau, *Zh. Eksp. Teor. Fiz.***30**, 1058 (1956).

[24] L. Landau, *Sov. Phys. JETP***3**, 920 (1957).

[25] A. A. Abrikosov and I. M. Khalatnikov, *Rep. Prog. Phys.* **22**, 329 (1959).

[26] J. M. Luttinger, Phys. Rev. **119**, 1153 (1960).

[27] J. S. Langer and V. Ambegaokar, *Phys. Rev.* **121**, 1090 (1961).

[28] D. C. Langreth, *Phys. Rev.* **150**, 516 (1966).

[29] D. B. McWhan *et al.*, *Phys. Rev.* B **7**, 1920 (1973).

[30] J. C. Hubbard, *Proc. R. Soc.* A **276**, 238 (1963).

[31] M. C. Gutzwiller, *Phys. Rev. Lett.* **10**, 59 (1963).

[32] J. Kanamori, Prog. Theor. Phys. **30**, 275 (1963).

[33] M. C. Gutzwiller, *Phys. Rev. Lett.* **10**, 159 (1963).

[34] J. C. Slater, *Phys. Rev.* **82**, 538 (1951).

[35] P. W. Anderson, *Phys. Rev.* **79**, 350 (1950).

[36] D. R. Penn, *Phys. Rev. Lett.* **142**, 350 (1966).

[37] D. Poilblanc and T. M. Rice, *Phys. Rev.* B **39**, 9749 (1989).

[38] A. R. Bishop, Europhys. Lett. **14**, 157 (1991).

[39] J. C. Hubbard, *Proc. R. Soc.* A **277**, 237 (1963).

[40] J. C. Hubbard, *Proc. R. Soc.* A **281**, 401 (1964).

[41] M. C. Gutzwiller, *Phys. Rev.* **134**, A923 (1964).

[42] G. Kotliar and A. E. Ruckenstein, *Phys. Rev. Lett.* **57**, 1362 (1986).

[43] E. H. Lieb and F. Y. Wu, *Phys. Rev. Lett.* **20**, 1445 (1968).

[44] W. Metznerand and D. Vollhardt, *Phys. Rev. Lett.* **62**, 324 (1989).

[45] A. Georges, G. Kotliar, W. Krauth, and M. J. Rozenberg, *Rev. Mod. Phys.* **68**, 13 (1996).

[46] P. W. Anderson, *Phys. Rev.* **124**, 41 (1961).

[47] J. R. Schrieffer and P. Wolff, *Phys. Rev.* **149**, 491 (1966).

[48] E. Müller-Hartmann, Z. Phys. B – Condensed Matter **74**, 507 (1989).

[49] M. Caffarel and W. Krauth, *Phys. Rev. Lett.* **72**, 1545 (1994).

[50] R. Bulla, *Phys. Rev.* B **83**, 136 (1999).

[51] M. Jarrell, *Phys. Rev. Lett.* **69**, 168 (1992).

[52] A. Georges and W. Krauth, *Phys. Rev. Lett.* **69**, 1240 (1992).

[53] A. Georges and W. Krauth, *Phys. Rev.* B **48**, 7167 (1993).

[54] M. J. Rozenberg, G. Kotliar, and X. Y. Zhang, *Phys. Rev.* B **49**, 10181 (1994).

[55] D. E. Logan, M. P. Eastwood, and M. A. Tusch, *J. Phys.: Condens. Matter* **10**, 2673 (1998).

[56] D. E. Logan and N. L. Dickens, *Eur. Phys. Lett.* **54**, 227 (1998).

[57] N. F. Mott, *Metal Insulator Transitions* (Taylor and Francis, Bristol, 1990).

[58] D. B. McWhan, T. M. Rice, and J. P. Remeika, *Phys. Rev. Lett.* **23**, 1384 (1969).

[59] A. Jayaraman, D. B. McWhan, J. P. Remeika, and P. D. Dernier, *Phys. Rev.* B **2**, 3751 (1970).

[60] D. B. McWhan, , and J. P. Remeika, *Phys. Rev.* B **2**, 3734 (1970).

[61] P. Limelette, A. Georges, P. W. D. Jérome, P. Metcalf, and J. M. Honig, Science **302**, 89 (2003).

[62] A. Sharoni *et al.*, Phys. Rev. Lett. **101**, 026404 (2008).

[63] G. Bertotti, *Hysteresis in Magnetism* (Academic Press, San Diego, 1998).

[64] M. M. Qazilbash *et al.*, Science **318**, 1750 (2007).

[65] R. Kubo, *J. Phys. Soc. Japan* **12**, 570 (1957).

[66] D. A. Greenwood, *Proc. Phys. Soc.* **71**, 585 (1957).

[67] G. D. Mahan, *Many-particle physics* (Plenum Press, New York, 1990).

[68] H. Barman and N. S. Vidhyadhiraja, *Int. J. Mod. Phys.* B**25**, 2461 (2011).

[69] N. S. Vidhyadhiraja and D. E. Logan, *J. Phys.: Condens. Matter* **39**, 313 (2004).

[70] P. Kumar and N. S. Vidhyadhiraja, *J. Phys.: Condens. Matter* **23**, 485601 (2011).

[71] D. Parihari and N. S. Vidhyadhiraja, *J. Phys.: Condens. Matter* **21**, 405602 (2009).

[72] C. M. Varma, P. B. Littlewood, S. Schmitt-Rink, E. Abrahams, and A. E. Ruckenstein, *Phys. Rev. Lett.* **63**, 1996 (1989).

[73] O. Perković, K. Dahmen, and J. P. Sethna, *Phys. Rev. Lett.* **75**, 4528 (1995).

[74] J. P. Sethna, K. A. Dahmen, and O. Perkovic, arXiv:cond-mat/0406320v3 [cond-mat.mtrl-sci] (2005).

[75] Kei Yosida and Kosaku Yamada, Supplement of the Progress of Theoretical Physics **46**, 244 (1970).

[76] F. Gebhard, *The Mott Metal-Insulator Transition* (Springer, Berlin, 1997).

[77] W. Anglin and J. Lambek, *The Heritage of Thales* (Springer-Verlag, New York, 1995), p. p 133.

[78] A. Georges, S. Florens, and T. A. Costi, J. Phys. IV France **114**, p 165 (2004).

[79] J. M. Honig and J. Spalek, Chem. Mater. **10**, 2910 (1998).

[80] N. Mori *et al.*, Solid State Physics under Pressure: Recent Adv. Anvil Devices p 247 (1985).

[81] C. Grygiel *et al.*, *J. Phys.: Condens. Matter* **20**, 472205 (2008).

[82] D. D. Sarma *et al.*, *Phys. Rev. Lett.* **93**, 097202 (2004).

[83] L. H. Mattheiss, *J. Phys.: Condens. Matter* **6**, 6477 (1994).

[84] T. Mutou and H. Kontani, *Phys. Rev.* B **74**, 115107 (2006).

[85] L. Baldassarre *et al.*, *Phys. Rev.* B **77**, 113107 (2008).

[86] A. Perucchi *et al.*, *Phys. Rev.* B **80**, 073101 (2009).

[87] S. Uchida *et al.*, *Phys. Rev.* B **43**, 7942 (1991).

[88] T. Katsufuji, Y. Okimoto, and Y. Tokura, *Phys. Rev. Lett.* **75**, 3497 (1995).

[89] M. Eckstein, M. Kollar, and D. Vollhardt, Journal of Low Temperature Physics **147**, 279 (2007).

[90] J. K. Freerick and T. P. Devereaux, *Physica* B **378–380**, 650 (2006).

[91] A. L. Fetter and J. D. Walecka, *Quantum Theory of Many-particle Systems* (McGraw-Hill, New York, 1971).

[92] K. Held *et al.*, *Phys. Rev. Lett.* **86**, 5345 (2001).

[93] D. Vollhardt *et al.*, *J. Phys. Soc. Japan* **74**, 136 (2005).

[94] G. Kotliar *et al.*, *Rev. Mod. Phys.* **78**, 865 (2006).

[95] R. Bulla, T. A. Costi, and D. Vollhardt, *Phys. Rev.* B **64**, 045103 (2001).

[96] V. E. Smith, D. E. Logan, and H. R. Krishnamurthy, *Eur. Phys. J.* B **32**, 49 (2003).

[97] D. E. Logan, M. P. Eastwood, and M. A. Tusch, *Phys. Rev. Lett.* **76**, 4785 (1996).

[98] D. E. Logan, M. P. Eastwood, and M. A. Tusch, *J. Phys.: Condens. Matter* **9**, 4211 (1997).

[99] M. P. Eastwood, Ph.D. thesis, The Queen's College, Oxford, University of Oxford, UK, 1998.

[100] E. Feenberg, *Phys. Rev.* **74**, 206 (1948).

[101] E. N. Economou, *Green's Functions in Quantum Physics* (Springer, Berlin, 1983).

[102] J. G. Bednorz and K. A. Müller, *Z. Phys.* B **64**, 189 (1986).

[103] H. Kajueter and G. Kotliar, *Phys. Rev. Lett.* **77**, 131 (1996).

[104] H. Kajueter, G. Kotliar, and G. Moeller, *Phys. Rev.* B **53**, 16241 (1996).

[105] M. Imada, A. Fujimori, and Y. Tokura, *Rev. Mod. Phys.* **70**, 1039 (1998).

[106] A. Macridin, M. Jarrell, and T. Maier, *Phys. Rev.* B **74**, 085104 (2006).

[107] M. Imada, *J. Phys. Soc. Japan* **73**, 1851 (2004).

[108] M. Eckstein, M. Kollar, M. Potthoff, , and D. Vollhardt, *Phys. Rev.* B **75**, 125103 (2007).

[109] N. Furukawa and M. Imada, *J. Phys. Soc. Japan* **61**, 3331 (1992).

[110] N. Furukawa and M. Imada, *Physica* B **186-188**, 931 (1993).

[111] P. Werner and A. J. Millis, *Phys. Rev.* B **75**, 085108 (2007).

[112] U. Schneider *et al.*, Science **322**, 1520 (2008).

[113] T. Arima, Y. Tokura, and S. Uchida, *Phys. Rev.* B **48**, 6597 (1993).

[114] Y. Tokura *et al.*, *Phys. Rev.* B **58**, R 1699 (1998).

[115] V. E. Smith, Ph.D. thesis, Balliol College, Oxford, University of Oxford, UK, 2004.

[116] P. A. Lee, N. Nagaosa, and X.-G. Wen, *Rev. Mod. Phys.* **78**, 17 (2006).

[117] N. E. Hussey *et al.*, *Phil. Trans. R. Soc.* A **369**, 1626 (2011).

[118] P. Majumdar and H. R. Krishnamurthy, arXiv:cond-mat/9604057v1 (1996).

[119] M. Ossadnik, C. Honerkamp, T. M. Rice, and M. Sigrist, *Phys. Rev. Lett.* **101**, 256405 (2008).

[120] M. Imada, *Phys. Rev.* B **72**, 075113 (2005).

[121] D. van der Marel *et al.*, Nature **425**, 271 (2003).

[122] G. A. Thomas *et al.*, *Phys. Rev. Lett.* **61**, 1313 (1988).

[123] J. Cardy, *Scaling and Renormalization in Statistical Physics* (Cambridge University Press, Cambridge, 1996).

[124] *The Science of Hysteresis*, edited by G. Bertotti and I. D. Mayergoyz (Elsevier, Oxford, 2006).

[125] F. J. Pérez-Reche, E. Vives, L. Mañosa, and A. Planes, *Phys. Rev. Lett.* **87**, 195701 (2001).

[126] A. Hubert and R. Schafer, *Magnetic Domains: The Analysis of Magnetic Microstructures*, 3rd ed. (Springer-Verlag, Berlin, 2009).

[127] E. C. Stoner and E. P. Wohlfarth, *Phil. Trans. R. Soc.* A **240**, 599 (1948).

[128] G. Durin and S. Zapperi, arXiv:cond-mat/0404512v1 [cond-mat.mtrl-sci]; "The Science of Hysteresis, Vol. II" edited by Giorgio Bertotti and I. Mayergoyz (2006), Elsevier, Amsterdom 181 (2004).

[129] B. Alessandro, C. Beatrice, G. Bertotti, and A. Montorsi, *J. Appl. Phys.* **68**, 2901 (1990).

[130] B. Alessandro, C. Beatrice, G. Bertotti, and A. Montorsi, *J. Appl. Phys.* **68**, 2908 (1990).

[131] *Spin glasses and random fields*, edited by A. P. Young (World Scientific, Singapore, 1998).

[132] J. P. Sethna, K. Dahmen, S. Kartha, J. A. Krumhansl, B. W. Roberts, and J. D. Shore, Phys. Rev. Lett **70**, 3347 (1993).

[133] K. Dahmen and J. P. Sethna, Phys. Rev. Lett. **71**, 3222 (1993).

[134] K. Dahmen and J. P. Sethna, Phys. Rev. B **53**, 14872 (1996).

[135] O. Perković, K. A. Dahmen, and J. P. Sethna, Phys. Rev. B **59**, 6106 (1999).

[136] L. Zhang *et al.*, Science **298**, 805 (2002).

[137] D. Stauffer and A. Aharony, *Introduction to Percolation Theory*, 2 ed. (Taylor & Francis Ltd,, London, 1994).

[138] S. Kirkpatrick, Rev. Mod. Phys. **45**, 574 (1973).

[139] E. Carlson, K. A. Dahmen, E. Fradkin, and S. A. Kivelson, Phys. Rev. Lett. **96**, 097003 (2006).

[140] H. E. Stanley, *Introduction to Phase Transitions and Critical Phenomena* (Oxford University Press,, London, 1971).

[141] T. R. Kirkpatrick and D. Belitz, Complex Behaviour of Glassy Systems, Lecture Notes in Physics vol. 492 (Springer, Berl) **492**, 241 (1997).

[142] S. Papanikolaou, R. M. Fernandes, E. Fradkin, P. W. Phillips, J. Schmalian, and R. Sknepnek, Phys. Rev. Lett. **100**, 026408 (2008).

[143] M. Plischke and B. Bergersen, *Equilibrium Statistical Physics*, 3rd ed. (World Scientific, Singapore, 2006).

[144] A. Clauset, C. R. Shalizi, and M. E. J. Newman, SIAM Review 51; arXiv:0706.1062v2 [physics.data-an] **51**, 661 (2009).

[145] H. Bauke, Eur. Phys. J. B **58**, 167 (2007).

[146] M. Kuntz and J. P. Sethna, J. Phys. C: Solid State Phys **18**, L927 (1985).

[147] M. E. J. Newman, Contemporary Physics; arXiv:cond-mat/0412004v3 [cond-mat.stat-mech] **46**, 323 (2005).

[148] M. L. Goldstein, S. A. Morris, and G. G. Yen, Eur. Phys. J. B **41**, 255 (2004).